



**UNIVERSITÀ DEGLI STUDI DI CATANIA**

IN CONVENZIONE CON



**UNIVERSITÀ DEGLI STUDI DI PALERMO**

---

**DOTTORATO DI RICERCA IN**

**SCIENZA DEI MATERIALI E NANOTECNOLOGIE - XXIX CICLO**

---

MARIANNA GAMBINO

**STRUCTURAL STUDY, COMPUTATIONAL ANALYSIS  
AND STRUCTURE-PROPERTY CORRELATIONS IN  
ANION CONDUCTING ELECTROLYTES FOR  
SOLID OXIDE FUEL CELLS**

TUTOR: PROF. ANTONINO MARTORANA

CO-TUTOR: DR. FRANCESCO GIANNICI

COORDINATORE: PROF. MARIA GRAZIA GRIMALDI

---

TESI PER IL CONSEGUIMENTO DEL TITOLO DI DOTTORE DI RICERCA



*“The very basic core of a man’s living spirit is his passion for adventure. The joy of life comes from our encounters with new experiences and hence there is no greater joy than to have an endlessly changing horizon, for each day to have a new and different sun.”*

Christopher McCandless



# Abstract

A combined experimental and theoretical approach has been used in order to investigate the local structural features that have an influence on ionic conductivity of IT-SOFC (Intermediate Temperature Solid Oxide Fuel Cell) electrolytes, in order to link the properties of these materials with their atomic and electronic structure.

Doped  $\delta$ -Bi<sub>2</sub>O<sub>3</sub> and LaGaO<sub>3</sub> electrolytes for AC-SOFC applications have been studied as model compounds for oxygen-ion diffusion in fluorite-like and perovskite-like materials, due to their incredibly high anion conductivity. A combined X-Ray Absorption Spectroscopy (XAS) and Density Functional Theory (DFT) study has been carried out with the aim to unveil the role of the dopants on the short range structure of these materials, to probe the preferential association of vacancies with both dopant and regular site cations, and to highlight the preferential oxygen-ion diffusion paths. This could help to define criteria for the design of new materials with improved properties.

The influence of the electrode-electrolyte interface on the overall fuel cell ionic conductivity has been also addressed. To this aim, a novel protocol to evaluate electrode-electrolyte compatibility through Scanning X-Ray Microscopy (SXM) has been developed and cation interdiffusion has been successfully probed at the interface between some electrolyte-cathode couples.



# Abstract

Il presente lavoro propone lo studio di elettroliti ceramici per IT-SOFC (Intermediate Temperature Solid Oxide Fuel Cell). In particolare, lo scopo della tesi è analizzare le caratteristiche strutturali a corto raggio aventi un'influenza sulla conducibilità ionica del materiale, al fine di collegare le proprietà degli elettroliti in esame con la loro struttura atomica ed elettronica.

Gli elettroliti a conduzione anionica studiati sono la fase  $\delta$  dell'ossido di bismuto ( $\delta$ -Bi<sub>2</sub>O<sub>3</sub>) e il lantanio gallato (LaGaO<sub>3</sub>). Data la loro elevatissima conducibilità anionica, tali materiali sono stati scelti come composti modello attraverso cui descrivere la diffusione di ioni ossigeno in elettroliti a struttura fluoritica e perovskitica. Il ruolo dei droganti sulla struttura a corto raggio di tali materiali è stata indagata mediante l'utilizzo combinato della X-Ray Absorption Spectroscopy (XAS) e della Density Functional Theory (DFT), allo scopo di svelare l'associazione preferenziale delle vacanze con i cationi (droganti e cationi del sito regolare) e individuare i cammini di diffusione dello ione ossigeno favoriti. Tali informazioni possono essere utilizzate nella definizione di criteri per la progettazione di nuovi materiali con migliorate proprietà.

Nel presente lavoro è stata inoltre studiata l'influenza dell'interfaccia elettrodo/elettrolita sulla conducibilità ionica complessiva della cella a combustibile. A tal fine, è stato sviluppato un nuovo protocollo per la valutazione della compatibilità elettrodo/elettrolita mediante Scanning X-Ray Microscopy (SXM) e l'interdiffusione cationica è stata rilevata con successo in alcune coppie catodo/elettrolita precedentemente sottoposte alle temperature operative della cella.





## **CHAPTER 1: Introduction**

<b>1. Solid Oxide Fuel Cells</b>	<b>1</b>
<b>1.1 Energy production and environment</b>	<b>1</b>
Environmental scenario	1
SOFC: an open challenge for market and for materials science	2
<b>1.2 SOFC devices and materials</b>	<b>3</b>
SOFC working scheme	3
SOFC materials	4
<b>2. Electrolytes for AC-SOFC</b>	<b>11</b>
<b>2.1 Fluorite-type and perovskite-type electrolytes.</b>	<b>11</b>
<b>2.2 <math>\delta</math>-Bi<sub>2</sub>O<sub>3</sub></b>	<b>13</b>
$\alpha$ , $\beta$ , $\gamma$ and $\delta$ Bi <sub>2</sub> O <sub>3</sub>	14
$\delta$ -Bi <sub>2</sub> O <sub>3</sub> : oxygen-ion sub lattice model for vacancy arrangement	15
Dopant effect on $\delta$ -Bi <sub>2</sub> O <sub>3</sub> stabilization	16
Ta-doped Bi <sub>2</sub> O <sub>3</sub>	18
<b>2.3 LaGaO<sub>3</sub></b>	<b>20</b>
Dopant and co-dopant effect on the ionic conductivity	21
Structural effect of A-site and B-site substitution	22
Vacancy interaction with B-site cations	23
Oxygen-ion diffusion mechanism	24
Cobalt co-doping on Mg B-site	25
<b>3. Cation interdiffusion at electrode-electrolyte interface</b>	<b>26</b>
<b>3.1 Electrode-electrolyte compatibility</b>	<b>26</b>
<b>3.2 Synchrotron X-Ray Microscopy to probe compatibility</b>	<b>27</b>

<b>4. Objectives</b>	28
<b>5. References</b>	30
<b>CHAPTER 2: Theoretical Background</b>	
<b>1. X-Ray Absorption Spectroscopy</b>	41
<b>1.1 X-Ray Absorption</b>	44
Golden rule	44
One-electron approximation	45
Dipole approximation	46
Sudden approximation	46
De-excitation mechanism	47
<b>1.2 The EXAFS function</b>	48
Monoatomic system	48
Biatomic system	49
Polyatomic system	51
Inelastic effects	51
Multiple Scattering effects	52
Disorder effects	53
<b>1.3 Experimental setup</b>	53
<b>1.4 Data analysis</b>	55
GNXAS and FEFF	57
<b>2. X-Ray Microscopy</b>	59
<b>2.1 Experimental setup</b>	61
<b>3. Density Functional Theory</b>	62
<b>3.1 Periodic Density Functional Theory</b>	66

CRYSTAL code	67
<b>4. References</b>	<b>68</b>
<b>CHAPTER 3: XAS and DFT study of <math>\text{Bi}_{1-x}\text{Ta}_x\text{O}_{1.5+x}</math> electrolytes</b>	
<b>1. Motivation of the study</b>	<b>71</b>
<b>2. Experimental and computational methods</b>	<b>72</b>
<b>3. Results and discussion</b>	<b>73</b>
<b>3.1 X-Ray Absorption Near Edge Structure</b>	<b>73</b>
<b>3.2 Extended X-Ray Absorption Fine</b>	<b>74</b>
Ta L <sub>3</sub> -edge	74
Bi L <sub>3</sub> -edge	76
<b>3.3 Density Functional Theory</b>	<b>81</b>
Geometry optimization	81
Density of States	83
<b>3.4 X-Ray Diffraction</b>	<b>84</b>
<b>3.5 Properties of V- and Nb-doped bismuth oxide</b>	<b>85</b>
<b>4. Conclusions</b>	<b>87</b>
<b>5. References</b>	<b>88</b>
<b>CHAPTER 4: XAS and DFT investigation on doped <math>\text{LaGaO}_3</math></b>	
<b>1. Motivation of the study</b>	<b>93</b>
<b>2. Experimental and computational methods</b>	<b>95</b>
<b>3. Results and discussion</b>	<b>96</b>
<b>3.1 Defect interaction and local structural distortion</b>	
in $\text{LaGa}_{0.875}\text{Mg}_{0.125}\text{O}_{2.93}$	96
Structural characterization	96

Configurational analysis by Symmetry Independent Classes (SIC)	99
Local structure distortions	102
Square pyramidal $\text{MO}_5\text{V}_o$ site	106
Tilting and dihedral distortions	107
Electronic structure	108
<b>3.2 Oxygen-ion diffusion paths in <math>\text{LaGa}_{0.875}\text{Mg}_{0.125}\text{O}_{2.93}</math></b>	112
<b>3.3 Effect of doping and co-doping on <math>\text{LaGaO}_3</math> perovskite-like structure</b>	115
<b>4. Conclusions</b>	122
<b>5. References</b>	123
<b>CHAPTER 5: Probing electrode-electrolyte interfaces by SXM</b>	
<b>1. Motivation of the study</b>	128
The LNC-LSM couple	129
<b>2. Experimental methods</b>	130
<b>3. Results and discussion</b>	131
<b>3.1 <math>\mu</math>-XRF: La <math>L_3</math>-edge</b>	131
<b>3.2 <math>\mu</math>-EXAFS: Mn K-edge</b>	133
<b>3.3 <math>\mu</math>-XANES: Nb <math>L_3</math>-edge</b>	135
<b>3.4 SXM analysis of the interfaces SDC-LSCF and SDC-LSM</b>	136
<b>4. Conclusions</b>	138
<b>5. References</b>	139
<b>CONCLUSIONS</b>	141
<b>S.1 SUPPORTING INFORMATION</b>	
<b>XAS and DFT study of <math>\text{Bi}_{1-x}\text{Ta}_x\text{O}_{1.5+x}</math> electrolytes</b>	144

## **S.2 SUPPORTING INFORMATION**

**XAS and DFT investigation on doped LaGaO<sub>3</sub>** 155

## **S.3 SUPPORTING INFORMATION**

**Probing electrode-electrolyte interfaces by SXM** 176

**Curriculum Vitae** 182

**Acknowledgements** 185

# CHAPTER 1

## Introduction

The purpose of this chapter is to draw a general overview of the state of the art of IT-SOFC technology and to contextualize the role of these devices in the development of novel clean power production strategies. A detailed description of the electrolyte materials studied in this work will be given and a novel method to probe electrode-electrolyte compatibility will be presented. Finally, the objectives of the thesis will be drawn.

### 1. Solid Oxide Fuel Cells

#### 1.1 Energy production and environment

##### *Environmental Scenario*

The overexploitation of fossil fuels ever since Industrial Revolution, has led to severe climate change consequences. The massive consumption and burning of oil, coal and natural gas during the last centuries has caused a dramatic increase of CO<sub>2</sub> and other greenhouse gases, that has relentlessly driven the earth to global warming issues.<sup>1</sup> It has been estimated that, in order to keep under control the damage cost related to temperature rising, global warming should not exceed 2°C above the average temperature of pre-industrial times.<sup>2,3</sup> The Intergovernmental Panel on Climate Change (IPCC) has foreseen that to have 50% of possibility to respect this limit, carbon emissions between 2011 and 2050 must not exceed 1,100 gigatonnes of carbon dioxide (Gt CO<sub>2</sub>);<sup>3-5</sup> to this end, during the 2015 Paris Conference COP21 the achievement of “a legally binding and universal agreement on climate” has been pursued, in order to keep global temperature rising under 2°C and limiting calamitous effects on the planet such as glaciers melting, rising of sea level and drought.<sup>6</sup>

The rising interest in finding new ways to produce energy constitutes a currently open challenge for the society. Actually, the European Framework Programme 8 (FP8) “Horizon2020” strongly promotes the study of advanced materials for clean energy production and addresses the European Union resources towards the development of

innovative technology, with the goal to obtain a 20% reduction of greenhouse gas emissions by 2020 and a further 80-95% reduction by 2050.<sup>7</sup>

In this context, the research devoted to Fuel Cell (FC) materials and in particular to Solid Oxide Fuel Cells has been strongly encouraged and funded, in order to develop new integrated networks for power production that could constitute a valid alternative to fossil fuels.

### ***Solid Oxide Fuel Cells: an open challenge for market and for materials science***

A Solid Oxide Fuel Cell (SOFC) is an electrochemical device for clean power production, that is able to produce electricity starting from pure hydrogen or carbon based fuels (natural gas or even biomasses). In the latter case, the cell is subjected to internal reforming, due to the high operating temperatures (600-1000°C).

The main advantage of this kind of technology is constituted by the low-impact emissions: if the device is fuelled by pure H<sub>2</sub> the only by-product of the reaction is water, while for other carbon-based fuels also CO<sub>2</sub>, SO<sub>x</sub> and NO<sub>x</sub> are released, but at very low levels if compared to fossil fuels.<sup>8</sup> Moreover, the device is not based on a thermodynamic cycle and actually has a much higher overall efficiency, not limited by the Carnot theorem.<sup>9</sup>

The widespread commercialization of SOFCs is currently hindered by some unsolved problems that still make the cost of this technology too high. In this context, the high operating temperatures (600-1000°C) play an important role: on one side, they have the advantage to ensure internal reforming within the cell (allowing the use of light hydrocarbons from natural gas, biogas or biomasses), to consequently avoid the use of noble metals catalysts and to produce heat that can be recycled in the so called “Combined Heat and Power Systems” (CHP) for co-generation.<sup>9,10</sup> On the other side, the major cost of plant design is linked to the operating temperatures, that have a determining influence on the choice of materials (as interconnect and sealing materials): the higher is the temperature, the higher is the cost to ensure the “balance of the plant”.<sup>10,11</sup> Fuel supply constitutes another problem that still limits the diffusion of SOFC technology. It is well established that the design of SOFC which can be competitive on the market has moved towards devices that can be fed up by carbon based fuels from natural gas or biomasses, due to the cost of hydrogen production and to the difficulty to manage with pure hydrogen fuel in terms of storage.

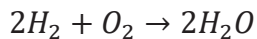
Other problems, which strongly influence the cost of the device in terms of efficiency and working life, are the long-term durability and the compatibility between components. Long-term failure is strongly related to high operating temperatures, that could enhance the degradation rate of materials, while poor compatibility between materials depends on different Thermal Expansion Coefficients (TEC), that produce mechanical stresses like cracking or delamination, and cation interdiffusion, hamper conduction or even give rise to non conductive phase segregation at the interface.

Reducing operating temperatures to the Intermediate Temperature (IT-SOFC, ~650-850°C ) or, more recently, even to a Low Temperature (LT-SOFC, ~400-650°C) range would contribute to the reduction of costs and would help to make this cells more appealing for a widespread and affordable market diffusion, imposing new challenges for material science and engineering research.

## 1.2. SOFC devices and materials

### *SOFC working scheme*

In a hydrogen-fuelled SOFC device, the overall redox reaction



takes place in the three basic FC compartments (**Figure 1.1**):

- *Anode*: the electrode where fuel oxidation takes place  
 $2H_2 \rightarrow 4H^+ + 4e^-$
- *Cathode*: the electrode where O<sub>2</sub> reduction takes place  
 $O_2 + 4e^- \rightarrow 2O^{2-}$
- *Electrolyte*: the ceramic membrane that is a pure ionic conductor that drives ions in between the two electrodes and hinders electronic conduction.

Electrons flow through an external conductor that closes the circuit and conveys electricity out from the cell.

Depending on the type of electrolyte, Solid-Oxide Fuel Cells can be classified as:

- **Anion-conducting devices (AC-SOFC)**, where O<sup>2-</sup> ions flow through the electrolyte membrane. In this kind of devices O<sub>2</sub> is reduced at the cathode, while water and other by-products are produced at the anode side, where H<sub>2</sub> is oxidized. (**Figure 1.1.a**)



- **Proton-conducting devices (PC-SOFC)**, conveying  $H^+$  ions flow through the electrolyte membrane. In this fuel cell protons produced at the anode side are carried out through the electrolyte and driven to the cathode, where the reduction semireaction takes place and water and other by-products are released. (**Figure 1.1.b**)

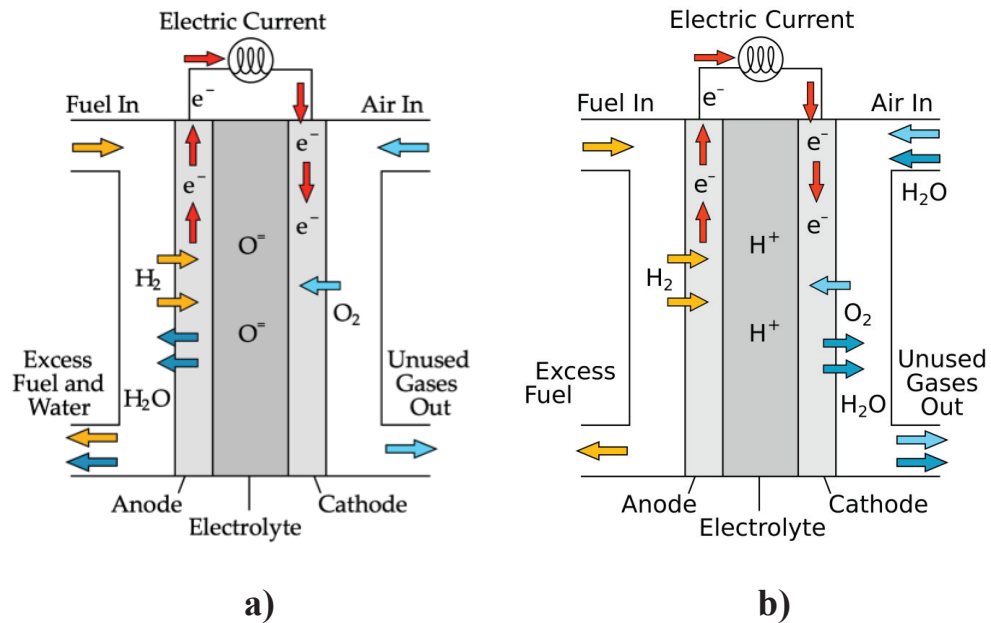


**Figure 1.1** Working scheme of **a)** anion conducting Solid Oxide Fuel Cell (AC-SOFC) and **b)** proton conducting Solid Oxide Fuel Cell (PC-SOFC).

### *SOFC materials*

**Electrolytes.** The electrolyte is a membrane that must carry  $O^{2-}$  in the case of AC-SOFCs and  $H^+$  in the case of PC-SOFCs. The main requirements of this component are:

- High ionic conductivity (ionic transference number close to unity);
- Negligible electronic conductivity, to ensure high conversion efficiency;
- High density, to ensure no gas diffusion;
- Chemical stability (it must be stable at operating temperature both to reducing and oxidizing atmospheres);
- TEC comparable to anode and cathode electrodes.<sup>9</sup>

Oxide-ion conducting electrolyte materials are typically:

- Fluorite-like materials;
- Perovskite-like materials;

- $\text{La}_2\text{Mo}_2\text{O}_9$  (LAMOX)
- Apatite and melilite structures.<sup>12</sup>

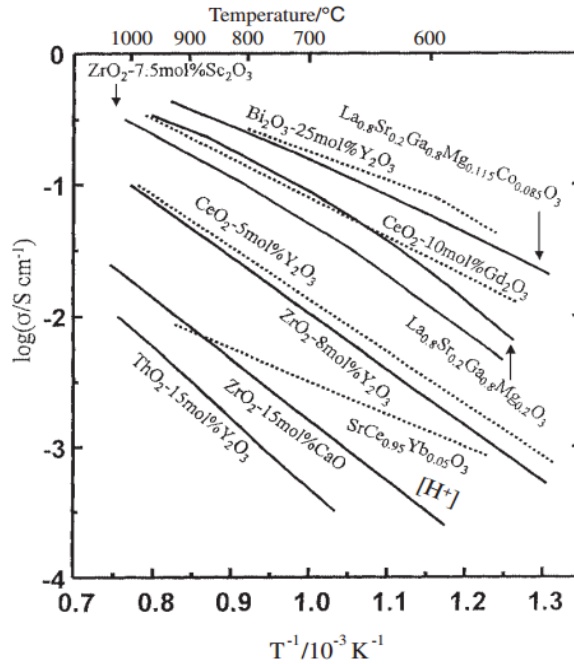


**Figure 1.2** Arrhenius plot for different electrolytes.<sup>128</sup>

Fluorite-like Ytria-stabilized  $\text{ZrO}_2$  (YSZ) is the current commercially available oxygen-ion conductor for SOFC applications, due to its long-term stability under operating conditions. If compared with other electrolytes (See **Figure 1.2**) YSZ has not a very high ionic conductivity ( $\sim 10^{-2}$  S/cm at 800-1000°C) and the need to use high operating temperatures makes this material not suitable for IT-SOFC and LT-SOFC devices, especially for small scale applications.<sup>11,12</sup> ScSZ (Sc-doped  $\text{ZrO}_2$ ) was also tested as electrolyte and showed superior oxygen-ion conductivity, but the expensive cost of Sc makes unfeasible the use of this material.<sup>12-14</sup>

Among  $\text{AO}_2$  fluorite-like materials, valid alternatives have been searched for, in order to replace YSZ in SOFC large-scale production and develop devices working at lower temperatures. Gd-doped and Sm-doped  $\text{CeO}_2$  (GDC and SDC) showed much higher oxygen-ion conductivity than YSZ in the range between 500-700°C.<sup>12,15</sup> It must be taken under consideration that at low  $p\text{O}_2$  and above 600°C these materials have a non-negligible amount of electronic n-type conductivity, due to the presence of the  $\text{Ce}^{4+}/\text{Ce}^{3+}$  redox couple, that must be controlled in order to avoid ohmic losses in the cell.<sup>16</sup>

Another fluorite-like oxygen-ion conductor is  $\delta$ -Bi<sub>2</sub>O<sub>3</sub>: among the AC-SOFC electrolytes this material shows the highest ionic conductivity in its pure form ( $\sim 1$  S/cm at 750°C).<sup>17</sup> Two main problems are related to the use of this electrolyte: *i*) due to the polymorphism of pure Bi<sub>2</sub>O<sub>3</sub>, the oxygen-ion conducting  $\delta$  phase exists only in the narrow range between 730-824°C; *ii*) the Bi<sub>2</sub>O<sub>3</sub> oxide is unstable under reducing atmospheres, where bismuth is reduced to Bi<sup>0</sup>. To solve the former problem various dopants, isovalent or aliovalent to Bi<sup>3+</sup>, can be added, while the use of Bi<sub>2</sub>O<sub>3</sub> in combination with more stable materials (e.g. doped CeO<sub>2</sub>) on the fuel side has been proposed to tackle with the latter issue.<sup>17-25</sup> Among ABO<sub>3</sub> perovskite-like materials, lanthanum gallate doped with Sr on the A site and Mg on the B site exhibits high ionic-conductivity.<sup>12,26-29</sup> Current issues for LaGaO<sub>3</sub> are related to the formation of secondary phases depending on dopant concentration.<sup>30,31</sup> On the other hand, it was also found that addition of very small amounts of Co or Fe on the B site, enhances ionic conductivity.<sup>32,33</sup> New electrolytes include La<sub>2</sub>Mo<sub>2</sub>O<sub>9</sub> (the so-called LAMOX). Again, this material has some issues related to the stabilization of the conducting polymorph (cubic  $\beta$ -phase), that can be achieved by doping the La site with alkaline or alkaline-earth cations, and the Mo site with less reducible cations (as W).<sup>12,34-36</sup> Another class of new materials is constituted by Bi<sub>4</sub>V<sub>2</sub>O<sub>11</sub>-related structures (BIMEVOX), belonging to the Aurivillius series. These structures are made up by alternating layers of Bi<sub>2</sub>O<sub>2</sub><sup>2+</sup> and perovskite VO<sub>3,5</sub><sup>2-</sup>. Also in this case room temperature stabilization of the conducting  $\gamma$  phase can be achieved by doping with Cu, Ni, Co.<sup>12,37-40</sup> Apatite and melilite structures, based on tetrahedral moieties XO<sub>4</sub>, were considered as novel electrolyte for SOFC applications. Si- and Ge-based lanthanum apatites, with La<sub>9,33+x</sub>(XO<sub>4</sub>)<sub>6</sub>O<sub>2+3x/2</sub> (X=Si, Ge) composition, show an ionic conductivity based on the presence of interstitial oxide-ions that can be driven through the bulk material.<sup>12,41,42</sup> Other electrolytes such as La<sub>1-x</sub>Ba<sub>1+x</sub>GaO<sub>4-x/2</sub> exhibit both oxide and proton conductivity. In this case oxygen-ions diffuse through the tetrahedral moieties of gallium.<sup>12,43</sup> Finally, also LaSrGa<sub>3</sub>O<sub>7</sub>, with a melilite structure, made up by layers of corner-sharing GaO<sub>4</sub> moieties that form pentagonal rings, has been taken under consideration because of its interstitial oxide-ion conductivity.<sup>12,44,45</sup>

In **Section 2**, doped lanthanum gallate and bismuth oxide electrolytes for IT-SOFC applications will be analyzed in detail.

**Anodes.** Anode SOFC materials must fulfill the following requirements:

- high catalytic activity towards the fuel oxidation semireaction;

- good ionic *and* electronic conductivity;
- stability under reducing atmosphere;
- high surface area to ensure the fuel diffusion of gases towards the electrolyte;
- good compatibility with the electrolyte.

Anode materials can be of two types:

- Ni/electrolyte cermets, that are porous composites constituted of Ni dispersed in the electrolyte material phase;
- Single phase, Mixed Ionic-Electronic Conductors (MIECs).

The use of Ni/electrolyte cermets<sup>46</sup> simultaneously ensures a very high catalytic activity towards fuel oxidation and avoids detrimental micro-structural effects typical of the use of the pure metal as electrode, such as coarsening of Ni grains and high thermal expansion coefficients. In the past years, other transition metals (ex. Fe, Pt and Au) were also tested for the use as anode materials, but Ni remains undefeated in terms of catalytic activity, playing the double role of catalyzing the H<sub>2</sub> oxidation and conducting electrons.<sup>9,47-49</sup>

The most used SOFC composite anode material is then Ni-YSZ cermet, that works at temperatures  $\geq 800^\circ\text{C}$ . The catalytic activity of this cermet is characterized by the so-called hydrogen spillover mechanism reported in **Figure 1.3**, where the Three-Phase Boundary (TPB) between Ni, YSZ and H<sub>2</sub> is represented. TPB is the active catalytic region where fuel oxidation takes place: at the TPB H<sub>2</sub> interacts with Ni<sup>0</sup> particles, which have the double role of catalyzing fuel oxidation and driving electrons to the external circuit. On the other side, the YSZ cermet component ensures the transport of the O<sup>2-</sup> anions, that react with H<sup>+</sup> to release water as by-product.

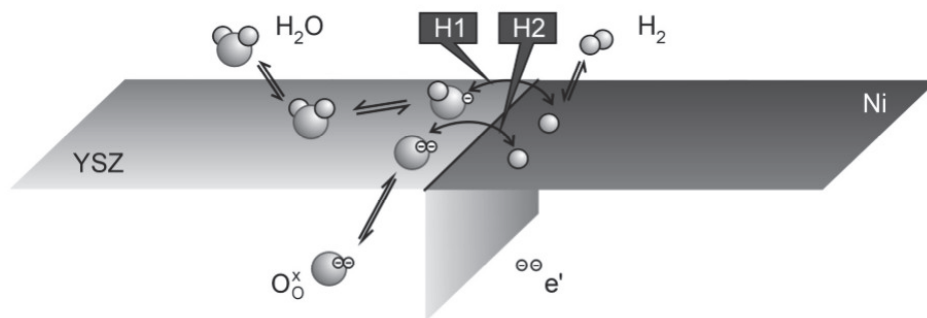
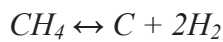


**Figure 1.3** Hydrogen spillover mechanism at the TPB zone.<sup>10,50</sup>

As outlined above, fuel supply is one of the most important issues related to the cost of SOFC technology, and the most affordable choice for the commercialization is the use, instead of pure hydrogen, of widely available hydrocarbon fuels. In this context, research is oriented towards fuelling with methane and short-chain hydrocarbons from natural gas, due to their larger availability. These fuels can be reformed inside the FC plant: the possible approaches use the heat produced by the FC operation for *i*) indirect reforming by an accessory reformer placed in close thermal contact with the FC compartment, or *ii*) direct internal fuel reforming. In the latter operation scheme, the reforming reaction is directly carried out at the anode compartment, with advantages in terms of heat transfer and exploitation of the steam produced at the anode. When methane feeds the SOFC, together with the oxidation reactions



also the following detrimental reaction takes place



leading to carbon deposition that causes poisoning of the electrode.<sup>51,52</sup> Moreover, H<sub>2</sub>S present in natural gas can lead to sulphur deposition, which is also detrimental for the anode catalytic activity. These sources of rapid poisoning with carbon involve of course hindering of direct oxidation of CH<sub>4</sub> at Ni-containing anodes.<sup>47,53</sup>

Alternative anodes to Ni-YSZ, with lower activity towards hydrocarbon cracking reaction have been proposed during past years. A composite anode consisting of Cu and 20 % Sm-doped CeO<sub>2</sub>(Cu-SDC) was proposed, due to the good electronic conductivity of Cu and simultaneously due to the low catalytic activity towards the C-H cracking<sup>54,55</sup> Cu alloys with Ni supported on silica or ceria were found to reduce the activity towards cracking: in particular, Ni/Cu-GDC was proved to have very good catalytic and redox properties towards CH<sub>4</sub> oxidation and decomposition.<sup>56</sup> Ni-Ce-ZrO<sub>2</sub> and Ni-Ce,Y-ZrO<sub>2</sub><sup>57</sup> were also proved to be valid cermet materials.

Talking about the goal of lowering SOFC operating temperatures, other Ni-ScSZ,<sup>58</sup> Ni-gadolinia-doped ceria (Ni-GDC), Ni - samarium-doped ceria (Ni-SDC)<sup>59-62</sup> and Ni-LSGM<sup>63</sup> anodes have been proposed as alternatives to Ni-YSZ cermet.<sup>10</sup>

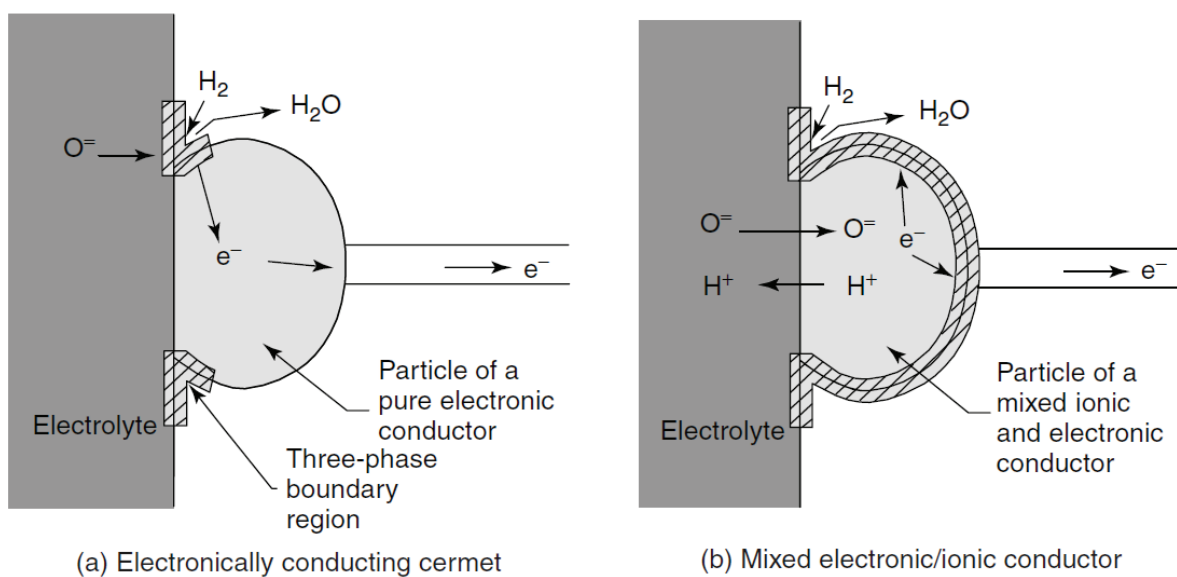


**Figure 1.4** Comparison between a TPB zone in a cermet and a TPB zone in a mixed electronic/ionic conductor (anode or cathode component)<sup>53</sup>

MIECs single-phase anodes were proposed as valid alternative to cermets. Anodes based on perovskite and fluorite-type materials have been proposed as suitable candidates that can promote direct oxidation of  $\text{CH}_4$ , limiting detrimental poisoning effects. Moreover, MIEC materials show an extended TPB if compared with cermets (**Figure 1.4**). Among MIECs,  $\text{ABO}_3$  perovskites were widely investigated: in these compounds the A site is doped with a bivalent cation (usually Sr) in order to introduce oxygen vacancies, while the B site is modified by insertion of a transition metal (Mn, Fe, Co, Ni) in order to obtain a redox centre. For instance, it was demonstrated that  $\text{La}_{1-x}\text{Sr}_x\text{Cr}_{1-y}\text{M}_y\text{O}_3$  ( $\text{M} = \text{Mn, Fe, Co, Ni}$ ) improves the catalytic properties for methane reforming.<sup>47,64</sup> While Ni doping on the B site seems to have the higher catalytic activity, it can undergo to Ni exsolution under reducing atmospheres.  $\text{La}_{1-x}\text{Sr}_x\text{Cr}_{1-y}\text{Fe}_y\text{O}_3$  shows a better catalytic activity than the most used  $\text{La}_{1-x}\text{Sr}_x\text{Cr}_{1-y}\text{Mn}_y\text{O}_3$ <sup>65</sup> and compositions such as LSCrF1030 were found to be able to catalyze the oxidation of  $\text{H}_2\text{S}$  to  $\text{SO}_2$  and to overcome sulphur deposition starting from  $600^\circ\text{C}$ .<sup>66</sup>

Doped fluorite-like  $\text{CeO}_2$  was also investigated as MIEC. Under the reducing anodic environment, cerium oxidation state is lowered from +4 to +3 and some oxygen vacancies are created. As in the case of perovskite anodes, doping ceria with transition metal introduces redox centres in the material. Examples of transition metal doped ceria used for anode applications are Mn- and Y-doped  $\text{CeO}_2$ ;<sup>67</sup> Mo- and rare earth metal-doped  $\text{CeO}_2$  is also reported in the literature.<sup>68</sup>

**Cathodes.** The requirements for cathode SOFC materials are:<sup>9</sup>

- Catalytic activity towards O<sub>2</sub> reduction;
- High electronic conductivity;
- High surface area to ensure O<sub>2</sub> a high concentration of available reduction centres;
- Thermal expansion comparable with the other FC components;
- Chemical stability towards operating conditions;
- Low solid state reactivity towards electrolyte membrane;

The oxygen reduction semireaction is accomplished through a mechanism involving several steps: *i*) dissociative O<sub>2</sub> adsorption at the cathodic surface; *ii*) electronic charge transfer; *iii*) O<sup>2-</sup> surface and bulk diffusion; *iv*) O<sup>2-</sup> transport to the electrode/electrolyte interface.<sup>10</sup> Due to the high activation energy of O<sub>2</sub> reduction reaction, lowering the temperatures entails that the cathode compartment is the major source of electrical losses.

The p-type semiconductor La<sub>1-x</sub>Sr<sub>x</sub>MnO<sub>3-δ</sub> (LSM) shows the electrode requirements previously listed for cathodes. However, LSM has a TPB zone limited to the region where O<sub>2</sub>, cathode an electrolyte are in contact (**Figure 1.4**); for this reason the LSM morphology and the formation of secondary phases at electrode/electrolyte interface can dramatically influence the catalytic activity of this cathodic material.<sup>69</sup>

Therefore, the preferred materials for cathode applications are MIECs perovskites, where TPB is extended to a 3D dimensionality. In these materials the O<sub>2</sub> surface exchange and bulk/surface diffusion are the rate determining steps of the O<sub>2</sub> reduction semireaction. The advantages in using MIECs are most evident for SOFCs operating at low temperatures (~650°C), because at lower operating temperatures the polarization of the cathode tends to increase.<sup>53</sup>

Among MIECs, three main classes can be identified:

- Simple ABO<sub>3</sub> perovskites (LaCoO<sub>3</sub>, BaCoO<sub>3</sub>, LaFeO<sub>3</sub>);
- Ruddlesden-Popper perovskites A<sub>n+1</sub>B<sub>n</sub>O<sub>3n+1</sub> (Ln<sub>2</sub>(Ni,Co, Fe, Cu)O<sub>4+d</sub> where Ln=Nd, La or Pr);
- Double perovskites AA'B<sub>2</sub>O<sub>6</sub> (RBaCo<sub>2</sub>O<sub>5+d</sub> where R=rare earth, 0≤x≤1).<sup>69</sup>

Among simple cubic perovskites, (La, Sr)(Co, Fe)O<sub>3</sub> (LSCF) has been extensively studied as cathode material. It has been noted that increasing Sr concentration enhances TEC<sup>69,70</sup> while

Fe doping has the opposite effect.<sup>10,69,71</sup> Another promising cathode for LT-SOFC and IT-SOFC applications is  $\text{Ba}_{0.5}\text{Sr}_{0.5}\text{Co}_{0.8}\text{Fe}_{0.2}\text{O}_3$ , that exhibits fast bulk and surface diffusion at 600°C.<sup>69</sup> Further cathodic materials can be found in the class of Ruddlesden-Popper perovskites. These oxides have composition  $\text{A}_{n+1}\text{B}_n\text{O}_{3n+1}$  and are made of  $n$   $\text{ABO}_3$  layers interposed in between AO rock-salt layers;<sup>69,72</sup> the A cations are usually alkaline or rare earth metals, while B species are transition metals. Examples of compounds with  $n=1$  are  $\text{La}_2\text{NiO}_{4+\delta}$  and  $\text{La}_2\text{CuO}_{4+\delta}$ , characterized by the presence of excess oxygen, that is interstitially hosted between two perovskite layers. It was proved that this oxygen in excess leads to a faster ion diffusion compared to defective cuprates, due to the anisotropic nature of oxygen-ion transport<sup>73</sup> through the  $ab$  plane of the rock-salt-like  $\text{A}_2\text{O}_2$  layer.<sup>74,75</sup> The advantage with respect to the isotropic diffusion in simple perovskites is that the Ruddlesden-Popper materials have not to be heavily substituted to induce the formation of oxygen vacancies and so they are not subjected to defect interaction.

Finally, double perovskites  $\text{AA}'\text{B}_2\text{O}_6$  ( $\text{A}$ =rare earth,  $\text{A}'$ =alkaline metal and  $\text{B}$ =Co, Mn) have been recently proposed as IT-SOFC and LT-SOFC cathodes. These materials have A and A' alternating layers, with oxygen vacancies mainly set on the A planes, so forming channels that enhance ionic conductivity.<sup>69,76</sup>

## 2. ELECTROLYTES FOR AC-SOFC

### 2.1. Fluorite and perovskite-type electrolytes

Conventional oxide-ion conducting electrolytes for AC-SOFC applications have the following types of structure:

- Fluorite-like ( $\text{AO}_2$ );
- Perovskite-like ( $\text{ABO}_3$ ).

Fluorite-like electrolytes show an  $\text{AO}_2$  structure, where A cations are arranged in an *fcc* network and have a cubic coordination with O atoms. Each oxygen is in turn coordinated with four A cations, leading to tetrahedral moieties. (**Figure 1.5 a**)

On the other side, perovskite-like materials have an  $\text{ABO}_3$  structure, where the A cation has an eight-fold coordination with the  $\text{BO}_6$  octahedra. (**Figure 1.5 b**)



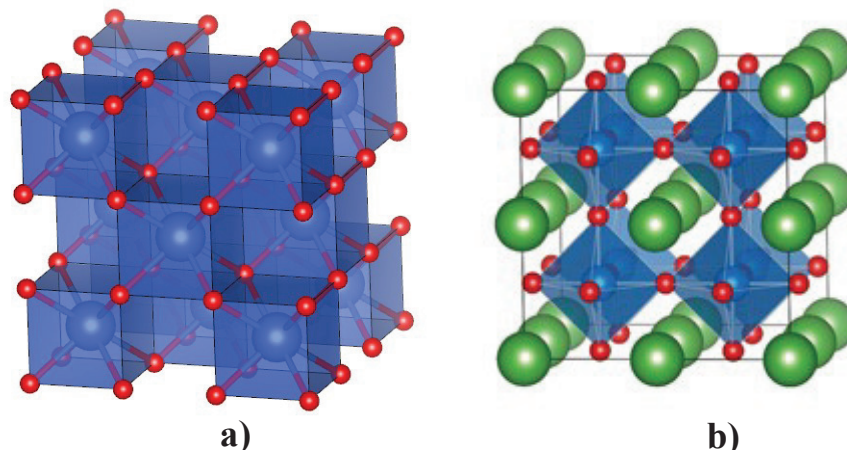


**Figure 1.5** a) Fluorite-like  $\text{AO}_2$  structure (A-site cations and  $\text{AO}_8$  polyhedra in blue and O atoms in red). b) Ideal cubic perovskite-like  $\text{ABO}_3$  structure (A-site cations in green, B-site cations and  $\text{BO}_6$  polyhedra in blue and O atoms in red).

The common features that make this kind of structures highly efficient oxygen-ion conductors are:

- **High concentration of oxygen vacancies ( $\text{V}_\text{O}$ ):** in order to allow anion diffusion inside the electrolyte sublattice,  $\text{V}_\text{O}$  defects must be introduced. Oxygen vacancies are commonly introduced by doping with cations having lower charge than the regular site cation. By the way, some solid electrolytes could have an intrinsically defective oxygen-ion sublattice in their undoped pure form.
- **Energy equivalence of the conductive sites:** the activation barrier of  $\text{O}^{2-}$  diffusion inside the structure is strongly influenced by the energetic equivalence of oxygen sites. Indeed, diffusion is favoured if  $\text{O}^{2-}$  diffusion paths are evenly distributed and then equally probable within the oxide matrix. Oxygen-ion diffusion can be typically hindered by a pronounced size mismatch between regular cation and dopant, that can lead to marked local distortions (for instance,  $\text{BO}_6$  octahedra tilting and deformation in perovskite-like structures), with consequent overall lowering of symmetry in the system.<sup>77</sup>
- **Limited defect interactions and low activation energy barrier (less than 1 eV):**<sup>78,79</sup> the amount of dopant and vacancies introduced in the lattice must be taken under control. Indeed, defect interaction could strongly affect the electrolyte performances, severely damping  $\text{O}^{2-}$  diffusion and enhancing the activation energy barrier that should be kept under 1 eV.

The scientific literature on fluorite and perovskite electrolytes is so huge that an attempt to give a comprehensive description of the advances in this field is helpless. Instead, the following **Sections 2.2** and **2.3** are dedicated to an account of the state-of-the-art for two representative oxides of these two classes of ionic conductors,  $\delta\text{-Bi}_2\text{O}_3$  and doped lanthanum gallate, respectively. These compounds are deeply investigated in this doctoral thesis due to their outstanding oxide ion conductivity and, consequently, to their interest as reference compounds to study the mechanism of oxide-ion solid state conduction.

## 2.2. $\delta\text{-Bi}_2\text{O}_3$

Among all solid electrolytes,  $\delta\text{-Bi}_2\text{O}_3$  exhibits the highest oxygen-ion conductivity known so far (about  $1 \text{ S}\cdot\text{cm}^{-1}$  at  $750^\circ\text{C}$ , two orders of magnitude higher than the commercially used YSZ) (See **Figure 1.2**) and for this reason it is considered the reference compound in the field of solid state anionic conduction.<sup>17</sup>

The high-temperature phase of bismuth oxide, the so-called  $\delta\text{-Bi}_2\text{O}_3$ , shows an average  $\text{AO}_2$  fluorite-like structure belonging to the  $Fm\text{-}3m$  space group. The incredibly high oxygen-ion conductivity of this phase is related to its intrinsically defective oxygen-ion sublattice, that exhibits a 25% of vacant oxygen sites in its unit cell, giving rise to a  $\text{BiO}_{1.5}(\text{V}_\text{O})_{0.5}$  stoichiometry.<sup>17,80</sup> Despite its stunning oxygen-ion conductivity,  $\text{Bi}_2\text{O}_3$  shows two main drawbacks concerning its concrete use as electrolyte in IT-SOFC technology:

- The  $\delta$  phase of bismuth oxide is thermodynamically stable only between  $730$  and  $825^\circ\text{C}$ .
- Bismuth oxide is unstable under  $\text{H}_2$  atmosphere, where  $\text{Bi}^{3+}$  is reduced to  $\text{Bi}^0$ .

The literature accounts first drawback can be easily solved by doping  $\text{Bi}^{3+}$  site with isovalent or aliovalent dopants, which stabilize the  $\delta$ -phase at room temperature, significantly extending the range of accessible temperatures.

Moreover, the presence of a huge concentration of intrinsic vacancies implies that the material can be doped with cations of the same or even higher valence than  $\text{Bi}^{3+}$ , so that  $\text{V}_\text{O}$  concentration can be strategically modulated in order to tailor the diffusion properties of the electrolyte.<sup>17-24</sup> For what concerns  $\text{Bi}^{3+}$  instability under reducing atmospheres, the use of bismuth oxide in combination with more stable materials (i.e. doped  $\text{CeO}_2$ , YSZ) on the fuel side (layered electrolytes) has been proposed to overcome this issue.<sup>25</sup>

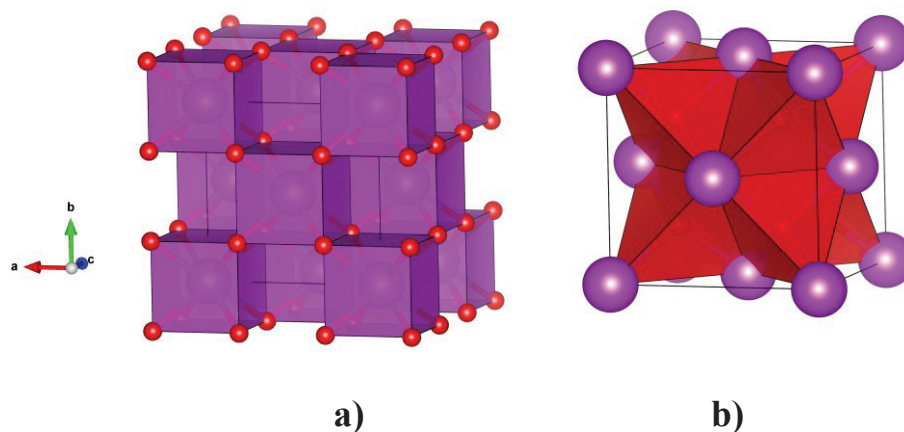


**Figura 1.6** a) Coordination polyhedra around Bi in ideal fluorite-like  $\delta\text{-Bi}_2\text{O}_3$  and b) coordination polyhedra around O. (Bi atoms and  $\text{BO}_8$  polyhedra in purple, O atoms and  $\text{OBi}_4$  polyhedra in red).

### *$\alpha$ , $\beta$ , $\gamma$ and $\delta\text{-Bi}_2\text{O}_3$*

Depending on the temperature range, bismuth oxide can adopt four allotropic forms, named  $\alpha$ ,  $\beta$ ,  $\gamma$  and  $\delta\text{-Bi}_2\text{O}_3$ .<sup>17</sup>

At room temperature, bismuth oxide exists as the non-conductive monoclinic  $\alpha\text{-Bi}_2\text{O}_3$ , belonging to the  $P2_1/c$  space group, where alternating layers of bismuth and oxygen atoms are arranged.  $\text{Bi}^{3+}$  coordination is comprised between five and six, leading to a distorted octahedral local environment and empty channels can be observed (**Figure 1.6 a**).<sup>81,82</sup>

At about  $730^\circ\text{C}$   $\alpha\text{-Bi}_2\text{O}_3$  undergoes a phase transition to  $\delta\text{-Bi}_2\text{O}_3$ , that exists up to  $825^\circ\text{C}$ , its melting point temperature.

$\delta\text{-Bi}_2\text{O}_3$  adopts an *fcc* network of four  $\text{Bi}^{3+}$  occupying the  $4a$  sites of the  $Fm\text{-}3m$  space group and having a defective cubic coordination: to ensure a neutral charge two oxygen vacancies per unit cell must be introduced. On the other side, oxygen-ion sublattice is composed by six atoms occupying the  $8c$  sites and having a tetrahedral coordination with Bi atoms (**Figure 1.6 a and b**).<sup>80,83–85</sup>

By cooling down the  $\delta$ -phase, two other metastable bismuth oxide polymorphs have been observed:  $\beta\text{-Bi}_2\text{O}_3$  (**Figure 1.7 b**) at and  $\gamma\text{-Bi}_2\text{O}_3$  (**Figure 1.7 c**).<sup>86–88</sup>

The tetragonal  $\beta\text{-Bi}_2\text{O}_3$  belongs to the  $P\text{-}42_1c$  space group; it is obtained at  $650^\circ\text{C}$  by cooling the  $\delta$ -form and shows a pseudo-bipyramidal trigonal coordination around  $\text{Bi}^{3+}$ . The  $\gamma\text{-Bi}_2\text{O}_3$

has body centred cubic  $I23$  symmetry and is characterized by an octahedral coordination of  $\text{Bi}^{3+}$ . It is obtained at 640 °C by slowly cooling down the  $\delta$ -phase.

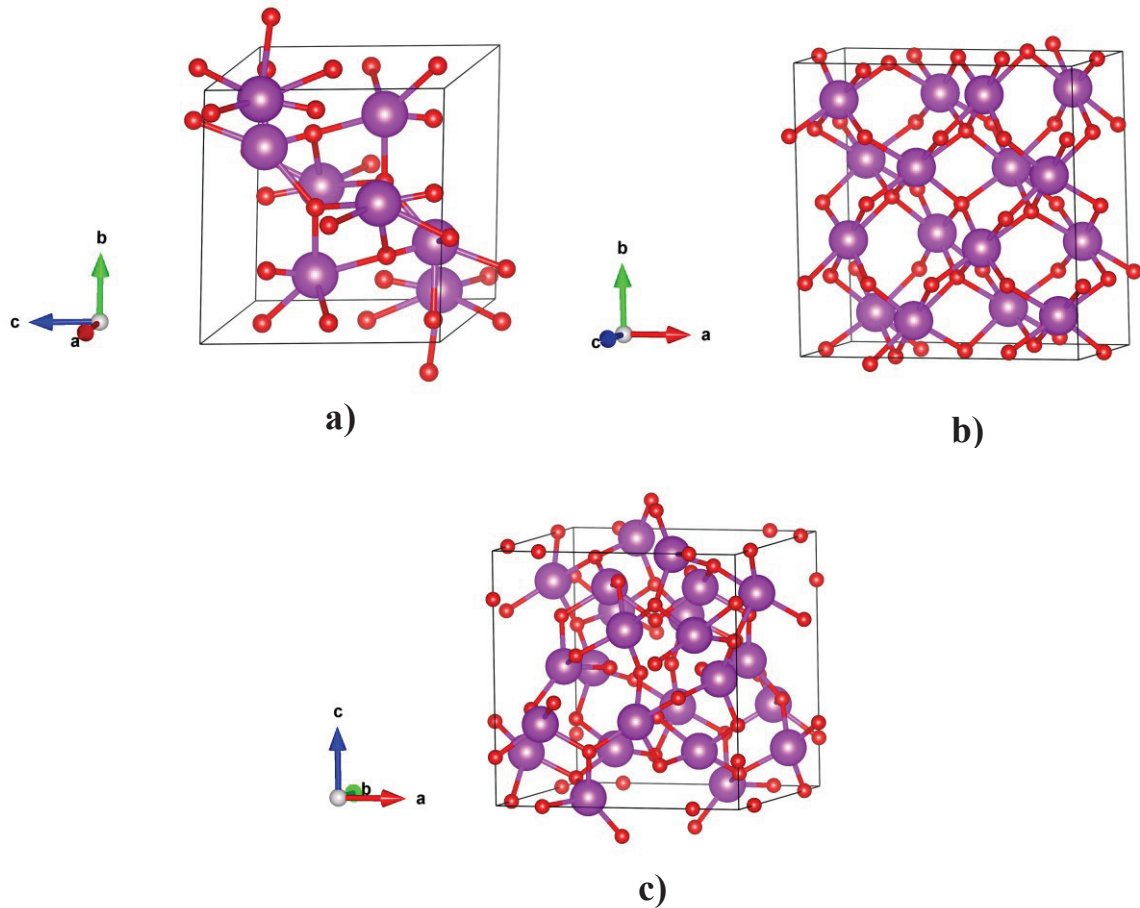


**Figure 1.7** a)  $\alpha\text{-Bi}_2\text{O}_3$ , b)  $\beta\text{-Bi}_2\text{O}_3$  and c)  $\gamma\text{-Bi}_2\text{O}_3$ .

### ***$\delta\text{-Bi}_2\text{O}_3$ : oxygen-ion sublattice models for vacancy arrangement***

Several models have been proposed to describe the oxygen vacancies arrangement in pure  $\delta\text{-Bi}_2\text{O}_3$ .

Sillen et al. suggested a  $\langle 111 \rangle$  ordered defect sublattice model, that was rejected by Gattow et al. who proposed a model where each of the oxygen  $\delta c$  sites has equal probability (75% of the sites) to be occupied.<sup>80,82</sup>

Willis et al. studied by Neutron Diffraction fluorite-type materials like  $\text{CaF}_2$ ,  $\text{UO}_2$  e  $\text{ThO}_2$ .<sup>89</sup> They demonstrated that the structure of the anionic sublattice of these oxides can be interpreted by a displacement of oxygen-ions from their regular tetrahedral  $\delta c$  site ( $\frac{1}{4}, \frac{1}{4}, \frac{1}{4}$ ), towards one of the four  $\langle 111 \rangle$  directions, giving rise to  $32f$  displaced sites ( $\frac{1}{4}+\delta, \frac{1}{4}+\delta, \frac{1}{4}+\delta$ ).

The same model could be extended to the  $\delta$  phase of bismuth oxide where the incredibly high ionic conductivity can be attributed to the presence of an increased number of conductive sites. Indeed, Battle et al. demonstrated through Neutron Diffraction that oxygen-ions in  $\delta$ - $\text{Bi}_2\text{O}_3$  have the same probability to occupy both  $8c$  and  $32f$  sites.<sup>83,84</sup>

By a pioneering X-Ray Absorption Spectroscopy experiment at high temperatures on undoped  $\delta$ - $\text{Bi}_2\text{O}_3$ , Koto et al. confirmed the displacement of oxygen-ions from their tetrahedral sites of the *fcc* cation network. They observed a distribution of two Bi-O distances in the first shell, in agreement with a random displacement of oxygen ions from their regular  $8c$  sites.<sup>85</sup>

It was also observed that, due to the stereochemically active  $6s^2$  lone pair on  $\text{Bi}^{3+}$ , intrinsic vacancies in fluorite-like bismuth oxide tend to orient themselves in preferential directions. In particular, pure  $\delta$ - $\text{Bi}_2\text{O}_3$  tend to order vacancies in the  $\langle 110 \rangle$  direction, that would ensure a high degree of disorder in the system, while doping with rare earth cations, that possess a lower polarizability than  $\text{Bi}^{3+}$ , induces a preferred vacancy allignement in the  $\langle 111 \rangle$  direction.<sup>83,84</sup>

### ***Dopant effect on $\delta$ - $\text{Bi}_2\text{O}_3$ stabilization***

As it has been previously explained, the stabilization of an average fluorite-type  $\delta$ -phase to room temperature can be achieved by doping bismuth oxide with cations isovalent or aliovalent to  $\text{Bi}^{3+}$ . However, even if doping bismuth oxide with various heteroatoms extends the stability of the cubic phase to lower temperatures, this usually happens at the expense of conductivity that is generally decreased if compared to pure  $\delta$ - $\text{Bi}_2\text{O}_3$ .

From a structural viewpoint, bismuth oxide is an extremely complex system and a great variety of possible phases can be achieved through a delicate balance between dopant concentration, temperature treatment and heating rate. Some isovalent and higher valence dopants were found to be very effective in both stabilizing the  $\delta$  phase and maintaining a good ionic conductivity in the material.<sup>17</sup> For example, the insertion of trivalent cations on the  $\text{Bi}^{3+}$  site can lead both to the stabilization of an *fcc* network, typical of the fluorite-like phase, or of a rhombohedral phase, depending on the size of the  $\text{M}^{3+}$  cation and on the dopant concentration.<sup>17</sup> It was observed that dopants with a relatively large radius stabilize the rhombohedral phase, while dopants with relatively small radius tend to stabilize the cubic phase. In particular  $(\text{Bi}_2\text{O}_3)_{1-x}(\text{M}_2\text{O}_3)_x$  solid solutions, where  $\text{M}=\text{Y}, \text{Er}, \text{Dy}, \text{Gd}$  generally lead to the stabilization of an *fcc* network, while solid solutions with  $\text{M}=\text{La}$ , generally stabilize the

rhombohedral phase. Among these highly conductive solid solutions,  $\text{Bi}_2\text{O}_3\text{-Er}_2\text{O}_3$  system was proved to have one of the highest ionic conductivity among doped systems (about  $0.4 \text{ S}\cdot\text{cm}^{-1}$  at  $700^\circ\text{C}$  in air for 20%mol of  $\text{M}_2\text{O}_3$  doping).<sup>17,90-92</sup>

The minimum concentration value ( $x_{min}$ ) required to stabilize the cubic phase in  $(\text{Bi}_2\text{O}_3)_{1-x}(\text{M}_2\text{O}_3)_x$  can be correlated with the dopant ionic radius, showing two opposite trends:

- the ionic conductivity increases with the ionic radius;
- $x_{min}$  value increases with the ionic radius.

It was also observed that doped bismuth oxide electrolytes with high values of  $x_{min}$  cause a low ionic conductivity in the material.<sup>17,91,92</sup>

Due to the presence of a 25% of intrinsic vacancies in pure  $\delta\text{-Bi}_2\text{O}_3$ , it is possible to dope the material with higher valence cations without severely affecting the overall oxygen vacancy concentration. In this context, doping of bismuth oxide with cations such as  $\text{Re}^{7+}$  or  $\text{Mo}^{6+}$ ,  $\text{V}^{5+}$ ,  $\text{Nb}^{5+}$ , and  $\text{Ta}^{5+}$  represents a continuing topic of research;<sup>19,20</sup> in particular, much interest has been devoted to the insertion of pentavalent  $\text{Ta}^{5+}$ ,  $\text{Nb}^{5+}$ , and  $\text{V}^{5+}$  cations.<sup>21-24,93</sup>

The role of such small and high-valence cations is thought to be two-fold:

- stabilizing the fluorite structure at low temperature;
- providing a favourable pathway for the anion conduction.

$(\text{Bi}_2\text{O}_3)_{1-x}(\text{M}_2\text{O}_5)_x$  solid solutions (with  $\text{M}=\text{V}, \text{Nb}, \text{Ta}$ ) show a great variety of superstructures, that have been characterized through diffraction techniques (ED, ND, XRD).<sup>93</sup> Indeed, from the viewpoint of structural analysis, not only the dopant ionic radius and concentration have a role, but also the charge unbalance introduced by  $\text{M}^{5+}$  cation must be carefully considered.  $\text{M}^{5+}$  cations in the matrix of  $\text{Bi}_2\text{O}_3$  show the tendency to gather in highly symmetric structural motives, giving rise to complex superstructures. The orientation of these motives and their interaction with the oxide matrix has two competitive driving forces:

- the charge balance (which depends on the amount of dopant introduced);
- the coordination of the dopant (which depends on the type of M cation).

For example, in  $(\text{Bi}_2\text{O}_3)_{1-x}(\text{V}_2\text{O}_5)_x$  solid solutions vanadium is organized in  $\text{VO}_4$  moieties that, depending on the concentration of the dopant, can be isolated in the  $\text{Bi}_2\text{O}_3$  lattice (Type I

superstructure) or further aggregated with other  $\text{VO}_4$  tetrahedra (Type II), where V cations are generally clustered in groups of four atoms.<sup>94,95</sup>

Vanadium-doped bismuth oxide is very conductive due to the possibility of a large local structure rearrangement around  $\text{V}^{5+}$ , that assists the anion diffusion through the flexible first shell  $\text{V}^{5+}$ -O coordination.<sup>21</sup>

Among higher valence dopants, Ta and Nb show very similar behaviour in the structural stabilization of  $\delta\text{-Bi}_2\text{O}_3$ , because they possess identical ionic radii. Nevertheless, Ta doping was generally less studied than Nb doping.<sup>93,96</sup>

Diffraction studies<sup>93,96</sup> showed that  $(\text{Bi}_2\text{O}_3)_{1-x}(\text{Nb}_2\text{O}_5)_x$  and  $(\text{Bi}_2\text{O}_3)_{1-x}(\text{Ta}_2\text{O}_5)_x$  solid solutions respectively adopt  $\text{NbO}_6$  and  $\text{TaO}_6$  rigidly coordinated octahedral environments. Depending on dopant concentration, these  $\text{NbO}_6$  and  $\text{TaO}_6$  octahedra could be isolated (Type I superstructure) or could further aggregate giving rise to pyrochlore-like  $\text{A}_2\text{B}_2\text{O}_7$  structures (Type II). Among these compositions, the highest anionic conductivity ( $0.19 \text{ S}\cdot\text{cm}^{-1}$ ) was observed for the system  $(\text{Bi}_2\text{O}_3)_{1-0.85}(\text{Nb}_2\text{O}_5)_{0.15}$ .<sup>17,97</sup>

### ***Ta-doped $\text{Bi}_2\text{O}_3$***

Diffraction studies demonstrated that  $\text{Bi}_2\text{O}_3\text{-Ta}_2\text{O}_5$  solid solutions adopt different types of superstructures, depending on the dopant concentration. Type I  $\text{Bi}_2\text{O}_3\text{-Ta}_2\text{O}_5$  superstructures are obtained below 10% of Ta and show isolated  $\text{TaO}_6$  octahedra. Between 10 and 25% of Ta,  $\text{TaO}_6$  structural motives related to the pyrochlore structure appear and give rise to the so-called Type II superstructure.<sup>96,98</sup>

In the  $\text{A}_2\text{B}_2\text{O}_7$  pyrochlore structure A and B cations are arranged in a *fcc* sublattice like in the fluorite network, while the  $\text{O}^{2-}$  anions form  $\text{AO}_8$  and  $\text{BO}_6$  coordination polyhedra. In this kind of compounds, three different structural motives involving the B species can be discerned (**Figure 1.8**):

- strings of  $\text{BO}_6$  octahedra oriented towards the  $\langle 110 \rangle$  directions;
- tetrahedral  $\text{B}_4\text{O}_{18}$  clusters, arising from the interconnection of two  $\text{BO}_6$  strings;
- $\text{B}_7\text{O}_{30}$  clusters formed by two corner-sharing  $\text{B}_4\text{O}_{18}$  tetrahedral clusters.

Because  $\text{Bi}_2\text{O}_3\text{-Ta}_2\text{O}_5$  solid solutions have an A:B ratio that is larger than 1 (with A = Bi, B = Ta), they show less interconnection between the octahedra with respect to the ideal pyrochlore structure, giving rise to “inflated pyrochlore” structures.<sup>93</sup> To properly account for the long-range order in  $\text{M}^{5+}$ -doped bismuth oxides, as required by the structural models based on

diffraction data, it was necessary to allow for a 3D incommensurate superlattice ordering.<sup>22,99,100</sup>

Although long range superstructures were characterized extensively in recent years by using a variety of structural techniques, such as synchrotron X-Ray Diffraction (SR-XRD), Electron Diffraction (ED),<sup>96</sup> High Resolution TEM<sup>98</sup> and Neutron Powder Diffraction (NPD),<sup>22</sup> there is a lack of studies about the local environment of cations in Ta-doped bismuth oxide, while a deeper knowledge of the local structure around the dopant site would help to shed light on the role of the dopant in the stabilization of the  $\delta$ -phase at room temperature and on the structural features that govern oxygen-ion conduction inside this material.

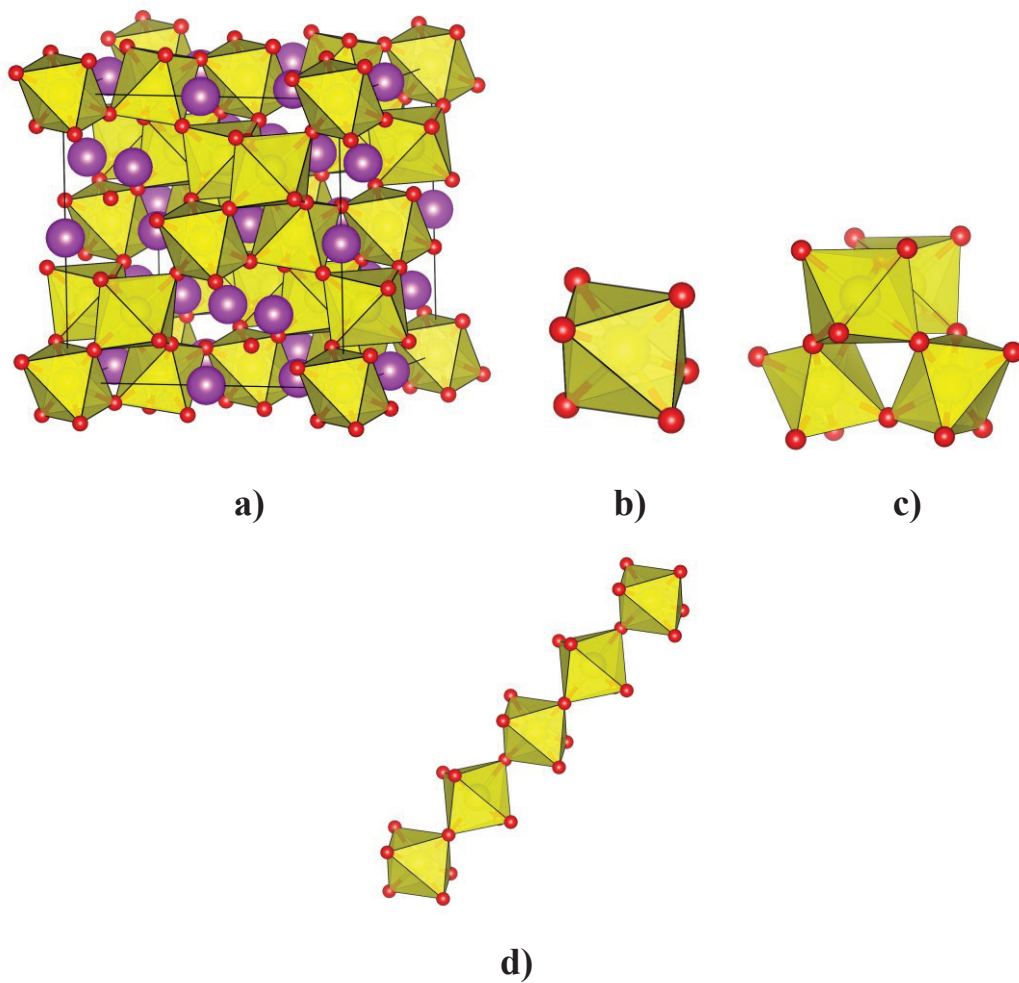


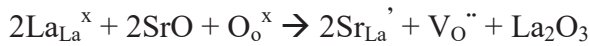
**Figure 1.8** a) Pyrochlore-like  $A_2B_2O_7$  b) isolated  $BO_6$  octahedra, c) tetrahedral  $B_4O_{18}$  clusters and d) strings of  $BO_6$  corner-sharing octahedra.



### 2.3. LaGaO<sub>3</sub>

Doped LaGaO<sub>3</sub> (LG) represents one of the top performing oxygen-ion conducting electrolytes known so far.<sup>12,101–104</sup>

This material is a perovskite-type oxide with ABO<sub>3</sub> structure belonging to the orthorhombic *Pbnm* (**Figure 1.9**) space group. The A cations have a 12-fold coordination with oxygen and an approximately cubic coordination with BO<sub>6</sub> octahedra. Due to the high structural flexibility typical of perovskite materials, doping with small percentages of Sr<sup>2+</sup> and Mg<sup>2+</sup> on the A and B sites, respectively, allows LG to accommodate a large concentration of anion vacancies, according to the following equations:



This doping with bivalent species allows reaching very high anionic conductivity, around 0.14 S/cm at typical IT-SOFC operating temperatures, for the compositions La<sub>0.9</sub>Sr<sub>0.1</sub>Ga<sub>0.9</sub>Mg<sub>0.1</sub>O<sub>2.85</sub> (LSGM1010), La<sub>0.9</sub>Sr<sub>0.1</sub>Ga<sub>0.8</sub>Mg<sub>0.2</sub>O<sub>2.85</sub> (LSGM1020) or La<sub>0.8</sub>Sr<sub>0.2</sub>Ga<sub>0.8</sub>Mg<sub>0.2</sub>O<sub>2.8</sub> (LSGM2020).<sup>26–29,104,105</sup> Moreover, a thermal expansion coefficient (TEC) of about 11.5x10<sup>-6</sup> K<sup>-1</sup>, is compatible with the most common SOFC electrodes.

However, some drawbacks must be taken into account. For example, secondary phases due to the loss of Ga<sub>2</sub>O<sub>3</sub> at sintering temperatures (around 1400°C) are usually formed during the preparation of the ceramic electrolyte, even if the presence of these phases does not drastically affect the conduction properties of the material.<sup>30,31</sup> Another problem related to the long term durability of the complete cell is that the mechanical and bending strength of this electrolyte at operating temperatures is not very good.<sup>104</sup>

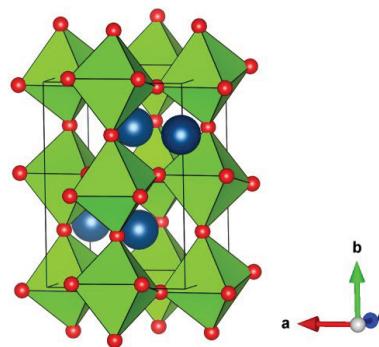


**Figure 1.9** LaGaO<sub>3</sub> unit cell belonging to the *Pbnm* space group. Ga octahedra are depicted in green, O atoms in red and La atoms in blue.

## ***Dopant and co-dopant effect on the ionic conductivity***

As previously described, doping  $\text{La}^{3+}$  and  $\text{Ga}^{3+}$  with alkaline earth elements, such as  $\text{Sr}^{2+}$  on the A-site and  $\text{Mg}^{2+}$  on the B-site, leads to a high anionic conductivity of LG materials (See **Figure 1.2**), due to the incorporation of  $\text{V}_\text{O}$  defects that are absent in the pure compound. In this way,  $\text{La}_{1-x}\text{Sr}_x\text{Ga}_{1-y}\text{Mg}_y\text{O}_{3-\delta}$  phases are formed, and the best conductivity values, that are definitely higher than YSZ at 800 °C, are found for  $x=0.10-0.20$  %mol and  $y=0.15-0.20$ %mol.<sup>26-29,104</sup>

The effect of other alkaline earth metals has been tested both on the A and B site, but  $\text{Sr}^{2+}$  and  $\text{Mg}^{2+}$  (1.44 Å and 0.72 Å) have similar size compared to  $\text{La}^{3+}$  and  $\text{Ga}^{3+}$  (1.36 Å and 0.62 Å), leading to the lowest size mismatch (and to the less amount of distortion) between dopant and regular site cations. Indeed, Ishihara et al. and Stevenson et al. tested  $\text{Ca}^{2+}$ ,  $\text{Sr}^{2+}$  and  $\text{Ba}^{2+}$  doping on the A-site and demonstrated that ionic conductivity is higher in the case of  $\text{Sr}^{2+}$ .<sup>27,33</sup>

It was further explained through Pair Distribution Function (PDF) analysis and Density Functional Theory (DFT) simulations, that the decrease in ionic conductivity in Ba-doped lanthanum gallate ( $\text{La}_{0.95}\text{Ba}_{0.05}\text{Ga}_{0.8}\text{Mg}_{0.2}\text{O}_{3-\delta}$ ) can be ascribed to a defect interaction between  $\text{Ba}^{2+}$  and  $\text{V}_\text{O}$  that limits oxygen-vacancy mobility.<sup>106</sup> On the other side, if  $\text{Ba}^{2+}$  is used as co-dopant together with  $\text{Sr}^{2+}$  on the  $\text{La}^{3+}$  site ( $\text{La}_{0.8}\text{Sr}_{0.2-x}\text{Ba}_x\text{Ga}_{0.8}\text{Mg}_{0.2}\text{O}_{2.8}$ ), an increase of conductivity of 44% with respect to LSGM was observed (i.e.  $\text{La}_{0.8}\text{Sr}_{0.15}\text{Ba}_{0.05}\text{Ga}_{0.8}\text{Mg}_{0.2}\text{O}_{2.8}$  has  $0.047 \text{ S}\cdot\text{cm}^{-1}$  at 800°C).<sup>107</sup>

From a computational viewpoint, Khan et al. tried the entire alkaline and alkaline-earth metal series, on the A and B-sites and demonstrated that  $\text{Sr}^{2+}$  and  $\text{Mg}^{2+}$  have respectively the lower solution energy (**Figure 1.10**).<sup>108</sup>

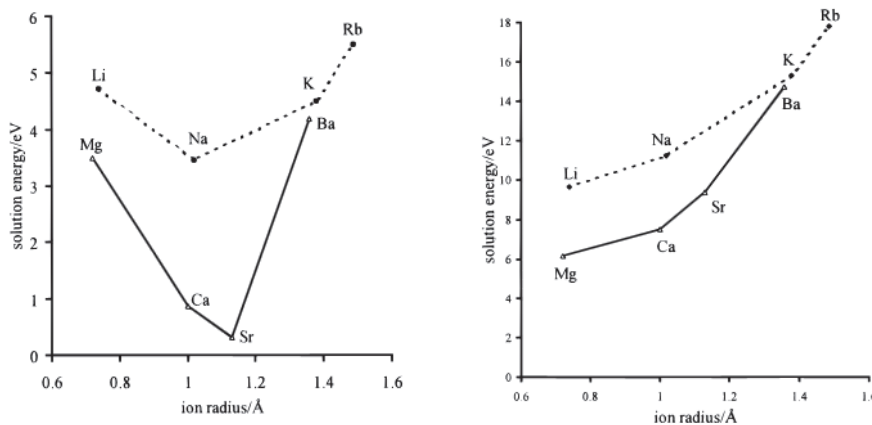


**Figure 1.10** Trend of the solution energy as function of the ionic radius of alkaline and alkaline earth series on both La A-site (left panel) and Ga B-site (right panel).<sup>108</sup>

Co-doping of the  $\text{La}^{3+}$  A-site with small amounts of rare-earth cations such as (Pr, Nd, Sm, Gd, Y, Yb) has also been tried and compositions like  $(\text{La}_{0.9}\text{Nd}_{0.1})_{0.8}\text{Sr}_{0.2}\text{Ga}_{0.8}\text{Mg}_{0.2}\text{O}_{3-\delta}$  and  $\text{La}_{0.45}\text{Pr}_{0.4}\text{Sr}_{0.2}\text{Ga}_{0.8}\text{Mg}_{0.2}\text{O}_{2.85}$  seem to have a lesser effect on the electronic conductivity than other rare earth dopants, while maintaining a good ionic conductivity.<sup>104,109</sup>

For what concerns the B-site,  $\text{Mg}^{2+}$  was proved to be the most effective dopant to enhance ionic conductivity.<sup>104</sup> While co-doping with Ni, Mn and Cr increases electronic conductivity, adding small amounts (about 5-10%mol) of Co or Fe minimize the ohmic resistance of the electrolyte and the overpotential of anodes and cathodes, maintaining an oxide-ion conductivity similar to the parent LSGM composition.<sup>32</sup>

### ***Structural effect of A-site and B-site substitution***

Pure LG has an orthorhombic  $Pbnm$  unit cell (see **Figure 1.9**) until  $160^\circ\text{C}$ , where it undergoes a phase transition to the  $R-3c$  rhombohedral phase, which is maintained up to  $800^\circ\text{C}$ . Although the two phases have the same local structure, they differ in the respective long-range arrangements.

Neutron Diffraction studies have demonstrated that doping with  $\text{Sr}^{2+}$  and  $\text{Mg}^{2+}$  on the A and B sites, respectively, induces a reduction of tilting that is intrinsically present in undoped LG, and increases the symmetry of the octahedral sites.<sup>110</sup>

Due to the structural flexibility of this material, the amount of dopant introduced on A and B sites can also have an influence on the long-range structure: for example, at the limit of no Sr substitution,  $\text{LaGa}_{1-x}\text{Mg}_x\text{O}_{3-x/2}$  (LGM) phases are obtained. Introducing 10%mol of Mg on the B site<sup>110</sup> leads to the orthorhombic  $Ibmm$  space group, while 20%mol does not modify the symmetry of the lattice and the original  $Pbnm$  space group is maintained, with only an expansion of the cell parameters with respect to pure LG. At this composition, the Goldschmidt tolerance factor approaches the value of 1 and  $\text{GaO}_6$  octahedra are close to the regular ones, with a slight lengthening of the Ga-O bond distances and a decrease of the tilting angle between adjacent Ga polyhedra. Some studies also report that, when 20% of Sr is introduced on the A site, a  $\text{La}_{1-y}\text{Sr}_y\text{Ga}_{1-x}\text{Mg}_x\text{O}_{3-(x+y/2)}$  phase with tolerance factor equal to 1 and a cubic  $Pn-3m$  symmetry is obtained. In this case,  $\text{GaO}_6$  octahedra show a shorter Ga-O average distance and the distortion in the perovskite is considerably lowered or even cancelled out.<sup>111</sup> For co-doping with cobalt on the B-site, Stevenson et al. reported the presence of a cubic, orthorhombic or rhombohedral phases.<sup>33</sup>

It is well acknowledged that the remarkable structural flexibility of doped LG certainly plays a determining role in the anion conduction mechanism inside the electrolyte, so that an intense research activity has been devoted to correlate dopant-vacancy interaction phenomena with oxygen-ion diffusion, both computationally and experimentally. Several studies exist about long-range characterization of lanthanum gallate through X-Ray Diffraction (XRD), but to the best of our knowledge there are no studies that can be found about the short-range characterization through X-Ray Absorption Spectroscopy (XAS). A detailed short-range characterization would allow completing the information about the local structure of doped LG that, together with an *ab initio* computational analysis of both dopant preferential configuration and dopant-vacancy interaction would shed light on the oxide-ion diffusion mechanism.

### ***Vacancy interaction with B-site cations***

LG B-site analysis is pivotal for the determination of the oxygen-ion diffusion mechanism. A better understanding of the interplay between B-site occupation and oxygen vacancy position, correlated with both the energetics of the system and the local structure distortions, would be extremely useful to shed light on the structural features that favour or hinder oxygen-ion transport.

From a modelling point of view, atomistic techniques have been extensively used to probe dopant vacancy interaction in lanthanum gallate electrolyte.<sup>108,112,113</sup>

Khan et al.<sup>108</sup> computed binding energies ( $E_{binding}$ ) for vacancy interaction with the A-site and B-site cations in an orthorhombic phase and found that oxygen vacancies tend to be “trapped” by  $Mg^{2+}$  defects with  $E_{binding}(Mg'_{Ga}V_0'') = -1.77$  eV, while there is less interaction with the  $Sr^{2+}$  defects, with  $E_{binding}(Sr'_{La}V_0'') = -0.37$  eV. This result is in agreement with the increase of activation energy and decrease of ionic conductivity at higher  $Mg^{2+}$  concentrations experimentally found for  $La_{0.8}Sr_{0.2}Ga_{1-y}Mg_yO_{3-\delta}$ , but disagrees with recent solid state NMR experimental findings and theoretical studies on doped lanthanum gallate.<sup>114,115</sup> In particular, a recent theoretical investigation, based on a DFT approach combined with experimental NMR measurements on  $^{71}Ga$ ,  $^{25}Mg$  and  $^{17}O$  nuclei for pure and doped lanthanum gallate, has demonstrated that oxygen vacancies are mainly set on Ga sites, while Mg coordination is found to be mainly octahedral. Moreover, chemical shifts on  $^{17}O$  nuclei, which are found to be sensitive to distinguish equatorial ( $O_{eq}$ ) and axial ( $O_{axial}$ ) oxygen atoms in  $GaO_5Vo$  local environments, revealed a heavily distorted square pyramidal geometry, with a shortening of 0.08-0.09 Å of the  $Ga-O_{axial}$  bond length. In addition, various configurations of the vacancy

with respect to Ga and Mg B sites in  $\text{LaGa}_{1-x}\text{Mg}_x\text{O}_{3-x/2}$  were already investigated by DFT calculations, considering three different Mg concentrations. In all cases, the Ga-Vo-Ga configurations were found to be the most stable ones. Nevertheless, for the  $x=0.250$  concentration, the energetic range of the configurations was  $16 \text{ kcal}\cdot\text{mol}^{-1}$ , while it was only half this value for the  $x=0.050$  and  $0.125$  cases, with a modest energy difference between the Ga-Vo-Ga, the Mg-Vo-Ga and the Mg-Vo-Mg configurations, suggesting only a slight energetic preference for the Ga-Vo-Ga configuration.<sup>113</sup>

### ***Oxygen-ion diffusion mechanism***

Another experimental NMR study confirmed that oxygen vacancies are mainly localized between two Ga atoms in bi-pyramidal coordination in the O1 apical position. The dynamics of the diffusion was modelled and two types of oxygen-ion motion were highlighted: i) slow diffusion-type random walk and ii) fast back and forth local jumps between two adjacent anion sites, that had different probability of Vo formation.<sup>115</sup>

Islam et al. investigated oxygen-ion diffusion through atomistic methods.<sup>108,112,113</sup> The defect energy was computed along the diffusion path, allowing the lattice to relax at each position. A vacancy hopping mechanism along the edges of  $\text{GaO}_6$  octahedra was highlighted: oxygen-ion migrates with a slightly curved trajectory in between two oxygen sites and this process would be promoted by the equivalence of the hopping sites of oxygen around B cation. The migration energy barrier of  $\text{O}^{2-} = 0.73 \text{ eV}$  is in good agreement with some experimental findings based on high temperature dc measurements (activation energy of  $0.66$  and  $0.727 \text{ eV}$ ) and SIMS data (activation energy of  $0.79 \text{ eV}$ ).<sup>113</sup>

In general, while atomistic and Molecular Dynamics (MD) methods have been largely used to probe doped lanthanum gallate,<sup>108,112,113,116</sup> very few studies based on a DFT approach<sup>117,118</sup> can be found and none of them reports an analysis of the oxygen-ion diffusion path. The anionic diffusion of electrolytes is mainly governed by **i)** the formation of oxygen vacancies and **ii)** the vacancy-mediated oxygen-ion migration. Sampling the potential energy surface of  $\text{O}^{2-}$  diffusion paths in correspondence of the most stable configurations with an *ab initio* method would have the advantage to correlate the anion conduction mechanism with the electronic structure.

## ***Cobalt co-doping on Mg B-site***

It has been recently reported that co-doping the B site with  $Mg^{2+}$  and very small amounts of Co, minimize the ohmic resistance of the electrolyte and the overpotential of anodes and cathodes, maintaining an oxide-ion conductivity similar to the parent LSGM composition in the temperature range between 500°C and 900°C: compositions like  $La_{0.8}Sr_{0.2}Ga_{0.8}Mg_{0.2-x}Co_xO_{3\pm\delta}$  with  $x=0.05$  and  $0.10$  (LSGMC2005, LSGMC2010) show an  $O^{2-}$  conductivity of 0.2 S/cm at 700°C.<sup>32</sup> Cobalt adopts different valence states (+2, +3, +4), depending on the temperature and oxygen partial pressure: this probably influences the local environment of Co site and consequently the conduction mechanism in LSGMC materials at SOFC operating conditions, involving simultaneous oxidizing and reducing environments on the two FC sides. Moreover, depending on the oxidation state and local environment, cobalt can show three different spin configurations:

- Low Spin (LS)
- Intermediate Spin (IS)
- High Spin (HS)

Considering the crystal field for an octahedral local environment typical of perovskite B-site,  $Co^{2+}$  always adopts the HS configuration ( $t_{2g}^5e_g^2$ ), while  $Co^{4+}$  always adopts a LS configuration ( $t_{2g}^5e_g^0$ ). In the case of  $Co^{3+}$ , the crystal field become very sensitive to the cobalt surrounding species and for this reason it can assume LS ( $t_{2g}^6e_g^0$ ), IS ( $t_{2g}^5e_g^1$ ) and HS ( $t_{2g}^4e_g^2$ ) configurations.<sup>119</sup>

It is known from TGA data that LSGMC materials show a reversible  $O_2$  weight loss in air at high temperature, which is thought to be compensated by a reduction of cobalt to  $Co^{2+}$  in two steps:<sup>33</sup>



On the other side, a study on LSGMC2005 tries to correlate the variation of oxidation number of Co with  $PO_2$  and temperature variations. The study observes that, while in LSGM oxygen nonstoichiometry does not depend on temperature and  $\log(PO_2)$ ,<sup>120</sup> in LSGMC electrolytes nonstoichiometry is strongly attributed to cobalt valence changes. In particular, oxygen vacancy concentration increases as  $\log PO_2$  decreases and the temperature increases, reaching

a plateau at about  $3-\delta=2.80$  (**Figure 1.11**) These data have been correlated with XANES measurements at both 5% $H_2$ -1.2%  $H_2O$ -Ar at 573 K and 100%  $O_2$  atmospheres at 473 K, revealing respectively  $Co^{2+}$  and  $Co^{4+}$  oxidation states in these conditions.<sup>120</sup>

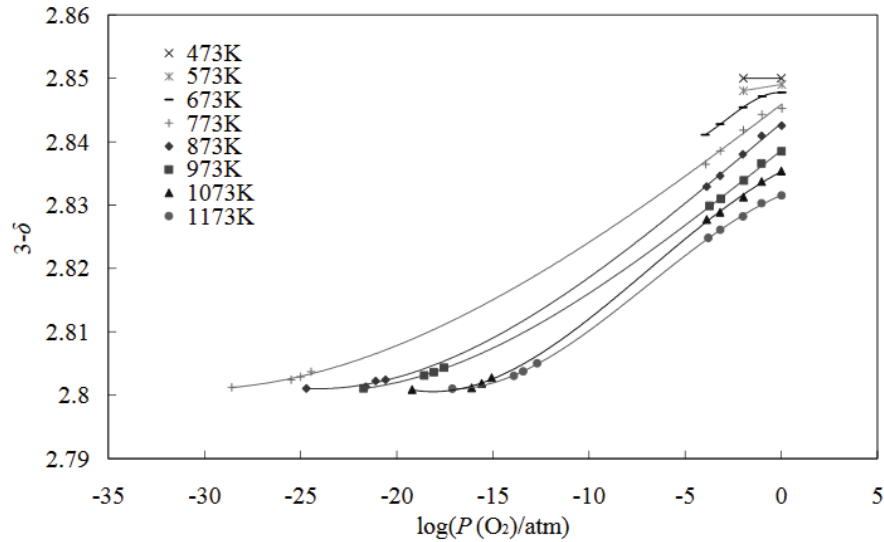


**Figure 1.11** oxygen partial pressure dependence of oxygen nonstoichiometry of LSGMC2005 at different temperatures.<sup>120</sup>

### 3. Cation interdiffusion at electrode-electrolyte interface

#### 3.1. Electrode-electrolyte compatibility

Chemical/physical compatibility between electrode and electrolyte components has a large impact on the overall performances of SOFC devices in terms of working life and ionic conductivity throughout the device in both AC-SOFC and PC-SOFC systems. In order to ensure robustness and conductivity, electrode and electrolyte materials must exhibit two main requirements:<sup>121</sup>

- similar thermal expansion coefficients, to avoid mechanical stresses (es. crackings, delaminations, etc.) at operating temperatures;
- limited interdiffusion of chemical species at the interface.

Even if the materials have similar thermal expansion, cation interdiffusion has a very high impact on the long-term durability of the cell and must be minimized, because it can give rise to insulating contact phases at the interface between the two components at operating temperatures and atmospheres. Moreover, even the co-sintering process of cathode and anode

on the ceramic electrolyte can lead to the formation of a contact phase, that can seriously affect cell performances since the manufacturing process of the device.<sup>122–125</sup>

### **3.2. Synchrotron X-Ray Microscopy to probe compatibility**

Studying interdiffusion phenomena at the electrode/electrolyte interface requires suitable techniques, whose choice is determined by the required resolution and by the type of needed information. In this context, compatibility issues have been traditionally investigated by means of electron microscopy (EM) techniques, such as Scanning Electron Microscopy (SEM), Transmission Electron Microscopy (TEM), High Resolution Transmission Electron Microscopy (HR-TEM) and Scanning Transmission Electron Microscopy (STEM).<sup>122–125</sup> The main advantage in using an electron probe certainly lies in both the outstanding spatial resolution (from nm to Å) and in the huge amount of information that can be simultaneously obtained about the morphology, the structure and the elemental composition of the sample.

The use of the techniques based on an electron beam probe allows to perform microchemical analysis on cross sections of the electrode/electrolyte assembly and to determine concentration profiles across the interface, in order to characterize the extent of cations interdiffusion between the two phases.<sup>122–125</sup>

Unfortunately, the use of EMs, has some serious drawbacks that can affect or limit the interface study. For example, electrons can cause aberrations, due to the electrostatic charging of the sample, that can affect the microscopy analysis. The attenuation length of the electron beam can be severely affected by the roughness of the surface during SEM analysis. TEM imaging requires a complex preparation of the sample, that must be extremely thin (about 100 nm), due to the strong scattering of the electrons. Moreover, studying interdiffusion phenomena at electrode/electrolyte interface requires a deep knowledge and control of the local structure around cations, that the EMs are not able to investigate. In some cases, contact phases or secondary phases have a composition that is only slightly different from the original structure (i.e. interdiffusion of cations inside a perovskite-type lattice), and working with diffraction tools is not enough to detect them.

In this context, even if the resolution is lower than EMs, X-Ray Microscopy (XRM) overcomes the drawbacks typical of EM (no electrostatic charging of sample, attenuation length of the beam large enough to ensure no influence by the surface roughness - about 1 to 5  $\mu\text{m}$  - and higher thickness of samples - from 5 to 100  $\mu\text{m}$ ) and simultaneously allows to



characterize not only the morphology of the electrode/electrolyte interface, but also to obtain detailed local structure and chemical state information, which are essential for the design of SOFC with higher efficiency and long term durability.<sup>126</sup>

Various types of XRM exist, working in different imaging modes: similarly to EMs techniques previously described, XRM can work in full-field mode, as in Transmission X-Ray Microscopy (TXM), or scanning mode, as in Scanning X-Ray Microscopy (SXM).

We have demonstrated in a recent study<sup>127</sup> that SXM is an extremely suitable technique for investigating compatibility between SOFC materials. This technique allows acquiring X-Ray Fluorescence (XRF) elemental distribution maps based on fluorescence contrast by raster scanning the sample in two dimensions, using a sub-micrometric beam. Moreover,  $\mu$ -XANES,  $\mu$ -EXAFS and  $\mu$ -XRF spectra can be recorded in selected points of the map by varying the energy around the absorption edge of the target element: in this way, information about elemental and chemical state can be achieved, together with quantitative mapping.

## 4. Objectives

The scientific literature concerning solid state electrolytes is extremely wide and the vast majority of the published papers are focused on the synthesis and functional characterization of these components.

**The aim of this research is to investigate some of the structural features that have an influence on ionic conductivity in fuel cells.**

The focus about electrolyte materials is on oxygen-ion diffusion in fluorite-like and perovskite-like structures. To this end, a **detailed analysis of the short range structure of the materials under investigation, combined with a computational approach, would allow to link the properties of these materials with the atomic structure and the electronic features.** This would help to define criteria for the design of new materials with improved properties.

In particular, two electrolytes for AC-SOFC applications, previously described in **Section 2** of this chapter, have been studied:

- **Fluorite-like  $\delta$ -Bi<sub>2</sub>O<sub>3</sub>.** With its average fluorite-like structure containing intrinsic vacancies in its undoped form, the high temperature  $\delta$ -phase of bismuth oxide is considered the reference compound in solid-state anionic conduction, with the highest conductivity known so far (1 S·cm<sup>-1</sup> at 750°C).

- **Perovskite-like LaGaO<sub>3</sub>.** Due to its high structural flexibility, this perovskite-like material can host lower-valence dopants on the A and B site, introducing oxygen vacancies inside the lattice and reaching a high oxygen-ion conductivity ( $0.14 \text{ S}\cdot\text{cm}^{-1}$  at  $800^\circ\text{C}$ ).

A combined experimental and theoretical approach has been used in order to probe:

- the dopant effect on the short-range structure and the local distortions;
- the interaction between dopant cation and oxygen-vacancy;
- the preferential paths of oxygen-ion diffusion.

Combining DFT with X-Ray Absorption Spectroscopy can lead to helpful complementary information about doped solid state electrolytes: while XAS allows to disclose the local structural features around regular and dopant cations, unveiling distortions and defect clustering phenomena, DFT allows to depict an energy stability scale of different configurations that sometimes cannot be distinguished by XAS technique accuracy, and to draw a detailed picture of the electronic features of the material.

**The mechanism of ionic transport is also strictly dependent on the assembly of the FC components**, due to cation interdiffusion that modifies the interface chemical composition and, in some cases, gives rise to the formation of new phases detrimental for ionic conductivity and device durability. To this concern, **this thesis proposes also a new approach to the issue of electrode/electrolyte compatibility, giving a detailed account of the first application of X-ray Microspectroscopy to the structural/elemental analysis of the LNC-LSM interface.**

To sum up, in **Chapter 2** the theoretical background concerning experimental and computational methods used in this work will be described.

**Chapter 3** is dedicated to the investigation of  $\text{Bi}_{1-x}\text{Ta}_x\text{O}_{1.5+x}$  solid electrolyte, with the aim to unveil the preferential aggregation motives around the dopant site that are involved in the stabilization of the fluorite-like phase at room temperature and shed light on the local coordination and electronic structure of bismuth site, which are supposed to play a key role in the high conductivity of this material. An overview of the role of  $\text{V}^{5+}$  and  $\text{Nb}^{5+}$  in the stabilization of the  $\delta$ -phase will be also given, with the aim to draw a comparison between different pentavalent dopants.

In **Chapter 4** results about doped  $\text{LaGaO}_3$  will be presented and discussed. In **Section 1**, a comprehensive study about  $\text{LaGa}_{0.875}\text{Mg}_{0.125}\text{O}_{2.935}$  material is presented, with the aim to understand the influence of Mg doping on the perovskite B-site, which is supposed to be the main contribution to the oxygen ion diffusion. The vacancy interaction with the B site, which is currently under debate in literature, together with the local distortion around the vacancy site (tilting and dihedral distortions) will be deeply analyzed through a configurational study. In **Section 2** the analysis of oxygen-ion diffusion paths around the B-site on  $\text{LaGa}_{0.875}\text{Mg}_{0.125}\text{O}_{2.935}$  electrolyte is reported, with the aim to unravel the activation energy barriers around both Ga regular site and Mg dopant site. In **Section 3** the influence of co-doping with Mg and Co on the local structure features around perovskite B-site in  $\text{La}_{1-x}\text{Sr}_x\text{Ga}_{1-y}(\text{Mg}, \text{Co})_y\text{O}_{3-\delta}$  will be reported.

Finally, **Chapter 5** reports a detailed study about the first application of synchrotron Scanning X-Ray Microscopy (SXM) to the investigation of electrode/electrolyte compatibility. The case of study, used to tune the experimental and data treatment protocols, concerns a PC-SOFC electrode/electrolyte bilayer, composed by the perovskite-like MIEC cathode  $\text{La}_{0.8}\text{Sr}_{0.2}\text{MnO}_{3-\delta}$  and the proton-conducting  $\text{La}_{0.98}\text{Ca}_{0.02}\text{NbO}_{4-x}$  electrolyte (LSM/LNC). An outlook is also given about the application of the technique to AC-SOFC materials.

## 5. References

- (1) <http://climate.nasa.gov/effects/>
- (2) UNFCCC. Report of the Conference of the Parties on Its Fifteenth Session, Held in Copenhagen from 7 to 19 December 2009, Addendum, Part Two: Action Taken by the Conference of the Parties at Its Fifteenth Session. *Unfccc* **2010**, 1–43.
- (3) McGlade, C.; Ekins, P. The Geographical Distribution of Fossil Fuels Unused When Limiting Global Warming to 2°C. *Nature* **2015**, *517* (7533), 187–190.
- (4) Meinshausen, M.; Meinshausen, N.; Hare, W.; Raper, S. C. B.; Frieler, K.; Knutti, R.; Frame, D. J.; Allen, M. R. Greenhouse-Gas Emission Targets for Limiting Global Warming to 2°C. *Nature* **2009**, *458* (7242), 1158–1162.
- (5) Clarke, L. et al. in *Climate Change 2014: Mitigation of Climate Change* (Edenhofer, O. et al.) Ch. 6 (Cambridge Univ. Press, 2014)
- (6) [www.cop21paris.org/about/cop21/](http://www.cop21paris.org/about/cop21/)
- (7) <https://ec.europa.eu/programmes/horizon2020/en/area/energy>
- (8) Singhal, S. C.; Kendall, K. *High-Temperature Solid Oxide Fuel Cells: Fundamentals*,

- Design and Applications*; Elsevier, 2003.
- (9) Singhal, S. C. Solid Oxide Fuel Cells for Power Generation. *Wiley Interdiscip. Rev. Energy Environ.* **2014**, 3 (2), 179–194.
  - (10) Gao, Z.; Mogni, L. V.; Miller, E. C.; Railsback, J. G.; Barnett, S. A. A Perspective on Low-Temperature Solid Oxide Fuel Cells. *Energy Environ. Sci.* **2016**, 9 (5), 1602–1644.
  - (11) Steele, B. C. H.; Heinzl, A. Materials for Fuel-Cell Technologies. *Nature* **2001**, 414 (6861), 345–352.
  - (12) Malavasi, L.; Fisher, C. A. J.; Islam, M. S. Oxide-Ion and Proton Conducting Electrolyte Materials for Clean Energy Applications: Structural and Mechanistic Features. *Chem. Soc. Rev.* **2010**, 39 (11), 4370–4387.
  - (13) Badwal, S. P. S.; Ciacchi, F. T.; Milosevic, D. Scandia-Zirconia Electrolytes for Intermediate Temperature Solid Oxide Fuel Cell Operation. *Solid State Ionics* **2000**, 136, 91–99.
  - (14) Devanathan, R.; Thevuthasan, S.; Gale, J. D. Defect Interactions and Ionic Transport in Scandia Stabilized Zirconia. *Phys. Chem. Chem. Phys.* **2009**, 11 (26), 5506–5511.
  - (15) Mogensen, M.; Sammes, N.; Tompsett, G. Physical, Chemical and Electrochemical Properties of Pure and Doped Ceria. *Solid State Ionics* **2000**, 129 (1–4), 63–94.
  - (16) Wang, S.; Inaba, H.; Tagawa, H.; Dokiya, M.; Hashimoto, T. Nonstoichiometry of  $\text{Ce}_{0.9}\text{Gd}_{0.1}\text{O}_{1.95-x}$ . *Solid State Ionics* **1998**, 107 (1), 73–79.
  - (17) Sammes, N. M.; Tompsett, G. A.; Näfe, H.; Aldinger, F. Bismuth Based Oxide Electrolytes-structure and Ionic Conductivity. *J. Eur. Ceram. Soc.* **1999**, 19 (10), 1801–1826.
  - (18) Wachsmann, E. D.; Marlowe, C. A.; Lee, K. T. Role of Solid Oxide Fuel Cells in a Balanced Energy Strategy. *Energy Environ. Sci.* **2012**, 5 (2), 5498–5509.
  - (19) Hervoches, C. H.; Greaves, C. Variable Temperature Neutron Diffraction Study of  $\text{Bi}_3\text{ReO}_8$  Oxide Ion Conductor. *Solid State Ionics* **2012**, 217, 46–53.
  - (20) Kuang, X.; Li, Y.; Ling, C. D.; Withers, R. L.; Evans, I. R. Oxide Ion Conductivity, Phase Transitions, and Phase Separation in Fluorite-Based  $\text{Bi}_{38-x}\text{Mo}_{7+x}\text{O}_{78+1.5x}$ . *Chem. Mater.* **2010**, 22 (15), 4484–4494.
  - (21) Kuang, X.; Payne, J. L.; Johnson, M. R.; Radosavljevic Evans, I. Remarkably High Oxide Ion Conductivity at Low Temperature in an Ordered Fluorite-Type Superstructure. *Angew. Chemie Int. Ed.* **2012**, 51 (3), 690–694.

- (22) Ling, C. D.; Schmid, S.; Blanchard, P. E. R.; Petricek, V.; McIntyre, G. J.; Sharma, N.; Maljuk, A.; Yaremchenko, A. A.; Kharton, V. V.; Gutmann, M.; et al. A (3+ 3)-Dimensional “Hypercubic” Oxide-Ionic Conductor: Type II Bi<sub>2</sub>O<sub>3</sub>-Nb<sub>2</sub>O<sub>5</sub>. *J. Am. Chem. Soc.* **2013**, *135* (17), 6477–6484.
- (23) Gomez, C. L.; Depablos-Rivera, O.; Medina, J. C.; Silva-Bermudez, P.; Muhl, S.; Zeinert, A.; Rodil, S. E. Stabilization of the Delta-Phase in Bi<sub>2</sub>O<sub>3</sub> Thin Films. *Solid State Ionics* **2014**, *255*, 147–152.
- (24) Struzik, M.; Malys, M.; Wrobel, W.; Abrahams, I.; Krok, F.; Dygas, J. R. Ordered Fluorite Phases in the Bi<sub>2</sub>O<sub>3</sub>-Ta<sub>2</sub>O<sub>5</sub> System: A Structural and Electrical Investigation. *Solid State Ionics* **2011**, *202* (1), 22–29.
- (25) Joh, D. W.; Park, J. H.; Kim, D. Y.; Yun, B.-H.; Lee, K. T. High Performance Zirconia-Bismuth Oxide Nanocomposite Electrolytes for Lower Temperature Solid Oxide Fuel Cells. *J. Power Sources* **2016**, *320*, 267–273.
- (26) Morales, M.; Roa, J. J.; Perez-Falcón, J. M.; Moure, A.; Tartaj, J.; Espiell, F.; Segarra, M. Correlation between Electrical and Mechanical Properties in La<sub>1-x</sub>Sr<sub>x</sub>Ga<sub>1-y</sub>Mg<sub>y</sub>O<sub>3-δ</sub> Ceramics Used as Electrolytes for Solid Oxide Fuel Cells. *J. Power Sources* **2014**, *246*, 918–925.
- (27) Ishihara, T.; Matsuda, H.; Takita, Y. Doped LaGaO<sub>3</sub> Perovskite Type Oxide as a New Oxide Ionic Conductor. *J. Am. Chem. Soc.* **1994**, *116* (9), 3801–3803.
- (28) Feng, M.; Goodenough, J. B. A Superior Oxide-Ion Electrolyte. *Eur. J. solid state Inorg. Chem.* **1994**, *31* (8–9), 663–672.
- (29) Huang, P.; Petric, A. Superior Oxygen Ion Conductivity of Lanthanum Gallate Doped with Strontium and Magnesium. *J. Electrochem. Soc.* **1996**, *143* (5), 1644–1648.
- (30) Polini, R.; Pamio, A.; Traversa, E. Effect of Synthetic Route on Sintering Behaviour, Phase Purity and Conductivity of Sr-and Mg-Doped LaGaO<sub>3</sub> Perovskites. *J. Eur. Ceram. Soc.* **2004**, *24* (6), 1365–1370.
- (31) Djurado, E.; Labeau, M. Second Phases in Doped Lanthanum Gallate Perovskites. *J. Eur. Ceram. Soc.* **1998**, *18* (10), 1397–1404.
- (32) Khorkounov, B. A.; Näfe, H.; Aldinger, F. Relationship between the Ionic and Electronic Partial Conductivities of Co-Doped LSGM Ceramics from Oxygen Partial Pressure Dependence of the Total Conductivity. *J. Solid State Electrochem.* **2006**, *10* (7), 479–487.
- (33) Stevenson, J. W.; Hasinska, K.; Canfield, N. L.; Armstrong, T. R. Influence of Cobalt

- and Iron Additions on the Electrical and Thermal Properties of (La, Sr)(Ga, Mg)O<sub>3-δ</sub>. *J. Electrochem. Soc.* **2000**, *147* (9), 3213–3218.
- (34) Lacorre, P.; Goutenoire, F.; Bohnke, O.; Retoux, R.; Laligant, Y. Designing Fast Oxide-Ion Conductors Based on La<sub>2</sub>Mo<sub>2</sub>O<sub>9</sub>. *Nature* **2000**, *404* (6780), 856–858.
- (35) Goutenoire, F.; Isnard, O.; Retoux, R.; Lacorre, P. Crystal Structure of La<sub>2</sub>Mo<sub>2</sub>O<sub>9</sub>, a New Fast Oxide-Ion Conductor. *Chem. Mater.* **2000**, *12* (9), 2575–2580.
- (36) Georges, S.; Goutenoire, F.; Laligant, Y.; Lacorre, P. Reducibility of Fast Oxide-Ion Conductors La<sub>2-x</sub>R<sub>x</sub>Mo<sub>2-y</sub>W<sub>y</sub>O<sub>9</sub> (R= Nd, Gd). *J. Mater. Chem.* **2003**, *13* (9), 2317–2321.
- (37) Vannier, R. N.; Chater, R. J.; Skinner, S. J.; Kilner, J. A.; Mairesse, G. Characterisation of the Oxygen Transfer in BIMEVOX Membranes under Applied Current Conditions. *Solid State Ionics* **2003**, *160* (3), 327–334.
- (38) Abraham, F.; Debreuille-Gresse, M. F.; Mairesse, G.; Nowogrocki, G. Phase Transitions and Ionic Conductivity in Bi<sub>4</sub>V<sub>2</sub>O<sub>11</sub> an Oxide with a Layered Structure. *Solid State Ionics* **1988**, *28*, 529–532.
- (39) Abrahams, I.; Krok, F. Defect Chemistry of the BIMEVOXes. *J. Mater. Chem.* **2002**, *12* (12), 3351–3362.
- (40) Watanabe, A.; Das, K. Time-Dependent Degradation due to the Gradual Phase Change in BICUVOX and BICOVOX Oxide-Ion Conductors at Temperatures below about 500° C. *J. Solid State Chem.* **2002**, *163* (1), 224–230.
- (41) Nakayama, S.; Kageyama, T.; Aono, H.; Sadaoka, Y. Ionic Conductivity of Lanthanoid Silicates, Ln<sub>10</sub>(SiO<sub>4</sub>)<sub>6</sub>O<sub>3</sub> (Ln= La, Nd, Sm, Gd, Dy, Y, Ho, Er and Yb). *J. Mater. Chem.* **1995**, *5* (11), 1801–1805.
- (42) Kendrick, E.; Islam, M. S.; Slater, P. R. Developing Apatites for Solid Oxide Fuel Cells: Insight into Structural, Transport and Doping Properties. *J. Mater. Chem.* **2007**, *17* (30), 3104–3111.
- (43) Kendrick, E.; Kendrick, J.; Knight, K. S.; Islam, M. S.; Slater, P. R. Cooperative Mechanisms of Fast-Ion Conduction in Gallium-Based Oxides with Tetrahedral Moieties. *Nat. Mater.* **2007**, *6* (11), 871–875.
- (44) Kuang, X.; Green, M. A.; Niu, H.; Zajdel, P.; Dickinson, C.; Claridge, J. B.; Jantsky, L.; Rosseinsky, M. J. Interstitial Oxide Ion Conductivity in the Layered Tetrahedral Network Melilite Structure. *Nat. Mater.* **2008**, *7* (6), 498–504.
- (45) Thomas, C. I.; Kuang, X.; Deng, Z.; Niu, H.; Claridge, J. B.; Rosseinsky, M. J. Phase

- Stability Control of Interstitial Oxide Ion Conductivity in the  $\text{La}_{1+x}\text{Sr}_{1-x}\text{Ga}_3\text{O}_{7+x/2}$  Melilite Family. *Chem. Mater.* **2010**, 22 (8), 2510–2516.
- (46) Spacil, H. S. Electrical Device Including Nickel-Containing Stabilized Zirconia Electrode. Google Patents 1970.
- (47) Atkinson, A.; Barnett, S.; Gorte, R. J.; Irvine, J. T. S.; McEvoy, A. J.; Mogensen, M.; Singhal, S. C.; Vohs, J. Advanced Anodes for High-Temperature Fuel Cells. *Nat. Mater.* **2004**, 3 (1), 17–27.
- (48) Baur, E.; Brunner, R. Über Die Eisenoxyd-Kathode in Der Kohle-Luft-Kette. *Zeitschrift für Elektrochemie und Angew. Phys. Chemie* **1937**, 43 (9), 725–727.
- (49) Möbius, H.-H. On the History of Solid Electrolyte Fuel Cells. *J. solid state Electrochem.* **1997**, 1 (1), 2–16.
- (50) Zhu, H.; Kee, R. J.; Janardhanan, V. M.; Deutschmann, O.; Goodwin, D. G. Modeling Elementary Heterogeneous Chemistry and Electrochemistry in Solid-Oxide Fuel Cells. *J. Electrochem. Soc.* **2005**, 152 (12), A2427-A2440.
- (51) Andersson, M.; Paradis, H.; Yuan, J.; Sundén, B. Review of Catalyst Materials and Catalytic Steam Reforming Reactions in SOFC Anodes. *Int. J. Energy Res.* **2011**, 35 (15), 1340–1350.
- (52) He, H.; Hill, J. M. Carbon Deposition on Ni/YSZ Composites Exposed to Humidified Methane. *Appl. Catal. A Gen.* **2007**, 317 (2), 284–292.
- (53) Larminie, J.; Dicks, A.; McDonald, M. S. *Fuel Cell Systems Explained*; J. Wiley Chichester, UK, 2003; Vol. 2.
- (54) Kan, W. H.; Thangadurai, V. Challenges and Prospects of Anodes for Solid Oxide Fuel Cells (SOFCs). *Ionics (Kiel)*. **2015**, 21 (2), 301–318.
- (55) Park, S.; Vohs, J. M.; Gorte, R. J. Direct Oxidation of Hydrocarbons in a Solid-Oxide Fuel Cell. *Nature* **2000**, 404 (6775), 265–267.
- (56) Bernardo, C. A.; Alstrup, I.; Rostrup-Nielsen, J. R. Carbon Deposition and Methane Steam Reforming on Silica-Supported Ni/Cu Catalysts. *J. Catal.* **1985**, 96 (2), 517–534.
- (57) Dong, W.-S.; Roh, H.-S.; Jun, K.-W.; Park, S.-E.; Oh, Y.-S. Methane Reforming over Ni/Ce-ZrO<sub>2</sub> Catalysts: Effect of Nickel Content. *Appl. Catal. A Gen.* **2002**, 226 (1), 63–72.
- (58) Ramos, T.; Søgaard, M.; Mogensen, M. B. Electrochemical Characterization of Ni/ScYSZ Electrodes as SOFC Anodes. *J. Electrochem. Soc.* **2014**, 161 (4), F434--

- F444.
- (59) Serra, J. M.; Vert, V. B.; Buchler, O.; Meulenber, W. A.; Buchkremer, H. P. IT-SOFC Supported on Mixed Oxygen Ionic-Electronic Conducting Composites. *Chem. Mater.* **2008**, *20* (12), 3867–3875.
- (60) Somalu, M. R.; Yufit, V.; Cumming, D.; Lorente, E.; Brandon, N. P. Fabrication and Characterization of Ni/ScSZ Cermet Anodes for IT-SOFCs. *Int. J. Hydrogen Energy* **2011**, *36* (9), 5557–5566.
- (61) Poulsen, F.; Hendriksen, P.; Bonanos, N.; Lybye, D.; Mogensen, M. Factors Controlling the Oxide Ion Conductivity of Fluorite and Perovskite Structured Oxides. *Solid State Ionics* **2004**, *174* (1–4), 279–286.
- (62) Zhang, X.; Ohara, S.; Maric, R.; Mukai, K.; Fukui, T.; Yoshida, H.; Nishimura, M.; Inagaki, T.; Miura, K. Ni-SDC Cermet Anode for Medium-Temperature Solid Oxide Fuel Cell with Lanthanum Gallate Electrolyte. *J. Power Sources* **1999**, *83* (1), 170–177.
- (63) Zhan, Z.; Bierschenk, D. M.; Cronin, J. S.; Barnett, S. A. A Reduced Temperature Solid Oxide Fuel Cell with Nanostructured Anodes. *Energy Environ. Sci.* **2011**, *4* (10), 3951–3954.
- (64) Sfeir, J.; Buffat, P. A.; Möckli, P.; Xanthopoulos, N.; Vasquez, R.; Mathieu, H. J.; Thampi, K. R.; others. Lanthanum Chromite Based Catalysts for Oxidation of Methane Directly on SOFC Anodes. *J. Catal.* **2001**, *202* (2), 229–244.
- (65) Tao, S.; Irvine, J. T. S. Catalytic Properties of the Perovskite Oxide  $\text{La}_{0.75}\text{Sr}_{0.25}\text{Cr}_{0.5}\text{Fe}_{0.5}\text{O}_{3-\delta}$  in Relation to Its Potential as a Solid Oxide Fuel Cell Anode Material. *Chem. Mater.* **2004**, *16* (21), 4116–4121.
- (66) Aliotta, C.; Liotta, L. F.; Deganello, F.; La Parola, V.; Martorana, A. Direct Methane Oxidation on  $\text{La}_{1-x}\text{Sr}_x\text{Cr}_{1-y}\text{Fe}_y\text{O}_{3-\delta}$  Perovskite-Type Oxides as Potential Anode for Intermediate Temperature Solid Oxide Fuel Cells. *Appl. Catal. B Environ.* **2016**, *180*, 424–433.
- (67) Handal, H. T.; Thangadurai, V. Evaluation of Chemical Stability, Thermal Expansion Coefficient, and Electrical Properties of Solid State and Wet-Chemical Synthesized Y and Mn-Codoped  $\text{CeO}_2$  for Solid Oxide Fuel Cells. *J. Power Sources* **2013**, *243*, 458–471.
- (68) Li, Q.; Thangadurai, V. A Comparative 2 and 4-Probe DC and 2-Probe AC Electrical Conductivity of Novel Co-Doped  $\text{Ce}_{0.9-x}\text{RE}_x\text{Mo}_{0.1}\text{O}_{2.1-0.5x}$  (RE= Y, Sm, Gd; X= 0.2,



- 0.3). *J. Mater. Chem.* **2010**, *20* (37), 7970–7983.
- (69) Tarancón, A.; Burriel, M.; Santiso, J.; Skinner, S. J.; Kilner, J. A. Advances in Layered Oxide Cathodes for Intermediate Temperature Solid Oxide Fuel Cells. *J. Mater. Chem.* **2010**, *20* (19), 3799–3813.
- (70) Petric, A.; Huang, P.; Tietz, F. Evaluation of La-Sr-Co-Fe-O Perovskites for Solid Oxide Fuel Cells and Gas Separation Membranes. *Solid State Ionics* **2000**, *135* (1), 719–725.
- (71) Tai, L.-W.; Nasrallah, M. M.; Anderson, H. U.; Sparlin, D. M.; Sehlin, S. R. Structure and Electrical Properties of  $\text{La}_{1-x}\text{Sr}_x\text{Co}_{1-y}\text{Fe}_y\text{O}_3$ . Part 1. The System  $\text{La}_{0.8}\text{Sr}_{0.2}\text{Co}_{1-y}\text{Fe}_y\text{O}_3$ . *Solid State Ionics* **1995**, *76* (3), 259–271.
- (72) Jorgensen, J. D.; Dabrowski, B.; Pei, S.; Richards, D. R.; Hinks, D. G. Structure of the Interstitial Oxygen Defect in  $\text{La}_2\text{NiO}_{4+\delta}$ . *Phys. Rev. B* **1989**, *40* (4), 2187.
- (73) Opila, E. J.; Tuller, H. L.; Wuensch, B. J.; Maier, J. Oxygen Tracer Diffusion in  $\text{La}_{2-x}\text{Sr}_x\text{CuO}_{4-y}$  Single Crystals. *J. Am. Ceram. Soc.* **1993**, *76* (9), 2363–2369.
- (74) Bassat, J.M.; Odier, P.; Villesuzanne, A.; Marin, C.; Pouchard, M. Anisotropic Ionic Transport Properties in  $\text{La}_2\text{NiO}_{4+\delta}$  Single Crystals. *Solid State Ionics* **2004**, *167* (3), 341–347.
- (75) Claus, J.; Borchardt, G.; Weber, S.; Hiver, J.-M.; Scherrer, S. Combination of EBSD Measurements and SIMS to Study Crystallographic Orientation Dependence of Diffusivities in a Polycrystalline Material: Oxygen Tracer Diffusion in  $\text{La}_{2-x}\text{Sr}_x\text{CuO}_{4-\delta}$ . *Mater. Sci. Eng. B* **1996**, *38* (3), 251–257.
- (76) Frontera, C.; Garcia-Munoz, J. L.; Llobet, A.; Aranda, M. A. G. Selective Spin-State Switch and Metal-Insulator Transition in  $\text{GdBaCo}_2\text{O}_{5.5}$ . *Phys. Rev. B* **2002**, *65* (18), 180405.
- (77) Glazer, A. M. Simple Ways of Determining Perovskite Structures. *Acta Crystallogr. Sect. A Cryst. Physics, Diffraction, Theor. Gen. Crystallogr.* **1975**, *31* (6), 756–762.
- (78) Islam, M. S. Computer Modelling of Defects and Transport in Perovskite Oxides. **2002**, *155*, 75–85.
- (79) Lupetin, P.; Giannici, F.; Gregori, G.; Martorana, A.; Maier, J. Effects of Grain Boundary Decoration on the Electrical Conduction of Nanocrystalline  $\text{CeO}_2$ . *J. Electrochem. Soc.* **2012**, *159* (4), B417–B425.
- (80) Gattow, G.; Schröder, H. Über Wismutoxide. III. Die Kristallstruktur Der Hochtemperaturmodifikation von Wismut (III)-Oxid ( $\delta\text{-Bi}_2\text{O}_3$ ). *Zeitschrift für Anorg.*

- und Allg. Chemie* **1962**, 318 (3–4), 176–189.
- (81) MALMROS, G. The Crystal Structure of alpha-  $\text{Bi}_2\text{O}_3$ . *Acta Chem. Scand* **1970**, 24 (2).
- (82) Sillén, L. G. On the Crystal Structure of Monoclinic alpha-  $\text{Bi}_2\text{O}_3$ . *Zeitschrift für Krist. Mater.* **1941**, 103 (1–6), 274–290.
- (83) Battle, P. D.; Catlow, C. R. A.; Heap, J. W.; Moroney, L. M. Structural and Dynamical Studies of  $\delta$ -  $\text{Bi}_2\text{O}_3$  Oxide Ion Conductors: I. The Structure of  $(\text{Bi}_2\text{O}_3)_{1-x}(\text{Y}_2\text{O}_3)_x$  as a Function of X and Temperature. *J. Solid State Chem.* **1986**, 63 (1), 8–15.
- (84) Battle, P. D.; Catlow, C. R. A.; Moroney, L. M. Structural and Dynamical Studies of  $\delta$ -  $\text{Bi}_2\text{O}_3$  Oxide-Ion Conductors: II. A Structural Comparison of  $(\text{Bi}_2\text{O}_3)_{1-x}(\text{Y}_2\text{O}_3)_x$  for M= Y, Er, and Yb. *J. Solid State Chem.* **1987**, 67 (1), 42–50.
- (85) Koto, K.; Suda, K.; Ishizawa, N.; Maeda, H. Oxide Ion Motion in Bismuth Sesquioxide ( $\sigma$ - $\text{Bi}_2\text{O}_3$ ). *Solid state ionics* **1994**, 72, 79–85.
- (86) Harwig, H. A.; Gerards, A. G. The Polymorphism of Bismuth Sesquioxide. *Thermochim. Acta* **1979**, 28 (1), 121–131.
- (87) Harwig, H. A. On the Structure of Bismuthsesquioxide: The  $\alpha$ ,  $\beta$ ,  $\gamma$ , and  $\delta$ -Phase. *Zeitschrift für Anorg. und Allg. Chemie* **1978**, 444 (1), 151–166.
- (88) Blower, S. K.; Greaves, C. The Structure of  $\beta$ -  $\text{Bi}_2\text{O}_3$  from Powder Neutron Diffraction Data. *Acta Crystallogr. Sect. C Cryst. Struct. Commun.* **1988**, 44 (4), 587–589.
- (89) Willis, B. T. M. The Anomalous Behaviour of the Neutron Reflexion of Fluorite. *Acta Crystallogr.* **1965**, 18 (1), 75–76.
- (90) Iwahara, H.; Esaka, T.; Sato, T.; Takahashi, T. Formation of High Oxide Ion Conductive Phases in the Sintered Oxides of the System  $\text{Bi}_2\text{O}_3$ - $\text{Ln}_2\text{O}_3$  (Ln= La, Yb). *J. Solid State Chem.* **1981**, 39 (2), 173–180.
- (91) Verkerk, M. J.; Burggraaf, A. J. High Oxygen Ion Conduction in Sintered Oxides of the  $\text{Bi}_2\text{O}_3$ - $\text{Ln}_2\text{O}_3$  System. *Solid State Ionics* **1981**, 3, 463–467.
- (92) Verkerk, M. J.; Keizer, K.; Burggraaf, A. J. High Oxygen Ion Conduction in Sintered Oxides of the  $\text{Bi}_2\text{O}_3$ - $\text{Er}_2\text{O}_3$  System. *J. Appl. Electrochem.* **1980**, 10 (1), 81–90.
- (93) Ling, C. D. Structural Relationships among Bismuth-Rich Phases in the  $\text{Bi}_2\text{O}_3$ - $\text{Nb}_2\text{O}_5$ ,  $\text{Bi}_2\text{O}_3$ - $\text{Ta}_2\text{O}_5$ ,  $\text{Bi}_2\text{O}_3$ - $\text{MoO}_3$ , and  $\text{Bi}_2\text{O}_3$ - $\text{WO}_3$  Systems. *J. Solid State Chem.* **1999**, 148 (2), 380–405.
- (94) Zhou, W. The Type II Superstructural Family in the  $\text{Bi}_2\text{O}_3$ - $\text{V}_2\text{O}_5$  System. *J. Solid State Chem.* **1990**, 87 (1), 44–54.
- (95) Zhou, W. Defect Fluorite-Related Superstructures in the  $\text{Bi}_2\text{O}_3$ - $\text{V}_2\text{O}_5$  System. *J. Solid*

- State Chem.* **1988**, 76 (2), 290–300.
- (96) Ling, C. D.; Withers, R. L.; Schmid, S.; Thompson, J. G. A Review of Bismuth-Rich Binary Oxides in the Systems  $\text{Bi}_2\text{O}_3\text{-Nb}_2\text{O}_5$ ,  $\text{Bi}_2\text{O}_3\text{-Ta}_2\text{O}_5$ ,  $\text{Bi}_2\text{O}_3\text{-MoO}_3$ , and  $\text{Bi}_2\text{O}_3\text{-WO}_3$ . *J. Solid State Chem.* **1998**, 137 (1), 42–61.
- (97) Takahashi, T.; Iwahara, H.; Esaka, T. High Oxide Ion Conduction in Sintered Oxide of the System  $\text{Bi}_2\text{O}_3\text{-M}_2\text{O}_5$ . *J. Electrochem. Soc.* **1977**, 124 (10), 1563–1569.
- (98) Zhou, W. Structural Chemistry and Physical Properties of Some Ternary Oxides in the  $\text{Bi}_2\text{O}_3\text{-Ta}_2\text{O}_5$  System. *J. Solid State Chem.* **1992**, 101 (1), 1–17.
- (99) Struzik, M.; Liu, X.; Abrahams, I.; Krok, F.; Malys, M.; Dygas, J. R. Defect Structure and Electrical Conductivity in the Pseudo-Binary System  $\text{Bi}_3\text{TaO}_7\text{-Bi}_3\text{NbO}_7$ . *Solid State Ionics* **2012**, 218, 25–30.
- (100) Holdynski, M.; Sinyureva, M.; Liu, X.; Wrobel, W.; Dygas, J. R.; Pisarek, M.; Nix, R. M.; Krok, F.; Abrahams, I. Phase and Electrical Behaviour in  $\text{Bi}_4\text{NbO}_{8.5}$ . *J. Phys. Condens. Matter* **2012**, 24 (4), 45904.
- (101) Fergus, J. W. Electrolytes for Solid Oxide Fuel Cells. *J. Power Sources* **2006**, 162 (1), 30–40.
- (102) Kharton, V. V.; Marques, F. M. B.; Atkinson, A. Transport Properties of Solid Oxide Electrolyte Ceramics: A Brief Review. *Solid State Ionics* **2004**, 174 (1–4), 135–149.
- (103) Hui, S. (Rob); Roller, J.; Yick, S.; Zhang, X.; Decès-Petit, C.; Xie, Y.; Maric, R.; Ghosh, D. A Brief Review of the Ionic Conductivity Enhancement for Selected Oxide Electrolytes. *J. Power Sources* **2007**, 172 (2), 493–502.
- (104) Morales, M.; Roa, J. J.; Tartaj, J.; Segarra, M. A Review of Doped Lanthanum Gallates as Electrolytes for Intermediate Temperature Solid Oxides Fuel Cells: From Materials Processing to Electrical and Thermo-Mechanical Properties. *J. Eur. Ceram. Soc.* **2016**, 36 (1), 1–16.
- (105) Yang, N.; D’Epifanio, A.; Di Bartolomeo, E.; Pugnolini, C.; Tebano, A.; Balestrino, G.; Licoccia, S.  $\text{La}_{0.8}\text{Sr}_{0.2}\text{Ga}_{0.8}\text{Mg}_{0.2}\text{O}_{3-\delta}$  Thin Films for IT-SOFCs: Microstructure and Transport Properties Correlation. *J. Power Sources* **2013**, 222, 10–14.
- (106) Kitamura, N.; Vogel, S. C.; Idemoto, Y. Local Structure Analysis on  $(\text{La,Ba})(\text{Ga,Mg})\text{O}_{3-\delta}$  by the Pair Distribution Function Method Using a Neutron Source and Density Functional Theory Calculations. *Solid State Commun.* **2013**, 163, 46–49.
- (107) Biswal, R. C.; Biswas, K. Novel Way of Phase Stability of LSGM and Its Conductivity Enhancement. *Int. J. Hydrogen Energy* **2015**, 40 (1), 509–518.

- (108) Khan, M. S.; and M. S. Islam; Bates, D. R. Dopant Substitution and Ion Migration in the LaGaO<sub>3</sub>-Based Oxygen Ion Conductor. *J. Phys. Chem. B* **1998**, *102* (17), 3099–3104.
- (109) Thangadurai, V.; Weppner, W. Synthesis and Electrical Properties of K- and Pr-Substituted LaGaO<sub>3</sub> and LaInO<sub>3</sub> Perovskites. *J. Electrochem. Soc.* **2001**, *148* (12), A1294–A1301.
- (110) Kajitani, M.; Matsuda, M.; Hoshikawa, A.; Harjo, S.; Kamiyama, T.; Ishigaki, T.; Izumi, F.; Miyake, M. In Situ Neutron Diffraction Study on Fast Oxide Ion Conductor LaGaO<sub>3</sub>-Based Perovskite Compounds. **2005**, No. 19, 4235–4243.
- (111) Kajitani, M.; Matsuda, M.; Hoshikawa, A.; Oikawa, K.; Torii, S.; Kamiyama, T.; Izumi, F.; and Miyake, M. Neutron Diffraction Study on Lanthanum Gallate Perovskite Compound Series. *Chem. Mater.* **2003**, *15* (18), 3468–3473.
- (112) Islam, M. S.; Davies, R. A. Atomistic Study of Dopant Site-Selectivity and Defect Association in the Lanthanum Gallate Perovskite. *J. Mater. Chem.* **2004**, *14* (1), 86–93.
- (113) Islam, M. S. Ionic Transport in ABO<sub>3</sub> Perovskite Oxides: A Computer Modelling Tour. *J. Mater. Chem.* **2000**, *10* (4), 1027–1038.
- (114) Blanc, F.; Middlemiss, D. S.; Gan, Z.; Grey, C. P. Defects in Doped LaGaO<sub>3</sub> Anionic Conductors: Linking NMR Spectral Features, Local Environments, and Defect Thermodynamics. *J. Am. Chem. Soc.* **2011**, *133* (44), 17662–17672.
- (115) Buzlukov, A.; Trokiner, A.; Kozhevnikov, V.; Verkhovskii, S.; Yakubovsky, A.; Leonidov, I.; Gerashenko, A.; Stepanov, A.; Baklanova, I.; Tankeyev, A. Vacancy Ordering and Oxygen Dynamics in Oxide Ion Conducting La<sub>1-x</sub>Sr<sub>x</sub>Ga<sub>1-x</sub>Mg<sub>x</sub>O<sub>3-x</sub> Ceramics: <sup>71</sup>Ga, <sup>25</sup>Mg and <sup>17</sup>O NMR. *J. Solid State Chem.* **2011**, *184* (1), 36–43.
- (116) Tealdi, C.; Mustarelli, P. Improving Oxygen Transport in Perovskite-Type LaGaO<sub>3</sub> Solid Electrolyte through Strain. *J. Phys. Chem. C* **2014**, *118* (51), 29574–29582.
- (117) Kuwabara, a; Tanaka, I. First Principles Calculation of Defect Formation Energies in Sr- and Mg-Doped LaGaO<sub>3</sub>. *J. Phys. Chem. B* **2004**, *108* (26), 9168–9172.
- (118) Wu, B.; Zinkevich, M.; Aldinger, F.; Zhang, W. Ab Initio Structural and Energetic Study of LaMO<sub>3</sub> (M= Al, Ga) Perovskites. *J. Phys. Chem. Solids* **2007**, *68* (4), 570–575.
- (119) Granger, P.; Parvulescu, V. I.; Kaliaguine, S.; Prellier, W. Perovskites and Related Mixed Oxides: Concepts and Applications. Wiley, Chichester 2016.
- (120) Nakayama, S.; Hashimoto, S.; Sato, K.; Yashiro, K.; Amezawa, K.; Mizusaki, J. High-

- Temperature Defect and Crystal Structure of Perovskite Type Oxide Ion Conductor  $\text{La}_{0.8}\text{Sr}_{0.2}\text{Ga}_{0.8}\text{Mg}_{0.15}\text{Co}_{0.05}\text{O}_{3-\delta}$ . *ECS Trans.* **2009**, 25 (2), 1701–1708.
- (121) Tsipis, E. V.; Kharton, V. V. Electrode Materials and Reaction Mechanisms in Solid Oxide Fuel Cells: A Brief Review. *J. Solid State Electrochem.* **2008**, 12 (11), 1367–1391.
- (122) Medvedev, D. A.; Lyagaeva, J. G.; Gorbova, E. V.; Demin, A. K.; Tsiakaras, P. Advanced Materials for SOFC Application: Strategies for the Development of Highly Conductive and Stable Solid Oxide Proton Electrolytes. *Prog. Mater. Sci.* **2016**, 75, 38–79.
- (123) Lin, Y.; Ran, R.; Zheng, Y.; Shao, Z.; Jin, W.; Xu, N.; Ahn, J. Evaluation of  $\text{Ba}_{0.5}\text{Sr}_{0.5}\text{Co}_{0.8}\text{Fe}_{0.2}\text{O}_{3-\delta}$  as a Potential Cathode for an Anode-Supported Proton-Conducting Solid-Oxide Fuel Cell. *J. Power Sources* **2008**, 180 (1), 15–22.
- (124) Li, Z.-P.; Mori, T.; Auchterlonie, G. J.; Guo, Y.; Zou, J.; Drennan, J.; Miyayama, M. Mutual Diffusion and Microstructure Evolution at the Electrolyte- Anode Interface in Intermediate Temperature Solid Oxide Fuel Cell. *J. Phys. Chem. C* **2011**, 115 (14), 6877–6885.
- (125) Backhaus-Ricoult, M. Interface Chemistry in LSM-YSZ Composite SOFC Cathodes. *Solid State Ionics* **2006**, 177 (19), 2195–2200.
- (126) Fornasini, P. Synchrotron Radiation-Basics, Methods and Applications. **2015**.
- (127) Giannici, F.; Canu, G.; Gambino, M.; Longo, A.; Salomé, M.; Viviani, M.; Martorana, A. Electrode-Electrolyte Compatibility in Solid-Oxide Fuel Cells: Investigation of the LSM-LNC Interface with X-Ray Microspectroscopy. *Chem. Mater.* **2015**, 27 (8), 2763–2766.
- (128) Ishihara, T.; Matsuda, H.; Takita, Y. Effects of Rare Earth Cations Doped for La Site on the Oxide Ionic Conductivity of  $\text{LaGaO}_3$ -Based Perovskite Type Oxide. *Solid State Ionics* **1995**, 79, 147 -151.

# CHAPTER 2

## THEORETICAL BACKGROUND

In this chapter the theoretical background concerning experimental and computational methods used in this work will be described, with the aim to give the reader an overview about X-Ray Absorption Spectroscopy and Scanning X-Ray Microscopy techniques with their data analysis treatment. Density Functional Theory approach will be also explained.

### 1. X-Ray Absorption Spectroscopy

X-Ray Absorption Spectroscopy (XAS) is a synchrotron technique based on the absorption of X-Ray beam of suitable energy by an absorbing atom. Basing on the photoelectric effect, the absorber emits a photoelectron from a core level to the continuum, and the photoelectron is scattered from the surrounding atoms, probing the local structure of the material.

XAS allows the determination of the local and electronic structure around the absorbing atom. Contrary to X-Ray Diffraction (XRD), XAS is selective for a given atomic species and for this reason it is particularly suitable to study the local structure around a dopant in a given matrix.

XAS experiments are carried out using synchrotron radiation, which is generated by charged particles (typically electrons) in a magnetic field that are forced to move in a curved trajectory at relativistic speeds.

A synchrotron light source (**Figure 2.1**) is composed by:

- **linear accelerator (linac)**. Has the task to accelerate electrons until their energy reaches several millions of electron volts (MeV) and to inject them into the booster ring;
- **booster ring**. Gives the electrons coming from the linac a boost in energy from millions to billions of electron volts (GeV) and injects the electron beam into the storage ring;
- **storage ring**. Ultra-high vacuum path made up by an array of magnets for focusing and bending the electron beam, connected by straight linear sections. The electrons,

constrained to a closed trajectory by the bending magnets, emit electromagnetic radiation (the synchrotron light). RF cavities are installed in the storage ring in order to restore the energy lost by the electrons during the emission of synchrotron radiation;

- **beamlines.** The experimental stations that use the emitted beam.

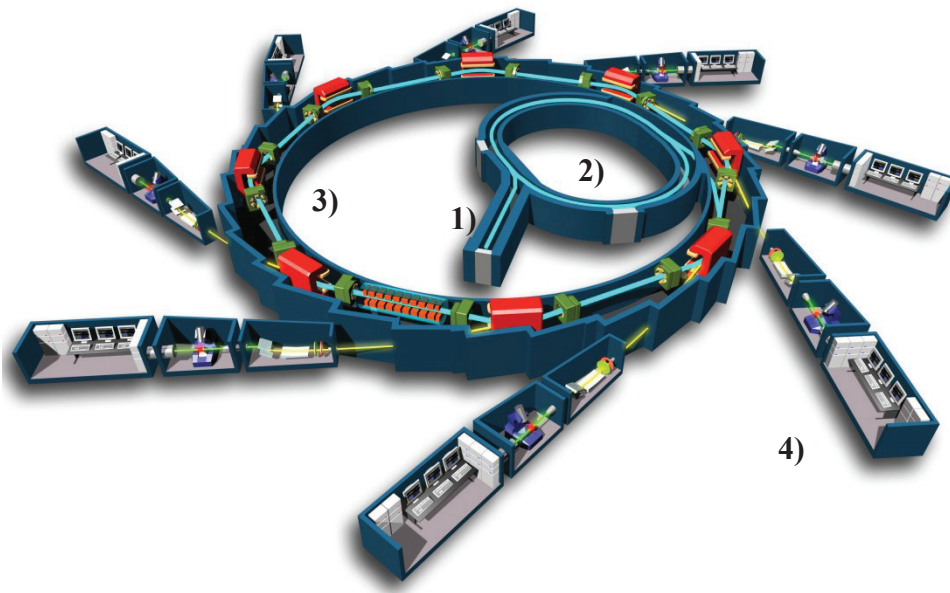


**Figure 2.1** Synchrotron ring scheme. 1) linac; 2) booster ring; 3) storage ring; 4) beamlines.

The high brilliance of the generated beam, its collimation, the wide spectral emission band and the high polarization of the beam make synchrotron radiation the ideal probe for XAS technique, allowing to study interatomic distances with an accuracy of about  $\pm 0.01 \text{ \AA}$ .

XAS technique is based (**Figure 2.2**) on the emission of a photoelectron from a core level of the absorbing atom. When an atom absorbs an X-Ray photon of higher energy than the binding energy of its core level, a photoelectron is emitted whose kinetic energy is

$$E_k = E_{X\text{-Ray}} - E_{\text{core}} \quad [1.1]$$

The emitted photoelectron is scattered by the neighbouring atoms, giving rise to interference between scattered and backscattered photoelectron wavefunction. This interference causes the modulation of the absorption coefficient  $\mu(E)$ , that contains information about the local structure around the absorber.

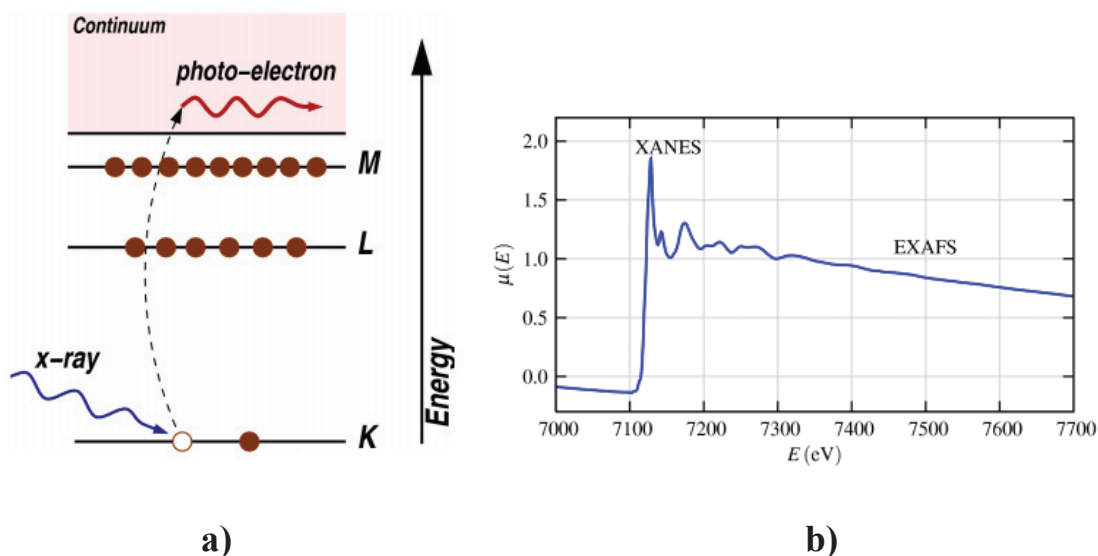


**Figure 2.2** a) photoelectron emission scheme. b) X-Ray Absorption Spectrum: XANES and EXAFS regions are highlighted.<sup>1</sup>

Two main regions can be highlighted in a XAS spectrum:

**X-ray Absorption Near Edge Structure (XANES).** This region is extended 50 eV before and above the edge. It gives information about the oxidation state and the coordination of the absorber. In this region of the spectrum multiple scattering has a large influence.

**Extended X-ray Absorption Fine Structure (EXAFS).** This region is extended from the XANES region up to the end of the spectrum (a thousand of eV). This region can give information about the local environment of the absorber in terms of interatomic distances  $R$ , coordination numbers  $N$  and disorder  $\sigma^2$  in the interatomic distances.

The theory concerning X-Ray Absorption Spectroscopy exposed in this chapter has been written basing on the reading of the books “Synchrotron Radiation – Basics, Methods and Applications”<sup>2,3</sup> given during the “13<sup>th</sup> School of Synchrotron Radiation: Fundamentals, Methods and Applications”, “EXAFS: Basics, Principles and Data analysis”<sup>4</sup> and other references listed at the end of this chapter.



## 1.1 X-Ray Absorption

When X-Rays interact with matter, the attenuation of the beam is described by the **Lambert-Beer law**

$$I_t = I_0 e^{-\mu \rho x} \quad [1.2]$$

where  $I_t$  is the transmitted intensity of photons,  $I_0$  intensity of incoming photons,  $\mu$  is the mass attenuation coefficient also called total cross section ( $\text{cm}^2/\text{g}$ ),  $\rho$  is the density of the material ( $\text{g}/\text{cm}^3$ ) and  $x$  is the distance travelled by the photons in the specimen.

The absorption coefficient  $\mu$  depends on the atomic number of the absorbing atoms and on the energy of the incoming beam according to the Victoreen law<sup>5</sup>

$$\mu \propto Z^4 \lambda^3 \quad [1.3]$$

The penetration depth ( $z$ ) of the X-Ray beam through the sample is given by:

$$z = \frac{1}{\mu} \quad [1.4]$$

This interaction between a monochromatic X-Ray beam, with frequency  $\omega = 2\pi\nu$ , and a specimen of a monoatomic system can be described considering initially an atom in its ground state  $|\psi_i\rangle$  of energy  $E_i$ . When interacting with an electromagnetic field, the atom absorbs an X-Ray photon with energy  $\hbar\omega$  and undergoes a transition to its final state  $|\psi_f\rangle$ , of energy  $E_f = E_i + \hbar\omega$  [1.5]

As previously explained, the photon energy can be used to excite an electron from a core level (excitation), or promote it to the continuum (ionization). In the final state, in both cases, a core hole is present in the system.

### **Golden rule**

This process can be described with a **semiclassical approach**, by treating the atom in a quantistic way, and the electromagnetic field with a classic approach.

The absorption coefficient  $\mu(\omega)$  depends on the atomic density of the sample and on the transition probability of the absorber from the initial state to the final state:

$$\mu(\omega) = n\sigma_a(\hbar\omega) = \left( \frac{2\hbar}{\varepsilon_0 \omega A_0^2 c} \right) n \sum_f w_{fi} \quad [1.6]$$

where

$n$  is the number of atoms per volume unit (atomic density);

$\sigma_a$  is the atomic absorption cross section;

$\frac{\varepsilon_0 \omega A_0^2 c}{2\hbar}$  is the photon flux, where  $A_0$  is the magnitude of the vector potential of the electromagnetic field and  $\varepsilon_0$  is the dielectric constant in the vacuum;

$w_{fi}$  is the transition rate from  $|\psi_i\rangle$  to  $|\psi_f\rangle$  (probability of transition per unit time).

According to the time-dependent perturbation theory,  $w_{fi}$  can be expressed as a matrix element between the stationary states  $|\psi_i\rangle$  and  $|\psi_f\rangle$ . The golden rule is then:

$$w_{fi} = \frac{2\pi}{\hbar} |\langle \psi_f | H' | \psi_i \rangle|^2 \rho(E_f) \quad [1.7]$$

where  $H'$  is the Hamiltonian operator that describes the interaction between the atom and the electromagnetic field,  $|\langle \psi_f | H' | \psi_i \rangle|$  is the matrix element between initial and final state and  $\rho(E_f)$  represents the density of the final states, compatible with energy conservation. The interaction Hamiltonian for the photoelectric absorption can be written, to the first order, as:

$$H' = i\hbar \frac{e}{m} \sum_j \mathbf{A}(\mathbf{r}_j) \cdot \nabla_j \quad [1.8]$$

where  $-i\hbar \nabla_j$  is the linear momentum operator of the  $j$ -th electron and  $\mathbf{A}(\mathbf{r}_j)$  is the vector potential of the electromagnetic field. By inserting **equation [1.8]** in **[1.7]**, the transition probability for the photoelectric absorption of a photon belonging to a monochromatic polarized beam is obtained

$$w_{fi} = \left( \frac{\pi e^2 A_0^2}{2\hbar m^2} \right) |\langle \psi_f | \sum_j e^{i\mathbf{k} \cdot \mathbf{r}_j} \mathbf{p}_j \cdot \hat{\boldsymbol{\eta}} | \psi_i \rangle|^2 \rho(E_f) \quad [1.9]$$

where the sum is over all the electrons inside the atom,  $\mathbf{p}_j$  is the momentum of the  $j$ -th electron,  $\hat{\boldsymbol{\eta}}$  and  $\mathbf{k}$  are respectively the polarization unit vector and the wave-vector of the electromagnetic field;  $\rho(E_f)$  is the density of the final states, with  $E_f = E_i + \hbar\omega$ .

In order to carry out the calculation of **equation [1.9]**, the approximations quoted below are usually applied.

### ***One-electron approximation***

The calculation of the initial state  $|\psi_i\rangle$  is relatively simple, because this state corresponds to the ground state of the atom. A more complex problem is constituted by the calculation of the final state  $|\psi_f\rangle$  because it involves a many-body interaction due to the absorption of the X-Ray photon that simultaneously involves all the electrons of the system.

Indeed, the absorption coefficient is given by the sum of elastic and inelastic contributions:

$$\mu(\omega) = \mu_{el}(\omega) + \mu_{inel}(\omega) \quad [1.10]$$

A large fraction of the absorption coefficient involves *elastic* transitions, where only one electron changes its state from  $|\psi_i\rangle$  to  $|\psi_f\rangle$  and the other  $N-1$  electrons relax their orbitals

around the core-hole. The remaining fraction  $\mu_{inel}$  of the absorption coefficient is caused by shake-up/shake-off processes, where the primary excitation of the core-electron causes secondary excitation of electrons from higher levels. In this case, the photon energy is distributed among all the excited electrons (*inelastic* transitions).

The elastic contribution can be written as:

$$\mu_{el}(\omega) \propto |\langle \psi_f^{N-1} \psi_f | e^{i\mathbf{k}\cdot\mathbf{r}_j} \hat{\boldsymbol{\eta}} \cdot \mathbf{p} | \psi_i^{N-1} \psi_i \rangle|^2 \rho(E_f) \quad [1.11]$$

where  $\psi^{N-1}$  is the Slater determinant of the wavefunction of the passive N-1 electrons and  $\psi_f$ ,  $\mathbf{r}$ ,  $\mathbf{p}$  and  $E_f$  are respectively the wavefunction, the vector position, the momentum and the final energy of the active electron. In this way, the interaction Hamiltonian operates on one electron.

### ***Dipole approximation***

Coming back to **equation [1.9]**, if  $|\mathbf{k} \cdot \mathbf{r}_j|^2 \ll 1$  the wavelength  $\lambda$  is much larger than the dimension of the system and the electric field can be considered constant in the analyzed region. This leads to the dipole approximation and **equation [1.9]** can be rewritten as

$$w_{fi} = (-e^2) |\langle \psi_f | \sum_j e^{i\mathbf{k}\cdot\mathbf{r}_j} \mathbf{p}_j \cdot \hat{\boldsymbol{\eta}} | \psi_i \rangle|^2 \rho(E_f) \quad [1.12]$$

In the one-electron approximation, the electromagnetic field interacts only with a core electron, whose extension is smaller than the X-Ray wavelength.

The dipole approximation is valid for K-edges up to 20-25 keV, and within this approximation angular momentum selection rules are valid:

$$\Delta\ell = \pm 1, \quad \Delta s = 0, \quad \Delta j = \pm 1, 0, \quad \Delta m = 0$$

For one-electron transitions, the selection rule  $\Delta\ell = \pm 1$  means that:

- If the electron is extracted from a  $s$  level ( $\ell=0$ , K and  $L_1$  edges), its final state will be a  $p$  symmetry state, with  $\ell=1$ .
- If the electron is extracted from a  $p$  level ( $\ell=1$ ,  $L_2$  and  $L_3$  edges), its final state will be a  $s$  or  $d$  symmetry state, with  $\ell=0$  or  $\ell=2$ .

It must be also said that dipole-forbidden transitions can also give non-negligible contributions to pre-edge and edge fine structure (typical case is the pre-edge peak in tetrahedral coordination complexes).

### ***Sudden approximation***

According to the sudden approximation, the interaction between the photoelectron with the passive electrons can be neglected in the EXAFS region, if the photoelectron energy is high enough. According to the sudden approximation, the initial and final states of the atoms can

be factorized, separating the initial and final states of the active electron,  $|\psi_i\rangle$  and  $|\psi_f\rangle$ , from the states  $|\psi_i^{N-1}\rangle$  and  $|\psi_f^{N-1}\rangle$  of the N-1 passive electrons

$$\mu_{el}(\omega) = n\sigma_{el} = n \left( \frac{\pi e^2 \omega}{\epsilon_0 c} \right) |\langle \psi_f | \hat{\mathbf{n}} \cdot \mathbf{p} | \psi_i \rangle|^2 S_0^2 \rho(E_f) \quad [1.13]$$

where  $S_0^2$  is the superposition integral:

$$S_0^2 = |\langle \psi_f^{N-1} | \psi_i^{N-1} \rangle|^2 \quad [1.14]$$

$S_0^2$  has generally a value in the range 0.7-0.9, and gives an evaluation of the fraction of total absorption due to elastic transitions (if the N-1 passive electrons ideally undergo no relaxation, the elastic component  $\mu_{el}$  would be the only contribution to  $\mu(\omega)$  in **equation [1.10]** and  $S_0^2$  would be 1). This approximation holds in the EXAFS region starting from about 10 eV above the edge.

### ***De-excitation mechanisms***

When a core-hole is created after the interaction between an X-Ray photon with the absorbing atom, two competitive de-excitation mechanisms can take place:

- Radiative de-excitation (fluorescence): the core-hole is filled by an electron from a higher level and this energy is released as an X-ray photon. Fluorescence emission is typical of high Z elements.
- Non-radiative de-excitation (Auger emission). The core-hole is filled by an electron from a higher level and the photon produced by this transition ejects another electron from an higher shell (Auger electron). The Auger emission is typical of low Z elements.

The probability of de-excitation mechanisms will determine the core-hole lifetime. The higher is the atomic number of the element (Z), the higher is the number of higher levels that can re-fill the core-hole, and the shorter is the core-hole lifetime  $\tau$ . The core-hole lifetime will determine the time during that the photoelectron explore the local structure around the absorbing atom.

## 1.2 The EXAFS function

### *Monoatomic system*

Basing on the previous analysis, the final photoelectron stationary state  $|\psi_f\rangle$  contains the local structure information.  $|\psi_f\rangle$  can be computed in many different ways, but it is generally treated basing on the Multiple Scattering (MS) formalism. Nevertheless, in the EXAFS region this formalism can be simplified and the Single Scattering (SS) approximation can be used.

As previously seen, the absorption coefficient in the one-electron approximation can be written as

$$\mu_{el}(\omega) \propto |\langle \psi_f | \hat{\mathbf{n}} \cdot \mathbf{p} | \psi_i \rangle|^2 \rho(E_f) \quad [1.15]$$

Supposing the inelastic contribution being null ( $S_0^2 = 1$ ), in the EXAFS region of the photoelectron the photoelectron density of final states  $\rho(E_f)$  varies slowly with the energy and the EXAFS oscillations are entirely described by the matrix element, where  $|\psi_i\rangle$  and  $|\psi_f\rangle$  are the initial and final states of the photoelectron.

If a K-edge is considered, for an isolated atom, the photoelectron is ionized from the atom and its final state  $|\psi_f^0\rangle$  is a spherical wave with  $\ell=1$ .

The photoelectron wave vector  $\mathbf{k}$  can be described by the following equation

$$k = \sqrt{\left(\frac{2m}{\hbar^2}\right) \varepsilon_f} = \sqrt{(2m/\hbar^2)(\hbar\omega - E_b)} \quad [1.16]$$

where  $E_b$  is the binding energy of the photoelectron.

For an isolated atom,  $\mu_0(\omega)$  is called atomic absorption coefficient and it can be written as

$$\mu_0(\omega) \propto |\langle \psi_f^0 | \hat{\mathbf{n}} \cdot \mathbf{p} | \psi_i \rangle|^2 \quad [1.17]$$

If the atom is not isolated, after the ejection from the core level, the photoelectron interacts with the surrounding atoms and undergoes to scattering.

In the EXAFS region the photoelectron energy is much higher than the interaction energy with the surrounding atoms and therefore the interaction can be treated as a weak perturbation of the final state of an isolated atom. Then, the absorption coefficient can be written as

$$\mu(\omega) \propto |\langle \psi_f^0 + \delta\psi_f | \hat{\mathbf{n}} \cdot \mathbf{p} | \psi_i \rangle|^2 \quad [1.18]$$

where  $\delta\psi_f$  is the backscattered wave. The interference of this backscattered wave with the

outcoming wave  $\psi_f^0$  causes a modulation of the total wavefunction of the final state and modifies its superposition integral with the initial state wavefunction  $\psi_i$ .

The normalized EXAFS function will be defined as

$$\chi(k) = \frac{(\mu - \mu_0)}{\mu_0} \quad [1.19]$$

where  $\mu$  is the absorption coefficient and  $\mu_0$  the atomic absorption coefficient. The absorption coefficients of the equations [1.17] and [1.18] can now be inserted into the equation [1.19]

$$\chi(k) = \frac{2\text{Re} \int [\psi_i(\mathbf{r}) \hat{\boldsymbol{\eta}} \cdot \mathbf{r} \psi_f^{0*}(\mathbf{r})] [\psi_i^*(\mathbf{r}) \hat{\boldsymbol{\eta}} \cdot \mathbf{r} \delta\psi_f(\mathbf{r})] d\mathbf{r}}{\int |\psi_i^*(\mathbf{r}) \hat{\boldsymbol{\eta}} \cdot \mathbf{r} \psi_f^0(\mathbf{r})|^2 d\mathbf{r}} \quad [1.20]$$

### ***Biatomic system***

In this section, a biatomic system A-B, where A is the absorbing atom, B the backscattering atom,  $\mathbf{R}_B$  the vector position will be considered at the K-edge.

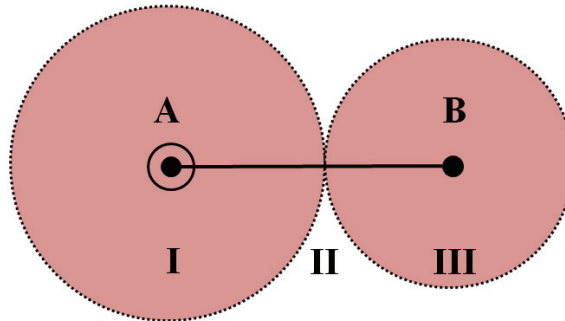


**Figure 2.3** different regions of potential considered in the muffin-tin scheme.

A muffin tin potential is generally used to describe the system. According to this scheme, three regions of potential (**Figure 2.3**) are defined in the A-B system:

- I. spherical potential centred on the A atom;
- II. constant potential in the interatomic region;
- III. spherical potential centred on the B atom;

the perturbation  $\delta\psi_f$  can be described by following step by step the photoelectron path.

The initial state wavefunction  $\psi_i$  (1s orbital,  $\ell=0$ ) is confined at the centre of the region I.

At the same time, also the isolated final state wavefunction  $\psi_f^0$  with  $\ell=0$  must be described only at the centre of region I, in order to evaluate the superposition integrals of **equations [1.17] and [1.20]**.

At the border of region I. the radial part of the photoelectron can be approximated for high enough energies ( $kr \gg 1$ ) as

$$\psi_f^0 \left( \frac{e^{ikr}}{2kr} \right) e^{i\delta_1} \quad [1.21]$$

where  $\delta_1$  takes into account the effect of the potential of region 1.

The interaction between the photoelectron and the backscatterer atom B in the region III will be now considered. The scattering between the photoelectron and the B atom can be restricted to a very small region if the photoelectron has high enough energy to consider significant only the interaction with the inner electrons of the B atom (**small atom approximation**). Moreover, the curvature of the spherical wave incoming on the B atom can be neglected (**plane wave approximation**).

The process can now be described as a complex amplitude  $f_B(k, \pi)$  of backscattering from B to A

$$f_B(k, \pi) = \left( \frac{1}{k} \right) \sum_{\ell=0}^{\infty} (-1)^\ell (2\ell + 1) e^{i\delta_\ell} \sin \delta_\ell \quad [1.22]$$

where  $\delta_\ell$  is the partial-wave phase-shift. The radial part of the backscattered wave at the limit of region III will be

$$\left[ \psi_f^0 \left( \frac{e^{ikR_B}}{2kR} \right) e^{i\delta_1} \right] f_B(k, \pi) \left[ \left( \frac{e^{ikr'}}{r'} \right) \right] \quad [1.23]$$

where  $\left[ \psi_f^0 \left( \frac{e^{ikR_B}}{2kR} \right) e^{i\delta_1} \right]$  is the wave impinging on B and  $\left[ \left( \frac{e^{ikr'}}{r'} \right) \right]$  the wave scattered by B, with  $r'$  being the distance from atom B.

The final wavefunction can be factorized as

$$\psi_f^0 \left( \frac{1}{2k} \right) e^{i\delta_1} \frac{e^{2ikR}}{R} f_B(k, \pi) \frac{e^{2ikR}}{R} e^{i\delta_1} \quad [1.24]$$

where the phase-shift  $\delta_1$  takes into account the effect of the potential on region I on the backscattered wavefunction. In this way, the perturbation is described as a series of interaction factors and propagators.

By inserting **equation [1.24]** in **[1.20]**

$$\chi(k) = 3(\hat{\boldsymbol{\eta}} \cdot \mathbf{R})^2 \left( \frac{1}{kR^2} \right) \text{Im}\{f_B(k, \pi) e^{2i\delta_1} e^{2ikR}\} \quad [1.25]$$

Magnitude and phase of the complex backscattering amplitude can be separated

$$f_B(k, \pi) e^{2i\delta_1} = |f_B(k, \pi)| e^{i\Phi} \quad [1.26]$$

and equation [1.25] can be rewritten as:

$$\chi(k) = 3(\hat{\boldsymbol{\eta}} \cdot \mathbf{R})^2 \left( \frac{1}{kR^2} \right) |f_B(k, \pi)| \sin[2kR + \Phi(k)] \quad [1.27]$$

**Equation [1.27]** represents the standard form of the EXAFS signal, which is characterized by sinusoidal oscillations, where the phase of the sine function is modified by the phase shift  $\Phi(k)$ .

### ***Polyatomic system***

For a system with N-atoms the treatment of the EXAFS function is relatively simple if the photoelectron Multiple Scattering is neglected, even if MS is not always negligible. In the Single Scattering (SS) approximation, the EXAFS function can be built up as the sum of many biatomic contributions:

$$\chi(k) = \left( \frac{1}{k} \right) \sum_j \left( \frac{1}{R_j^2} \right) \text{Im}\{f_B(k, \pi) e^{2i\delta_1} e^{2ikR_j}\} \quad [1.28]$$

where  $R_j$  is the distance of the j-th atom from the absorber.

A series of corrections must be taken into account for many-atomic systems and will be described in the following sections.

### ***Inelastic effects***

Inelastic effects are not taken into account in the previous treatment of EXAFS equation. Indeed, two main inelastic effects can be highlighted:

- *intrinsic inelastic effects*: are caused by multiple excitations that modify the photoelectron energy and the interference between incoming and outgoing waves. The intrinsic inelastic effects cause a reduction in the coherent EXAFS signal that is corrected by the previously described  $S_0^2$  factor.
- *extrinsic inelastic effects*: are referred to the photoelectron mean free path  $\lambda$ . The photoelectron mean free path is affected by two phenomena: *i*) the core-hole lifetime  $\tau_h$  (depending on  $Z$ ) that describes the maximum distance ( $\lambda_h = v\tau_h$ ) explored by the



photoelectron before de-excitation of the absorbing atom; *ii*) the energy-dependent photoelectron mean free path  $\lambda_e(k)$ , that is caused by the inelastic collisions of the photoelectron with electrons outside the absorbing atom. The total  $\lambda$  can be written as

$$\frac{1}{\lambda} = \frac{1}{\lambda_h} + \frac{1}{\lambda_e} \quad [1.29]$$

It must be said that at low energies, in the XANES region,  $\lambda$  is determined by  $\lambda_h$  contribution, while in the EXAFS region is determined by  $\lambda_e$ .

Therefore, the EXAFS equation can be modified taking into account inelastic contributions

$$\chi(k) = \left(\frac{S_0^2}{k}\right) \sum_j \left[ \frac{e^{-\frac{2R_j}{\lambda(k)}}}{R_j^2} \right] \text{Im} \{f_j(k, \pi) e^{2i\delta_1} e^{2ikR_j}\} \quad [1.30]$$

If the backscattering atoms are organized in coordination shells, each one made up of  $N_s$  atoms at distance  $R_s$ , where the  $s$  index labels the coordination shells, the previous equation can be rewritten as

$$\chi(k) = \left(\frac{S_0^2}{k}\right) \sum_s N_s \text{Im} \left\{ f_s(k, \pi) e^{2i\delta_1} \left[ \frac{e^{-\frac{2R_s}{\lambda(k)}}}{R_s^2} \right] e^{2ikR_s} \right\} \quad [1.31]$$

### ***Multiple Scattering effects***

MS events are generally more important in the XANES region and are weak in the EXAFS part of the absorption spectrum. In order to take into account the MS effects, the absorption coefficient can be written as:

$$\mu(k) = \mu_0(k) [1 + \chi_2(k) + \chi_3(k) + \dots \chi_p(k) + \dots] \quad [1.32]$$

where  $p$  is the number of bonds involved in the MS path. The term  $\chi_2(k) \equiv \chi(k)$  corresponds to the single scattering contribution that will be considered in the following discussion. Indeed, this series is fast convergent in the EXAFS region.

The MS contribution can be expressed as

$$\chi_p(k) = A_p(k, \{\mathbf{r}\}_p) \sin[kR_p + \Phi_p(k, \{\mathbf{r}\}_p)] \quad [1.33]$$

where  $\{\mathbf{r}\}_p$  is the set of vector distances inside a path and  $R_p$  is the total path length; the amplitude  $A_p$  and the phase-shift  $\Phi_p$  are functions depending on the potential acting on the photoelectron.

## ***Disorder effects***

Disorder effects are not taken into account in the previous equation, which is referred to a system where atoms are frozen at their equilibrium position.<sup>6</sup>

Indeed three types of disorder generally can affect the system:

- **static disorder:** it is generated by the presence of structural disorder that modifies the distribution of the interatomic distances;
- **compositional disorder:** the presence of different type of atoms in the same coordination shell generates disorder, which in this case is called compositional disorder;
- **dynamic disorder:** it is caused by thermal vibrations that are not negligible, even at 0 K. The amplitude of thermal vibrations increases with temperature.

The EXAFS formula must be therefore corrected also for disorder contribution, so obtaining the standard EXAFS equation:

$$\chi(k) = \left(\frac{S_0}{k}\right)^2 N_s \frac{e^{-\frac{2R_s}{\lambda}}}{R_s^2} e^{(-2k^2\sigma_s^2)} |f_s(k, \pi)| \sin[2kR_s + \Phi(k)] \quad [1.34]$$

The term  $\exp(-2k^2\sigma_s^2)$  is generally referred to as the Debye Waller factor of EXAFS and takes into account the distribution of the s-shell absorber-backscatterer distance.

## **1.3 Experimental setup**

X-Ray Absorption Spectroscopy measures the X-Ray absorption coefficient as function of the photon energy. The experimental apparatus of a XAS beamline, drawn in **Figure 2.4**, is composed by an optical part (monochromator and X-Ray mirrors) and a measurement apparatus (sample holder and detector).

**Monochromator:** is the device that, basing on X-Ray diffraction (Bragg law), selects the energy of the beam from the synchrotron radiation spectrum and allows performing scans in a selected energy range.

**X-Ray mirrors:** have the task to reject harmonics, collimate and focalize the beam. By choosing the incidence angle of the beam on the mirrors, only the fundamental wavelengths are reflected, while the harmonics are rejected.

**Sample holder:** it can be chosen according to the experimental needs. Measurements can be acquired at:

- low temperature, in order to characterize the local structure of materials at static disorder conditions, cancelling out thermal disorder effects. In this case, the measurement is carried out at liquid nitrogen (77 K) or liquid helium (4 K) temperature using a cryostat;
- high temperature, if temperature-dependent phase transitions, lattice dynamics or other types of temperature effect has to be probed, suitable cells can be used (e.g., the “microtomo furnace”, see **Chapter 4**);
- high pressure, performed with cells that can reach up to tens of GPa;
- catalytic conditions. To this end, measurements are carried out in suitable reactors, at operating conditions (temperature, gas atmosphere, etc.).

**Detector:** has the task to measure the absorption coefficient of the selected element according to

$$\mu = \frac{\ln\left(\frac{\Phi_0}{\Phi}\right)}{x} \quad [1.35]$$

where  $\Phi_0$  is the incident photon flux,  $\Phi$  is the transmitted one and  $x$  is the distance travelled by the photon through the specimen.

Two different type of detection have been used in this work and each one requires a particular type of detector:

- **Transmission measurements.** The photon fluxes  $\Phi_0$  and  $\Phi$  are measured by two ionization chamber detectors. Ionization chambers transform the fluxes in two low intensity electric currents  $I_0$  and  $I$  ( $10^{-10}$ - $10^{-8}$  A). The absorption coefficient  $\mu(\omega)$  is then given by

$$\mu(\omega)x = \ln\left(\frac{\Phi_0}{\Phi}\right) = \ln\left(\frac{I_0}{I}\right) - C \quad [1.36]$$

where  $C$  is a constant depending on the detector efficiency. The thickness of the sample ( $x$ ) must be of the order of magnitude of 10  $\mu\text{m}$ , in order to avoid low signal-to-noise ratio. Transmission measurements are not suitable for diluted samples or for surface characterization.

- **Fluorescence measurements.** Fluorescence detectors are often solid state detectors or crystals and have different tasks, such as ensuring the minimization of Compton scattering background and cancel out unwanted fluorescence lines. Fluorescence measurements are very suitable for diluted and thin samples. In this kind of setup, the final intensity  $I_f$  of the fluorescence

beam emitted at the fixed frequency  $\omega_f$  of the absorbing atom  $A$ , is measured as a function of the incident X-Ray energy. At an angle of  $90^\circ$  between  $I_f$  and  $I_0$  the noise due to the scattered photons is minimized.

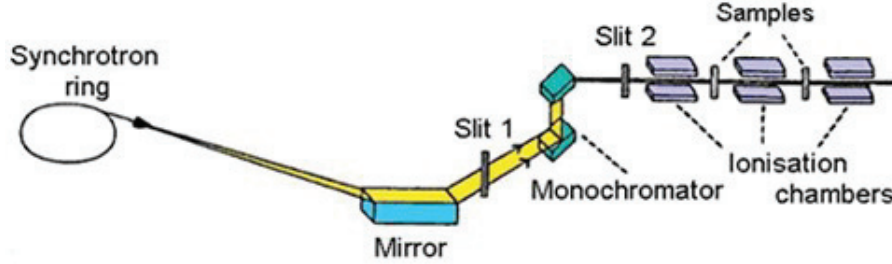


**Figure 2.4** Scheme of the principal components of a XAS beamline.<sup>38</sup>

## 1.4 Data analysis

EXAFS data analysis involves the following analysis steps:

- **Extraction of the EXAFS signal  $\chi(k)$ .** It is different depending on the detection method used. For example, considering a transmission experiment at the K-edge of a given element, the K-edge absorption coefficient  $\mu(\omega)x$  is extracted from the experimental signal by

$$\mu(\omega)x = \ln\left(\frac{I_0}{I}\right) - \mu_n(\omega)x \quad [1.37]$$

where  $\mu_n$  represents the other excitations of considered element plus the excitations of the other elements of the specimen. In the pre-edge region,  $\mu_n(\omega)x = \ln\left(\frac{I_0}{I}\right)$ , while above the edge  $\mu_n(\omega)x$  is calculated from

$$\frac{\mu}{\rho} = C\lambda^3 - D\lambda^4 + \frac{\sigma_{K-N}NZ}{A} \quad [1.38]$$

The photoelectron wave vector is experimentally defined as

$$k = \sqrt{\frac{2m}{\hbar^2}(\hbar\omega - E_s)} \quad [1.39]$$

where  $E_s$  is usually chosen at the first inflection point of the absorption edge.

The difference  $E_0 = E_b - E_s$  between the binding energy of the core electron and  $E_s$  is *a priori* unknown.  $E_0$  is generally treated as a free parameter in the fitting procedure.

Nevertheless, the same criterion must be used in the choice of  $E_s$  for the sample and the reference compound.

The evaluation of  $\mu_0$ , necessary in order to calculate the EXAFS function

$$\chi(k) = \frac{\mu - \mu_0}{\mu_0} \quad [1.40]$$

is usually carried out by a polynomial spline curve that represents the average of the oscillations of the experimental  $\mu$ .

- **Fourier Transform and back-transform.** Once the EXAFS signal  $\chi(k)$  is obtained, it is possible to start the fitting procedure. The preferred method to cope with the high number of parameters to be refined consists in isolating the contribution of the different coordination spheres of the absorber by applying a Fourier Transform (FT) filtering.

First of all, the FT from the  $k$  space to the  $r$  space must be applied

$$F(r) = \int_{k_{min}}^{k_{max}} \chi(k)W(k)k^n \exp(2ikr) dk \quad [1.41]$$

In **equation [1.41]**  $W(k)$  is a window function that reduces the spurious oscillations induced by the finite  $k$  range,  $k^n$  can be  $n = 1 - 3$  and it is used to enhance the low- $k$  or high- $k$  regions of the signal. Usually the  $k$ -range is chosen starting from  $k_{min} > 2 - 4$ , in order to cancel out the low- $k$  region, where the EXAFS equation is not valid, due to a low signal to noise ratio. The amplitude of  $F(r)$

$$|F(r)| = \sqrt{[ReF(r)]^2 + [ImF(r)]^2} \quad [1.42]$$

does not represent a real radial distribution function, because the position of the peaks is shifted at shorter distances, due to the phase shift  $\Phi_s$  of each scattering path. Some general hints that should be taken into account for the FT analysis are: **i)** peaks found at lower distances than the first shell peak are symptomatic of a bad evaluation of  $\mu_0$ , involving that the extraction procedure must be repeated; **ii)** the comparison of different FT for the same sample is useful to highlight effects induced by temperature, pressure, chemical environment, etc.; **iii)** the comparison between different samples can highlight the structural differences in terms of interatomic distances and disorder effects; **iv)** peaks not corresponding to interatomic differences can be diagnostic of marked multiple scattering effects. The contribution of selected scattering paths can be determined by applying the inverse FT (back-transform) in a given  $r_{min} - r_{max}$  interval

$$\chi'(k) = \frac{2}{\pi} \int_{F_{min}}^{F_{max}} F(r)W'(r) \exp(-2ikr) dr \quad [1.43]$$

The real part of this back-transform represents the filtered signal, which is cleaned up from the artefacts introduced by the FT and back-scattering procedure.

- **Quantitative determination of structural parameters.** Once the EXAFS signal is obtained, it is possible to refine the structural parameters  $R_s$ ,  $N_s$  and  $\sigma_s$  previously described. To this end, it is necessary to know the physical parameters that appear in the EXAFS formula: the scattering amplitudes  $|f_s(k)|$ , the phase shifts  $\Phi_s(k)$  and the inelastic factors  $S_0$  and  $\lambda(k)$ . The majority of the data analysis packages pinpoint the relevant SS and MS paths and perform an *ab initio* calculation of these physical parameters for each path (we will compare this procedure for FEFF<sup>8,10</sup> and GNXAS<sup>8,11,12</sup> codes in the next section). The theoretical  $\chi_{sim}(k)$  signal, generated from a starting model structure, is then compared with the experimental one,  $\chi_{exp}(k)$ , through a minimization procedure. The maximum amount of information that can be extrapolated from EXAFS data can be evaluated by means of the Nyquist formula:

$$N \approx \frac{2\Delta K \Delta R}{\pi} + 2 \quad [1.44]$$

where  $\Delta K$  is the range in the k space,  $\Delta R$  is the R range of the Fourier Transform and N is the number of independent points. As a guide-criterion, the number of fitting parameters (P) and the degree of freedom ( $\nu=N-P$ ) should be kept to a value which is the half of N.

$$P = \nu = \frac{N}{2} \quad [1.45]$$

## GNXAS and FEFF

Data analysis methods based on the use of the SS and plane wave approximations are not suitable for fitting beyond the first coordination shell.<sup>7-9</sup> In order to perform a correct prediction of low-angle scattering effects and expression for MS contributions, it is necessary to use a spherical wave approach.<sup>7-9</sup> Advanced methods based on *ab initio* simulations of the X-Ray Absorption cross section have demonstrated to be highly effective in the short range characterization of condensed matter.<sup>7-9</sup> XAS spectra and excited states electronic structure are deeply connected, and the many-body interactions can be efficiently described by the one-electron Green's function of the system. The theoretical development of methods based on

this concept is mainly focused on the inclusion of MS terms and on the use of optical potentials capable to account for inelastic effects. Advanced data analysis packages based on these methods have been developed, and the most known codes for XAS data analysis are currently FEFF,<sup>8,10</sup> GNXAS<sup>8,11,12</sup> and EXCURVE<sup>8,13</sup>. The difference between these codes lies in the way the MS terms are taken into account and in the configurational average computation.

In this work FEFF9<sup>10</sup> and GNXAS<sup>11,12</sup> approaches have been used to compute the physical parameters of the solid-state electrolytes under analysis.

Let us make a brief comparison of the two methods used. **Figure 2.5** shows a comparison between data analysis performed with FEFF9<sup>10</sup> code (fitting procedure carried out with Viper<sup>14</sup>) and with GNXAS<sup>11,12</sup> for undoped LaGaO<sub>3</sub> at Ga K-edge.

**GNXAS.** In this method, the local environment around the absorber is decomposed into configurations containing  $2, \dots, n$  atoms. The EXAFS signal is calculated by the expansion of the signal as the sum of  $\gamma^2, \gamma^3, \dots, \gamma^{(n)}$   $n$ -body contributions, which take into account all the possible SS and MS path within a  $n$ -atom configuration. Each  $\gamma^{(n)}$  signal accounts for an infinite number of MS terms and as consequence the expansion results in a better convergence rate than the MS series. During the fitting procedure, for MS paths of higher order than 2-body configurations, the angles describing a given MS path are also refined. This approach is particularly suitable for amorphous systems<sup>15</sup> and in those situations where a detailed characterization of the angles is required, as needed in this work for the study of tilting angles in the perovskite-like lanthanum gallate described in **Chapter 4**.

**FEFF.** In this procedure, given a model cluster, all the possible MS paths around the absorbing atom are identified and parameterized similarly to SS paths, with a path-by-path MS approach (Rehr-Albers formalism).<sup>8,9,16,17,18</sup> A routine (the so-called “heap algorithm”) evaluates the high number of paths and retains only those that are shorter than a given path-length cut-off. For what concerns degeneracy, only those paths with amplitudes above a selected cut-off are considered. These filters ensure that only a small part of MS paths within the model cluster need to be computed (usually around 100 paths).

Extraction and fitting procedures can be carried out with various *ad hoc* programs.<sup>14,19</sup> In this work, Viper<sup>14</sup> software has been used to carry out these procedures for Ta-doped bismuth oxide fluorite-like system (**Chapter 3**) and for EXAFS data analysis in the electrode-electrolyte compatibility study (**Chapter 5**).

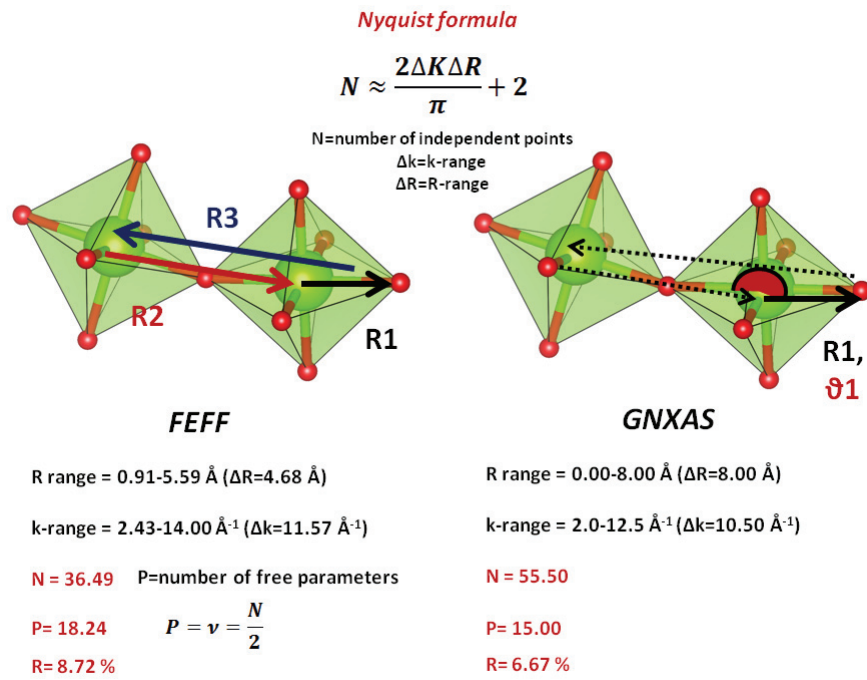


**Figure 2.5** Example of EXAFS data analysis performed with FEFF (fitting procedure achieved with Viper) and GNXAS.

## 2. X-Ray Microscopy

The same theoretical principles explained for XAS technique are valid also for Scanning X-Ray Microscopy.<sup>2,3,20</sup>

As previously seen, when X-Rays interact with matter the attenuation of the beam is described by the Lambert-Beer law

$$I_t = I_0 e^{-\mu \rho x} \quad [2.1]$$

$\mu$  depends on the atomic number of the absorbing atoms and on the energy of the incoming photons:

$$\mu \propto Z^4 \lambda^3 \quad [2.2]$$

The penetration depth ( $z$ ) of the X-Ray beam through the sample is given by:

$$z = \frac{1}{\mu} \quad [2.3]$$

The interaction of the X-Rays with the sample is described by the complex index of refraction  $n$ :



$$n = 1 - \delta - i\beta \quad [2.4]$$

where  $\delta$  is the refractive index decrement (real part) and  $\beta$  is the absorption index (imaginary part). While  $\delta$  depicts photon refraction,  $\beta$  evaluates the attenuation of photons in the material, and it is linked to  $\mu$  through the relation:

$$\mu = \frac{4\pi\beta}{\lambda} \quad [2.5]$$

$\mu$  can also be described in the X-Ray range by:

$$\mu(E) = \tau(E) + \sigma_{coh}(E) + \sigma_{inc}(E) \quad [2.6]$$

where  $\tau(E)$  is the photoelectric mass absorption coefficient (absorption of X-Rays),  $\sigma_{coh}(E)$  is the coherent mass absorption coefficient (coherent scattering, i.e. Rayleigh, Thomson) and  $\sigma_{inc}(E)$  is the incoherent mass absorption coefficient (incoherent Compton scattering).

Based on these theoretical considerations, XRFs can use three different types of contrast:

- **Absorption contrast:** is based on the measurement of the imaginary part  $\beta$  of the complex index of refraction  $n$  (**equation 2.4**). The sample is irradiated with X-Ray photons having an energy which is slightly higher than the ionization threshold of an atomic core level of the target element: a photoelectron is ejected in the continuum and the X-Ray intensity transmitted by the sample is measured giving rise to an absorption edge, which depends on the atomic number  $Z$  (**equation 2.2**). This type of contrast allows using an EXAFS approach, that gives information about the local structure around the absorber, and a XANES approach, that can reveal the electronic properties of the absorber (chemical state, electronic correlations and density of states).
- **Fluorescence contrast:** X-Ray Fluorescence (XRF) is the direct consequence of X-Ray Absorption. When the energy of the incoming beam is tuned just above the edge of the element of interest, a characteristic fluorescence line of this element and of the elements with lower  $Z$  in the matrix is also emitted. Fluorescence emission is strictly governed by selection rules that govern permitted transitions. This type of contrast represents a powerful tool for microchemical analysis.
- **Phase contrast:** it is based on the measurement of the refractive index decrement  $\delta$  (**equation 2.4**). This type of contrast is strictly linked to refraction, diffraction, interferences, and the phase of the incident X-Rays. It has the advantage to permit

the imaging of weakly absorbing materials and to have a high sensitivity for sample morphology. This sensitivity to materials with a weak absorption depends on the fact that  $\delta$  is inversely proportional to  $\lambda^2$ , so it produces significant variations when absorption is low. The phase contrast technique is very suitably combined with fluorescence, because the former is able to detect low  $Z$  elements, while the latter can detect elements in trace.

## 2.1 Experimental Setup

In the SXM technique, the beam is focused down to a submicron probe by a fixed curvature Kirkpatrick-Baez (KB) mirrors system. The microscope is operated in a vacuum chamber to avoid air absorption and scattering of the beam. The change of sample is performed through a load-lock chamber. The flat sample is aligned in the focal plane of the KB mirrors with an optical videomicroscope, which allows an accurate positioning of the selected region of interest. The experimental setup is depicted in **Figure 2.6**.

The X-ray fluorescence (XRF) photons emitted by the sample are collected using a 80 mm<sup>2</sup> Silicon Drift Diode (SDD) detector (Bruker, Germany). The sample is raster-scanned in two-dimensions by the micro-beam using piezoelectric actuators to produce a 2D XRF map.

A complete fluorescence spectrum is acquired for each pixel, allowing off-line fitting of the spectra and deconvolution of the elemental distributions using the PyMca software.<sup>21</sup>

In selected spots, a microXRF spectrum can be collected alongside the microEXAFS and microXANES signals.

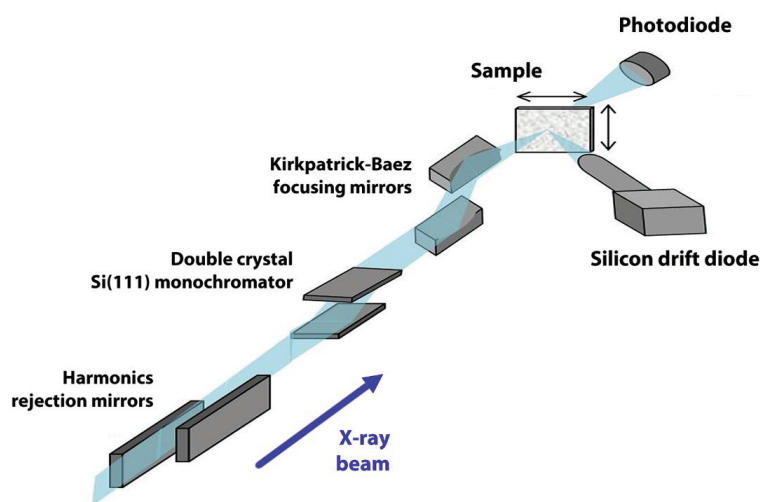


**Figure 2.6** Scanning X-ray microscopy setup.<sup>22</sup>

### 3. Density Functional Theory

DFT is a method to obtain an approximate solution of the Schrödinger equation of a  $N$ -electron system through the replacement of the wavefunction  $\psi$  (Hartree-Fock method), depending on  $3N$  spatial variables and  $N$  spin variables, with the electronic density  $\rho$ , which is a measurable physical observable:

$$\rho(\vec{r}_1) = N \int \dots \int |\psi(\vec{r}_1, \vec{r}_2, \dots, \vec{r}_N)|^2 d\vec{r}_2 \dots d\vec{r}_N \quad [3.1]$$

The theory is based on the Hohenberg-Kohn theorems.<sup>23</sup> The **first theorem** proves that any observable is a functional of the electronic density  $\rho(\vec{r})$  of the system. Then, the electronic density state contains all the necessary information to define an atomic or molecular system, under the assumption of the Born-Oppenheimer approximation<sup>24</sup> that the electrons respond instantaneously to the motion of the ions. The first theorem of Hohenberg and Kohn applies in particular to the energy functional, which can be written as:

$$E[\rho] = \int \rho(\vec{r}) V_{Ne} d\vec{r} + F_{HK}[\rho] \quad [3.2]$$

where  $V_{Ne}(\vec{r})$  is the interaction potential between electrons and nuclei and  $F_{HK}[\rho]$ , the Hohenberg-Kohn functional, is given by

$$F_{HK}[\rho] = T[\rho] + J[\rho] + E_{ncl}[\rho] \quad [3.3]$$

where  $T[\rho]$  is the kinetic energy functional,  $J[\rho]$  is the coulombic classic contribution to the repulsion, and  $E_{ncl}[\rho]$  is the non classic contribution to the electron-electron interaction. Finding approximate expression for  $T[\rho]$  and  $E_{ncl}[\rho]$  represents the most difficult challenge for the DFT-based methods.

The **second theorem** of Hohenberg-Kohn states that the ground state energy  $E_0$  can be obtained variationally: the density that minimizes the total energy is the exact real electronic density of the system.

The electronic density  $\rho(\vec{r})$  is described in term of monoelectronic functions called Kohn-Sham<sup>25</sup> spinorbital  $\theta_i(\vec{r})$

$$\rho(\vec{r}) = \sum_i^N |\theta_i(\vec{r})|^2 \quad [3.4]$$

the kinetic energy functional  $T[\rho]$  is expressed as the following sum

$$T[\rho] = T_s[\rho] + T_c[\rho] \quad [3.5]$$

where  $T_s[\rho]$  is the kinetic energy functional for a system of non-interacting electrons and  $T_c[\rho]$  is the residual kinetic energy, which is incorporated in the exchange-correlation functional  $E_{xc}[\rho]$

$$E_{xc}[\rho] = T_c[\rho] + E_{ncl}[\rho] \quad [3.6]$$

that contains all the unknown contributions to the energy of the system. Given an approximation for this functional, according to the second theorem of Hohenberg-Kohn the best evaluation of  $E_0$

$$E_0[\rho] = E_{Ne}[\rho] + T_s[\rho] + J[\rho] + E_{xc}[\rho] \quad [3.7]$$

is achieved by a variational procedure carried out to find the electronic density  $\rho$  that minimizes  $E_0$ .

The Kohn-Sham approach<sup>25</sup> involves the definition of the Kohn-Sham equations

$$\left[ \frac{1}{2} \nabla^2 + \int \frac{\rho(\vec{r}_2)}{r_{12}} d\vec{r}_2 - \sum_A^M \frac{Z_A}{R_{1A}} + V_{xc}(\vec{r}_1) \right] \vartheta_i(\vec{r}_1) = \varepsilon_i \vartheta_i(\vec{r}_1) \quad [3.8]$$

where non-classic contributions are expressed as the exchange-correlation potential  $V_{xc}$  in its unknown form.  $V_{xc}$  can be described as the one-electron operator, for which the expectation value of the corresponding energy is the exchange-correlation energy  $E_{xc}$

$$V_{xc}[\rho] = \frac{\delta E_{xc}}{\delta \rho} \quad [3.9]$$

**Equation [3.8]** can be expressed as the monoelectronic Kohn-Sham operator

$$\hat{f}^{KS} \theta_i = \varepsilon_i \theta_i \quad [3.10]$$

These equations must be iteratively solved, because  $\hat{f}^{KS}$  depends on  $\rho$ .

At this point the main problem in DFT calculation is constituted by the contribution  $E_{xc}$ , which is unknown. Taking into account **equation [3.7]**, the following expression can be written:

$$E_{xc}[\rho] = (T_{rea}[\rho] - T_s[\rho]) + (V_{ee}[\rho] - J[\rho]) = \Delta T - \Delta V_{ee} \quad [3.11]$$

where  $\Delta T$  is the correction to the kinetic energy deriving from the interacting nature of the electrons while  $\Delta V_{ee}$  represents all the non-classical corrections to the electron-electron repulsion energy.

The most common approximations to  $E_{xc}[\rho]$  are the following ones:

- **Local Density Approximation (LDA):**<sup>26</sup> this approximation considers a uniform gas of electrons where negative particles are moving in a positive charge distribution and the system is neutral. The exchange-correlation functional is written as:

$$E_{xc}^{LDA}[\rho] = \int \rho(\vec{r}) \varepsilon_{xc}[\rho(\vec{r})] d\vec{r} \quad [3.12]$$

where  $\varepsilon_{xc}[\rho(\vec{r})]$  is the exchange-correlation energy per particle, that can be divided in two contributions

$$\varepsilon_{xc}[\rho(\vec{r})] = \varepsilon_x[\rho(\vec{r})] + \varepsilon_c[\rho(\vec{r})] \quad [3.13]$$

where

$$\varepsilon_x[\rho] = -\frac{3}{4} \sqrt{\frac{3\rho(\vec{r})}{\pi}} \quad [3.14]$$

is the Slater functional for the exchange, while  $\varepsilon_c[\rho]$  is extrapolated from simulations of the electron gas. Analytical description of this term based on sophisticated interpolation schemes have been developed.

- **Local Spin Density (LSD).** It is an alternative approximation used when electrons with spin  $\alpha$  and  $\beta$  must be described separately

$$E_{xc}^{LSD}[\rho_\alpha, \rho_\beta] = \int [\rho_\alpha(\vec{r}) + \rho_\beta(\vec{r})] \varepsilon_{xc}[\rho_\alpha(\vec{r}), \rho_\beta(\vec{r})] d\vec{r} \quad [3.15]$$

LDA and LSD are more suitable for metallic system than for molecular systems, where it is not realistic to consider uniform the electronic density.

- **Generalized Gradient Approximation (GGA).** In this approximation also the gradient of the electronic density is included in the exchange-correlation energy

$$E_{xc}^{GGA}[\rho_\alpha, \rho_\beta] = \int f(\rho_\alpha, \rho_\beta, \nabla\rho_\alpha, \nabla\rho_\beta) \rho(\vec{r}) d\vec{r} \quad [3.16]$$

while LDA and LSD are expressed as first-term truncation of the Taylor expansion of  $E_{xc}$ , in this case the functional  $E_{xc}^{GGA}$  is divided in two contributions, which are separately treated

$$E_{xc}^{GGA} = E_x^{GGA} + E_c^{GGA} \quad [3.17]$$

The exchange functional  $E_x^{GGA}$  is generally described as the correction of the corresponding LDA functional

$$E_{xc}^{GGA} = E_x^{LDA} - \sum_\sigma F(s_\sigma) \rho_\sigma^{\frac{4}{3}}(\vec{r}) d\vec{r} \quad [3.18]$$

where

$$s_{\sigma}(\vec{r}) = \frac{|\nabla\rho_{\sigma}(\vec{r})|}{\rho_{\sigma}(\vec{r})^{\frac{4}{3}}} \quad [3.19]$$

and  $F$  can be expressed in various forms (the most famous are those developed by Becke and Perdew). Another correlation functional is the one developed by Lee, Yang and Parr (LYP). The first one was developed by Becke.<sup>27</sup> One of the most famous are the LYP functional by Lee, Yang and Parr,<sup>28</sup> the Perdew-Wang PWGGA<sup>29</sup> and the Perdew-Burke-Ernzerhof PBE.<sup>30</sup>

- **Hybrid functionals.** The exchange energy is the major contribution to exchange-correlation energy. An accurate description of the exchange functional is an essential requirement for the validity of a given DFT approach. Nevertheless, it is not possible to incorporate the whole exact exchange and approximate only the correlation functional. Indeed, the electronic distribution of a molecule is described in terms of exchange-correlation holes, that are portions of empty space around each electron which lower the probability that another electron is found nearby. These holes can be divided in Fermi holes (exchange part) and Coulomb holes (repulsion term). These holes are intimately related to ensure the localization and therefore these contribution cannot be considered individually. To overcome this problem, and simultaneously describe the system with more accuracy than the GGA, hybrid functional incorporates a portion of exact exchange from the Hartree-Fock theory with exchange and correlation from other sources, that could be *ab initio* or empirical.

B3LYP:<sup>31</sup> where the exchange part is described by the Becke<sup>27</sup> functional and the correlation part by the LYP<sup>28</sup> functional.

$$E_{xc}^{B3LYP} = E_x^{LDA} + \alpha_0(E_x^{HF} - E_x^{LDA}) + \alpha_x(E_x^{GGA} - E_x^{LDA}) + E_c^{LDA} + \alpha_c(E_c^{GGA} - E_c^{LDA}) \quad [3.20]$$

Where the three parameters  $\alpha_0 = 0.20$ ,  $\alpha_x = 0.72$  and  $\alpha_c = 0.81$  are empirical coefficients calculated from the fitting of the B3PW91 functional to a set of ionization energies, ionization potentials, proton affinities and total atomic energies.<sup>32,33</sup>

PBE0: which combines PBE functional with a 25% of Hartree-Fock, which is not empirical but derived basing on perturbation theory.<sup>34,35</sup>

$$E_{xc}^{PBE0} = \frac{1}{4}E_x^{HF} + \frac{3}{4}E_x^{PBE} + E_c^{PBE} \quad [3.21]$$

### 3.1 Periodic Density Functional Theory

Density Functional Theory (DFT) is a powerful computational method based on quantum mechanics, which allows describing the electronic structure of materials. This section describes the general DFT approach used for periodic systems.<sup>36</sup>

The approach to the investigation of solid state systems is different from that used to study molecular systems. A perfect crystal is a periodic three-dimensional array of atoms, ions or molecules. A few of these atoms, ions or molecules form a basic unit which is repeated throughout the crystal and the point symmetry and translational properties of the crystal determine the space group. From a computational point of view, periodic DFT calculations use the symmetry properties of the crystal basing on the band theory approach. Therefore, the potential energy of a crystal must be a periodic function with the same periodicity of the lattice

$$V(\mathbf{r} - \mathbf{g}) = V(\mathbf{r}) \quad [3.22]$$

for any lattice vector  $\mathbf{g}$ .

Due to symmetry requirements, the Schrödinger equation

$$\hat{H}(\mathbf{r})\psi(\mathbf{r}) = E\psi(\mathbf{r}) \quad [3.23]$$

must be translation invariant. This means that

$$\hat{H}(\mathbf{r} - \mathbf{g})\psi(\mathbf{r} - \mathbf{g}) = E\psi(\mathbf{r} - \mathbf{g}) \quad [3.24]$$

Eigenfunctions with appropriate symmetry associated to the potential of **equation [3.22]** obey the Bloch theorem

$$\Phi(\mathbf{r} + \mathbf{g}; \mathbf{k}) = e^{i\mathbf{k}\mathbf{g}}\Phi(\mathbf{r}; \mathbf{k}) \quad [3.25]$$

and provide a relation between the values of an eigenfunction at the equivalent points of a lattice. As  $\Phi$  satisfies the Bloch theorem, it is called "Bloch function" and is a function of the position  $r$  and of the wave vector  $\mathbf{k}$ .

The Bloch function  $\Phi(\mathbf{r}; \mathbf{k})$  is an eigenfunction of the Hamiltonian in **equation [3.23]**, that can then be rewritten as

$$\hat{H}(\mathbf{r} - \mathbf{g})\Phi(\mathbf{r} - \mathbf{g}; \mathbf{k}) = E(\mathbf{k})\Phi(\mathbf{r} - \mathbf{g}; \mathbf{k}) \quad [3.26]$$

As a consequence of periodicity (**equation [3.22]**):

$$\hat{H}(\mathbf{r})e^{-i\mathbf{k}\cdot\mathbf{g}}\phi(\mathbf{r};\mathbf{k}) = E(\mathbf{k})e^{-i\mathbf{k}\cdot\mathbf{g}}\phi(\mathbf{r};\mathbf{k}) \quad [3.27]$$

where  $e^{-i\mathbf{k}\cdot\mathbf{g}}$  is a constant factor with unitary module. The Bloch function can be written as product of a plane wave and a periodic function  $u(\mathbf{r};\mathbf{k})$  with the same periodicity of the lattice:

$$\phi(\mathbf{r};\mathbf{k}) = e^{-i\mathbf{k}\cdot\mathbf{g}}u(\mathbf{r};\mathbf{k}) \quad [3.28]$$

Bloch functions have translational properties in the reciprocal space, and this behaviour limits the solution of the Schrödinger equation to selected  $k$  points in the first Brillouin Zone (BZ).

The general solutions of the Schrödinger equation

$$\hat{H}\psi_n(\mathbf{r};\mathbf{k}) = E_n\psi_n(\mathbf{r};\mathbf{k}) \quad [3.29]$$

can be expanded as a linear combination of Bloch functions:

$$\psi_n(\mathbf{r};\mathbf{k}) = \sum_j c_{jn}(\mathbf{k})\phi_j(\mathbf{r};\mathbf{k}) \quad [3.30]$$

The  $\psi_n(\mathbf{r};\mathbf{k})$  functions are called "crystalline orbitals".

Bloch functions are commonly represented as:

- **Atomic Orbitals (AO)**; this approach is more suitable to describe chemical bonds, but becomes problematic in the description of free or nearly free electron conductors, due to numerical instability problems.
- **Plane Waves (PW)**; this approach is more suitable for metals and to describe delocalized electrons.

### ***CRYSTAL code***

CRYSTAL code<sup>36,37</sup> is based on the expansion of the crystalline orbitals as a linear combination of atom-centred Gaussian orbitals  $\chi_\mu$ . For a given  $\mu$ -th AO, with origin at  $\mathbf{r}_\mu$

$$\phi_\mu^k(\mathbf{r}) = \frac{1}{\sqrt{N}} \sum_g e^{i\mathbf{k}\cdot\mathbf{g}} \chi_\mu^g(\mathbf{r} - \mathbf{r}_\mu) \quad [3.31]$$

Considering for example a Hartree-Fock calculation, the main steps followed by the code are:<sup>36</sup>

- a) Linear combination of atomic orbitals (LCAO) as contraction of Gaussian functions, in order to represent the set of Bloch functions. The overlap matrix in the local basis set is evaluated.



- b) The Fock matrix elements are evaluated in direct space in the local basis set.
- c) The Fourier Transform of the Fock matrix is applied to the matrix in order to switch from the direct space to the reciprocal space.
- d) The Schrödinger equation is then solved maintaining the orthogonality for each  $k$  vector.
- e) The Fermi energy ( $E_F$ ), the highest energy value of an occupied state in the first Brillouin zone, is computed. The density matrix is evaluated and Fourier antitransformation in the direct space is applied, in order to transform the integral computed on the  $k$  points in a volume  $V_{BZ}$  of the first Brillouin zone. The integration is limited to the states with  $E < E_F$ , and a step function  $\theta$  allows to exclude the eigenvectors relative to empty states.
- f) The total energy per cell  $E_{TOT}$  is then calculated and steps from b) to f) are repeated until self consistency.

## 4. References

- (1) Newville, M. Fundamentals of XAFS. *Rev. Mineral. Geochemistry* **2014**, 78 (1), 33–74.
- (2) AA.VV., P. Synchrotron Radiation-Basics, Methods and Applications. **2015**.
- (3) Fornasini, P. Introduction to X-Ray Absorption Spectroscopy. Synchrotron Radiation-Basics, Methods and Applications. **2015**.
- (4) EXAFS, B. K. T. Basic Principles and Data Analysis. *Inorg. Chem. Concepts* **1986**, 9.
- (5) Victoreen, J. A. The Calculation of X-Ray Mass Absorption Coefficients. *J. Appl. Phys.* **1949**, 20 (12), 1141–1147.
- (6) Fornasini, P.; Grisenti, R. On EXAFS Debye-Waller Factor and Recent Advances. *J. Synchrotron Radiat.* **2015**, 22 (5), 1242–1257.
- (7) Stern, E. A.; Bunker, B. A.; Heald, S. M. Many-Body Effects on Extended X-Ray Absorption Fine Structure Amplitudes. *Phys. Rev. B* **1980**, 21 (12), 5521.
- (8) Rehr, J. J.; Albers, R. C. Theoretical Approaches to X-Ray Absorption Fine Structure. *Rev. Mod. Phys.* **2000**, 72 (3), 621.
- (9) Kas, J. J.; Jorissen, K.; Rehr, J. J. Real-Space Multiple-Scattering Theory of X-Ray Spectra. *X-Ray Absorpt. X-Ray Emiss. Spectrosc. Theory Appl.* **2016**, 51.
- (10) Rehr, J. J.; Kas, J. J.; Vila, F. D.; Prange, M. P.; Jorissen, K. Parameter-Free Calculations of X-Ray Spectra with FEFF9. *Phys. Chem. Chem. Phys.* **2010**, 12 (21), 5503–5513.

- (11) Filipponi, A.; Di Cicco, A. X-Ray-Absorption Spectroscopy and N-Body Distribution Functions in Condensed Matter. II. Data Analysis and Applications. *Phys. Rev. B* **1995**, *52* (21), 15135.
- (12) Filipponi, A.; Di Cicco, A.; Natoli, C. R. X-Ray-Absorption Spectroscopy and N-Body Distribution Functions in Condensed Matter. I. Theory. *Phys. Rev. B* **1995**, *52* (21), 15122.
- (13) Binsted, N.; Gurman, S. J.; Campbell, J. W. EXCURVE 9.2. *Daresbury Lab.* **1998**.
- (14) Klementev, K. V. Extraction of the Fine Structure from X-Ray Absorption Spectra. *J. Phys. D. Appl. Phys.* **2001**, *34* (2), 209.
- (15) Eisenberger, P.; Brown, G. S. The Study of Disordered Systems by EXAFS: Limitations. *Solid State Commun.* **1979**, *29* (6), 481–484.
- (16) Rehr, J. J.; Albers, R. C. Scattering-Matrix Formulation of Curved-Wave Multiple-Scattering Theory: Application to X-Ray-Absorption Fine Structure. *Phys. Rev. B* **1990**, *41* (12), 8139.
- (17) Rehr, J. J.; Albers, R. C.; Zabinsky, S. I. High-Order Multiple-Scattering Calculations of X-Ray-Absorption Fine Structure. *Phys. Rev. Lett.* **1992**, *69* (23), 3397.
- (18) Zabinsky, S. I.; Rehr, J. J.; Ankudinov, A.; Albers, R. C.; Eller, M. J. Multiple-Scattering Calculations of X-Ray-Absorption Spectra. *Phys. Rev. B* **1995**, *52* (4), 2995.
- (19) Ravel, B.; Newville, M. ATHENA, ARTEMIS, HEPHAESTUS: Data Analysis for X-Ray Absorption Spectroscopy Using IFEFFIT. *J. Synchrotron Radiat.* **2005**, *12* (4), 537–541.
- (20) Eichert, D. X-Ray Microscopy. In *Synchrotron Radiation*; Springer, 2015; pp 409–436.
- (21) Solé, V. A.; Papillon, E.; Cotte, M.; Walter, P.; Susini, J. A Multiplatform Code for the Analysis of Energy-Dispersive X-Ray Fluorescence Spectra. *Spectrochim. Acta Part B At. Spectrosc.* **2007**, *62* (1), 63–68.
- (22) Salomé, M.; Bleuet, P.; Bohic, S.; Cauzid, J.; Chalmin, E.; Cloetens, P.; Cotte, M.; De Andrade, V.; Martinez-Criado, G.; Petitgirard, S.; et al. Fluorescence X-Ray Micro-Spectroscopy Activities at ESRF. In *Journal of Physics: Conference Series*; 2009; Vol. 186, p 12014.
- (23) Hohenberg, P. *Phys. Rev.* 1964, *136*, b864--b871; B) W. Kohn, Lj Sham. *Phys. Rev* **1965**, *140*, A1133--A1138.
- (24) Born, M.; Oppenheimer, R. Zur Quantentheorie Der Molekeln. *Ann. Phys.* **1927**, *389* (20), 457–484.

- (25) Kohn, W.; Sham, L. J. Self-Consistent Equations Including Exchange and Correlation Effects. *Phys. Rev.* **1965**, *140* (4A), A1133.
- (26) Dirac, P. A. M. Note on Exchange Phenomena in the Thomas Atom. *Math. Proc. Cambridge Philos. Soc.* **1930**, *26* (3), 376–385.
- (27) Becke, A. D. Density-Functional Thermochemistry. III. The Role of Exact Exchange. *J. Chem. Phys.* **1993**, *98* (7), 5648–5652.
- (28) Lee, C.; Yang, W.; Parr, R. G. Development of the Colle-Salvetti Correlation-Energy Formula into a Functional of the Electron Density. *Phys. Rev. B* **1988**, *37* (2), 785.
- (29) Perdew, J. P.; Wang, Y. Accurate and Simple Analytic Representation of the Electron-Gas Correlation Energy. *Phys. Rev. B* **1992**, *45* (23), 13244.
- (30) Perdew, J. P.; Burke, K.; Ernzerhof, M. Generalized Gradient Approximation Made Simple. *Phys. Rev. Lett.* **1996**, *77* (18), 3865.
- (31) Stephens, P. J.; Devlin, F. J.; Chabalowski, Cf.; Frisch, M. J. Ab Initio Calculation of Vibrational Absorption and Circular Dichroism Spectra Using Density Functional Force Fields. *J. Phys. Chem.* **1994**, *98* (45), 11623–11627.
- (32) Vosko, S. H.; Wilk, L.; Nusair, M. Accurate Spin-Dependent Electron Liquid Correlation Energies for Local Spin Density Calculations: A Critical Analysis. *Can. J. Phys.* **1980**, *58* (8), 1200–1211.
- (33) Curtiss, L. A.; Raghavachari, K.; Trucks, G. W.; Pople, J. A. Gaussian-2 Theory for Molecular Energies of First-and Second-Row Compounds. *J. Chem. Phys.* **1991**, *94* (11), 7221–7230.
- (34) Adamo, C.; Barone, V. Toward Reliable Density Functional Methods without Adjustable Parameters: The PBE0 Model. *J. Chem. Phys.* **1999**, *110* (13), 6158–6170.
- (35) Ernzerhof, M.; Scuseria, G. E. Assessment of the Perdew-Burke-Ernzerhof Exchange-Correlation Functional. *J. Chem. Phys.* **1999**, *110* (11), 5029–5036.
- (36) Dovesi, R.; Civalleri, B.; Orlando, R.; Roetti, C.; Saunders, V. R.; Giuria, V.; Iam, C.; Torino, I.-. Ab Initio Quantum Simulation in Solid State Chemistry. *21*.
- (37) Dovesi, R.; Orlando, R.; Erba, A.; Zicovich-Wilson, C. M.; Civalleri, B.; Casassa, S.; Maschio, L.; Ferrabone, M.; De La Pierre, M.; D’Arco, P.; et al. CRYSTAL14: A Program for the Ab Initio Investigation of Crystalline Solids. *Int. J. Quantum Chem.* **2014**, *114* (19), 1287–1317.
- (38) <http://sabotin.ung.si/~arcon/xas/xas/xas.htm>

# CHAPTER 3

## XAS and DFT study of $\text{Bi}_{1-x}\text{Ta}_x\text{O}_{1.5+x}$ electrolytes

In this chapter the results concerning a combined X-Ray Absorption Spectroscopy (XAS) and periodic Density Functional Theory (DFT) study of  $\text{Bi}_{1-x}\text{Ta}_x\text{O}_{1.5+x}$  solid electrolyte are presented and discussed. The aim of the study is to unveil the preferential aggregation motives around the dopant site and shed light on the local coordination and electronic structure of bismuth site, which are supposed to play a key role in the high conductivity of this material. The following results have been object of a publication in *Journal of Physical Chemistry C*.<sup>1</sup>

### 1. Motivation of the study

As reported in **Section 2** of **Chapter 1**, due to its extremely high ionic conductivity (about  $1 \text{ S}\cdot\text{cm}^{-1}$  at  $750^\circ\text{C}$ ),  $\delta\text{-Bi}_2\text{O}_3$  represents a reference compound for anion conducting electrolytes. Bismuth oxide has several polymorphs, and doping the pure material with certain transition metals allows the stabilization of the oxygen-ion conducting  $\delta$ -phase.<sup>2,3</sup> Among these doping transition metals, pentavalent dopants such as  $\text{Ta}^{5+}$  have been found to stabilize the  $\delta\text{-Bi}_2\text{O}_3$  phase, with an only limited depletion of oxygen vacancies.<sup>4-8</sup> The long-range structure of  $\text{Bi}_{1-x}\text{Ta}_x\text{O}_{1.5+x}$  has been previously characterized by Neutron Diffraction, and structural motives typical of pyrochlore-like structures have been highlighted.<sup>4,5</sup> However, the local environment of  $\text{Bi}_{1-x}\text{Ta}_x\text{O}_{1.5+x}$  was never studied: such approach would permit to achieve a better understanding of the dopant-matrix interaction, in order to highlight the structural features involved in the stabilization of the  $\delta$  phase and in the anion conduction mechanism.<sup>9</sup>

Despite the exploitation of bismuth oxide-based materials in the FC technology is hopeless for well-known chemical stability problems, unless combined with more stable electrolytes (i.e. doped  $\text{CeO}_2$ , YSZ) on the fuel side (layered electrolytes),<sup>10,11</sup> the investigation of these materials remains a matter of great interest for achieving a deeper comprehension of the mechanism of solid-state anion conduction.

XAS has been proved to be a powerful probe for the investigation of the local structural features of ceramic electrolytes.<sup>9,12-15</sup> In particular, in this study the XAS analysis allowed to:

- have an insight on the pyrochlore-related Ta<sub>4</sub>O<sub>18</sub> structural motives that stabilize the  $\delta$ -Bi<sub>2</sub>O<sub>3</sub> to room temperature at different Ta concentrations;
- investigate the local environment of conducting sites, providing evidences of favourable pathways for oxygen-ion conductive sites.

Moreover, the integration of XAS with a periodic DFT approach, permitted to

- identify the favoured connectivity between Ta<sub>4</sub>O<sub>18</sub> aggregates inside the  $\delta$ -Bi<sub>2</sub>O<sub>3</sub> matrix from the energetic point of view;
- shed light on the local coordination of Bi<sup>3+</sup> and its electronic structure. Specifically, the calculated density of states (DOS) was found to be similar in both doped and undoped Bi<sub>2</sub>O<sub>3</sub> due to the presence of Bi 6s<sup>2</sup> lone pair, that influences the local disorder of the Bi first coordination shell.<sup>16</sup>

This chapter is organized as follows. In **Section 2** experimental and computational methods are reported. **Section 3** is dedicated to results and discussion. In **Section 3.1** and **Section 3.2** the results obtained by X-ray Absorption Near Edge Structure (XANES) and Extended X-Ray Absorption Fine Structure (EXAFS) at the Ta and Bi L<sub>3</sub>-edges, are respectively presented and discussed. **Section 3.3** shows the computational results and the discussion concerning energetic stability and DOS analysis of different Ta<sub>4</sub>O<sub>18</sub> cluster configurations. **Section 3.4** reports some considerations about the  $\delta$ -phase stabilization based on X-Ray Diffraction (XRD) analysis. In **Section 3.5** an overview of the role of V<sup>5+</sup> and Nb<sup>5+</sup> in the stabilization of the  $\delta$ -phase is also given, with the aim to draw a comparison between different pentavalent dopants. Finally, conclusions are drawn in **Section 4**.

## 2. Experimental and computational methods

**Synthesis.** Bi<sub>1-x</sub>Ta<sub>x</sub>O<sub>1.5+x</sub> samples in the concentration range between x=0.075 and 0.30, were prepared by solid-state synthesis. Stoichiometric amounts of Bi<sub>2</sub>O<sub>3</sub> (Sigma-Aldrich, 99.9%) and Ta<sub>2</sub>O<sub>5</sub> (Sigma-Aldrich, 99.9%) powders were mixed in an agate mortar with the aid of 1 mL of ethanol or 2-propanol (Panreac 96%) and dried in oven at 80°C to remove the solvent. Then the powders were calcined twice at 750°C for 12 h, using a ramp of 150°C/h. After the first calcinations, an intermediate 30 minutes grinding in a Retsch MM200 vibrating ball-mill was carried out, using zirconia jar and spheres.

**Characterization.** X-Ray Diffraction measurements were acquired with a Siemens D-500 diffractometer using Cu K $\alpha$  radiation and a graphite monochromator on the diffracted beam in the  $2\theta$  range 20-120°, with a step of 0.02° and accumulation time of 4 s per step. Calibration of the instrument was made with corundum powder before and after every measurement. Rietveld analysis was performed with GSAS<sup>17</sup>.

X-Ray Absorption Spectroscopy measurements were acquired at the Bi and Ta L<sub>3</sub>-edges at the Dubble BM26A beamline of the European Synchrotron Radiation Facility (ESRF). All the measurements were carried out in transmission mode at liquid nitrogen temperature (80 K), using a Si detector. EXAFS data analysis was carried out with Viper<sup>18</sup> and Feff9.<sup>19</sup> Samples for XAS measurements were prepared by diluting the Bi<sub>1-x</sub>M<sub>x</sub>O<sub>1.5+x</sub> powders with polyvinylpyrrolidone and pressing the mixture in a 13-mm die.

**Computational methods.** Periodic Density Functional Theory (DFT) calculations were carried out using the CRYSTAL09 code,<sup>20</sup> which is based on the expansion of the crystalline orbitals as a linear combination of atom-centred Gaussian orbitals. Density functional and basis sets were validated on the  $\alpha$ -Bi<sub>2</sub>O<sub>3</sub> structure, which is stable at room temperature. The hybrid functional B3LYP<sup>21,22</sup> has been used for both full geometry optimization (atomic positions and cell parameters) and Density Of States (DOS) analysis, after testing several functionals. For bismuth a Hay and Wadt small core pseudopotential was used together with a quadruple- $\zeta$  split valence basis set<sup>23</sup> and for tantalum an ECP60MDF pseudopotential was used, together with a double- $\zeta$  split valence basis set.<sup>24</sup> A Durand and Barthelat large-core pseudopotential was used for oxygen, together with a double- $\zeta$  split valence basis set<sup>25-27</sup>. Calculations were carried out using a Monkhorst-Pack grid, with a shrinking factor of 4x4x4, corresponding to 36 points in the irreducible Brillouin zone. The Coulomb and exchange series were truncated with threshold values of 10<sup>-7</sup>, 10<sup>-7</sup>, 10<sup>-7</sup>, 10<sup>-7</sup> and 10<sup>-14</sup>. An extrafine grid was used for numerical DFT integration.

### 3. Results and discussion

#### 3.1. X-Ray Absorption Near Edge Structure

The XANES features of Bi<sub>1-x</sub>M<sub>x</sub>O<sub>1.5+x</sub>, acquired at the Bi and Ta L<sub>3</sub>-edges (**Figure 3.1**), were qualitatively compared with Bi<sub>2</sub>O<sub>3</sub> and Ta<sub>2</sub>O<sub>5</sub> reference compounds. The shape and position of the edges confirm an oxidation state of +3 and +5 respectively for Bi and Ta. In particular,

XANES spectra at the Bi L<sub>3</sub>-edge were compared with pure Bi<sub>2</sub>O<sub>3</sub> and NaBiO<sub>3</sub> compounds, where Bi is present in a 3+ oxidation state in the first case, and in a +5 oxidation state in the second case. In the investigated Bi<sub>1-x</sub>Ta<sub>x</sub>O<sub>1.5+x</sub> samples the pre-edge peak characteristic of Bi<sup>5+</sup> is absent, while a small bump typical of undoped Bi<sub>2</sub>O<sub>3</sub> can be noticed (See **Supporting information S.1**).<sup>28</sup> For what concerns Ta L<sub>3</sub>-edge, the Bi<sub>1-x</sub>Ta<sub>x</sub>O<sub>1.5+x</sub> XANES spectra were compared with a Ta<sub>2</sub>O<sub>5</sub> standard: the position of the edge strongly supports the presence of a +5 oxidation state, while the splitting of the main peak observed in Bi<sub>1-x</sub>M<sub>x</sub>O<sub>1.5+x</sub> spectra suggests the presence of a single Ta<sup>5+</sup> environment, unlike what happens in the Ta<sub>2</sub>O<sub>5</sub> reference sample, where two low-symmetry sites (distorted octahedra and pentagonal bipyramids) coexist.<sup>29</sup>

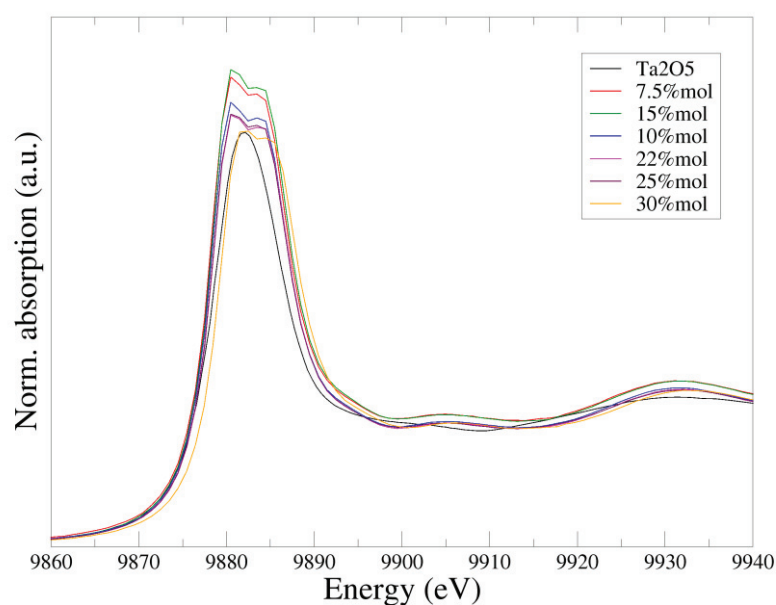


**Figure 3.1 a.** Ta L<sub>3</sub>-edge XANES spectra of Ta-doped samples and reference Ta<sub>2</sub>O<sub>5</sub> acquired on Ta L<sub>3</sub>-edge.

## 3.2 Extended X-Ray Absorption Fine Structure

### *Ta L<sub>3</sub>-edge*

The fitting results on Ta L<sub>3</sub>-edge are reported in **Table 3.1** The Ta-O first shell was modelled with a single distance, with a fitted coordination number close to 6 in all the compositions, corresponding to an octahedral local environment for Ta site. This evidence is strongly

corroborated also by the first shell Ta-O distance, set at around 1.99 Å, in good agreement with an octahedrally coordinated Ta<sup>5+</sup> local environment.<sup>30</sup> In order to model dopant aggregation, the Ta-M (M=Ta, Bi) second shell was simulated using Ta-Bi and Ta-Ta contributions sharing the same disorder factor. Dopant clustering was confirmed for all the samples, except for the most diluted one (x=0.075), where the absence of a Ta-Ta contribution suggested the presence of isolated TaO<sub>6</sub> octahedra. Moreover, the Ta-Bi distance (3.4 to 3.5 Å) was found to be always longer than Ta-Ta (3.3 to 3.4 Å), as expected from the larger ionic radius of Bi<sup>3+</sup>. The average second-shell distance Ta-M (M=Ta, Bi) decreases with increasing Ta content. Finally, in order to obtain a satisfactory fitting of the Ta-O shell, the third-shell Ta-O coordination number was constrained according to stoichiometry and split in two contributions, sharing the same multiplicity and disorder factor.

Experimental coordination numbers N (Ta-Ta) were compared with several models having the appropriate Ta concentration and formed by TaO<sub>6</sub> octahedra linked together in a δ-Bi<sub>2</sub>O<sub>3</sub> matrix (**Figure 3.4**). When Ta-Ta contributions are absent, TaO<sub>6</sub> octahedra are isolated in the δ-Bi<sub>2</sub>O<sub>3</sub> matrix. N (Ta-Ta) values around 3 strongly suggest the clustering of TaO<sub>6</sub> into Ta<sub>4</sub>O<sub>18</sub> tetrahedral clusters not connected to each other, whereas N (Ta-Ta) values close to 4 point to a higher degree aggregation between dopant moieties. In particular, two types of structural motives can be associated to a coordination number of 4: *i*) Ta<sub>8</sub>O<sub>37</sub> clusters, arising from two Ta<sub>4</sub>O<sub>18</sub> linked by an oxygen and *ii*) Ta<sub>7</sub>O<sub>30</sub> clusters, arising from two Ta<sub>4</sub>O<sub>18</sub> clusters sharing a TaO<sub>6</sub> octahedron.

Some possible structures compatible with the experimental N(Ta-Ta) values are represented in **Figure 3.5**, where the Ta<sub>8</sub>O<sub>37</sub> and Ta<sub>7</sub>O<sub>30</sub> are also evidenced. Each one of the aggregation schemes is inserted in a volume of 2.5 × 2.5 × 2.5 cells of the ideal fluorite cell. In the sample with x=0.075 the absence of the Ta-Ta contribution suggests that in this case the dopant atoms are isolated. For x = 0.1, the coordination number N (Ta-Ta) = 3.1 is compatible with either isolated Ta<sub>4</sub>O<sub>18</sub> or Ta<sub>8</sub>O<sub>37</sub>/Ta<sub>7</sub>O<sub>30</sub>. For x > 0.1, the experimentally determined N (Ta-Ta) points clearly to a higher degree of dopant aggregation.



**Table 3.1** Results from the EXAFS analysis on the Ta L<sub>3</sub>-edge. Distances (R, in Å), coordination numbers (N) and disorder factors ( $\sigma^2$ , in  $10^{-3} \text{ \AA}^2$ ) are reported with uncertainties in parentheses.

Sample		x = 0.075	x = 0.10	x = 0.15	x = 0.22	x = 0.25	x = 0.30
Ta-O	N	5.9(2)	6.0(1)	6.2(2)	6.1(1)	6.1(1)	6.4(3)
	R	1.99(1)	1.98(1)	1.99(1)	1.99(2)	1.99(1)	1.99(1)
	$\sigma^2$	10.3(2)	9.3(1)	9.1(1)	9.3(1)	8.4(3)	9.2(2)
Ta-Bi	N	12.0	8.9(3)	8.2(2)	8.2(2)	8.1(2)	8.1(3)
	R	3.46(1)	3.45(1)	3.45(1)	3.46(1)	3.42(1)	3.42(1)
	$\sigma^2$	11.5(2)	8.8(2)	8.0(1)	7.1(1)	9.6(2)	8.3(1)
Ta-Ta	N	--	3.1(3)	3.8(2)	3.8(2)	3.9(2)	3.9(3)
	R	--	3.36(4)	3.36(1)	3.37(1)	3.31(1)	3.31(1)
Ta-O	N	9.5	9.6	9.9	10.3	10.5	10.8
	R	3.66(1)	3.63(1)	3.62(1)	3.63(1)	3.59(1)	3.60(1)
	$\sigma^2$	8.2(3)	8.0(3)	5.2(2)	4.9(2)	8.3(2)	7.1(4)
Ta-O	N	9.5	9.6	9.9	10.3	10.5	10.8
	R	4.04(1)	4.02(1)	4.03(1)	4.04(1)	4.06(1)	4.02(1)

### ***Bi L<sub>3</sub>-edge***

The fitting results at the Bi L<sub>3</sub>-edge are reported in **Table 3.2**. Bi-O first shell was modelled using two Bi-O distances, respectively centred on 2.1 and 2.6 Å. The presence of two first-shell contributions strongly agrees with the model proposed by Koto et al. on the basis of EXAFS high-temperature data measured for undoped  $\delta$ -Bi<sub>2</sub>O<sub>3</sub>, where the displacement of an oxygen-ion from the centroid of its OBi<sub>4</sub> coordination tetrahedron takes place (**Figure 3.2**).<sup>9,31</sup> This would correspond to a displacement from the ideal  $8c$  oxygen site of the fluorite-like structure, to a new  $32f$  site which would be linked to a decreased activation energy for oxygen-ion diffusion.<sup>32</sup> Moreover, also in the local structural analysis performed by Hull et al. using neutron diffraction data, a distribution of distances from 2.1 to 2.7 Å is

observed in  $\delta\text{-Bi}_2\text{O}_3$ .<sup>16</sup> A similar distribution of distances was found in the same study for the low-temperature  $\alpha$  and  $\beta$  forms. Such first shell environment can be attributed to the effect of the  $6s^2$  lone pair on  $\text{Bi}^{3+}$ , which is supposed to be the cause of the strongly asymmetric local environment around Bi. The first-shell Debye-Waller factor of about  $0.01 \text{ \AA}^2$  is found to be on the same order of magnitude as  $\delta\text{-Bi}_2\text{O}_3$  at high temperatures ( $\sim 0.011 \text{ \AA}^2$  at 700–800 °C).<sup>9</sup> This value is very high for a first shell and it is caused by the highly disordered local environment around Bi, in terms of asymmetry and coexistence of different Bi coordination states. Also the second shell Bi-M (M=Ta, Bi) could not be reproduced by a single distance and had to be split in two contributions, that were refined assuming a total coordination number of 12. Again, the observed Bi–Bi distances, ranging from 3.76 to 4.06 Å, are compatible with the  $\beta\text{-Bi}_2\text{O}_3$  phase.<sup>33</sup> Finally, the third shell Bi-O was modelled by fixing the coordination numbers according to the average anion stoichiometry. The disorder of the second and third shells shows even higher values ( $>0.02 \text{ \AA}^2$ ).

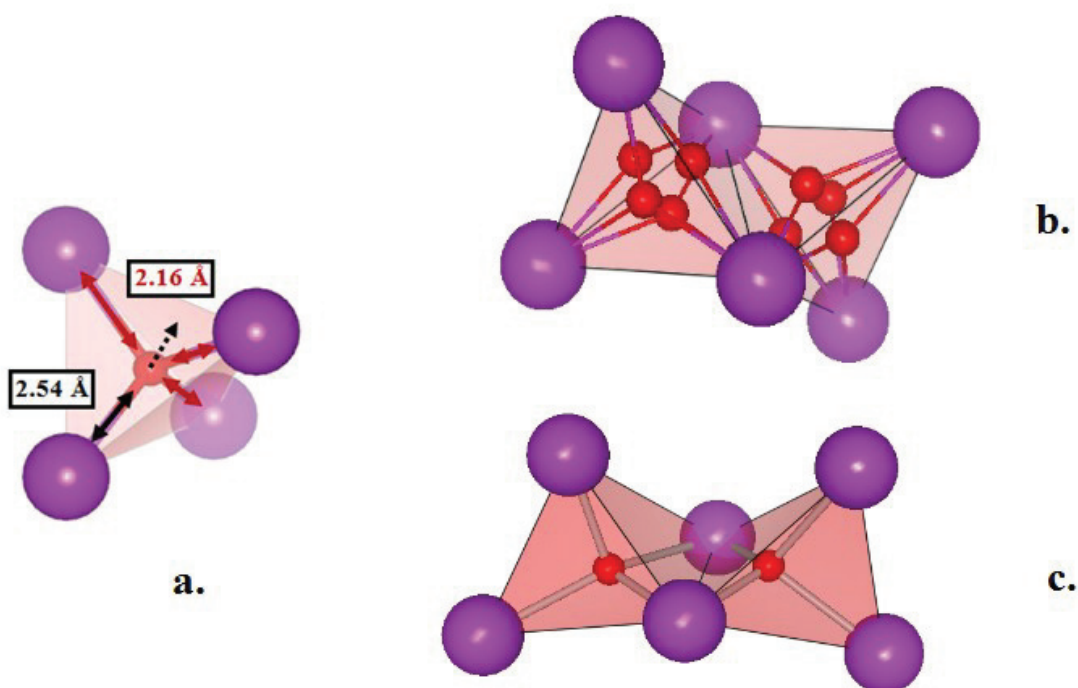


**Figure 3.2** a) Oxygen-ion coordination tetrahedron (red) with four bismuth atoms (purple). The black dotted arrow represents the oxygen-ion displacement from the centroid of the coordination tetrahedron ( $\delta c$  site) to one of the possible random directions. The black double arrow shows the longest O-Bi distance, while the red double arrows indicate the shorter ones. b) Edge sharing coordination tetrahedra of O with Bi atoms, in  $\delta\text{-Bi}_2\text{O}_3$ ; c) edge sharing coordination tetrahedra of O with Bi atoms in  $\alpha\text{-Bi}_2\text{O}_3$ .

**Table 3.2** Results from the EXAFS analysis on the Bi L<sub>3</sub>-edge for samples with x = 0.075, 0.10 and 0.15. Distances (R, in Å), coordination numbers (N) and disorder factors ( $\sigma^2$ , in 10<sup>-2</sup> Å<sup>2</sup>) are reported with uncertainties in parentheses.

Sample		x = 0.075	x = 0.10	x = 0.15
Bi-O	N	4.2(2)	4.3(1)	4.4(2)
	R	2.11(1)	2.13(1)	2.14(1)
	$\sigma^2$	1.27(4)	1.26(5)	1.25(5)
Bi-O	N	2.1(2)	2.2(1)	2.3(2)
	R	2.58(2)	2.54(1)	2.57(2)
Bi-Bi	N	6.2(2)	6.2(2)	8(1)
	R	3.86(1)	3.84(2)	3.85(2)
	$\sigma^2$	0.8(4)	1.4(3)	2.0(3)
Bi-Bi	N	5.8(2)	5.8(2)	4(1)
	R	4.06(1)	4.05(1)	4.04(2)
Bi-O	N	18.9	19.2	19.8
	R	4.70(1)	4.65(1)	4.56(2)
	$\sigma^2$	3.1(5)	4(1)	4(1)

**Table 3.3** Results from the EXAFS analysis on the Bi L<sub>3</sub>-edge for samples with x = 0.22, 0.25 and 0.30. Distances (R, in Å), coordination numbers (N) and disorder factors ( $\sigma^2$ , in 10<sup>-2</sup> Å<sup>2</sup>) are reported with uncertainties in parentheses.

Sample		x = 0.22	x = 0.25	x = 0.30
Bi-O	N	5.0(1)	4.9(2)	4.6(4)
	R	2.19(1)	2.18(1)	2.17(1)
	$\sigma^2$	1.32(4)	1.27(4)	1.28(4)
Bi-O	N	2.1(1)	2.48(2)	3.1(1)
	R	2.58(1)	2.59(1)	2.58(1)
Bi-Ta	N	3.8(9)	3(1)	4.3(1)
	R	3.60(5)	3.59(2)	3.55(1)
	$\sigma^2$	2.4(2)	2.7(3)	3.0(3)
Bi-Bi	N	8.2(9)	9(1)	7.7(1)
	R	3.86(1)	3.88(1)	3.99(2)
Bi-O	N	20.6	21	21.6
	R	4.60(2)	4.58(2)	4.42(3)
	$\sigma^2$	2.50(3)	3.3(5)	8(1)

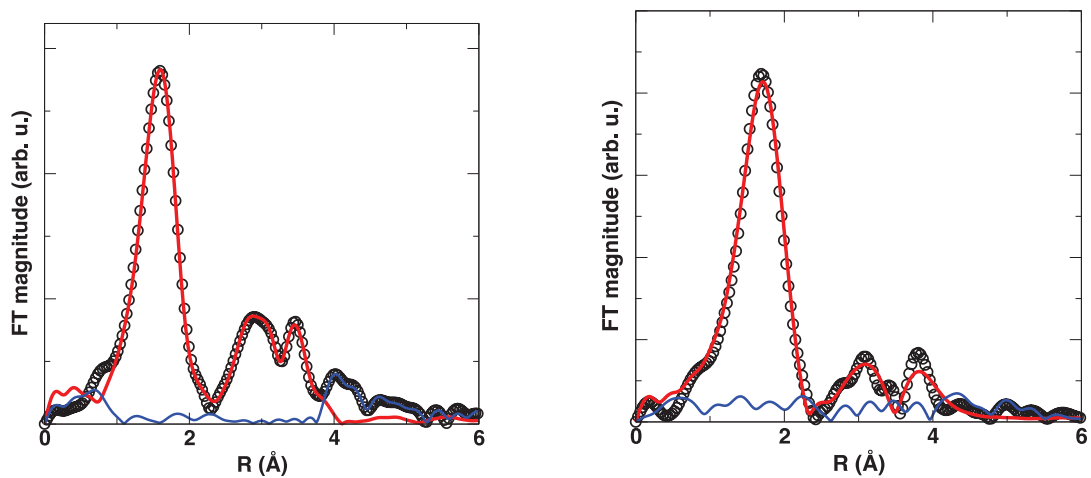


**Figure 3.3** FT EXAFS data (black circles), best fit (red), and residual (blue) for sample with  $x = 0.25$ . Left: Ta edge. Right: Bi edge.

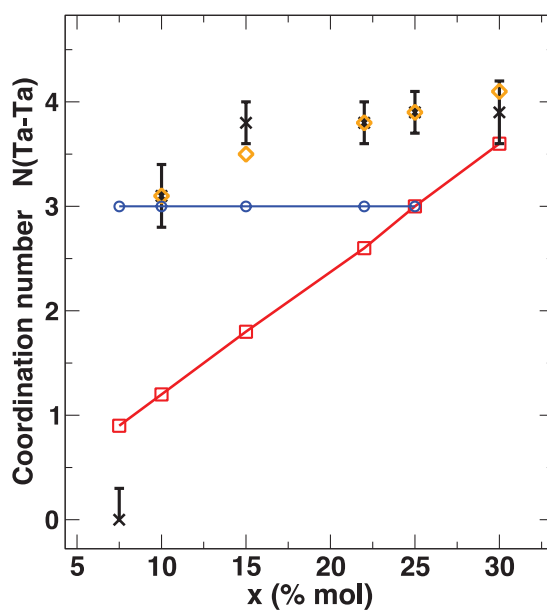


**Figure 3.4** Coordination number  $N(\text{Ta-Ta})$  vs. concentration of Ta. Random configuration (red), isolated  $\text{Ta}_4\text{O}_{18}$  clusters (blue), experimental data (black) are shown. Orange points represent the Ta-Ta coordination numbers corresponding to the structural models shown in **Figure 3.5**.

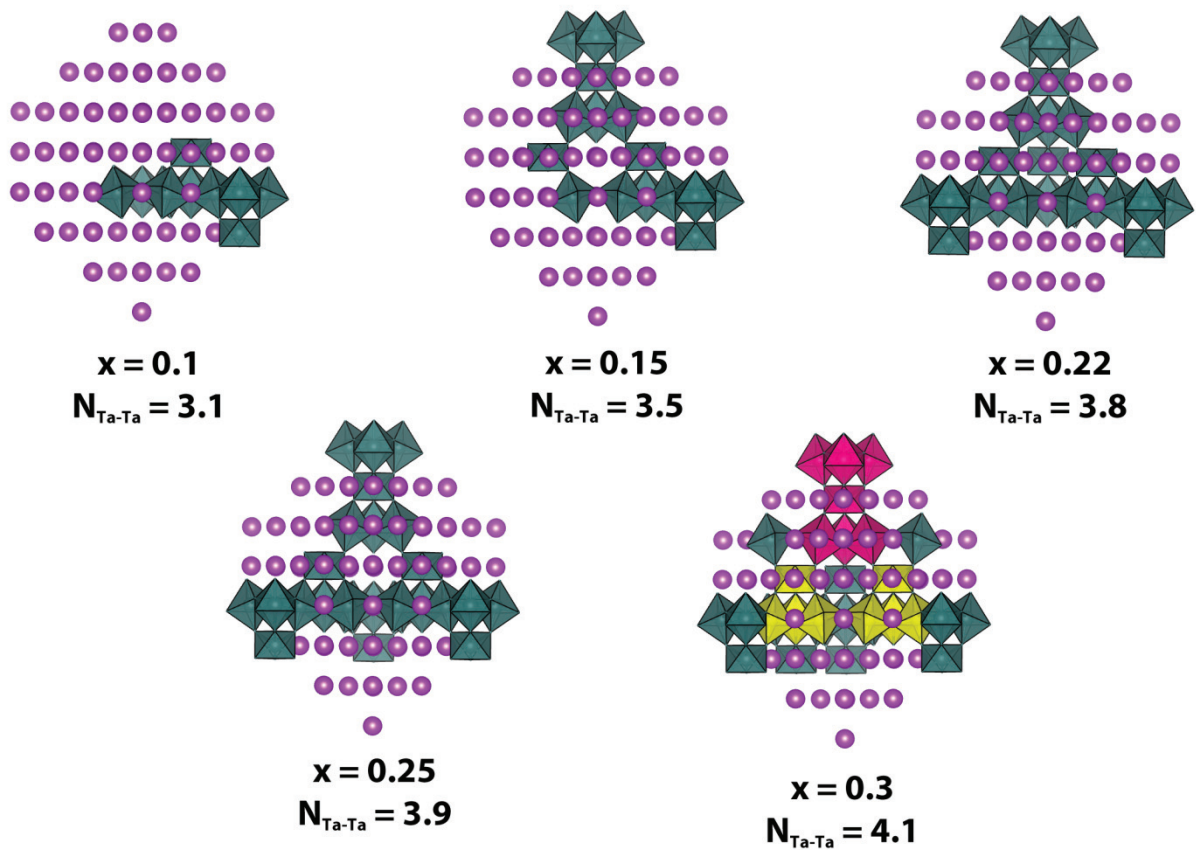


**Figure 3.5** Configurations of Ta aggregation compatible with the experimentally determined Ta-Ta coordination numbers. Bismuth in purple,  $\text{TaO}_6$  octahedra in green. The coordination polyhedra around bismuth are omitted for clarity. The Ta stoichiometry and the average Ta-Ta coordination number are reported for each structure. For  $x = 0.3$ , the  $\text{Ta}_8\text{O}_{37}$  and  $\text{Ta}_7\text{O}_{30}$  aggregates are evidenced in yellow and red, respectively.

### 3.3 Density Functional Theory calculations

#### *Geometry optimization*

Three different  $\text{Bi}_{0.75}\text{Ta}_{0.25}\text{O}_{1.75}$  configurations, reported in **Figure 3.6**, were fully optimized in order to evaluate the energy stabilization due to dopant clustering. In the configurations analyzed, the dopant is respectively arranged in *i*) isolated  $\text{Ta}_4\text{O}_{18}$  clusters (**configuration A**, **Figure 3.6 a**); *ii*) two  $\text{Ta}_4\text{O}_{18}$  clusters linked by an oxygen atom in the  $\langle 110 \rangle$  direction (**configuration B**, **Figure 3.6 b**); *iii*) two  $\text{Ta}_4\text{O}_{18}$  sharing a  $\text{TaO}_6$  octahedron oriented in the  $\langle 111 \rangle$  direction of the cell (**configuration C**, **Figure 3.6 c**).

In **Table 3.4** the energetic stability of the three configurations is reported. Optimization results confirm the tendency for tantalum to adopt a higher degree of clustering, with the configuration C having the ground state stability and the configuration B being slightly less stable (7.65 kcal/mol). On the other side, the configuration A is strongly unfavoured at this Ta concentration, due to the high  $\Delta E$  (60.46 kcal/mol).

Configuration	$\Delta E$ (kcal/mol)
C	0
B	7.65
A	60.46

**Table 3.4** Relative energy ( $\Delta E$ ) for A, B and C configurations for  $\text{Bi}_{0.75}\text{Ta}_{0.25}\text{O}_{1.75}$  composition. Configuration A, with isolated  $\text{Ta}_4\text{O}_{18}$  clusters; configuration B, with linked  $\text{Ta}_4\text{O}_{18}$  strings; configuration C, with two  $\text{Ta}_4\text{O}_{18}$  sharing a  $\text{TaO}_6$  octahedron.

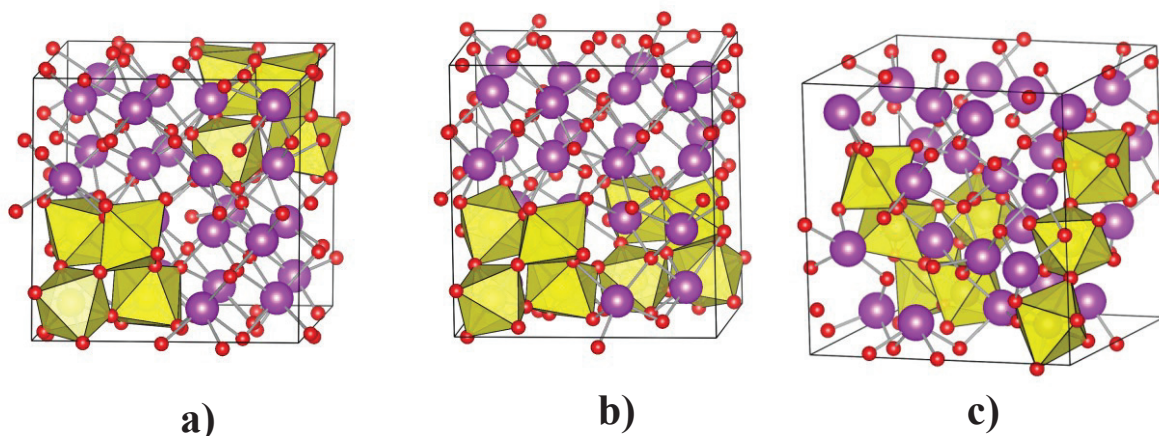


**Figure 3.6** Optimized structures of  $\text{Bi}_{0.75}\text{Ta}_{0.25}\text{O}_{1.75}$ . **a)** Configuration A: isolated  $\text{Ta}_4\text{O}_{18}$  clusters; **b)** configuration B: linked  $\text{Ta}_4\text{O}_{18}$  strings; **c)** configuration C: two  $\text{Ta}_4\text{O}_{18}$  clusters sharing a  $\text{TaO}_6$  octahedron. Bismuth in purple, oxygen in red, coordination octahedra around Ta are shown in yellow.

## Density of States

As we can see from total and partial (Bi, Ta and O contributions) density of states (DOS), the electronic structure of  $\text{Bi}_{0.75}\text{Ta}_{0.25}\text{O}_{1.75}$  (**Figure 3.7 b**) is extremely similar to  $\alpha\text{-Bi}_2\text{O}_3$  (**Figure 3.7 a**), especially for what concerns the role of the Bi  $6s^2$  states, which lie 10 eV below the Fermi level and show negligible superposition with oxygen orbitals. This feature is exactly the same for  $\text{Bi}_{0.75}\text{Ta}_{0.25}\text{O}_{1.75}$  A, B and C configurations. Indeed, the Bi  $6s^2$  lone pair does not participate directly in bonding but nevertheless affects the coordination environment of  $\text{Bi}^{3+}$  (the so-called inert pair effect),<sup>34</sup> causing the distortion of ligands around the cation. Comparing the DOS of  $\alpha\text{-Bi}_2\text{O}_3$  and of  $\text{Bi}_{0.75}\text{Ta}_{0.25}\text{O}_{1.75}$ , we can assert that the force governing the local coordination of Bi is essentially the same in all forms of doped and undoped  $\text{Bi}_2\text{O}_3$ , and this is strongly connected to XAS features, where the splitting of the Bi-O first shell is present in both Ta-doped samples and  $\alpha\text{-Bi}_2\text{O}_3$  (see **Supporting Information S.1**).

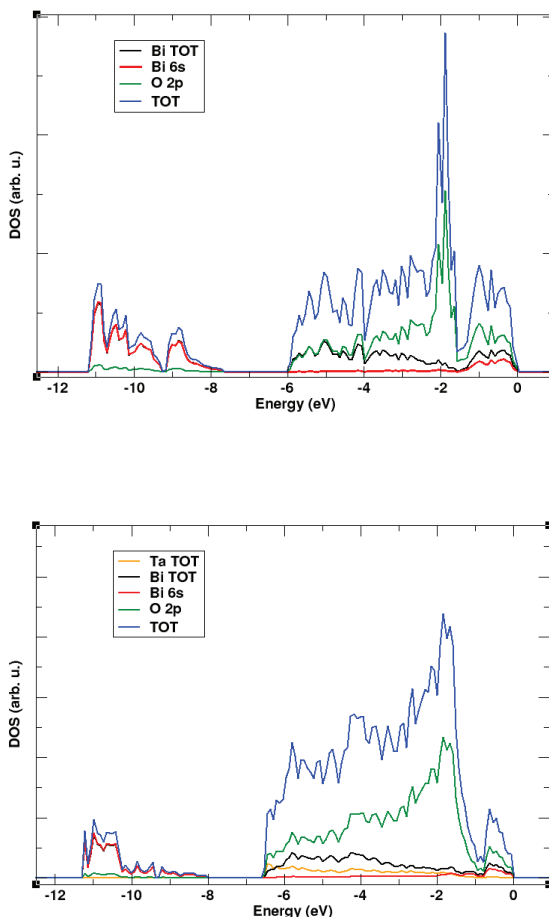


**Figure 3.7** – Top panel: calculated DOS of  $\alpha\text{-Bi}_2\text{O}_3$  ; Bottom panel: calculated DOS of  $\text{Bi}_{0.75}\text{Ta}_{0.25}\text{O}_{1.75}$  (configuration B). DOSS for A and C configurations are reported in the **Supporting Information S.1**.



### 3.4 X-Ray Diffraction

XRD patterns show some variability, depending on the dopant concentration inside the solid solution. In particular, it was observed that increasing the dopant concentration tends to stabilize an average fluorite-like structure (**Figure 3.8** and **Figure 3.9**). This observation, combined with the XAS local structure analysis, leads to the conclusion that the apparent  $Fm\bar{3}m$  symmetry of the most doped samples is actually an average of similar local structures arranged in a highly disordered way. The consequent deduction is that the local oxygen-ion migration inside doped and undoped  $\delta\text{-Bi}_2\text{O}_3$  is essentially governed by the same mechanism, and it is favoured by the possibility of a large number of trajectories created by the presence of the displaced  $32f$  sites occupied by the oxide ions. The coordination around Ta is found to be strictly octahedral no matter of dopant concentration, indicating that  $\text{TaO}_6$  octahedra constitute an obstacle for oxygen-ion diffusion. Then, the proposed picture of Ta-doped  $\text{Bi}_2\text{O}_3$  is that the strain induced in the bismuth oxide matrix by the Ta islands stabilizes the structure of undoped  $\delta\text{-Bi}_2\text{O}_3$  at low temperature. However, the restricted volume for diffusion paths due to the stiff Ta clusters lowers the conductivity with respect to the undoped material (see **Supporting Information S.1**).

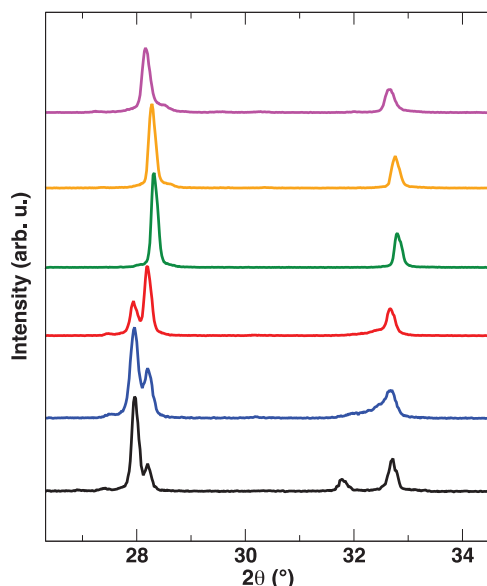


**Figure 3.8** – XRD patterns of Ta-doped samples. From top to bottom:  $x = 0.3, 0.25, 0.22, 0.15, 0.1, 0.075$ .

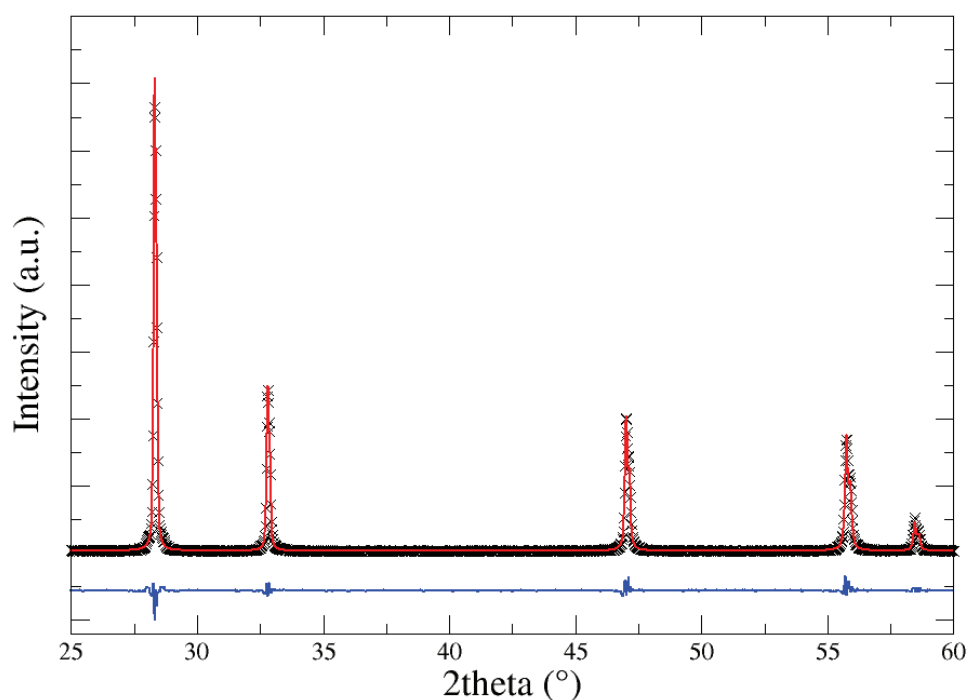


**Figure 3.9** Rietveld analysis for sample with 22%mol of Ta. Experimental data (black points), theoretical curve (red line) and residuals (blue line) are shown.

### 3.5 Properties of V- and Nb-doped bismuth oxide

Finally, an overview of the effect of  $V^{5+}$  and  $Nb^{5+}$  dopant cations is given, in order to draw a more complete picture of the structural features that have an influence on the average fluorite-like phase stabilization of  $\delta\text{-Bi}_2\text{O}_3$  by pentavalent dopants.

Like tantalum, also vanadium and niobium stabilize the fluorite structure of bismuth oxide, but with a different local arrangement.

XAS spectra are acquired at the V K-edge for  $\text{Bi}_{1-x}\text{V}_x\text{O}_{3+\delta}$  samples ( $x=0.095$  and  $0.11$ ) and from the XANES profile it is immediately clear that the local environment around  $V^{5+}$  is tetrahedrally coordinated, in agreement with previous studies.<sup>8,35,36</sup> Indeed, a sharp pre-edge peak due to the transition  $1s \rightarrow 3d$  can be observed: this transition is forbidden in the octahedral symmetry, but becomes allowed when the symmetry degree is lowered by loss of inversion around the cation centre.<sup>37</sup> On the contrary, it is well known from literature that doping bismuth oxide with niobium stabilizes the average fluorite-like matrix through pyrochlore-like structural motives, similarly to Ta-doped samples.<sup>4,5,7</sup>

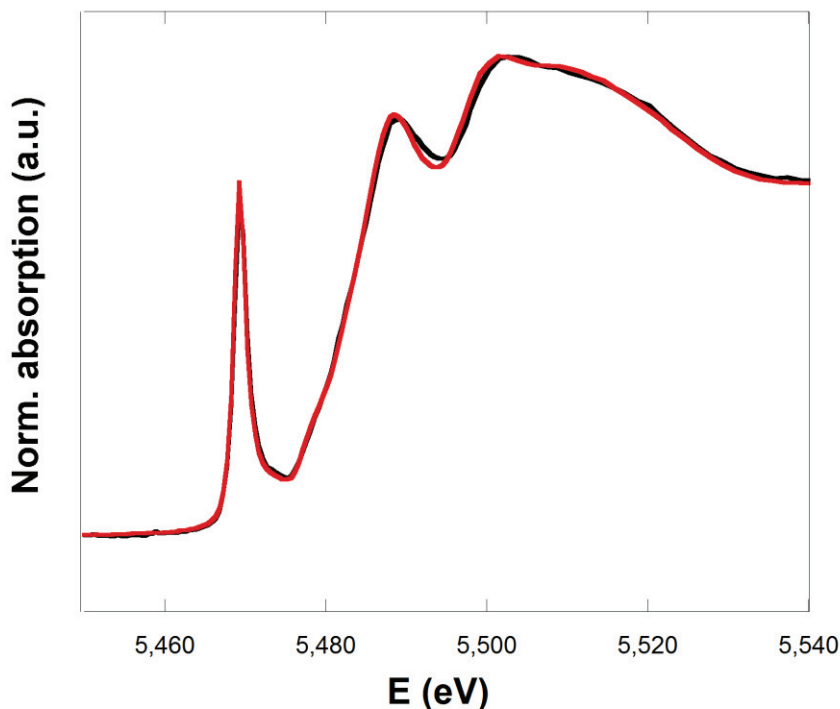


**Figure 3.10** XANES spectra of V-doped samples ( $x=0.11$  red and  $x=0.095$  black) acquired at the V K-edge.

A DFT investigation on the same dopant structural motives previously analyzed for  $\text{Bi}_{0.75}\text{Ta}_{0.25}\text{O}_{1.7}$  samples has been carried out also for  $\text{Bi}_{0.75}\text{Nb}_{0.25}\text{O}_{1.7}$ . Again, A, B and C configurations have been fully optimized using the B3LYP functional and the same supercell, where Ta atoms were substituted with Nb atoms.<sup>21,22</sup> A relative stability scale analogous to  $\text{Bi}_{0.75}\text{Ta}_{0.25}\text{O}_{1.7}$  can be observed also for  $\text{Bi}_{0.75}\text{Nb}_{0.25}\text{O}_{1.7}$  (**Table 3.5**). Nevertheless, the maximum  $\Delta E$  between A and C configurations (21.60 kcal/mol) is by far smaller than the corresponding  $\Delta E$  value found for Ta-doping (60.46 kcal/mol). This result is compatible with a more flexible local environment for Nb dopant.

In summary, the experimental and computational evidences point to a definitely different behaviour of vanadium, which prefers a tetrahedral coordination, with respect to niobium and tantalum as concerns the local structure. Also the conduction mechanism seems to be completely different. Actually, according to the *ab initio* molecular dynamics study by Kuang et al.,<sup>8</sup> the tetrahedral configuration of vanadium is dynamically varying and the ability of V to change its local environment from four- to five-coordinated favours the diffusive paths around the V-doped sites.

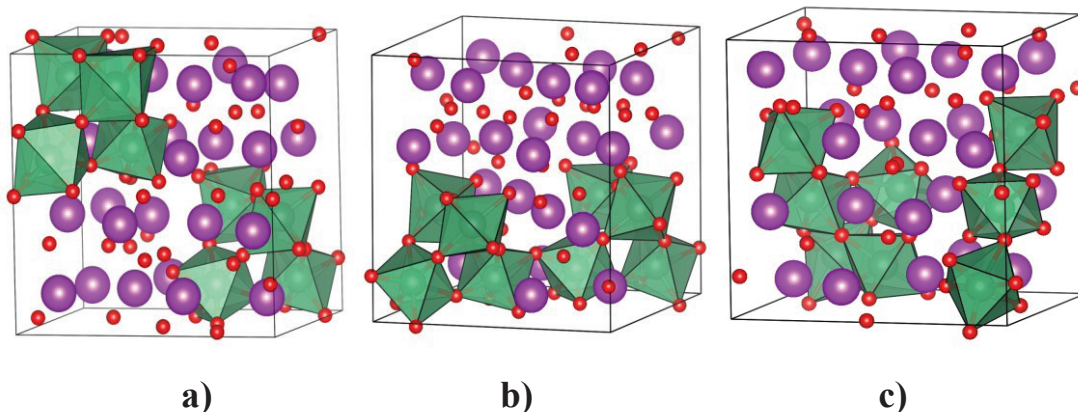


**Figure 3.11** Optimized structures of  $\text{Bi}_{0.75}\text{Nb}_{0.25}\text{O}_{1.75}$ . **a)** Configuration A: isolated  $\text{Nb}_4\text{O}_{18}$  clusters; **b)** configuration B: linked  $\text{Nb}_4\text{O}_{18}$  strings; **c)** configuration C: two  $\text{Nb}_4\text{O}_{18}$  clusters sharing a  $\text{NbO}_6$  octahedron. Bismuth in purple, oxygen in red, coordination octahedra around Nb are shown in green.

**Table 3.5** Relative energy ( $\Delta E$ ) for A, B and C configurations for  $\text{Bi}_{0.75}\text{Nb}_{0.25}\text{O}_{1.75}$  composition. Configuration A, with isolated  $\text{Nb}_4\text{O}_{18}$  clusters; configuration B, with linked  $\text{Nb}_4\text{O}_{18}$  strings; configuration C, with two  $\text{Nb}_4\text{O}_{18}$  sharing a  $\text{NbO}_6$  octahedron.  $\Delta E$  (kcal/mol) defines the relative stability.

Model	$\Delta E$ (kcal/mol)
C	0
B	16.25
A	21.60

## 4. Conclusions

To sum up, a detailed local structural analysis of Ta-doped bismuth oxide samples has been performed in order to unveil the preferential aggregation motives around the dopant site that are involved in the stabilization of the fluorite-like phase at room temperature. The integrated XAS and computational approach shed light on the local coordination and electronic structure of bismuth site, which are supposed to play a key role in the high conductivity of this material. From this study we can conclude that Ta is organized in octahedral  $\text{TaO}_6$  units that

are gathered as Ta<sub>4</sub>O<sub>18</sub> clusters. These clusters give rise to further association into Ta<sub>7</sub>O<sub>30</sub> or higher order aggregates, as demonstrated by XAS analysis on Ta L<sub>3</sub>-edge.

DFT calculations strongly support from the energetic point of view the experimental evidence, confirming the preferential association of Ta<sub>4</sub>O<sub>18</sub> clusters into larger aggregates. Such tendency, together with the fixed octahedral TaO<sub>6</sub> local environment, would hinder the oxygen-ion diffusion inside the δ-Bi<sub>2</sub>O<sub>3</sub> matrix.

XAS analysis shows that the local environment of Bi is similar for all the investigated samples and is characterized by the displacement of the oxygen-ions towards one of the faces of the OBi<sub>4</sub> coordination tetrahedron. This feature can be correlated with the electronic structure of the compound, taking into account the effect of the Bi 6s<sup>2</sup> lone pair.

The apparent discrepancy by local structure evidenced by XAS and the long-range arrangement observed by XRD is likely recovered taking into account that the fluorite *Fm-3m* symmetry could result from an average of the randomly oriented displacements of oxygen from the centre of the OBi<sub>4</sub> tetrahedra.

Oxygen-ion diffusion is enhanced by the average fluorite structure *and* by the local arrangement characterized by the displacement of oxygen from the centre of the OBi<sub>4</sub> tetrahedra.

Finally, an overview of the effect of V<sup>5+</sup> and Nb<sup>5+</sup> dopant cations (belonging as Ta<sup>5+</sup> to the VB group of the periodic table) on the average fluorite-like phase stabilization of δ-Bi<sub>2</sub>O<sub>3</sub> has been given. While vanadium adopts a tetrahedral local environment, niobium seems to prefer a local environment similar to tantalum but with a less marked preference for Nb<sub>4</sub>O<sub>18</sub> linked configurations with respect to isolated Nb<sub>4</sub>O<sub>18</sub> clusters.

## 5. References

- (1) Gambino, M.; Giannici, F.; Longo, A.; Di Tommaso, S.; Labat, F.; Martorana, A. Dopant Clusterization and Oxygen Coordination in Ta-Doped Bismuth Oxide: A Structural and Computational Insight into the Mechanism of Anion Conduction. *J. Phys. Chem. C* **2015**, *119* (47), 26367–26373.
- (2) Sammes, N. M.; Tompsett, G. A.; Näfe, H.; Aldinger, F. Bismuth Based Oxide Electrolytes—structure and Ionic Conductivity. *J. Eur. Ceram. Soc.* **1999**, *19* (10),

1801–1826.

- (3) Gattow, G.; Schröder, H. Über Wismutoxide. III. Die Kristallstruktur Der Hochtemperaturmodifikation von Wismut (III)-Oxid ( $\delta$ -Bi<sub>2</sub>O<sub>3</sub>). *Zeitschrift für Anorg. und Allg. Chemie* **1962**, *318* (3–4), 176–189.
- (4) Ling, C. D.; Withers, R. L.; Schmid, S.; Thompson, J. G. A Review of Bismuth-Rich Binary Oxides in the Systems Bi<sub>2</sub>O<sub>3</sub>- Nb<sub>2</sub>O<sub>5</sub>, Bi<sub>2</sub>O<sub>3</sub>-Ta<sub>2</sub>O<sub>5</sub>, Bi<sub>2</sub>O<sub>3</sub>-MoO<sub>3</sub>, and Bi<sub>2</sub>O<sub>3</sub>-WO<sub>3</sub>. *J. Solid State Chem.* **1998**, *137* (1), 42–61.
- (5) Ling, C. D. Structural Relationships among Bismuth-Rich Phases in the Bi<sub>2</sub>O<sub>3</sub>- Nb<sub>2</sub>O<sub>5</sub>, Bi<sub>2</sub>O<sub>3</sub>-Ta<sub>2</sub>O<sub>5</sub>, Bi<sub>2</sub>O<sub>3</sub>-MoO<sub>3</sub>, and Bi<sub>2</sub>O<sub>3</sub>- WO<sub>3</sub> Systems. *J. Solid State Chem.* **1999**, *148* (2), 380–405.
- (6) Kuang, X.; Li, Y.; Ling, C. D.; Withers, R. L.; Evans, I. R. Oxide Ion Conductivity, Phase Transitions, and Phase Separation in Fluorite-Based Bi<sub>38-x</sub>Mo<sub>7+ x</sub>O<sub>78+1.5x</sub>. *Chem. Mater.* **2010**, *22* (15), 4484–4494.
- (7) Ling, C. D.; Schmid, S.; Blanchard, P. E. R.; Petricek, V.; McIntyre, G. J.; Sharma, N.; Maljuk, A.; Yaremchenko, A. A.; Kharton, V. V; Gutmann, M.; et al. A (3+ 3)-Dimensional “Hypercubic” Oxide-Ionic Conductor: Type II Bi<sub>2</sub>O<sub>3</sub>-Nb<sub>2</sub>O<sub>5</sub>. *J. Am. Chem. Soc.* **2013**, *135* (17), 6477–6484.
- (8) Kuang, X.; Payne, J. L.; Johnson, M. R.; Radosavljevic Evans, I. Remarkably High Oxide Ion Conductivity at Low Temperature in an Ordered Fluorite-Type Superstructure. *Angew. Chemie Int. Ed.* **2012**, *51* (3), 690–694.
- (9) Koto, K.; Suda, K.; Ishizawa, N.; Maeda, H. Oxide Ion Motion in Bismuth Sesquioxide ( $\sigma$ -Bi<sub>2</sub>O<sub>3</sub>). *Solid state ionics* **1994**, *72*, 79–85.
- (10) Wachsman, E. D.; Jayaweera, P.; Jiang, N.; Lowe, D. M.; Pound, B. G. Stable High Conductivity Ceria/bismuth Oxide Bilayered Electrolytes. *J. Electrochem. Soc.* **1997**, *144* (1), 233–236.
- (11) Joh, D. W.; Park, J. H.; Kim, D. Y.; Yun, B.-H.; Lee, K. T. High Performance Zirconia-Bismuth Oxide Nanocomposite Electrolytes for Lower Temperature Solid Oxide Fuel Cells. *J. Power Sources* **2016**, *320*, 267–273.
- (12) Giannici, F.; Gregori, G.; Aliotta, C.; Longo, A.; Maier, J.; Martorana, A. Structure and Oxide Ion Conductivity: Local Order, Defect Interactions and Grain Boundary Effects

- in Acceptor-Doped Ceria. *Chem. Mater.* **2014**, *26* (20), 5994–6006.
- (13) Payne, J. L.; Farrell, J. D.; Linsell, A. M.; Johnson, M. R.; Evans, I. R. The Mechanism of Oxide Ion Conductivity in Bismuth Rhenium Oxide,  $\text{Bi}_{28}\text{Re}_2\text{O}_{49}$ . *Solid State Ionics* **2013**, *244*, 35–39.
- (14) Crumpton, T. E.; Mosselmans, J. F. W.; Greaves, C. Structure and Oxide Ion Conductivity in  $\text{Bi}_{28}\text{Re}_2\text{O}_{49}$ , a New Bismuth Rhenium Oxide Containing Tetrahedral and Octahedral Re (Vii). *J. Mater. Chem.* **2005**, *15* (1), 164–167.
- (15) Walsh, A.; Watson, G.; Payne, D.; Edgell, R.; Guo, J.; Glans, P.-A.; Learmonth, T.; Smith, K. Electronic Structure of the  $\alpha$  and  $\delta$  Phases of  $\text{Bi}_2\text{O}_3$ : A Combined Ab Initio and X-Ray Spectroscopy Study. *Phys. Rev. B* **2006**, *73* (23), 235104.
- (16) Hull, S.; Norberg, S. T.; Tucker, M. G.; Eriksson, S. G.; Mohn, C. E.; Stølen, S. Neutron Total Scattering Study of the  $\delta$  and  $\beta$  Phases of  $\text{Bi}_2\text{O}_3$ . *Dalt. Trans.* **2009**, No. 40, 8737–8745.
- (17) Larson, A. C.; Von Dreele, R. B. GSAS Manual (Los Alamos Natl. Lab., Los Alamos, NM). *Rep. LAUR* **1988**, *86*, 748.
- (18) Klementev, K. V. Extraction of the Fine Structure from X-Ray Absorption Spectra. *J. Phys. D. Appl. Phys.* **2001**, *34* (2), 209.
- (19) Rehr, J. J.; Kas, J. J.; Vila, F. D.; Prange, M. P.; Jorissen, K. Parameter-Free Calculations of X-Ray Spectra with FEFF9. *Phys. Chem. Chem. Phys.* **2010**, *12* (21), 5503–5513.
- (20) Dovesi, R.; Saunders, V. R.; Roetti, C.; Orlando, R.; Pascale, F.; Civalleri, B.; Doll, K.; Harrison, N. M.; Bush, I. J.; Llunell, M.; et al. Crystal09 2.0.1. **2013**, 1–307.
- (21) Becke, A. D. Density-Functional Thermochemistry. III. The Role of Exact Exchange. *J. Chem. Phys.* **1993**, *98* (7), 5648–5652.
- (22) Wachsman, E. D.; Marlowe, C. A.; Lee, K. T. Role of Solid Oxide Fuel Cells in a Balanced Energy Strategy. *Energy Environ. Sci.* **2012**, *5* (2), 5498–5509.
- (23) Wehrich, R.; Anusca, I. Halbantiperowskite II: Zur Kristallstruktur Des  $\text{Pd}_3\text{Bi}_2\text{S}_2$ . *Zeitschrift für Anorg. und Allg. Chemie* **2006**, *632* (2), 335–342.
- (24) Sophia, G.; Baranek, P.; Sarrazin, V.; Rerat, M.; Dovesi, R. Systematic Influence of

Atomic Substitution on the Phase Diagram of  $ABO_3$  Ferroelectric Perovskites. Unpublished 2014.

- (25) Berthelat, J. C.; Durand, P. Recent Progress of Pseudopotential Methods in Quantum Chemistry. *Gazz. Chim. Ital.* **1978**, *108* (5–6), 225–236.
- (26) Durand, P.; Barthelat, J.-C. A Theoretical Method to Determine Atomic Pseudopotentials for Electronic Structure Calculations of Molecules and Solids. *Theor. Chim. Acta* **1975**, *38* (4), 283–302.
- (27) Barthelat, J. C.; Durand, P.; Serafini, A. Non-Empirical Pseudopotentials for Molecular Calculations: I. The PSIBMOL Algorithm and Test Calculations. *Mol. Phys.* **1977**, *33* (1), 159–180.
- (28) Mizoguchi, H.; Hosono, H.; Kawazoe, H.; Yasukawa, M.; Fujitsu, S.; Fukumi, K. Valence States of Bismuth in New Mixed-Valence Oxides:  $Bi_{1-x}Y_xO_{1.5+\delta}$  ( $X=0.4$ ) by XANES. *Mater. Res. Bull.* **1999**, *34* (3), 373–379.
- (29) Paek, S.-M.; Kim, Y.-I. Ta  $L_3$ -Edge XANES Study of Perovskite Oxynitrides  $ATaO_2N$  ( $A=Ca, Sr, Ba$ ). *J. Alloys Compd.* **2014**, *587*, 251–254.
- (30) Shannon, R. D. t. Revised Effective Ionic Radii and Systematic Studies of Interatomic Distances in Halides and Chalcogenides. *Acta Crystallogr. Sect. A Cryst. Physics, Diffraction, Theor. Gen. Crystallogr.* **1976**, *32* (5), 751–767.
- (31) Battle, P. D.; Catlow, C. R. A.; Heap, J. W.; Moroney, L. M. Structural and Dynamical Studies of  $\delta$ - $Bi_2O_3$  Oxide Ion Conductors: I. The Structure of  $(Bi_2O_3)_{1-x}(Y_2O_3)_x$  as a Function of  $x$  and Temperature. *J. Solid State Chem.* **1986**, *63* (1), 8–15.
- (32) Boyapati, S.; Wachsman, E. D.; Jiang, N. Effect of Oxygen Sublattice Ordering on Interstitial Transport Mechanism and Conductivity Activation Energies in Phase-Stabilized Cubic Bismuth Oxides. *Solid State Ionics* **2001**, *140* (1–2), 149–160.
- (33) Blower, S. K.; Greaves, C. The Structure of  $\beta$ - $Bi_2O_3$  from Powder Neutron Diffraction Data. *Acta Crystallogr. Sect. C Cryst. Struct. Commun.* **1988**, *44* (4), 587–589.
- (34) Seshadri, R.; Hill, N. A. Visualizing the Role of Bi 6s “lone Pairs” in the off-Center Distortion in Ferromagnetic  $BiMnO_3$ . *Chem. Mater.* **2001**, *13* (9), 2892–2899.
- (35) Zhou, W. The Type II Superstructural Family in the  $Bi_2O_3$ - $V_2O_5$  System. *J. Solid State*



*Chem.* **1990**, 87 (1), 44–54.

- (36) Zhou, W. Defect Fluorite-Related Superstructures in the  $\text{Bi}_2\text{O}_3$  - $\text{V}_2\text{O}_5$  System. *J. Solid State Chem.* **1988**, 76 (2), 290–300.
- (37) Wong, J.; Lytle, F. W.; Messmer, R. P.; Maylotte, D. H. K-Edge Absorption Spectra of Selected Vanadium Compounds. *Phys. Rev. B* **1984**, 30 (10), 5596.

# CHAPTER 4

## XAS and DFT investigation on doped LaGaO<sub>3</sub>

In this chapter a comprehensive XAS and DFT study about perovskite-like lanthanum gallate will be presented, with the aim to understand: *i)* the interaction of oxygen vacancy with B-site cations, *ii)* the favoured oxygen-ion diffusion paths, *iii)* the influence of doping and co-doping on the local structure, and *iv)* the electronic features around perovskite B-site. The materials under consideration are LaGa<sub>0.875</sub>Mg<sub>0.125</sub>O<sub>2.935</sub>, La<sub>1-x</sub>Sr<sub>x</sub>Ga<sub>1-y</sub>Mg<sub>y</sub>O<sub>3-δ</sub> and La<sub>1-x</sub>Sr<sub>x</sub>Ga<sub>1-y</sub>(Mg,Co)<sub>y</sub>O<sub>3-δ</sub>. Results concerning LaGa<sub>0.875</sub>Mg<sub>0.125</sub>O<sub>2.935</sub> are object of a recently submitted publication.

### 1. Motivation of the study

As reported in **Section 2.3 of Chapter 1** LaGaO<sub>3</sub> (LG) represents one of the top performing electrolytes for IT-SOFC<sup>1-5</sup>: its perovskite structure (ABO<sub>3</sub>), if opportunely doped with small percentages of Sr<sup>2+</sup> in the A site and Mg<sup>2+</sup> in the B site, can accommodate a large concentration of anion vacancies and this leads to a very high anionic conductivity at IT-SOFC operating temperatures. To date, the most conductive compositions (around 0.14 S/cm at 800°C) are La<sub>0.9</sub>Sr<sub>0.1</sub>Ga<sub>0.8</sub>Mg<sub>0.2</sub>O<sub>2.85</sub> (LSGM1020) and La<sub>0.8</sub>Sr<sub>0.2</sub>Ga<sub>0.8</sub>Mg<sub>0.2</sub>O<sub>2.8</sub> (LSGM2020).<sup>5-10</sup> Moreover, it has been reported that co-doping the B site with Mg<sup>2+</sup> and small amounts of Co minimize the ohmic resistance of the electrolyte and the overpotential of anodes and cathodes, maintaining an oxide-ion conductivity similar to the parent LSGM composition.<sup>11</sup> La<sub>0.8</sub>Sr<sub>0.2</sub>Ga<sub>0.8</sub>Mg<sub>0.2-x</sub>Co<sub>x</sub>O<sub>3±δ</sub>, with  $x \leq 10\%$ mol, were found to slightly increase the electrical conductivity only at low temperatures (due to the introduction of electronic charge carriers into the lattice), but at high temperatures conductivity was found to be almost completely ionic. Increasing the concentration of cobalt over the 10% mol leads to a lower activation energy barrier for electrical conductivity, that affects the electrolyte activity of the compound.<sup>12,13</sup>

The functional properties of LG-based materials have been extensively studied during the last years, but the influence of doping and co-doping on the local structure and the correlation

with ionic conductivity still need a thorough elucidation. To this end, this study is articulated in three main points:

- probing the influence of  $\text{Mg}^{2+}$  dopant on the perovskite-type  $\text{LaGa}_{0.875}\text{Mg}_{0.125}\text{O}_{2.935}$  material (LGM0125 in the following). This composition was chosen in order to avoid the contribution of  $\text{Sr}^{2+}$  doping on the A site. Therefore, the computational approach is focused only on the vacancy interaction with the B site, which is supposed to provide the main contribution to the mechanism of oxygen ion diffusion. The issues of vacancy interaction with the B site and of local distortion around the vacancy site (tilting and dihedral distortions) are actually under debate in literature,<sup>14–17</sup> and are worth to be deeply investigated by a DFT configurational study.
- Analysis of the oxygen-ion diffusion paths around the B-site on  $\text{LaGa}_{0.875}\text{Mg}_{0.125}\text{O}_{2.935}$  electrolyte, in order to unravel the activation energy barriers around both Ga regular site and Mg dopant site.
- Assessment of the influence of Sr doping and of co-doping with Mg and Co on the local structure of  $\text{La}_{1-x}\text{Sr}_x\text{Ga}_{1-y}\text{Mg}_y\text{O}_{3-\delta}$  and  $\text{La}_{1-x}\text{Sr}_x\text{Ga}_{1-y}(\text{Mg},\text{Co})_y\text{O}_{3-\delta}$ , to unveil how local distortions vary with dopant concentration. In particular, XAS data at the Co K-edge both at static disorder conditions (77 K) and *in situ* (25-750°C, 10°C/min) are collected, in order to understand how cobalt insertion modifies the electronic and atomic structure of LSGM.

This chapter is organized as follows. In **Section 2** experimental and computational methods are reported. **Section 3** is dedicated to results and discussion. In **Section 3.1** a combined XAS and DFT study on  $\text{LaGa}_{0.875}\text{Mg}_{0.125}\text{O}_{2.935}$  electrolyte is presented. **Section 3.2** contains preliminary theoretical results concerning oxygen-ion diffusion paths in  $\text{LaGa}_{0.875}\text{Mg}_{0.125}\text{O}_{2.935}$ . In **Section 3.3** EXAFS data analysis at the Ga K-edge of  $\text{La}_{1-x}\text{Sr}_x\text{Ga}_{1-y}\text{Mg}_y\text{O}_{3-\delta}$  and  $\text{La}_{1-x}\text{Sr}_x\text{Ga}_{1-y}(\text{Mg},\text{Co})_y\text{O}_{3-\delta}$  is presented and discussed, together with the XANES spectra acquired *in situ* at the Co K-edge. Finally, conclusions are drawn in **Section 4**.

## 2. Experimental and computational methods

**Synthesis.**  $\text{LaGaO}_3$ ,  $\text{LaGa}_{0.875}\text{Mg}_{0.125}\text{O}_{2.93}$ ,  $\text{La}_{1-x}\text{Sr}_x\text{Ga}_{1-y}\text{Mg}_y\text{O}_{3-\delta}$  and  $\text{La}_{1-x}\text{Sr}_x\text{Ga}_{1-y}(\text{Mg}, \text{Co})_y\text{O}_{3-\delta}$  were prepared by solution combustion synthesis. Commercial nitrates  $\text{La}(\text{NO}_3)_3 \cdot 6\text{H}_2\text{O}$ ,  $\text{Ga}(\text{NO}_3)_3 \cdot x \text{H}_2\text{O}$  and  $\text{Mg}(\text{NO}_3)_2 \cdot 6\text{H}_2\text{O}$  were dissolved in distilled water with citric acid ( $\text{C}_6\text{H}_8\text{O}_7$ ) and stirred until dissolution. pH was raised to 6 with  $\text{NH}_3$  in order to ensure the complexation of metals, and the mixture was then stirred at  $80^\circ\text{C}$  until gel formation. Next, the temperature was raised until ignition of self-combustion, and the powder obtained was calcined first at  $1000^\circ\text{C}$  and then at  $1450^\circ\text{C}$ .

X-ray absorption spectra were acquired at the Ga and Co K-edges at the Dubble BM26A beamline of the European Synchrotron Radiation Facility (ESRF). Ga K-edge data were collected in transmission mode, while experiments at the Co K-edge were carried out in fluorescence mode at liquid nitrogen temperature ( $77 \text{ K}$ ). *In situ* measurements at Co K-edge were acquired using the “microtomo furnace” in order to reach high temperatures and collect sequential measurements in the range  $25\text{-}750^\circ\text{C}$  ( $10^\circ\text{C}/\text{min}$ ) in air and He atmospheres. EXAFS data analysis was carried out with GNXAS software.<sup>18,19</sup> X-ray diffraction (XRD) patterns were acquired with a Siemens D-500 diffractometer using  $\text{Cu K}\alpha$  radiation and a graphite monochromator on the diffracted beam. Rietveld analysis was performed with GSAS.<sup>20</sup>

**Computational methods.** Periodic DFT calculations were carried out with the CRYSTAL14 code,<sup>21</sup> which is based on the expansion of the crystalline orbitals as a linear combination of atom-centred Gaussian orbitals. The hybrid exchange-correlation functional PBE0,<sup>22,23</sup> with 25% of Hartree-Fock exchange, has been considered throughout, after testing the ability of several functionals to correctly describe the orthorhombic *Pbnm* unit cell of undoped LG, which is the most stable phase at room temperature (see **Supporting Information S.2, Tables S.2.1 and S.2.2**). For La, a Hay and Wadt small core pseudopotential was used together with a 411(1d)G basis set,<sup>24</sup> while all electron triple-zeta basis sets were chosen for Ga and Mg.<sup>25</sup> Finally, a Durand and Barthelat large core pseudopotential was used for oxygen, together with a double- $\zeta$  split valence basis set.<sup>26,27</sup>

The configurational analysis performed on LGM0125 was carried out using the recently-implemented tool for disordered systems and solid solutions in CRYSTAL,<sup>28,29</sup> which allows to obtain the number of possible dopant configurations (for a given dopant concentration) by combinatorial analysis. This tool classifies degenerate configurations in Symmetry

Independent Classes (SICs) through symmetry operator analysis, indicating for each SIC its own multiplicity. The chosen (2x1x2) supercell is large enough to avoid defect interactions from one cell to the other.

To create the oxygen vacancy, one oxygen atom was removed from the supercell, leaving its corresponding basis set centred at the original oxygen atomic position. All structures were then fully optimized (lattice parameters and atomic positions). Convergence was determined from the root-mean-square and absolute value of the largest component of the forces and displacements, considering default values.<sup>21</sup> Calculations were carried out using a Monkhorst Pack grid with shrinking factor 6x6x6, corresponding to 112  $k$  points in the irreducible Brillouin zone. The Coulomb and exchange series were truncated with threshold values of  $10^{-7}$ ,  $10^{-7}$ ,  $10^{-7}$ ,  $10^{-7}$  and  $10^{-14}$ .<sup>21</sup> A pruned grid, with 55 radial points and 434 angular points, was used for numerical DFT integration.

**Oxygen-ion diffusion paths.** Diffusion barriers for oxygen-ion paths were qualitatively estimated performing a relaxed scan of the geometry of the defective system. The 2x1x2 supercell with the Mg-layered LGM0125 configuration, that shows the highest equivalence of oxygen-ion conducting sites (See **Section 3.1, Energetic scale of the generated configurations**), was chosen for this study. For each step of the scan, the atomic positions of a fragment of 51 atoms set around the vacancy and the diffusing oxygen-ion were fully relaxed, while cell parameters were kept fixed.

## 3. Results and discussion

### 3.1 Defect interaction and local structural distortions in $\text{LaGa}_{0.875}\text{Mg}_{0.125}\text{O}_{2.93}$

#### *Structural characterization*

X-Ray diffraction technique was used to check the stability of the  $Pbnm$  phase for doped LGM0125 and LG. XRD results are reported in **Table 4.1**. Rietveld refinements obtained for LG and LGM0125 are shown in **Figure S.2.2** of **Supporting Information S.2**.

Theoretical unit cell parameters found for undoped LG ( $a=5.543$  Å,  $b=5.472$  Å,  $c=7.759$  Å using PBE0 functional) are in agreement with the experimental ones, with the largest discrepancy concerning the  $b$  parameter (0.4%). Moreover, it can be observed a moderate

expansion of the lattice parameters going from LG to LGM0125, caused by the introduction of a dopant with larger ionic radius on the Ga B-site.

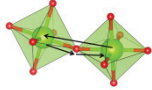
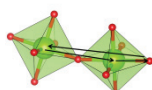
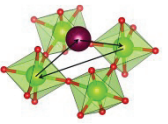
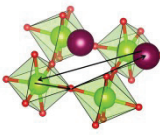
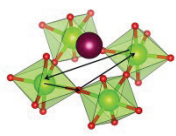
**Table 4.1** Experimental cell parameters for undoped LG and doped LGM0125.

SAMPLE	a(Å)	b(Å)	c(Å)
LG	5.525(2)	5.493(2)	7.776(2)
LGM0125	5.542(1)	5.504(1)	7.801(1)

The results concerning LG and LGM0125 EXAFS data analysis at the Ga K-edge are shown in **Table 4.2**. The data have been fitted generating a cluster of 79 atoms with the *Pbnm* symmetry. EXAFS signal and Fourier transform data, together with the corresponding fittings are reported in **Figure 4.1 a** and **b**. The fitting procedure has been carried out by using only two direct distances: a Ga-O<sub>1</sub> first neighbour and a Ga-La second neighbour, respectively centred on average at 1.95 Å and 3.41 Å. For these contributions, only the distances ( $R_1$  and  $R_2$ ) and the variances ( $\sigma_1^2$  and  $\sigma_2^2$ ) were allowed to vary, while the coordination numbers  $N_1$  and  $N_2$  were respectively fixed to 6 and 8. Ga-O first shell coordination number was kept fixed to 6 also for LSGM0125, because the first shell coordination number of 5.875 expected for this sample is below the EXAFS accuracy.<sup>30</sup> All other contributions involving the higher shells have been considered including Multiple Scattering paths (MS), which are function of previously defined two body distances and of the angles ( $\vartheta$ ) of the three bodies configuration used together with their Debye Waller factors (See figures in **Table 4.2**).<sup>31</sup> In order to describe tilting angles, Ga-O-M (M=Ga, Mg) path, with  $N_1$  fixed to 6, was used and a higher distortion was found for LGM0125 where GaO<sub>6</sub> octahedra have a tilting angle of 161°, while for pure LG tilting angle is 166°. However, the local distortions concerning vacancy sites induced by Mg doping are barely discernible in the EXAFS spectra of LGM0125, due to the larger population of fully coordinated Ga atoms and to the low number of oxygen-vacancies. To this aim, DFT simulations can help to shed light on the local distortion of the GaO<sub>5</sub>Vo and MgO<sub>5</sub>Vo configurations. These configurations, containing the conductive site, have a key role in the oxygen-ion diffusion mechanism.

No significant differences of the  $\vartheta$  angle values for the Ga-M-O, a Ga-La-M, a Ga-O-La and Ga-O-M three-body configurations used in the fitting procedure were found between the doped and undoped samples.

**Table 4.2** Results of the EXAFS data analysis relative to LG and LGM0125 at the Ga K-edge (R in Å,  $\sigma^2$  and  $s^2$  in Å<sup>2</sup> and  $\vartheta$  in °), with the corresponding MS paths (Ga atoms and polyhedra drawn in green, O in red and La atoms in purple). Debye-Waller factors related to the two-body distances are labelled with  $\sigma^2$ , while those related to the MS paths are labelled with  $s^2$ . R-factor values are respectively 6.71% for pure LG and 6.73% for LGM0125. Uncertainties are on the last digit.

			LG	LGM0125
	<b>Ga-O</b>	<b>R<sub>1</sub></b>	1.95	1.94
		<b><math>\sigma_1^2</math></b>	0.0058	0.0070
	<b>Ga-La</b>	<b>R<sub>2</sub></b>	3.42	3.40
		<b><math>\sigma_2^2</math></b>	0.0087	0.0082
<b>MULTIPLE SCATTERING</b>				
	<b>Ga-O-M</b>	<b><math>\vartheta_1</math></b>	166	161
		<b><math>s_1^2</math></b>	1	1
	<b>Ga-Ga-O</b>	<b><math>\vartheta_2</math></b>	150	151
		<b><math>s_2^2</math></b>	1	1
	<b>Ga-La-M</b>	<b><math>\vartheta_3</math></b>	108	109
		<b><math>s_3^2</math></b>	1	4
	<b>Ga-O-La</b>	<b><math>\vartheta_4</math></b>	112	114
		<b><math>s_4^2</math></b>	1	1
	<b>Ga-O-M</b>	<b><math>\vartheta_5</math></b>	154	157
		<b><math>s_5^2</math></b>	10	10

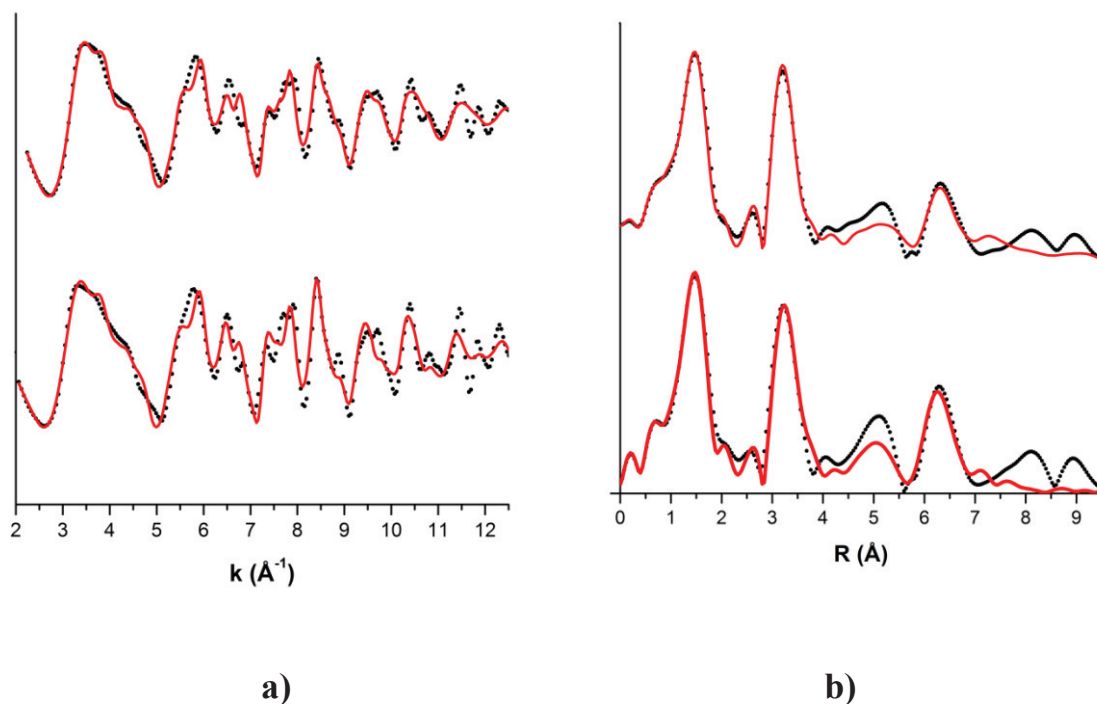


**Figure 4.1** **a)** EXAFS signal and **b)** Fourier Transform of pure LG (bottom) and LGM0125 (top). Data are drawn as black circles and model as a red line.

### ***Configurational analysis by the Symmetry Independent Classes (SIC) method***

**Models and notations.** The number of Symmetry Independent Configurations (SICs) was first computed for LGM0125. A 2x1x2 supercell (80 atoms), with a fractional occupancy of 12.5%mol of Mg (2 atoms) on Ga sites (16 atoms) was build up from the *Pbnm* unit cell, leading to 120 configurations, further divided in 9 SICs (see **Supporting Information S.2**). These 9 SICs were further gathered in three macro-classes: **i)** *Mg*-layered, where Mg lies in every B-site layer parallel to the *ac* plane, and Mg-Vo-Mg configurations are absent; **ii)** *Mg*-clustered, where equatorially linked Mg-Vo-Mg configurations are allowed; **iii)** *Mg*, *Ga*-layered, where alternating Mg/Ga and undoped Ga layers are present, and equatorial Mg-Vo-Mg links are excluded (see **Figures 4.2 a**, **4.2 b** and **4.2 c**). Among these SICs, only the most diluted dopant configurations were investigated, while configurations that present linear sequences or ordered dopant arrangements were excluded. One single representative configuration was finally chosen for each of these three macro-classes, in order to carry out the oxygen vacancy configurational analysis.



In all cases, to allow electrical charge compensation over the unit cell, two Mg atoms were simultaneously introduced in the lattice together with one oxygen vacancy, according to the following reaction:



This resulted in twenty eight possible oxygen vacancies configurations which were all fully-optimized by varying unit cell lattice constant and the atomic positions. The results about these configurations are reported in the **Supporting Information S.2, Section S.2.6**. For sake of clarity, to refer to these configurations, we introduce the following notation:  $X\text{-V}_O^n\text{-Y}_{ax}$  and  $X\text{-V}_O^n\text{-Y}_{eq}$  which correspond to configurations where cations X and Y, and oxygen vacancy  $\text{V}_O$  are axially or equatorially linked, respectively, with the dopant Mg atom being the n-th neighbour of the oxygen vacancy.

**Energetic scale of the generated configurations.** The relative electronic energy ( $\Delta E$ ) values, show that the axial configurations ( $\text{Ga-V}_O\text{-Ga}_{ax}$  or  $\text{Mg-V}_O\text{-Ga}_{ax}$ ) are always the most stable (**Table 4.3**). The  $\Delta E$  range of each macro-class is: 8.91 kcal/mol for the Mg-clustered macro-class, which shows the largest energy range, 6.52 kcal/mol for the Mg,Ga-layered macro-class and 5.46 kcal/mol for the Mg-layered one. The energy difference between these systems is quite low, suggesting the equivalence of different vacancy sites, which is an essential requirement for efficient oxygen-ion conducting materials. Nevertheless, the energetics of the three different Mg configurations indicate a slight preference for a more diluted accommodation of Mg dopant in the B-site. Notably the computed  $\Delta E$  values are in good agreement with previously-reported data by Blanc et al.,<sup>14</sup> who obtained a  $\Delta E$  range of 8.37 kcal/mol for the 12.5mol% Mg concentration.

The calculations indicate that  $\text{V}_O$  preferentially adopts axial environments, both in  $\text{Ga-V}_O\text{-Ga}$  and  $\text{Mg-V}_O\text{-Ga}$  configurations. As a common trend in the three macro-classes, we can also underline that the equatorial  $\text{Mg-V}_O\text{-Ga}$  configuration is in all the cases considered one of the less favored, with differences with respect to the most stable configuration of each class ranging from 5.46 to 7.07 kcal/mol (obtained for the Mg-layered and Mg-clustered classes, respectively) (See **Supporting information S.2, Table S.2.6**).

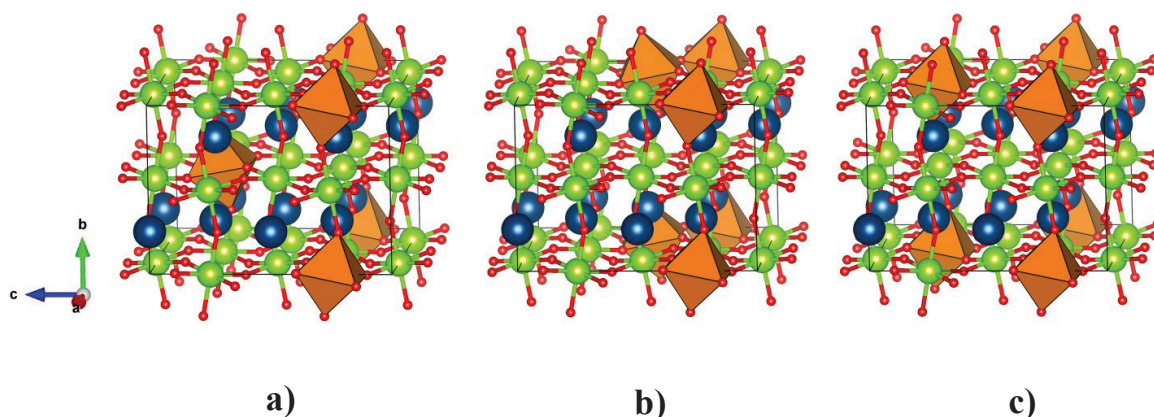


**Figure 4.2** Mixed ball-and-stick and polyhedra representation of one configuration for each of the three macro-classes obtained from the SIC analysis: **a)** *Mg-layered*, **b)** *Mg-clustered* and **c)** *Mg, Ga-layered* for a (2x1x2) supercell of LGM0125. Oxygen, lanthanum and gallium as red, blue and green balls, respectively. Brown polyhedra denote coordination around Mg atoms. The unit cell is shown as a solid black line. All the 28 configurations considered are shown in the Supporting Information.

**Table 4.3** Relative Energy ( $\Delta E$ ) of different oxygen vacancy positions, obtained from the SIC analysis of LGM0125, broken down into macro-classes. All data in kcal/mol. For details about configuration notation, see above the section “**Configurational analysis by the Symmetry Independent Classes (SIC) method**”.

Configuration	$\Delta E$
<b>Mg-layered</b>	
Ga-Vo <sup>3</sup> -Ga <sub>ax</sub>	0.00
Ga-Vo <sup>5</sup> -Ga <sub>ax</sub>	0.06
Mg-Vo <sup>1</sup> -Ga <sub>ax</sub>	0.76
Ga-Vo <sup>3</sup> -Ga <sub>eq</sub>	2.19
Ga-Vo <sup>5</sup> -Ga <sub>eq</sub>	2.46
Mg-Vo <sup>1</sup> -Ga <sub>ax</sub>	2.64
Ga-Vo <sup>3</sup> -Ga <sub>eq</sub>	2.79
Ga-Vo <sup>3</sup> -Ga <sub>eq</sub>	3.04

Ga-Vo <sup>3</sup> -Ga <sub>eq</sub>	3.06
Mg-Vo <sup>1</sup> -Ga <sub>eq</sub>	4.77
Ga-Vo <sup>3</sup> -Ga <sub>eq</sub>	4.90
Ga-Vo <sup>3</sup> -Ga <sub>eq</sub>	5.20
Mg-Vo <sup>1</sup> -Ga <sub>eq</sub>	5.46
<b>Mg-clustered</b>	
Mg-Vo <sup>1</sup> -Ga <sub>ax</sub>	0.00
Ga-Vo <sup>3</sup> -Ga <sub>ax</sub>	1.92
Ga-Vo <sup>3</sup> -Ga <sub>ax</sub>	2.07
Mg-Vo <sup>1</sup> -Mg <sub>eq</sub>	2.37
Ga-Vo <sup>3</sup> -Ga <sub>ax</sub>	5.66
Ga-Vo <sup>3</sup> -Ga <sub>eq</sub>	6.55
Ga-Vo <sup>1</sup> -Mg <sub>eq</sub>	7.07
Ga-Vo <sup>5</sup> -Ga <sub>eq</sub>	7.78
Ga-Vo <sup>5</sup> -Ga <sub>eq</sub>	8.91
<b>Mg, Ga-layered</b>	
Ga-Vo <sup>5</sup> -Ga <sub>ax</sub>	0.00
Ga-Vo <sup>3</sup> -Ga <sub>ax</sub>	0.48
Mg-Vo <sup>1</sup> -Ga <sub>ax</sub>	2.34
Ga-Vo <sup>5</sup> -Ga <sub>eq</sub>	3.45
Ga-Vo <sup>3</sup> -Ga <sub>eq</sub>	4.56
Mg-Vo <sup>1</sup> -Ga <sub>eq</sub>	6.52

### ***Local structure distortions***

In the following, we focus on the Mg-layered class, for which the smallest  $\Delta E$  range has been obtained (5.46 kcal/mol), considering only the three most stable (**Figures 4.4 a, 4.4 b and 4.4 c**) and the two less stable configurations (**Figures 4.4 e and 4.4 f**). M-O distances around

vacancy site (**Figure 4.5**),  $\text{Ga}_x\text{-O}_{ax}\text{-Ga}_x'$  tilting angles (**Figure 4.3 c, left** and **Figure 4.5 c** and **d**) and dihedral angles  $d_\beta$ ,  $d_\gamma$  and  $d_\delta$  (**Figure 4.3 c, right** and **Figure 4.5 e** and **f**), will be analyzed in the following sections.

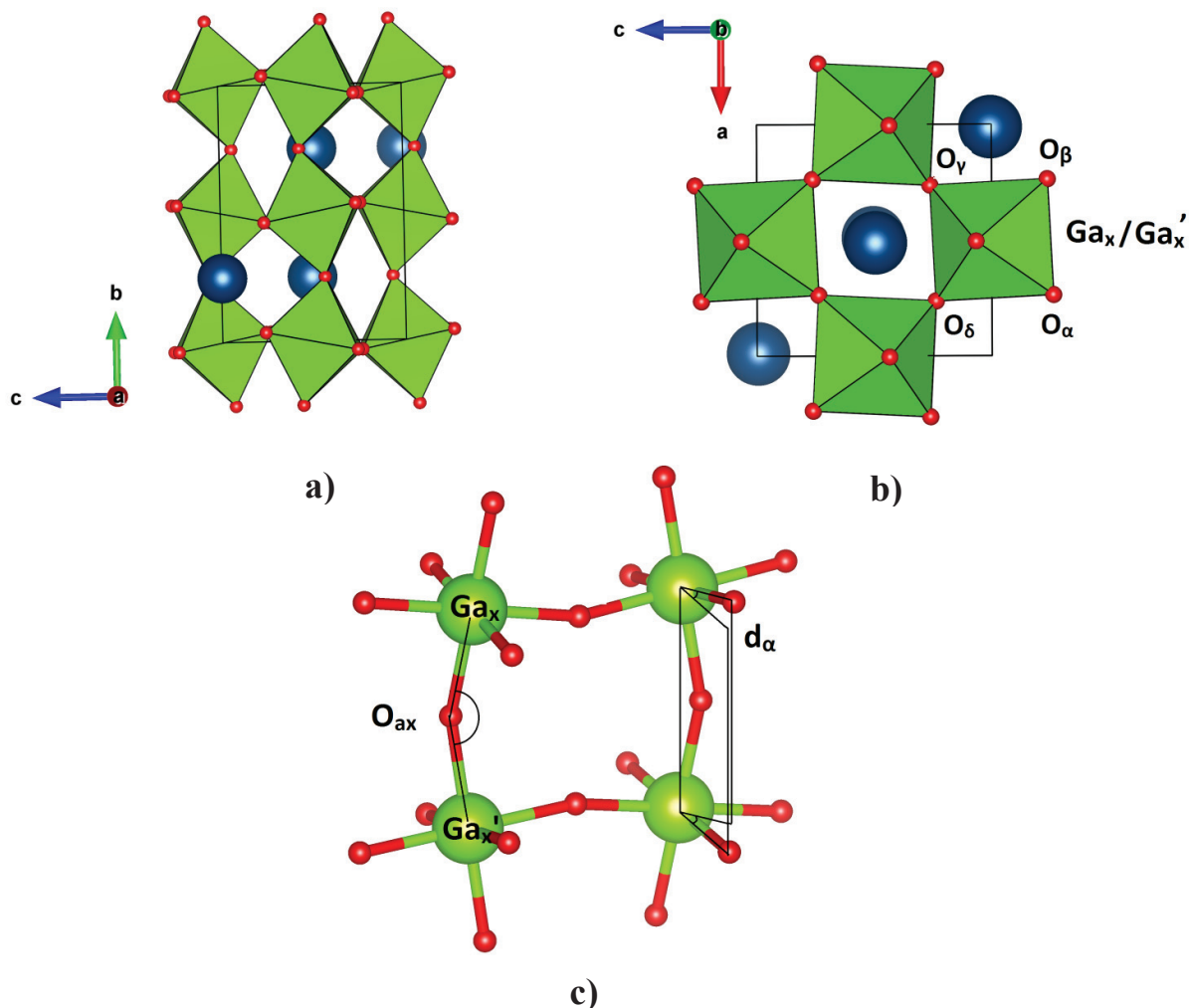


**Figure 4.3**  $Pbnm$  unit cell of LG viewed along the **a)**  $a$  axis and **b)**  $b$  axis. Equatorial oxygen atoms around  $\text{Ga}_x$  labeled as  $\text{O}_\alpha$ ,  $\text{O}_\beta$ ,  $\text{O}_\gamma$  and  $\text{O}_\delta$ . Gallium and equatorial oxygen atoms in the underlying layer are respectively labeled as  $\text{Ga}'_x$ ,  $\text{O}'_\alpha$ ,  $\text{O}'_\beta$ ,  $\text{O}'_\gamma$  and  $\text{O}'_\delta$ , taking as reference the view along the  $b$  axis, **c)** on the right: dihedral angle  $d_\alpha$  showing staggering between polyhedra related to  $\text{O}_\alpha$  ( $\text{O}_\alpha\text{-Ga-Ga}'\text{-O}_\alpha'$ ). The dihedral angles  $\text{O}_\beta\text{-Ga-Ga}'\text{-O}_\beta'$ ,  $\text{O}_\gamma\text{-Ga-Ga}'\text{-O}_\gamma'$  and  $\text{O}_\delta\text{-Ga-Ga}'\text{-O}_\delta'$ , will be respectively named  $d_\beta$ ,  $d_\gamma$  and  $d_\delta$ . On the left:  $\text{Ga-O}_{ax}\text{-Ga}'$  angles showing tilting between polyhedra. Ga polyhedra drawn in green, La atoms in blue and oxygen atoms in red.

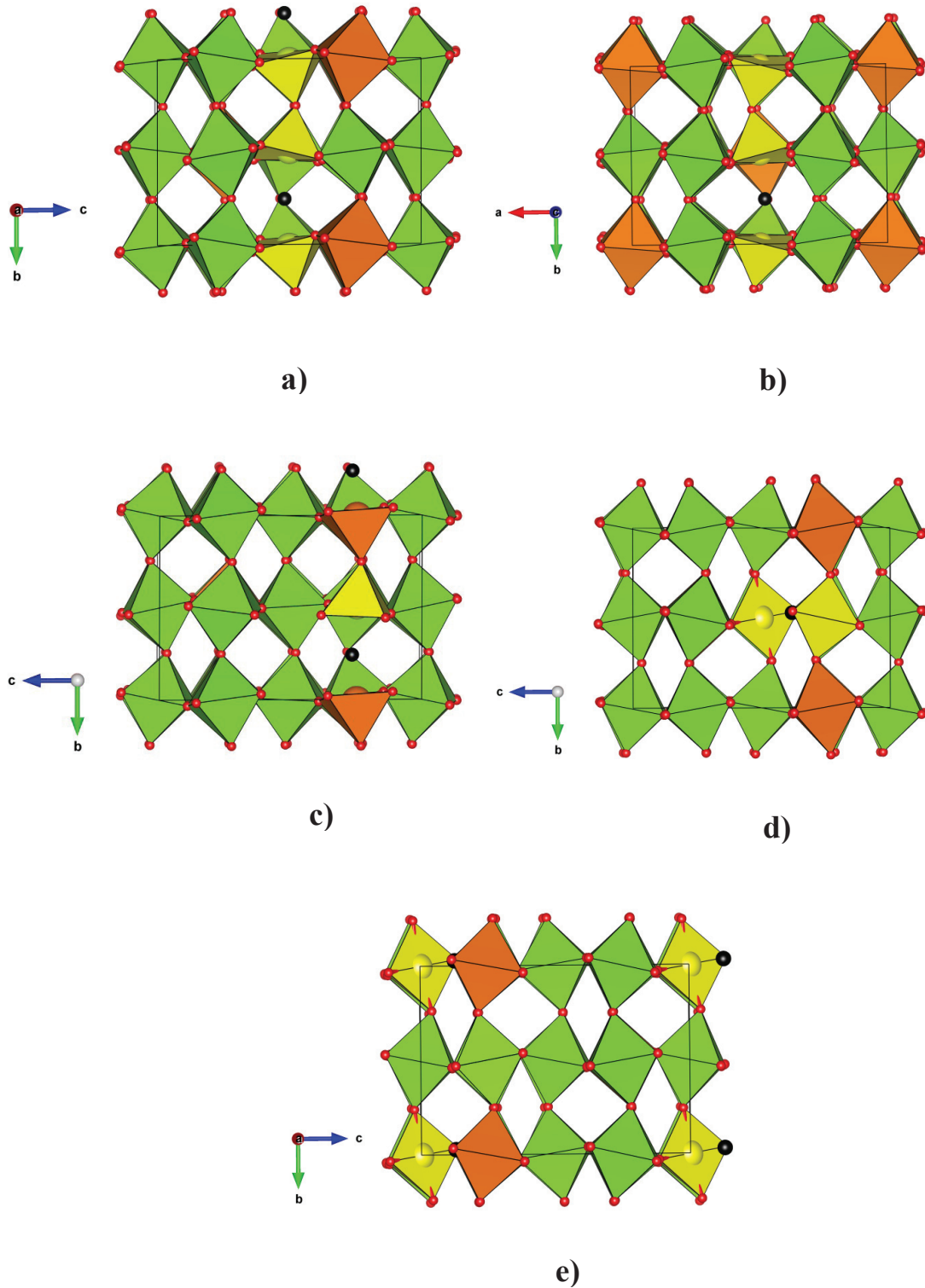


**Figure 4.4**  $(2 \times 1 \times 2)$  supercells (80 atoms) of the five configurations of the doped LGM0125 belonging to the Mg-layered macro-class considered for structural analysis: **a)**  $\text{Ga-Vo}^3\text{-Ga}_{\text{ax}}$ ; **b)**  $\text{Ga-Vo}^5\text{-Ga}_{\text{ax}}$ ; **c)**  $\text{Mg-Vo}^1\text{-Ga}_{\text{ax}}$ ; **d)**  $\text{Ga-Vo}^3\text{-Ga}_{\text{eq}}$ ; **e)**  $\text{Ga-Vo}^1\text{-Mg}_{\text{eq}}$ . Ga polyhedra are drawn in green, Ga polyhedra hosting the oxygen vacancy in yellow, Mg polyhedra in orange, oxygen atoms in red and vacancy site in black. La atoms are omitted for clarity.

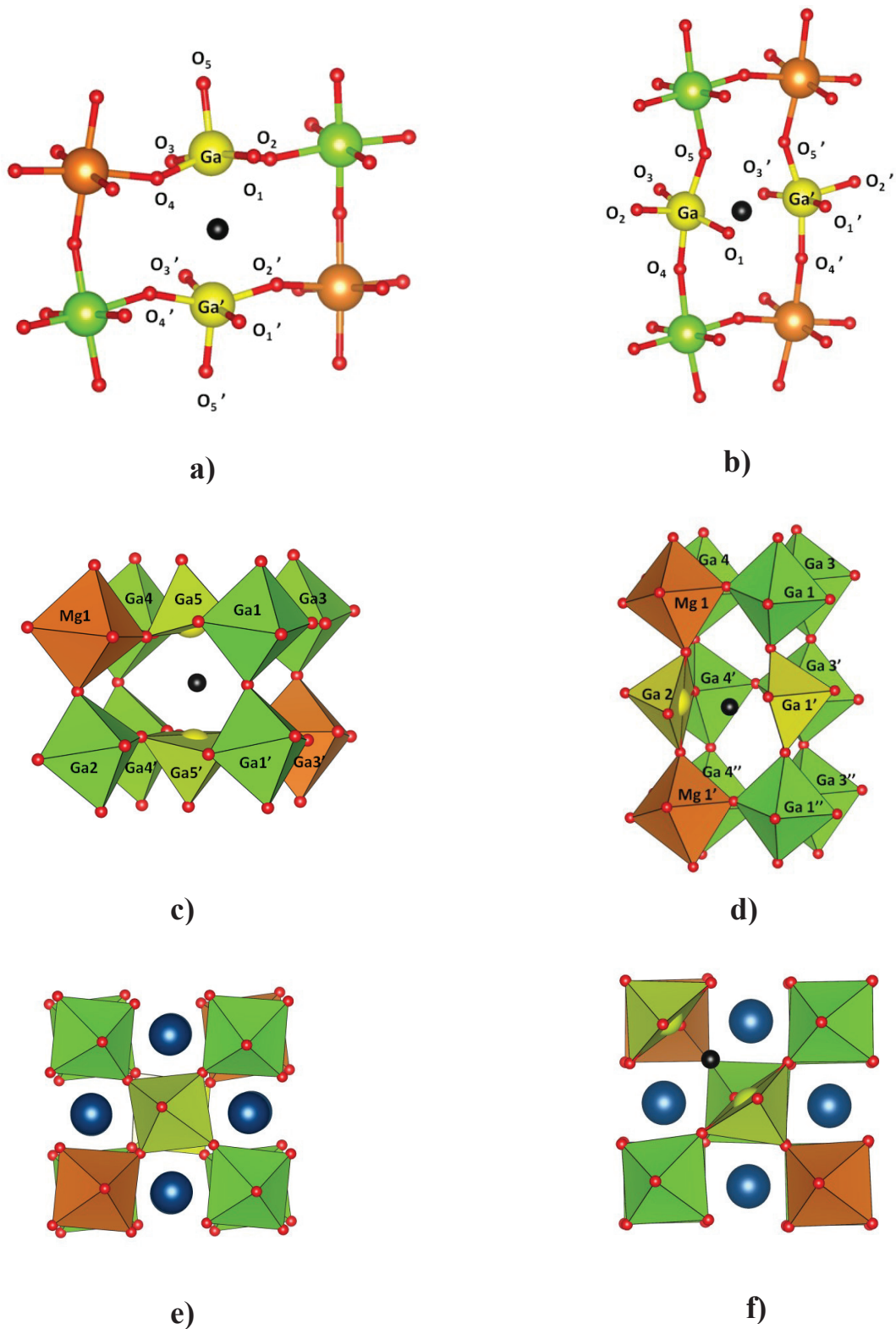


**Figure 4.5** a) Square pyramidal  $MO_5Vo$  site, drawn for a) the  $Ga-Vo^3-Ga_{ax}$  configuration, b)  $Ga-Vo^3-Ga_{eq}$ . A detailed picture of Ga-O distances and  $O_{ax}-M-O_{eq}$  is given in the **Supporting Information S.2**. Representation of Ga- $O_{ax}$ -Ga' tilting angles for c) the  $Ga-Vo^3-Ga_{ax}$  configuration, d)  $Ga-Vo^3-Ga_{eq}$ . Dihedral distortion causing octahedra mutual rotation along

the b axis for e) the Ga-Vo<sup>3</sup>-Ga<sub>ax</sub> configuration, f) Ga-Vo<sup>3</sup>-Ga<sub>eq</sub>. Ga atom hosting Vo in yellow, Ga octahedrally coordinated in green, Mg in orange and O in red.

### ***Square pyramidal MO<sub>5</sub>Vo site***

A common feature in the most stable Ga-Vo-Ga and Mg-Vo-Ga configurations, is that in Mg-layered LGM0125 both GaO<sub>5</sub>Vo and MgO<sub>5</sub>Vo polyhedra exhibit a square pyramidal local environment with an “umbrella-like” distortion, where equatorial oxygen-ions are heavily bent towards the vacancy site. (See **Figure 4.5 a and b**) From the DFT calculations, both axial and equatorial M-Vo-Ga (M=Mg,Ga) configurations show two main features: **a)** shortening of M-O distance opposite to the vacancy sites and **b)** increase of O<sub>ax</sub>-M-O<sub>eq</sub> bond angles with respect to undoped LaGaO<sub>3</sub>. In particular, all the configurations show three main M-O distances, at about 1.86 Å, 1.92 Å and 1.97 Å and three main O<sub>ax</sub>-M-O<sub>eq</sub> bond angles, at about 94.1°, 98.1° and 103.5°. The shortening of axial M-O distances can be related to the repulsive interaction between the two cations hosting the vacancy, that are placed at a larger distance (4.09-4.16 Å) in the doped compound. These cations tend to displace from their regular sites, while oxygen ions move towards the vacancy to minimize this repulsive interaction.

For all three axial configurations considered, M-O<sub>5</sub> axial distances generally correspond to the shortest M-O distances, while equatorial distances are split in **i)** two shorter distances M-O<sub>2</sub> and M-O<sub>4</sub> (M'-O<sub>2</sub>' and M'-O<sub>4</sub>') and **ii)** two longer distances M-O<sub>1</sub> and M-O<sub>3</sub> (M'-O<sub>1</sub>' and M'-O<sub>3</sub>'), except for the Mg-Vo<sup>1</sup>-Ga<sub>ax</sub> configuration, where Mg-O<sub>1</sub>', Mg-O<sub>2</sub>', Mg-O<sub>3</sub>' and Mg-O<sub>4</sub>' distances are around 1.96 Å. The vicinity of Mg with respect to the vacancy seems to lead to larger distortions of the local geometry around the vacancy. Indeed, in the case of Ga-Vo<sup>3</sup>-Ga<sub>ax</sub>, where Mg is 3<sup>rd</sup> neighbour to Vo, the local environment around the conducting site is less symmetric than in the case of Ga-Vo<sup>5</sup>-Ga<sub>ax</sub>, where Mg is 5<sup>th</sup> neighbour: in the first case, O<sub>ax</sub>-M-O<sub>eq</sub> angles are strongly different to each other, with only O<sub>4</sub> and O<sub>2</sub>' heavily bent towards the vacancy site with an angle of about 106°, while in the second case O<sub>2</sub>, O<sub>4</sub>, O<sub>2</sub>' and O<sub>4</sub>' are all bent towards the vacancy at about 105° (see **Table S.2.7** of the **Supporting Information S.2**). In the case of Mg-Vo<sup>1</sup>-Ga<sub>ax</sub> we have again only O<sub>2</sub> on Ga and the O<sub>4</sub>' on Mg bent towards the vacancy with a lower angle than in the Ga-Vo<sup>3</sup>-Ga<sub>ax</sub>.

For the two equatorial configurations considered, axial M-O<sub>2</sub> and M'-O<sub>2</sub>' distances are also strongly shortened. In Ga-Vo<sup>3</sup>-Ga<sub>eq</sub>, the Ga axially surrounded by two Mg has a more strained local environment, with Ga'-O<sub>4</sub>' and Ga'-O<sub>5</sub>' showing a very short distance at 1.86 Å and Ga'-O<sub>1</sub>' and Ga'-O<sub>3</sub>' a longer one at 1.98 Å. On the other side Ga axially surrounded by two

Ga atoms has all the Ga-O equatorial distances centred at 1.93 Å. Finally, the Mg-Vo<sup>1</sup>-Ga<sub>eq</sub> configuration present a more symmetric local environment, with all the Ga-O<sub>eq</sub> distances centred at 1.94 Å and all the Mg-O<sub>eq</sub> distances centred at 1.98 Å. In addition, both equatorial configurations considered show less markedly bent equatorial oxygen sites, with O<sub>ax</sub>-M-O<sub>eq</sub> angles between 98-102°.

All in all, oxygen ions are strongly bent towards the vacancy in the case of the three axial configurations considered, while they are less markedly bent in the case of the two less stable equatorial configurations. (See **Table S.2.7** of the **Supporting Information S.2**).

### ***Tilting and dihedral distortion***

Another noteworthy structural feature of doped lanthanum gallate concerns the distortion related to **a)** the Ga-O<sub>ax</sub>-M' bond angles (M'=Ga, Mg) (**Figure 4.5 c** and **d**), which describe the tilting along the *b* axis between corner sharing GaO<sub>6</sub> or MgO<sub>6</sub> octahedra, and **b)** the O<sub>eq</sub>-Ga-M'-O<sub>eq</sub>' dihedral angles referred to the *ac* plane of O<sub>eq</sub> of corner sharing octahedra. All data corresponding to tilting and dihedral angles computed are respectively reported in **Table S.2.8** and **Table S.2.9** of the **Supporting Information S.2**. Angles involved in tilting (Ga-O<sub>ax</sub>-Ga') and dihedral distortion (d<sub>α</sub>, corresponding to O<sub>α</sub>-Ga-Ga'-O<sub>α</sub>' dihedral angle) for undoped LG are represented in **Figure 4.3 c**.

In undoped LG (**Figure 1.a**), a marked tilting of GaO<sub>6</sub> octahedra, with Ga-O<sub>ax</sub>-Ga angle of about 159° was found in our calculations, which is slightly smaller than the experimental value arising by EXAFS data analysis (166°). Dihedral distortion between GaO<sub>6</sub> octahedra is absent in the undoped material, with a null O<sub>eq</sub>-Ga-Ga'-O<sub>eq</sub>' dihedral angle. When two Mg cations and one vacancy are simultaneously introduced in a (2x1x2) LG supercell, local effects on these angles appear due to the size mismatch between ionic radii on the octahedral B site (Ga<sub>VI</sub><sup>3+</sup>= 0.62 Å and Mg<sub>VI</sub><sup>2+</sup>=0.72 Å).

Two main effects can influence Ga-O<sub>ax</sub>-M' bond angles: **a)** the axial or equatorial position of the vacancy with respect to Ga or Mg; **b)** the proximity of Mg to the vacancy and to the other cation involved in the bond angle. While the first effect seems to have an influence on the energy of the system (axial vacancy configurations are generally more stable than equatorial ones), the proximity of Mg to the vacancy does not seem to affect the stabilization of the different configurations (e.g. axial Ga-Vo<sup>3</sup>-Ga<sub>ax</sub> and Ga-Vo<sup>5</sup>-Ga<sub>ax</sub> configurations having Mg



as 3<sup>rd</sup> or 5<sup>th</sup> neighbour with respect to the vacancy have the same stability), but seems to have a marked effect on the local distortions around the vacancy site.

When the vacancy is in axial position (favourite energetic condition), regardless of its location between two Ga atoms or between Ga and Mg, the Ga-O<sub>ax</sub>-M' tilting angles are always similar. For Ga-Vo<sup>3</sup>-Ga<sub>ax</sub> and Mg-Vo<sup>1</sup>-Ga<sub>ax</sub>, where Mg is 3<sup>rd</sup> and 1<sup>st</sup> neighbour with respect to the vacancy, two angle distributions can be found at about 157° and 162°, while for Ga-Vo<sup>5</sup>-Ga<sub>ax</sub>, where Mg is 5<sup>th</sup> neighbour, the tilting angles are centred at about 157°. In every case, the tilting computed in axial configurations is very similar to the one theoretically found for undoped LG, around 159°.

On the other hand, if the vacancy is in equatorial position, the local structure is much more strained and a large difference can be highlighted between Ga-O<sub>ax</sub>-M' tilting angles (See **Supporting Information S.2, Table S.2.9**). Equatorial Ga-Vo<sup>3</sup>-Ga<sub>eq</sub> and Mg-Vo<sup>1</sup>-Ga<sub>eq</sub> configurations show a distribution of three tilting angle values, of about 151°, 159° and 165°. In every case, LGM0125 theoretical tilting angles are in agreement with the experimentally found average value arising from EXAFS data analysis (161°).

Finally, dihedral distortions between adjacent corner sharing octahedra on the *ac* plane can also be evidenced for LGM0125 (see **Figure 4.3 c** and) and reported in **Table S.2.10** of the **Supporting Information S.2**. Dihedral distortions between octahedra are again dependent on the proximity of the Mg to the vacancy: they are present by the same amount (10-14°) only for axial Ga-Vo<sup>1</sup>-Mg<sub>ax</sub> and Ga-Vo<sup>3</sup>-Ga<sub>ax</sub> where Mg is 1<sup>st</sup> and 3<sup>rd</sup> neighbour with respect to the vacancy, while, for Ga-Vo<sup>5</sup>-Ga<sub>ax</sub> where Mg is 5<sup>th</sup> neighbour of the Vo, they are negligible (0.02 to 0.74°), almost like in undoped LG. Clearly, this result contrasts with tilting related to Ga-Vo-M' angles, where the strained angles can be found only in proximity of the vacancy.

### ***Electronic Structure***

In oxygen-ion conductors, when an acceptor dopant (e.g. Mg<sup>2+</sup> on Ga<sup>3+</sup> B-site) is introduced in the lattice to ensure the formation of oxygen vacancies, new electronic states are created close to edge of the conduction band. This leads to the formation of a new defect state in the band gap taking up some of the Mg electron density, and to a decrease of the electronic band gap when going from the undoped to the doped compound.<sup>32,33</sup> When electronic properties of such materials are accurately investigated and understood, hybrid functionals or other formulations correcting for self-interaction error are therefore required.<sup>34</sup> Few theoretical

calculations of the band gap for both undoped and doped LaGaO<sub>3</sub> have been reported so far in literature. (see Ref.<sup>32,35</sup> for some recent publications). A band gap value of 3.5 eV was reported for undoped LG in a previous DFT investigation performed at the PBE level,<sup>32</sup> which is in reasonable agreement with the PBE value obtained here (4.29 eV), especially if we are only interested in a qualitative comparison of the electronic structures of the different configurations. In the following, only PBE0 data for all density of states (DOS) and band gap calculations have been considered.

From **Table 4.4**, as expected, it is clear that the band gap energy decreases when going from undoped LG (7.10 eV) to the Mg-doped compound, with values ranging between 5.50 and 6.03 eV, the lowest band gaps being obtained for the two least stable equatorial configurations.

**Table 4.4** Computed PBE0 band gaps for undoped LG and five different configurations of the Mg-layered macro-class for LGM0125.

Compound	Configuration	Band Gap (eV)
LG	--	7.11
LGM0125 (Mg-layered)	Ga-Vo <sup>3</sup> -Ga <sub>ax</sub>	5.86
	Ga-Vo <sup>5</sup> -Ga <sub>ax</sub>	6.03
	Ga-Vo <sup>1</sup> -Mg <sub>ax</sub>	5.79
	Ga-Vo <sup>3</sup> -Ga <sub>eq</sub>	5.50
	Ga-Vo <sup>1</sup> -Mg <sub>eq</sub>	5.70

Since total and partial DOS show similar features for all the axial and equatorial vacancy configurations investigated for Mg-layered LGM0125, in **Figure 4.6** we only present DOS computed for undoped LG and the most-stable Ga-Vo<sup>3</sup>-Ga<sub>ax</sub> configuration of the Mg-layered macro-class of LGM0125. DOS of all other four configurations belonging to the Mg-layered macro-class are given as supplementary material.

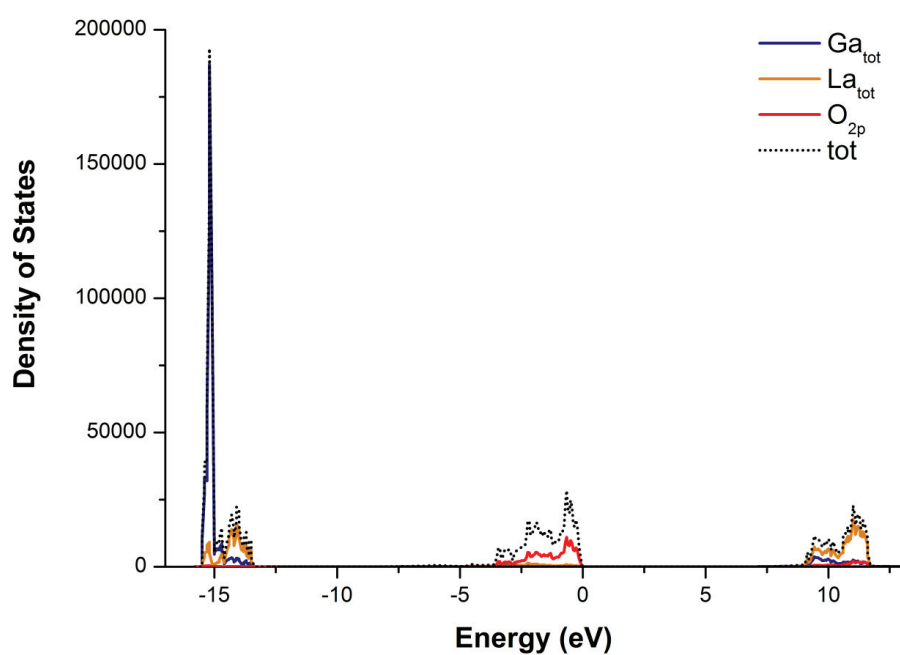
From **Figure 4.6**, it is clear that only subtle differences can be evidenced between undoped LG and the doped material. In particular, a small contribution around 6eV can be observed for the latter compound, corresponding to the O vacancies introduced in the material. In addition, the overlap between  $O_{2p}$  and  $Ga_{3d}$  or  $La_{3d}$  contributions is very small, suggesting a dominant ionic character of the Ga-O and La-O bonds. A weak overlap can be evidenced at the top of the valence band at around -15 eV. Another interesting feature arising from the DOS analysis is that the Ga total contribution ( $Ga_{tot}$ ) corresponds almost exactly to the  $Ga_{3d}$  one, suggesting that the 3d orbitals are the main contributors to the bonding with  $O_{2p}$  in LGM0125, the valence  $Ga_{4s}$  and  $Ga_{4p}$  orbitals having negligible contributions in the energy interval considered.

Interestingly,  $Ga_{3d}$  contribution of a Ga cation far from the Vo site ( $Ga_{3d}^f$ , where “f” means “far”) are shifted of about 0.5 eV at higher energies than those close to it ( $Ga_{3d}^c$ , where “c” means “close”). This can be related to the presence of the vacancy between two Ga atoms, which induces repulsion between these two cations, as they tend to be displaced from their regular sites due to a stronger interaction with the surrounding oxygen ions. This then leads to a larger Ga-Ga distance and shorter Ga-O bonds with respect to the undoped LG compound. On the other hand, if we compare the  $O_{2p}$  partial DOS of the 5 oxygen-ions group surrounding one Ga that host the Vo ( $O_{2p}^c$ ) with the group of 6 oxygen-ions surrounding a Ga far from the Vo ( $O_{2p}^f$ ), almost no significant differences can be evidenced in terms of position of the DOS contribution, suggesting that O atoms are too far from the vacancy for their contribution to the DOS to be significantly affected.

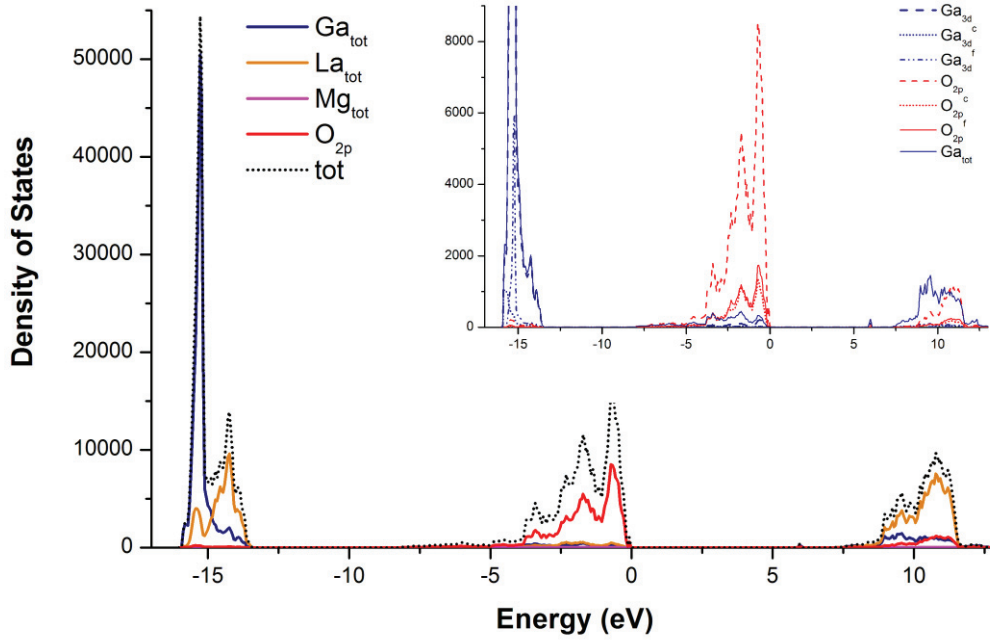
Finally, for all oxygen vacancy configurations investigated, we note that the averaged computed Mulliken atomic charges of 2.4, 1.4, 1.6 and -1.3 [ $e^-$ ] for La, Ga, Mg and O atoms, respectively, are very close to the values obtained for undoped LG, confirming the mostly ionic nature of the chemical bonds described previously. Some slight differences can however be evidenced when considering atoms as a function of their distance from the O vacancy. In particular, for Ga, from **Table 5**,  $Ga^f$  values are very similar to those of undoped LG while  $Ga^c$  ones have smaller values, due to the residual negative charge left on the vacancy site upon doping.

**Table 4.5** Mulliken atomic charges for the five configurations of the Mg-layered macro-class of LGM0125 considered, along with undoped LG. Gallium atoms far ( $\text{Ga}^f$ ) and close ( $\text{Ga}^c$ ) to the oxygen vacancy ( $\text{Vo}$ ) are considered for LGM0125.

SYSTEM	CONFIGURATION	$\text{Ga}^f$	$\text{Ga}^c$	Vo
LGM0125	$\text{Ga-Vo}^3\text{-Ga}_{\text{ax}}$	1.40	1.27	-0.12
	$\text{Ga-Vo}^5\text{-Ga}_{\text{ax}}$	1.37	1.28	-0.11
	$\text{Ga-Vo}^1\text{-Mg}_{\text{ax}}$	1.39	1.25	-0.17
	$\text{Ga-Vo}^3\text{-Ga}_{\text{eq}}$	1.38	1.22	-0.13
	$\text{Ga-Vo}^1\text{-Mg}_{\text{eq}}$	1.38	1.22	-0.18
		<b>Ga</b>		
LG	-	1.39		



a)



b)

**Figure 4.6** Total and partial PBE0 density of states of (a) undoped LG and (b) doped Ga-Vo<sup>3</sup>-Ga<sub>ax</sub>. The inset shows the atomic (Ga<sub>tot</sub>) and 3d (Ga<sub>3d</sub>) contributions of all Ga, those close (Ga<sub>3d<sup>c</sup></sub>) and far (Ga<sub>3d<sup>f</sup></sub>) from the O vacancy, as well as that of the 2p orbitals of all O atoms (O<sub>2p</sub>), and those close (O<sub>2p<sup>c</sup></sub>) and far (O<sub>2p<sup>f</sup></sub>) from the O vacancy.

### 3.2 Oxygen-ion diffusion paths in LaGa<sub>0.875</sub>Mg<sub>0.125</sub>O<sub>2.935</sub>

The oxygen-ion diffusion paths explored for the LGM0125 Mg-layered macro-class are drawn in **Figure 4.7**. Mg-Vo<sup>1</sup>-Ga<sub>eq</sub> and Ga-Vo<sup>5</sup>-Ga<sub>eq</sub> configurations have been chosen as starting point, in order to probe the diffusion paths around Mg and around Ga B-sites. To this end, relaxed scan calculations for one oxygen diffusing from its lattice position to the selected vacant site has been carried out. For each configuration, three paths (two “equatorial- to-equatorial” and one “axial-to-equatorial”) have been explored and the activation energy barriers (E<sub>a</sub>) have been evaluated and reported in **Table 4.6**.

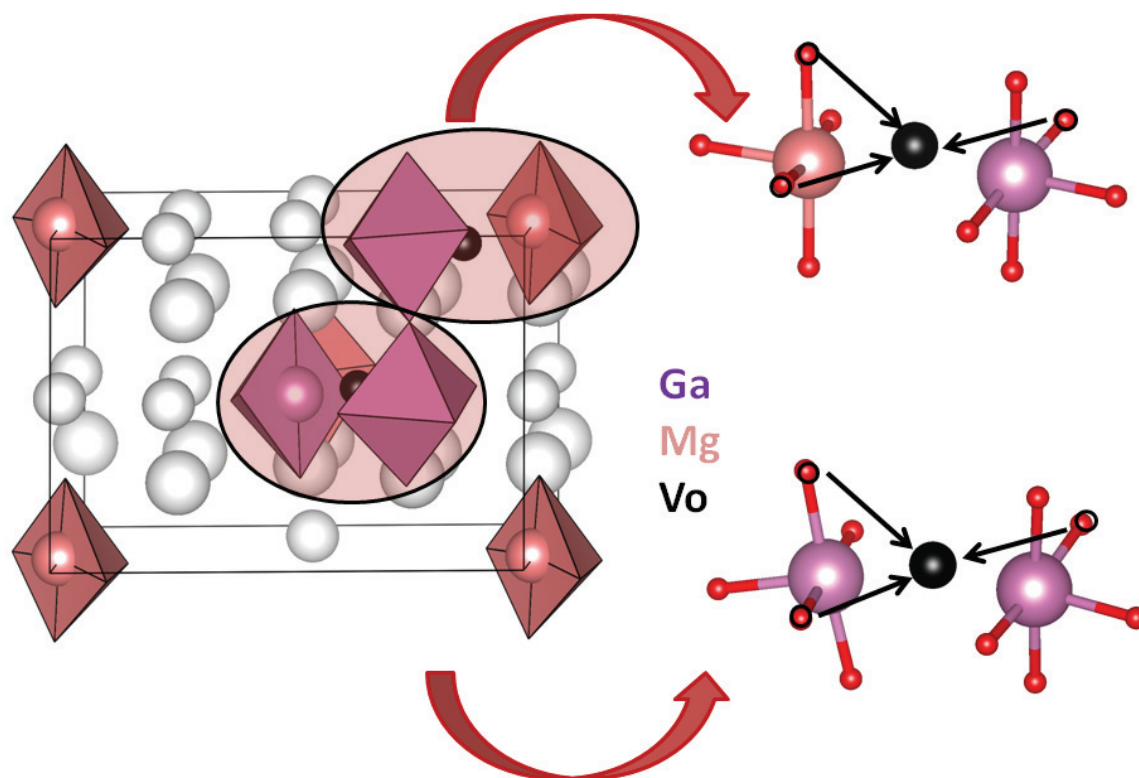


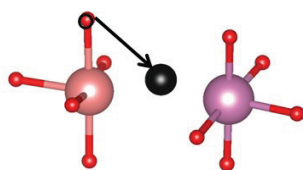
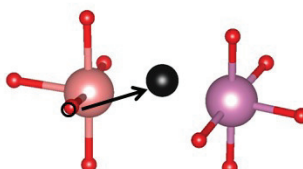
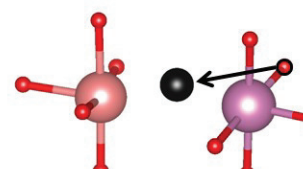
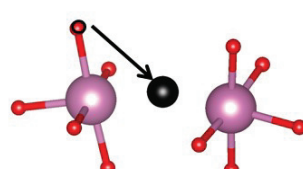
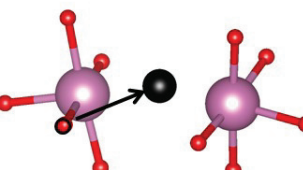
**Figure 4.7** oxygen-ion diffusion paths selected for 2x1x2 LGM0125 supercell. Mg are drawn in pink, Ga in purple and O in red. Atoms not involved in the considered diffusion path are depicted in grey for clarity. Black arrows indicate the direction of the diffusing ion.

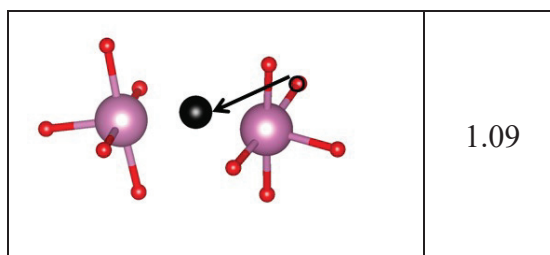
It is clear that the activation energy barrier is much larger for oxygen diffusion around Mg, with values ranging from 1.56 to 1.99 eV for the Mg-Vo<sup>1</sup>-Ga<sub>eq</sub> configuration. On the other side, the activation energy barrier is lower for the diffusion around Ga in Ga-Vo<sup>5</sup>-Ga<sub>eq</sub> configuration, with values from 0.99 eV to 1.17 eV.

In general, there is not a big energy difference between the diffusion from an axial site to an equatorial one or from an equatorial site to another equatorial site, but a significant difference can be found between diffusion around Ga site, which seems much favoured, and Mg site. This feature can be attributed to the higher local distortions around Mg sites, previously discussed in **Section 3.1**, which are found to affect the equivalence of oxygen-ion conducting sites.

Diffusion paths are underway to be tested also for the Ga-Vo<sup>3</sup>-Ga configuration, where Mg is 3rd neighbour with respect to the vacancy, in order to compare with the conducting sites depicted in the previous Section.

**Table 4.6** Activation energy barrier (Ea) in eV for the analyzed oxygen-ion diffusion paths. Again, Mg is drawn in pink, Ga in purple and O in red. Black arrows indicate the direction of the diffusing ion.

Oxygen-ion diffusion path	Ea (eV)
	1.99
	1.86
	1.56
	1.17
	0.99



### 3.3 Effect of doping and co-doping on LaGaO<sub>3</sub> perovskite-like structure

In Sections 3.1 and 3.2 the effect of Mg doping on the B-site in term of local distortions, interaction between vacancy and B-site cations and favoured oxygen-ion diffusion paths has been evaluated by computational modelling limited to B-site doping. Nevertheless, it is extremely important to evaluate the local structural features of the La<sub>1-x</sub>Sr<sub>x</sub>Ga<sub>1-y</sub>Mg<sub>y</sub>O<sub>3-δ</sub> and La<sub>1-x</sub>Sr<sub>x</sub>Ga<sub>1-y</sub>(Mg,Co)<sub>y</sub>O<sub>3-δ</sub> electrolytes, that show the highest ionic conductivity at intermediate temperatures.

To this end, the Ga K-edge EXAFS data analysis is reported in this section, with the aim to draw a complete picture about:

- the structural effects induced by the simultaneous doping of the A- and B-site of LaGaO<sub>3</sub>;
- the structural effect of Mg and Co B-site co-doping.

These features are related to the functional properties of the materials and some perspectives about further development of the study are given.

Moreover, static and *in situ* XAS data, acquired at the Co K-edge, are collected in order to assess the effect on the Co electronic structure of SOFC operative temperatures.

**Table 4.7** shows the results concerning X-Ray Diffraction characterization. The long range structure of these compositions is strongly affected by Sr concentration. Indeed, compositions with 20%mol of Sr in the A site belongs to *R-3c* rhombohedral space group (**Figure 4.8 b**), while under this concentration the materials retain the *Pbnm* orthorhombic structure (**Figure 4.8 a**), typical of undoped LG (See **Supporting information S.2**).



**Table 4.7** Space group for LSGM and LSGMC samples from XRD characterization.

SAMPLE	FORMULA	SPACE GROUP
LSGM1020	$\text{La}_{0.9}\text{Sr}_{0.1}\text{Ga}_{0.8}\text{Mg}_{0.2}\text{O}_{2.85}$	Pbnm
LSGM2020	$\text{La}_{0.8}\text{Sr}_{0.2}\text{Ga}_{0.8}\text{Mg}_{0.2}\text{O}_{2.80}$	R3-c
LSGMC0505	$\text{La}_{0.95}\text{Sr}_{0.05}\text{Ga}_{0.8}\text{Mg}_{0.15}\text{Co}_{0.05}\text{O}_{2.875}$	Pbnm
LSGMC1005	$\text{La}_{0.9}\text{Sr}_{0.1}\text{Ga}_{0.8}\text{Mg}_{0.15}\text{Co}_{0.05}\text{O}_{2.85}$	Pbnm
LSGMC2005	$\text{La}_{0.8}\text{Sr}_{0.2}\text{Ga}_{0.8}\text{Mg}_{0.15}\text{Co}_{0.05}\text{O}_{2.80}$	R-3c + two different segregation
LSGMC2010	$\text{La}_{0.8}\text{Sr}_{0.2}\text{Ga}_{0.8}\text{Mg}_{0.1}\text{Co}_{0.1}\text{O}_{2.80}$	R-3c (P4-21m melilite <4%)

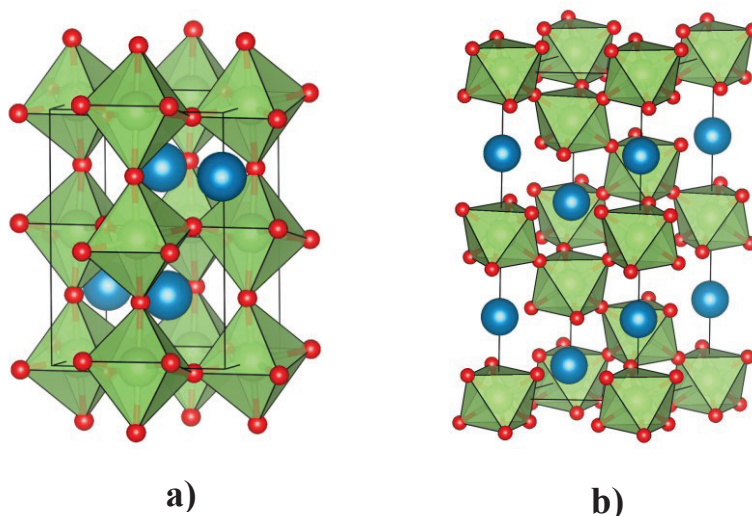
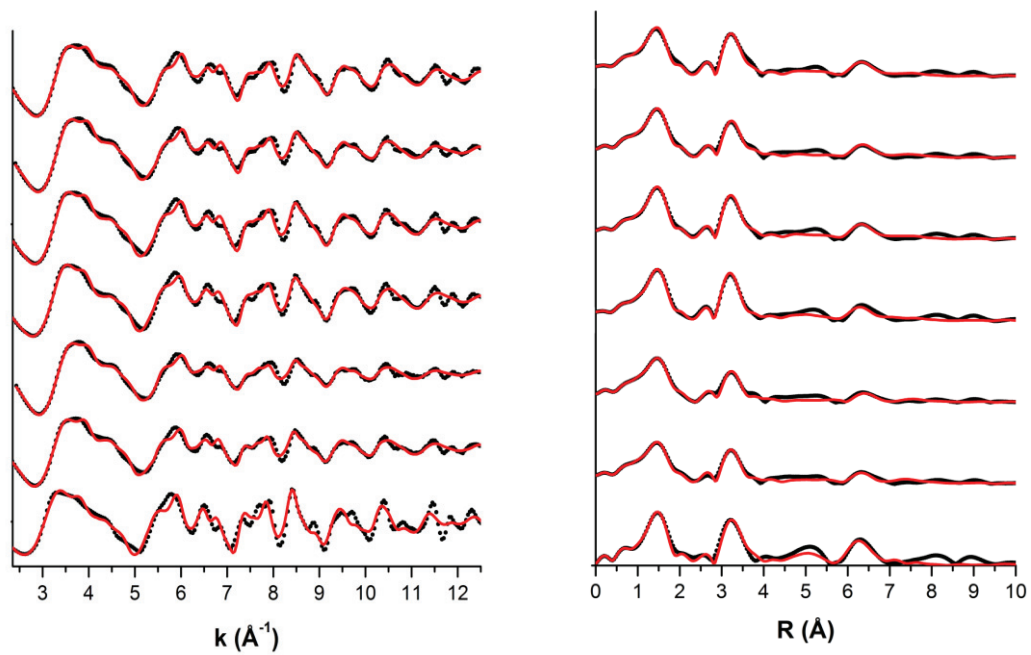


**Figure 4.8** a) orthorhombic *Pbnm* and b) rhombohedral *R-3c* unit cells. Ga polyhedra are depicted in green, La in blue and oxygen in red.

EXAFS data analysis on Ga K-edge (**Table 4.8, Figure 4.9**) was carried out using exactly the same model previously described for the modelling of LG and LGM0125. The results concerning the Ga-O-M (M=Ga, Mg or Co) environment reveal that both doping the A-site with Sr and co doping the B-site with Co have an influence on the octahedra tilting angles. On one hand, it can be observed that compositions without cobalt co-doping (LSGM1020 and LSGM2020) exhibit similar tilting angles centred at  $173^\circ$  and  $170^\circ$ , regardless of the different Sr concentrations. On the other hand, compositions with cobalt co-doping, where the sum of Mg and Co concentrations is always fixed to 20%mol, behave in a different way: for example, in LSGMC0505 and LSGMC2005, that contain the same amount of Co (5%mol), but different amounts of Sr (respectively, 5 and 20%mol), Ga-O-M tilting angle significantly increase from  $157$  to  $171^\circ$ . This angle further increase from LSGMC2005 to LSGMC2010 from  $171$  to  $178^\circ$ , where the increased amount of Co from 5 to 10%mol seems to further

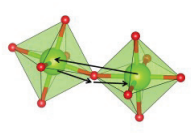
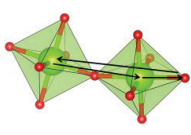
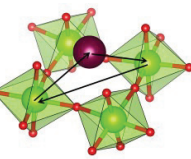
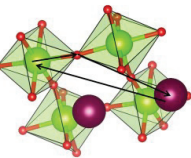
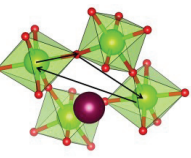
lower the distortion. Except for LSGM0505, these values are higher than the average Ga-O-M tilting angle of  $161^\circ$  found for the optimized rhombohedral unit cell of undoped LG and it is in line with previous studies about the perovskite-like  $\text{LaCoO}_3$ ,<sup>36</sup> where it is found that Sr doping on La A-site can attenuate the rhombohedral distortion, improving the Co-O-Co alignment. The decrease in tilting angle would be induced by the higher ionic radius of Sr ( $1.58 \text{ \AA}$ ) compared to La ( $1.50 \text{ \AA}$ ) in  $\text{LaCoO}_3$ , even if in our system a further effect could be attributed to the increased Co concentration.

As previously seen in **Section 4.1**, compositions with Co concentration  $\leq$  to 10%mol are optimal for electrolyte conductivity. In particular LSGMC2005 and LSGMC2010 have the highest activation energy barriers for electronic conductivity (0.30-0.35 eV) at low temperatures, and can be used as improved electrolytes with lower ohmic resistance and overpotential<sup>11,12</sup>. In these compositions Ga-O-M tilting angle values was respectively found at about  $170^\circ$  and  $178^\circ$ : this would suggest that, as previously deduced from the configurational study performed for LGM0125, a decrease of the local distortions around perovskite B-site, with a better alignment of adjacent octahedra could be one of the promoting factors for evenly distributed oxygen-ion diffusion paths inside the electrolyte, due to the enhancement of the energetic equivalence of oxygen sites.



**Figure 4.9** From the bottom to the top: EXAFS signal (left panel) and Fourier Transform (right panel) of pure LG, LSGM1020, LSGM2010, LSGMC0505, LSGMC1005, LSGMC2005, LSGMC2010. Data are drawn as black circles and model as a red line.

**Table 4.8** Results for the EXAFS data analysis at Ga K-edge ( $R$  in Å,  $\sigma^2$  and  $s^2$  in Å<sup>2</sup> and  $\vartheta$  in °), with the corresponding MS paths (Ga atoms and polyhedra drawn in green, O in red and La atoms in purple). Debye-Waller factors related to the two-body distances are labelled with  $\sigma^2$ , while those related to the MS paths are labelled with  $s^2$ .

			LG	LSGM 1020	LSGM 2020	LSGMC 0505	LSGMC 1005	LSGMC 2005	LSGMC 2010
	Ga-O	$R_1$	1.95	1.93	1.94	1.94	1.94	1.93	1.93
		$\sigma_1^2$	0.0058	0.0100	0.0098	0.0070	0.0070	0.0082	0.0083
	Ga-La	$R_2$	3.42	3.41	3.41	3.39	3.40	3.41	3.40
		$\sigma_2^2$	0.0087	0.0094	0.0107	0.0083	0.0084	0.0093	0.0080
<b>MULTIPLE SCATTERING</b>									
	Ga-O-M	$\vartheta_1$	166	173	170	157	164	171	178
		$s_1^2$	1	1	2	1	1	1	1
	Ga-Ga-O	$\vartheta_2$	150	156	156	151	153	155	153
		$s_2^2$	1	2	10	5	2	10	10
	Ga-La-M	$\vartheta_3$	108	109	109	109	108	108	108
		$s_3^2$	1	3	10	4	7	6	5
	Ga-O-La	$\vartheta_4$	112	114	115	113	113	113	113
		$s_4^2$	1	2	3	2	2	2	3
	Ga-O-M	$\vartheta_5$	154	159	159	155	156	156	155
		$s_5^2$	10	10	10	10	10	10	10

XAS measurements on these samples were acquired also at the Co K-edge. EXAFS data modelling of Co local environment, together with XANES spectra simulations are currently under analysis, in order to unravel the role of cobalt local environment in the oxygen-ion conductivity of the material. For what concerns XANES spectra (**Figure 4.10**), all the samples show edge features typical of  $\text{Co}^{3+}$  in a  $\text{LaCoO}_3$ -type environment.<sup>36,37</sup> The main absorption (edge position at about 7725 eV) can be attributed to the  $1s \rightarrow 4p$  transition. Moreover, the near edge spectra show two pre-edge features appearing below 7715 eV, that can be attributed to  $\text{Co}^{3+} 1s \rightarrow 3d$  transitions: these two features are probably related to the splitting of 3d orbitals in  $t_{2g}$  and  $e_g$  orbitals, according to the octahedral crystal field.<sup>36</sup>

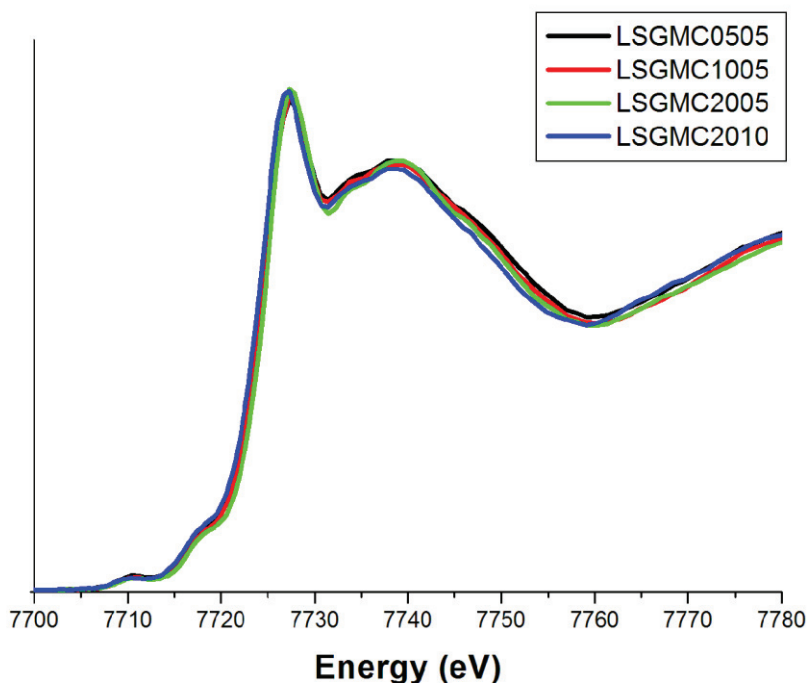
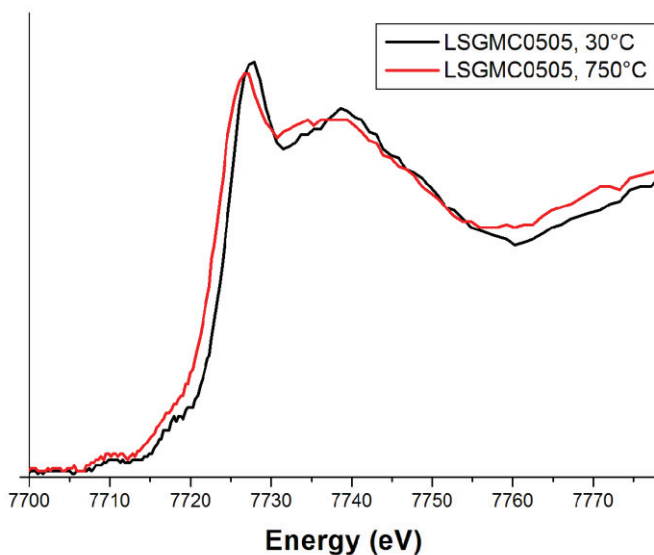


**Figure 4.10** XANES spectra of co-doped samples acquired at Co K-edge (77 K).

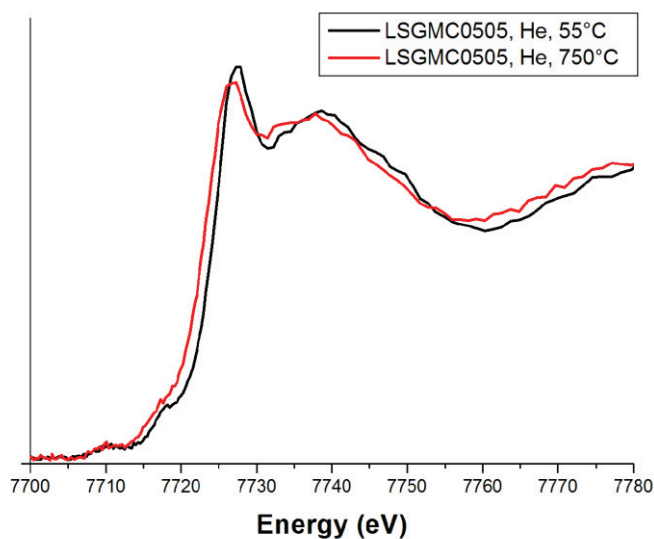
The Co K-edge *in situ* XAS experiments on the  $\text{La}_{1-x}\text{Sr}_x\text{Ga}_{1-y}(\text{Mg},\text{Co})_y\text{O}_{3-\delta}$  electrolytes yielded useful data to the aim of studying the influence of Co dopant on the electronic structure and the oxygen-ion diffusion in the temperature range 25-750°C (IT-SOFC operating temperature).

As the temperature increases, an edge shift towards lower energies ranging from 0.43 eV to 1.6 eV can be found, with LSGMC0505 having the larger shift both in air (1.3 eV) and in He

atmosphere (1.6 eV) (**Figure 4.11 a and 4.11 b**). This result is compatible with a low spin ( $t_{2g}^6 e_g^0$ ) to high spin ( $t_{2g}^4 e_g^2$ ) transition in the  $\text{Co}^{3+}$  electronic structure.<sup>38</sup> Further analysis is underway in terms of XANES simulation, in order to model Co K-edge transitions and study the electronic structure of the material.



a)



b)

**Figure 4.11** XANES spectra at different temperatures on Co K-edge acquired for LSGMC0505 a) in air and b) in He atmosphere.

## 4. Conclusions

In this chapter a comprehensive XAS and DFT study about perovskite-like lanthanum gallate has been presented, with the aim to understand the vacancy interaction with the B-site cations, the favoured oxygen-ion diffusion paths and the influence of doping and co-doping on the local structure and the electronic features around perovskite B-site.

In **Section 3.1** a comprehensive investigation of the B-site interaction with oxygen vacancy defects in perovskite-type LGM0125 using a combined DFT, EXAFS and XRD approach has been reported. Through EXAFS analysis, the average bond distances, disorder factors and MS bond angles were characterized, resulting in an increasing of Ga-O-M tilting between  $\text{GaO}_6$  octahedra upon B-site substitution. The DFT simulations of specific defective sites allowed overcoming the average picture provided by EXAFS and in particular the preferential distribution of oxygen vacancies around Ga was confirmed.

To probe the structural features and local distortions of the conducting site, and to find the most stable Mg dopant configurations, the DFT approach was combined with a comprehensive configurational analysis based on symmetry-independent classes. Among the three macro-classes evidenced, the Mg-layered one showed the narrower energy range for all configurations generated and hence an overall greater equivalence of conductive sites, which might potentially enhance oxide conductivity.

Simulations of defective sites of type Ga-Vo-Mg and Ga-Vo-Ga, belonging to the Mg-layered class, evidenced umbrella-like distortions, characterized by oxygen-ions heavily bent towards the vacancy site. Both axial and equatorial oxygen vacancy arrangements were considered, and the former were found the most stable. This evidence was explained by local distortion arguments involving tilting and dihedral distortions around the conducting site related to the position of Mg with respect to the oxygen vacancy.

The electronic structure investigation highlighted a prevailing ionic character of the Ga-O bond, dominated by  $\text{Ga}_{3d}$  and  $\text{O}_{2p}$  orbitals, with only minor differences between the parent undoped LG compound and the doped material.

In conclusion, the computational approach reported in **Section 3.1** clarifies the structural rearrangements involved by the insertion of  $\text{Mg}^{2+}$  in the B-site of lanthanum gallate.

Basing on these results, in **Section 3.2** oxygen-ion diffusion paths have been investigated for the Mg-layered configuration of LGM0125, in order to clarify the influence of B-site cation on the ionic conductivity. From the activation energy values it is clear that diffusion is much favoured around Ga sites, while it is hindered around Mg dopant. This could be connected to the higher degree of distortion found around Mg site, that lowers the energetic equivalence of oxygen sites.

Finally, in **Section 3.3** the influence of Sr doping on the A-site and co-doping with Mg and Co on the local structure features around Ga B-site in the complete  $\text{La}_{1-x}\text{Sr}_x\text{Ga}_{1-y}\text{Mg}_y\text{O}_{3-\delta}$  and  $\text{La}_{1-x}\text{Sr}_x\text{Ga}_{1-y}(\text{Mg},\text{Co})_y\text{O}_{3-\delta}$  electrolytes has been probed. Compositions without cobalt co-doping (LSGM1020 and LSGM2020) exhibit similar tilting angles centred at  $173^\circ$  and  $170^\circ$ , while compositions with cobalt co-doping, where the sum of Mg and Co concentrations is always fixed to 20%mol, behave in a different way: in LSGMC0505 and LSGMC2005, Ga-O-M tilting angle significantly increase from  $157^\circ$  to  $171^\circ$ . This angle further increases (from  $171^\circ$  to  $178^\circ$ ) going from LSGMC2005 to LSGMC2010, showing that the increased amount of Co further attenuates the distortion and likely favours oxygen-ion conductivity due to more evenly distributes diffusion paths within the LG matrix.

XANES data taken at 77K and *in situ* ( $25\text{--}750^\circ\text{C}$ ,  $10^\circ\text{C}/\text{min}$ ) at the Co K-edge have been also presented. These XANES spectra allow to determine that Co is present in the LG matrix as  $\text{Co}^{3+}$ . The shift towards lower energy, observed as the temperature increases, is compatible with a LS $\rightarrow$ HS transition, with the maximum shift observed for LSGMC0505 sample. This preliminary interpretation, that should be corroborated by Co K-edge simulations, allows to obtain information about the electronic structure of cobalt co-dopant at low and IT operative temperature, useful for further computational analyses.

## 5. References

- (1) Fergus, J. W. Electrolytes for Solid Oxide Fuel Cells. *J. Power Sources* **2006**, *162* (1), 30–40.
- (2) Kharton, V. V; Marques, F. M. B.; Atkinson, A. Transport Properties of Solid Oxide Electrolyte Ceramics: A Brief Review. *Solid State Ionics* **2004**, *174* (1–4), 135–149.



- (3) Hui, S.; Roller, J.; Yick, S.; Zhang, X.; Decès-Petit, C.; Xie, Y.; Maric, R.; Ghosh, D. A Brief Review of the Ionic Conductivity Enhancement for Selected Oxide Electrolytes. *J. Power Sources* **2007**, *172* (2), 493–502.
- (4) Malavasi, L.; Fisher, C. A. J.; Islam, M. S. Oxide-Ion and Proton Conducting Electrolyte Materials for Clean Energy Applications: Structural and Mechanistic Features. *Chem. Soc. Rev.* **2010**, *39* (11), 4370–4387.
- (5) Morales, M.; Roa, J. J.; Tartaj, J.; Segarra, M. A Review of Doped Lanthanum Gallates as Electrolytes for Intermediate Temperature Solid Oxides Fuel Cells: From Materials Processing to Electrical and Thermo-Mechanical Properties. *J. Eur. Ceram. Soc.* **2016**, *36* (1), 1–16.
- (6) Morales, M.; Roa, J. J.; Perez-Falcón, J. M.; Moure, A.; Tartaj, J.; Espiell, F.; Segarra, M. Correlation between Electrical and Mechanical Properties in  $\text{La}_{1-x}\text{Sr}_x\text{Ga}_{1-y}\text{Mg}_y\text{O}_{3-\delta}$  Ceramics Used as Electrolytes for Solid Oxide Fuel Cells. *J. Power Sources* **2014**, *246*, 918–925.
- (7) Ishihara, T.; Matsuda, H.; Takita, Y. Doped  $\text{LaGaO}_3$  Perovskite Type Oxide as a New Oxide Ionic Conductor. *J. Am. Chem. Soc.* **1994**, *116* (9), 3801–3803.
- (8) Feng, M.; Goodenough, J. B. A Superior Oxide-Ion Electrolyte. *Eur. J. solid state Inorg. Chem.* **1994**, *31* (8–9), 663–672.
- (9) Huang, P.; Petric, A. Superior Oxygen Ion Conductivity of Lanthanum Gallate Doped with Strontium and Magnesium. *J. Electrochem. Soc.* **1996**, *143* (5), 1644–1648.
- (10) Yang, N.; D’Epifanio, A.; Di Bartolomeo, E.; Pugnolini, C.; Tebano, A.; Balestrino, G.; Licoccia, S.  $\text{La}_{0.8}\text{Sr}_{0.2}\text{Ga}_{0.8}\text{Mg}_{0.2}\text{O}_{3-\delta}$  Thin Films for IT-SOFCs: Microstructure and Transport Properties Correlation. *J. Power Sources* **2013**, *222*, 10–14.
- (11) Wang, S.-Z. High Performance Fuel Cells Based on  $\text{LaGaO}_3$  Electrolytes. *Acta Phys. - Chim. Sin.* **2004**, *20* (1).
- (12) Stevenson, J. W.; Hasinska, K.; Canfield, N. L.; Armstrong, T. R. Influence of Cobalt and Iron Additions on the Electrical and Thermal Properties of  $(\text{La}, \text{Sr})(\text{Ga}, \text{Mg})\text{O}_{3-\delta}$ . *J. Electrochem. Soc.* **2000**, *147* (9), 3213–3218.
- (13) Trofimenko, N.; Ullmann, H. Transition Metal Doped Lanthanum Gallates. *Solid State Ionics* **1999**, *118* (3–4), 215–227.

- (14) Blanc, F.; Middlemiss, D. S.; Gan, Z.; Grey, C. P. Defects in Doped LaGaO<sub>3</sub> Anionic Conductors: Linking NMR Spectral Features, Local Environments, and Defect Thermodynamics. *J. Am. Chem. Soc.* **2011**, *133* (44), 17662–17672.
- (15) Khan, M. S.; and M. S. Islam; Bates, D. R. Dopant Substitution and Ion Migration in the LaGaO<sub>3</sub>-Based Oxygen Ion Conductor. *J. Phys. Chem. B* **1998**, *102* (17), 3099–3104.
- (16) Islam, M. S.; Davies, R. A. Atomistic Study of Dopant Site-Selectivity and Defect Association in the Lanthanum Gallate Perovskite. *J. Mater. Chem.* **2004**, *14* (1), 86–93.
- (17) Islam, M. S. Ionic Transport in ABO<sub>3</sub> Perovskite Oxides: A Computer Modelling Tour. *J. Mater. Chem.* **2000**, *10* (4), 1027–1038.
- (18) Filippini, A.; Di Cicco, A.; Natoli, C. R. X-Ray-Absorption Spectroscopy and N-Body Distribution Functions in Condensed Matter. I. Theory. *Phys. Rev. B* **1995**, *52* (21), 15122.
- (19) Filippini, A.; Di Cicco, A. X-Ray-Absorption Spectroscopy and N-Body Distribution Functions in Condensed Matter. II. Data Analysis and Applications. *Phys. Rev. B* **1995**, *52* (21), 15135.
- (20) Larson, A. C.; Von Dreele, R. B. GSAS Manual (Los Alamos Natl. Lab., Los Alamos, NM). *Rep. LAUR* **1988**, *86*, 748.
- (21) Dovesi, R.; Orlando, R.; Erba, A.; Zicovich-Wilson, C. M.; Civalleri, B.; Casassa, S.; Maschio, L.; Ferrabone, M.; De La Pierre, M.; D’Arco, P.; et al. CRYSTAL14: A Program for the Ab Initio Investigation of Crystalline Solids. *Int. J. Quantum Chem.* **2014**, *114* (19), 1287–1317.
- (22) Adamo, C.; Barone, V. Toward Reliable Density Functional Methods without Adjustable Parameters: The PBE0 Model. *J. Chem. Phys.* **1999**, *110* (13), 6158–6170.
- (23) Ernzerhof, M.; Scuseria, G. E. Assessment of the Perdew-Burke-Ernzerhof Exchange-Correlation Functional. *J. Chem. Phys.* **1999**, *110* (11), 5029–5036.
- (24) Evarestov, R. A.; Kotomin, E. A.; Mastrikov, Y. A.; Gryaznov, D.; Heifets, E.; Maier, J. Comparative Density-Functional LCAO and Plane-Wave Calculations of LaMnO<sub>3</sub> Surfaces. *Phys. Rev. B* **2005**, *72* (21), 214411.

- (25) Peintinger, M. F.; Oliveira, D. V.; Bredow, T. Consistent Gaussian Basis Sets of Triple-Zeta Valence with Polarization Quality for Solid-State Calculations. *J. Comput. Chem.* **2013**, *34* (6), 451–459.
- (26) Barthelat, J. C.; Durand, P.; Serafini, A. Non-Empirical Pseudopotentials for Molecular Calculations: I. The PSIBMOL Algorithm and Test Calculations. *Mol. Phys.* **1977**, *33* (1), 159–180.
- (27) Berthelat, J. C.; Durand, P. Recent Progress of Pseudopotential Methods in Quantum Chemistry. *Gazz. Chim. Ital.* **1978**, *108* (5–6), 225–236.
- (28) Mustapha, S.; D’Arco, P.; De La Pierre, M.; Noël, Y.; Ferrabone, M.; Dovesi, R. On the Use of Symmetry in Configurational Analysis for the Simulation of Disordered Solids. *J. Phys. Condens. Matter* **2013**, *25* (10), 105401.
- (29) D’Arco, P.; Mustapha, S.; Ferrabone, M.; Noël, Y.; De La Pierre, M.; Dovesi, R. Symmetry and Random Sampling of Symmetry Independent Configurations for the Simulation of Disordered Solids. *J. Phys. Condens. Matter* **2013**, *25* (35), 355401.
- (30) Giannici, F.; Gregori, G.; Aliotta, C.; Longo, A.; Maier, J.; Martorana, A. Structure and Oxide Ion Conductivity: Local Order, Defect Interactions and Grain Boundary Effects in Acceptor-Doped Ceria. *Chem. Mater.* **2014**, *26* (20), 5994–6006.
- (31) Laulhé, C.; Hippert, F.; Kreisel, J.; Maglione, M.; Simon, A.; Hazemann, J. L.; Nassif, V. EXAFS Study of Lead-Free Relaxor Ferroelectric  $\text{BaTi}_{1-x}\text{Zr}_x\text{O}_3$  at the Zr K Edge. *Phys. Rev. B* **2006**, *74* (1), 14106.
- (32) Wungu, T. D. K.; Sakaue, M.; Aspera, S. M.; Thuy, T. L. P.; Alaydrus, M.; Kasai, H.; Ishihara, T. First Principles Study on the Electronic Structure and Properties of Sr-and Mg-Doped  $\text{LaGaO}_3$ . *ECS Trans.* **2013**, *57* (1), 2715–2722.
- (33) Ricca, C.; Ringuedé, A.; Cassir, M.; Adamo, C.; Labat, F. Revealing the Properties of the Cubic  $\text{ZrO}_2$  (111) Surface by Periodic DFT Calculations: Reducibility and Stabilization through Doping with Aliovalent  $\text{Y}_2\text{O}_3$ . *Rsc Adv.* **2015**, *5* (18), 13941–13951.
- (34) Corà, F.; Alfredsson, M.; Mallia, G.; Middlemiss, D. S.; Mackrodt, W. C.; Dovesi, R.; Orlando, R. The Performance of Hybrid Density Functionals in Solid State Chemistry.

In *Principles and Applications of Density Functional Theory in Inorganic Chemistry II*; Springer, 2004; pp 171–232.

- (35) Salehi, H.; Hejaz, F. Calculation of Electronic and Structural Properties of  $\text{LaGaO}_3$  Using DFPT.
- (36) Hueso, J. L.; Holgado, J. P.; Pereñíguez, R.; Mun, S.; Salmeron, M.; Caballero, A. Chemical and Electronic Characterization of Cobalt in a Lanthanum Perovskite. Effects of Strontium Substitution. *J. Solid State Chem.* **2010**, *183* (1), 27–32.
- (37) Soldati, A. L.; Baqué, L.; Napolitano, F.; Serquis, A. Cobalt--Iron Redox Behavior in Nanostructured  $\text{La}_{0.4}\text{Sr}_{0.6}\text{Co}_{0.8}\text{Fe}_{0.2}\text{O}_{3-\delta}$  Cathodes. *J. Solid State Chem.* **2013**, *198*, 253–261.
- (38) Haas, O.; Struis, R.; McBreen, J. M. Synchrotron X-Ray Absorption of  $\text{LaCoO}_3$  Perovskite. *J. Solid State Chem.* **2004**, *177* (3), 1000–1010.

# CHAPTER 5

## Probing electrode-electrolyte interfaces by SXM

In this chapter the results concerning the electrode-electrolyte compatibility probed by Scanning X-Ray Microscopy (SXM) are presented and discussed. The aim of the study is to demonstrate that SXM is a powerful tool to probe chemical compatibility between SOFC components. The technique was applied for the first time to the study of an electrode-electrolyte interface and the couple LNC-LSM was chosen for tuning the experimental and data analysis procedures. These results were object of a publication in *Chemistry of Materials*.<sup>1</sup> An application of SXM to the couples LSCF-SDC and LSM-SDC has been also reported.

### 1. Motivation of the study

Electrode-electrolyte compatibility is a fundamental issue of a SOFC device assembly. Indeed, the choice of the materials is strongly influenced by the chemical compatibility between components and cation interdiffusion at the interface must be minimized, in order to avoid hampering of ionic transport and to ensure long-term durability and efficiency of the cell.

Synchrotron Scanning X-Ray Microscopy (SXM) is a widely used technique in the fields of cultural heritage, biology and geology.<sup>2-6</sup> Basing on X-Ray Fluorescence (XRF) contrast, SXM allows acquiring XRF maps that constitute a powerful tool for the microchemical analysis ( $\mu$ -XRF). Moreover, information about the local structure and chemical state of the constituent chemical species ( $\mu$ -EXAFS and  $\mu$ -XANES) can be achieved in selected points, together with quantitative mapping: these additional information are not obtainable by electron probe based techniques<sup>7-9</sup> and add local structure details about the fate of the interdiffusing cations.

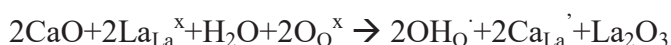
The aim of this work is to demonstrate that SXM is a powerful technique to probe electrode-electrolyte compatibility in SOFC assembly. The technique is applied for the first time to the

LNC-LSM couple and a detailed report of the kind of information that can be obtained is given. Results relative to selected electrode-electrolyte couples are also given.

This chapter is organized as follows. After a short description of the investigated LNC-LSM couple, in **Section 2** the experimental methods are reported. **Section 3** is dedicated to results and discussion. In **Sections 3.1, 3.2** and **3.3** results relative to  $\mu$ -XRF analysis at La L<sub>3</sub>-edge,  $\mu$ -EXAFS at Mn K-edge and  $\mu$ -XANES at Nb L<sub>3</sub>-edge are presented and discussed. In **Section 3.4** an overview of the application of SXM to AC-SOFC assemblies is given for LSCF/SDC and LSM/SDC. Finally, conclusions are drawn in **Section 4**.

### *The LNC-LSM couple*

LNC (Ca-doped lanthanum niobate) is a proton conductor having the scheelite structure. Proton insertion in the LNC matrix is accomplished by the defect reaction:



clearly demonstrating the 1:1 relation existing between Ca dopants and lattice protons hosted in the lanthanum niobate matrix. LSM (Sr-doped lanthanum manganate) is a cathodic material with a perovskite-like structure, characterized by good electronic conductivity and activity toward oxygen reduction. **Figure 5.1** reports the SEM image of the joint LNC-LSM and the drawings of the respective atomic structures.

Magrasò et al. have extensively investigated LNC electrolyte compatibility in both partial and complete cell assembly with LSM cathode and developed a complete LNC- based PC-SOFC.<sup>7-9</sup> Due to the low area specific resistance (ASR), the LSM-LNC cathode/electrolyte couple was selected to be the most performing among less performing candidates.

By the way, despite the overall good chemical compatibility between LNC and LSM cathode previously demonstrated and the good stability under CO<sub>2</sub> atmospheres, the complete cell exhibit fairly low performances.<sup>9</sup>

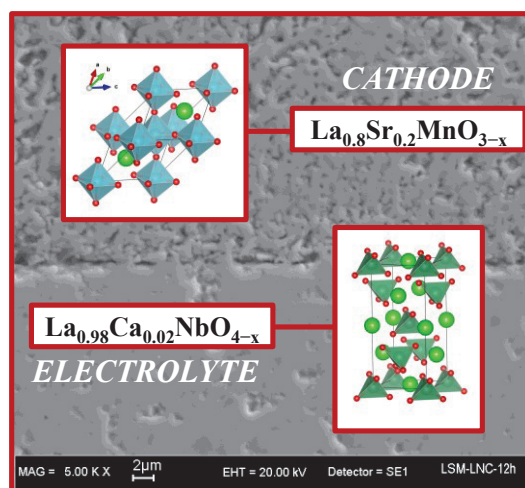


**Figure 5.1.** SEM micrograph for LSM-LNC assembly at the interface. LSM cathode and LNC electrolyte phases are drawn together with the unit cell structures.

## 2. Experimental methods

**Electrode-electrolyte assembly.**  $\text{La}_{0.8}\text{Sr}_{0.2}\text{MnO}_{3-x}/\text{La}_{0.98}\text{Ca}_{0.02}\text{NbO}_{4-x}$  (LSM/LNC) bilayers were prepared at the IENI-CNR in Genova by Dr. Giovanna Canu. The cathode/electrolyte assembly was prepared by pressing together the dense LNC pellet with LSM powder and the resulting bilayers were treated in three different ways:

- i) Sample A: 1150°C for 12 hours;
- ii) Sample B: 1150°C for 36 hours;
- iii) Sample C: 1250°C for 72 hours.

All the assembled bilayers were embedded in epoxy-resin, cut and polished, in order to expose the interlayer surface.

**Characterization.** Cation interdiffusion at the interface was characterized by synchrotron Scanning X-Ray Microscopy (SXM) at the beamline ID21 of the European Synchrotron Radiation Facility (ESRF).  $\mu$ -XRF maps were acquired at La  $L_3$ -edge, Nb  $L_3$ -edge and Mn K-edge, by scanning the electrode/electrolyte bilayer in two dimensions with a submicrometric beam, using a size step tuneable between 0.25  $\mu\text{m}$  and 1  $\mu\text{m}$ . The X-ray fluorescence (XRF) photons emitted by the sample are collected using an 80-mm<sup>2</sup> Silicon Drift Diode (SDD) detector (Bruker, Germany). Each pixel of the  $\mu$ -XRF map contains a

complete fluorescence spectrum bearing the information about the elemental distribution in that point. The mass fraction of each element can be determined by modeling the  $\mu$ -XRF spectra either pixel-by-pixel, or integrating the intensity over a region.  $\mu$ -XANES and  $\mu$ -EXAFS measurements were acquired in selected points of the fluorescence maps, in order to probe the chemical state and resolve the local structure around the absorber.

Fitting of the  $\mu$ -XRF spectra and deconvolution of the elemental distributions was carried out using the PyMca software<sup>10</sup> (See **Supporting Information S.3** for details).  $\mu$ -EXAFS data analysis was performed with Viper.<sup>11</sup> XANES simulations were performed with FEFF9.<sup>12</sup>

### 3. Results and discussion

#### 3.1 $\mu$ -XRF: La-L<sub>3</sub> edge

Elemental distribution analysis was carried out at the La L<sub>3</sub>-edge, due to the suitability of this energy (5.5 keV) for the calcium determination (Ca K-edge at 4.0 keV). Indeed, the absence of overlap between the K <sub>$\alpha$</sub>  lines of Ca and the L lines of La allows determining without interferences the concentration profiles across different regions of the  $\mu$ -XRF map.

Elemental distribution analysis was carried out on Sample A, annealed for 12 hours at 1150°C. In **Figure 5.2**, the  $\mu$ -XRF map showing the Ca<sup>2+</sup> concentration is drawn, together with the concentration profiles measured across the boundary between LSM and LNC. Ca<sup>2+</sup> diffuses towards the LSM cathode, giving rise to a sharp segregation of the dopant in the LSM region at the interface with the LNC electrolyte. This Ca<sup>2+</sup> segregation is extremely detrimental for the performance of the device, because dopant depletion involves a consequent decreased concentration of the mobile H<sup>+</sup>.

The quantitative elemental analysis was carried out on three different regions of the map, drawn in **Figure 5.2a**:

- i) Region 1: bulk LSM cathode.
- ii) Region 2: LSM/LNC interface.
- iii) Region 3: bulk LNC electrolyte.

Concentration map and profiles acquired at La L<sub>3</sub>-edge are shown in **Figure 5.3 a and b**.



The XRF spectra (**Figure 5.2 b, c and d**) were extrapolated from these regions and fitted with the Pymca software<sup>10</sup> to accomplish the deconvolution of the different fluorescence lines. The results of the data analysis are reported in **Table 5.1**.

The diffusion of  $\text{Ca}^{2+}$  towards the cathode is favoured by the high structural flexibility of perovskite-like oxides, that can afford compositional changes by tilting and deformations of the octahedral structural units. The Ca insertion into the cathode perovskite-like structure is proved by the elemental mapping (**Figure 5.2 a**) and further confirmed by the  $\mu$ -EXAFS data analysis acquired at Mn K-edge, reported in the next section.

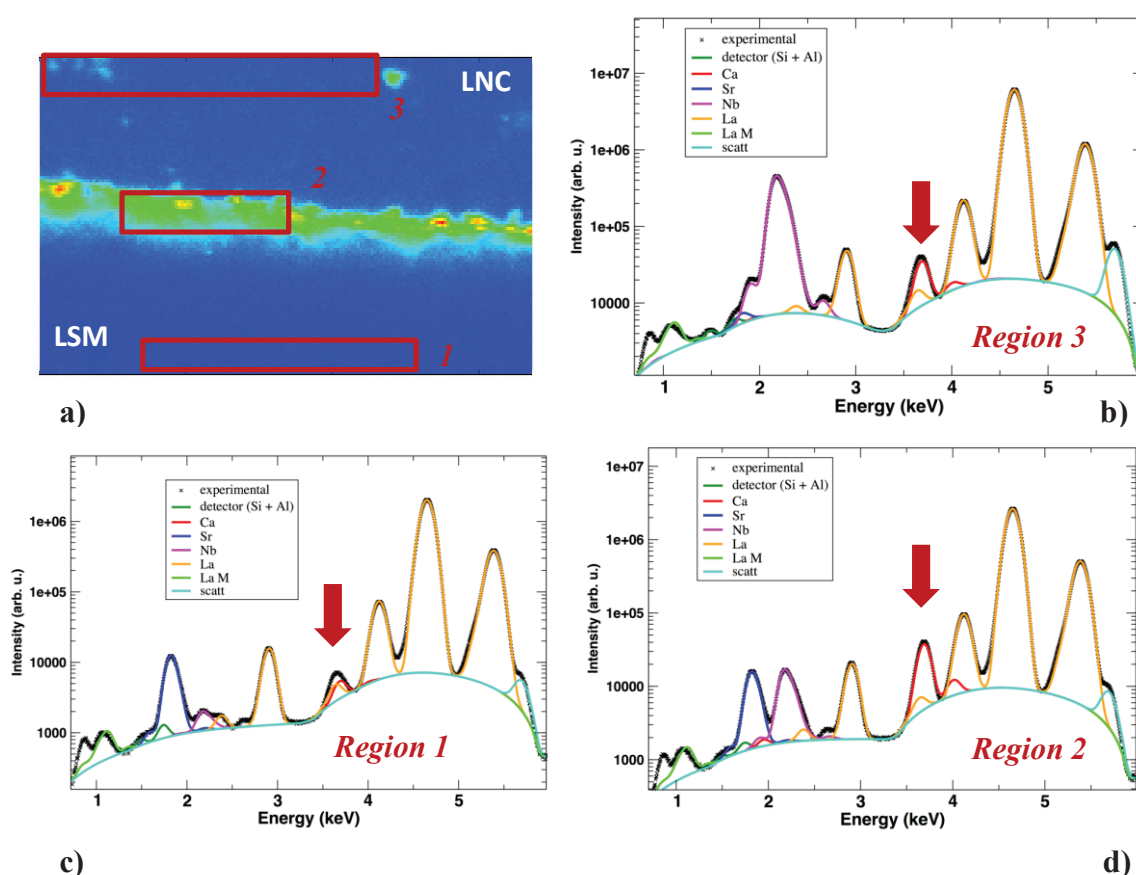


**Figure 5.2.** SAMPLE A: **a)** concentration map of  $\text{Ca}^{2+}$  from  $\mu$ -XRF data acquired at La  $L_{3}$ -edge. Region 1 (bulk LSM), Region 2 (interface) and Region 3 (bulk LNC) are depicted on the maps. XRF spectra showing **b)** Region 3, **c)** Region 1 and **d)** Region 2.  $\mu$ XRF spectra (black crosses) and best fitting components are depicted. The global fitting model obtained by summing the component peaks is omitted for clarity. The fluorescence peaks due to the experimental chamber and detector (Al and Si) are depicted in dark green.

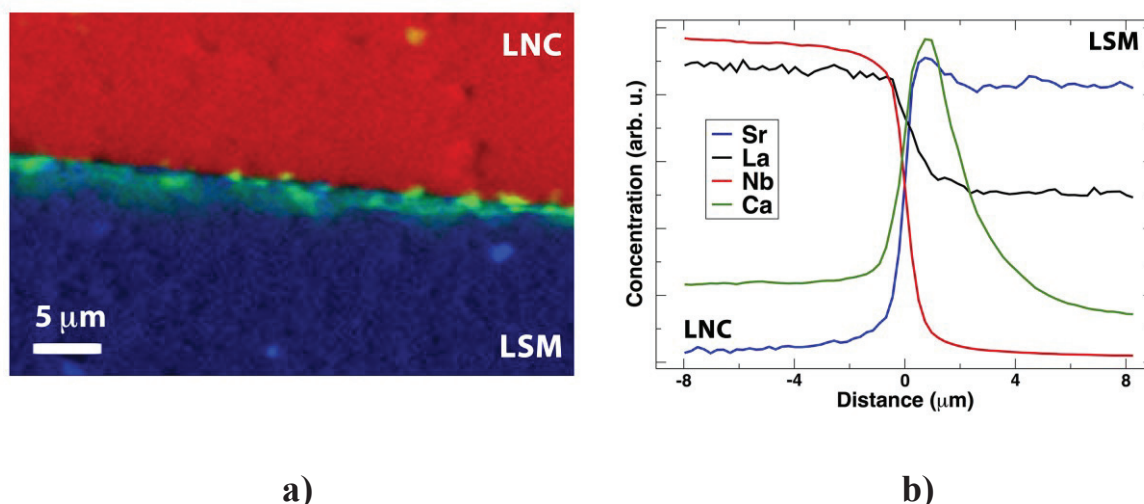


**Figure 5.3** Sample A. **a)** Concentration map from  $\mu$ -XRF data at the La  $L_3$ -edge: Nb in red, Ca in green, Sr in blue; **b)** Concentration profiles of Sr, La, Nb and Ca measured across the boundary between LSM and LNC phases, rescaled for clarity.

**Table 5.1** SAMPLE A: Elemental Composition (Weight %) of the three Regions of Sample A. Manganese content is determined by difference. Such estimation is confirmed by  $\mu$ -XRF analysis at the Mn K-edge on the same regions (see **Supporting Information S.3**). Regions 1–3 are depicted in **Figure 5.2**.

Element	Region 1 (LSM)	Region 2 (interface)	Region 3 (LNC)	LSM (nominal)	LNC (nominal)
La	47.71	46.78	46.66	47.98	46.33
Sr	8.765	8.176	0.071	7.56	0
Ca	0.0407	0.3425	0.1494	0	0.27
Nb	0.2822	1.775	31.2637	0	31.62
Mn	23.121	22.584	0.18	23.72	0

### 3.2 $\mu$ -EXAFS: Mn K-edge

$\mu$ -EXAFS data analysis at the Mn K-edge was carried out on Sample C, annealed at 1250° for 72 hours. By this treatment, it was possible to enhance the concentration of  $\text{Ca}^{2+}$  in the LSM phase and to obtain a good quality  $\mu$ -EXAFS signal of Ca in the local environment of Mn. The collected data were modelled up to 4 Å. The first-shell Mn-O distance was determined at

about 1.99 Å and the coordination number was fixed at the octahedral value of 6. Three contributions, centred on average at 3.32 Å, were used to model the Mn-A contribution (A = La, Sr, Ca), fixing the coordination numbers according to the stoichiometry arising from  $\mu$ -XRF analysis ( $\text{La}_{0.7}\text{Sr}_{0.2}\text{Ca}_{0.1}\text{MnO}_3$ ). Finally, one single Mn-Mn contribution at 3.92 Å was used to model the B-B 3rd shell interaction. The quality of the fitting to the  $\mu$ -EXAFS data, reported in **Figure 5.4**, is satisfactory and, taking into account that La, Sr and Ca are very easily distinguishable when fitting EXAFS data, it can be concluded that  $\text{Ca}^{2+}$  drifts into the perovskite A-site of LSM.

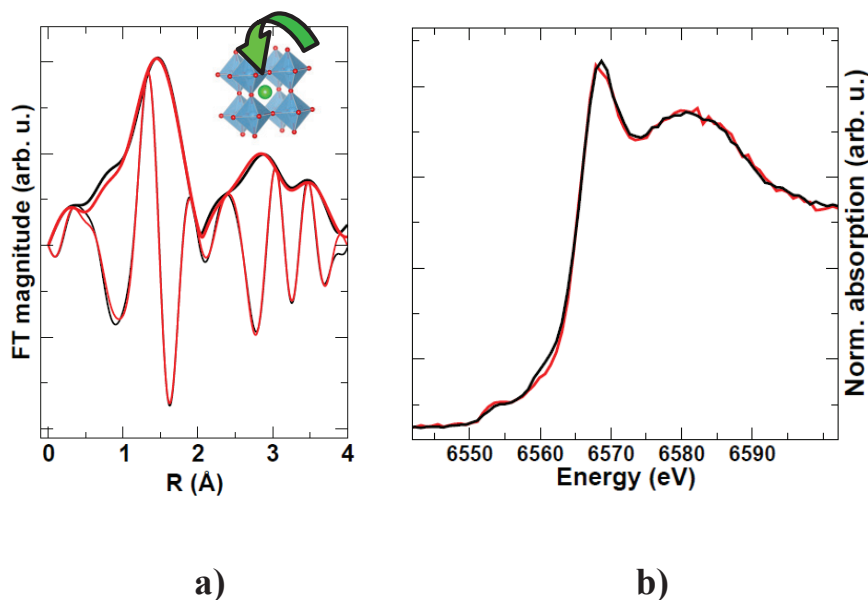


**Figure 5.4** Sample C. **a)** Mn K-edge  $\mu$ -EXAFS at the LNC-LSM interface. Experimental data, black; fit, red. **b)** Experimental Mn K-edge  $\mu$ -XANES at the LNC-LSM interface (black) and in bulk LSM (red).

**Table 5.2** Elemental composition (weight %) of three regions of sample A from XRF analysis at the Mn K-edge. The nominal compositions of LNC and LSM are reported for comparison. Regions 1-3 are depicted in **Figure 5.2 a**.

	Distance (Å)	Debye-Waller factor (Å <sup>2</sup> )
Mn-O	1.99(2)	0.009(4)
Mn-(La, Sr, Ca)	3.32(3)	0.016(4)
Mn-Mn	3.92(3)	0.016(4)

### 3.3 $\mu$ -XANES

The changes in the  $\mu$ -XANES spectra at the LSM-LNC interface and LSM bulk phase at Mn K-edge (**Figure 5.4 b**), further confirm that the local environment of Mn at the interface is modified by calcium. Therefore, the diffusion of calcium could be promoted by the formation of a perovskite-like phase (La,Ca,Sr)MnO<sub>3</sub>: indeed, it was recently reported that doping lanthanum manganite with Ca on the A-site results in the highest stability compared with Sr or Ba doping.<sup>13</sup>

Finally, **Figure 5.5** reports the  $\mu$ -XANES spectra acquired at the Nb L<sub>3</sub>-edge respectively in bulk LNC and in LSM. The XANES region, which is very sensitive to the local coordination and oxidation state of Nb, clearly shows that Nb has a definitely different environment in bulk LNC (right top panel) and in LSM (right bottom). The drawings show the local structures of Nb in the two materials and the red curves, relative to the simulation of the respective XANES spectra, confirm that Nb is in tetrahedral coordination in LNC and in the octahedral B-site in LSM. Contrary to other cations, Nb<sup>5+</sup> has a slower diffusion, that can not be appreciated in sample A, treated at high temperatures for the shorter time.

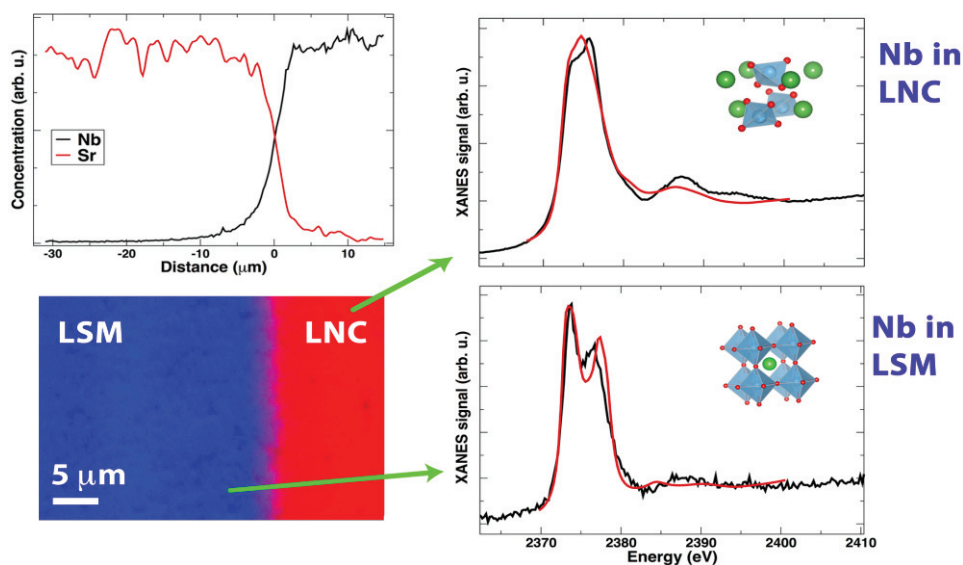


**Figure 5.5** Sample B. Left panel, bottom: concentration map of Nb from  $\mu$ -XRF data at the Nb L<sub>3</sub>-edge (lowest (blue) to highest (red)). Left panel, top: concentration profiles of Nb and Sr in the map, rescaled for clarity. Right panel, bottom: experimental Nb L<sub>3</sub>-edge  $\mu$ -XANES spectrum from the LSM region, and simulated signal for Nb placed in the B-site of the perovskite LSM structure. Right panel, top: experimental Nb L<sub>3</sub>-edge  $\mu$ -XANES spectrum from the LNC region, and simulated signal for Nb placed in the monoclinic LNC structure. In the right panels, the experimental data are plotted in black, and the simulations in red.

### 3.4 SXM analysis of the interfaces SDC-LSCF and SDC-LSM

Two more examples are reported, in order to show the suitability of SXM technique for the investigation of the cation interdiffusion processes involved in different electrode-electrolyte couples for AC-SOFC applications.

$\mu$ -XRF colour maps for  $\text{La}_{0.6}\text{Sr}_{0.4}\text{Co}_{0.5}\text{Fe}_{0.5}\text{O}_3/\text{Ce}_{0.8}\text{Sm}_{0.2}\text{O}_2$  (LSCF/SDC) and  $\text{La}_{0.8}\text{Sr}_{0.2}\text{MnO}_3/\text{Ce}_{0.8}\text{Sm}_{0.2}\text{O}_2$  (LSM) bilayers annealed for 72 hours were acquired respectively at Fe (**Figure 5.6**) and Mn (**Figure 5.7**) K-edges.

It can be observed that in both cases interdiffusion phenomena at the interface take place. In particular, the interface region show a marked interdiffusion of Sm towards the LSCF phase in LSCF/SDC: this exsolution of Sm from the bulk of the SDC phase is supposed to be detrimental for the oxygen-ion diffusion inside the electrolyte, due to a decrease of  $\text{V}_\text{O}$  defects. Moreover, a segregation of Fe and Sm in the same region where Ce is depleted in the

electrolyte phase can be observed. Also the presence of these islands with mixed valence cation Fe could be detrimental for the assembly, because iron could introduce electronic conductivity in the electrolyte phase.

Also the LSM/SDC bilayer (**Figure 5.7**) show segregation islands in the electrolyte phase, caused by the diffusion of Mn from the cathode to regions where a slight depletion of Ce takes place.

Underway  $\mu$ -XANES and  $\mu$ -EXAFS analysis will allow knowing the fate of these cations in terms of oxidation states and local structure.

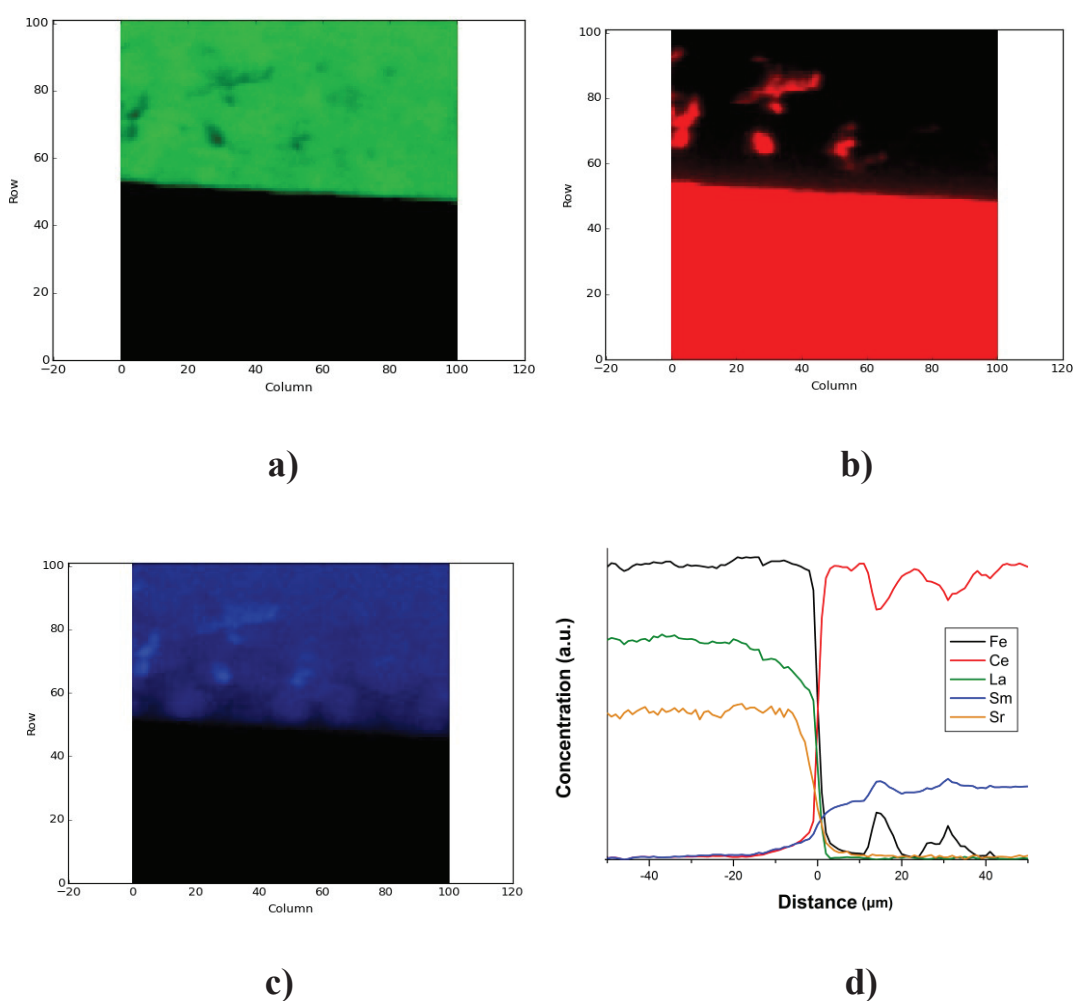


**Figure 5.6** a) cerium, b) iron and c) samarium  $\mu$ -XRF concentration maps in the LSCF/SDC bilayer (annealed for 72 h), acquired at Fe K-edge. d) Concentration profiles for Fe, Ce, La, Sm and Sr across the interface.

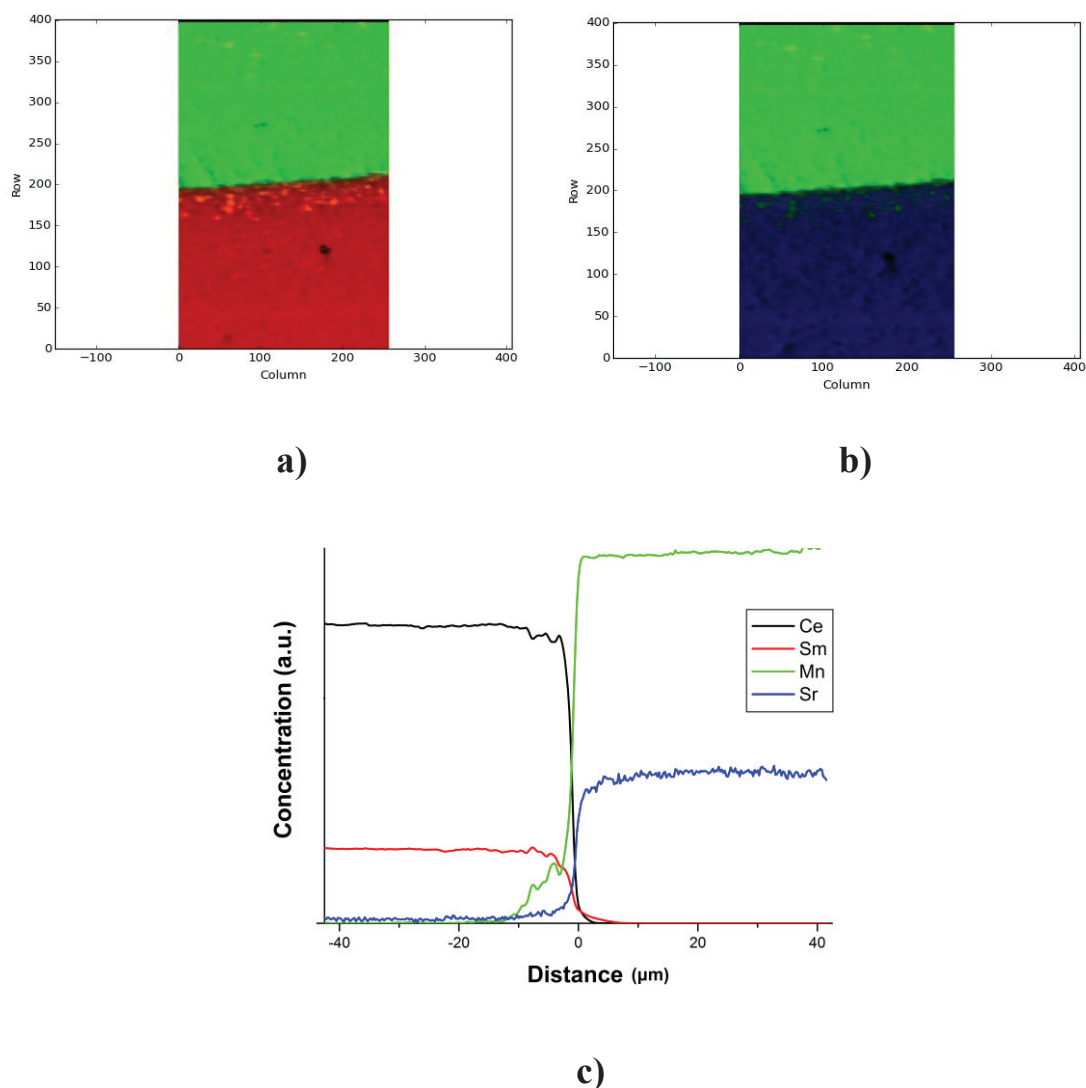


**Figure 5.7** **a)** Manganese (green) and samarium (red), **b)** manganese (green) and cerium (blue)  $\mu$ -XRF concentration maps in the LSM/SDC bilayer (annealed for 72 h), acquired at Mn K-edge. **c)** Concentration profiles for Ce, Sm, Mn and Sr across the interface.

## 4. Conclusions

SXM has been successfully used to study compatibility between SOFC components. In particular, this technique was employed to probe LSM-LNC PC-SOFC bilayer, in order to unravel cation interdiffusion phenomena.

$\mu$ -XRF analysis demonstrates that  $\text{Ca}^{2+}$  tends to drift from the electrolyte LNC phase towards the cathode LSM phase. This migration is likely balanced by  $\text{La}^{3+}$  counterdiffusion and, as a consequence of the opposite cation flows, the suppression of proton defects in the electrolyte phase takes place. Calcium exsolution is therefore detrimental for LNC ionic conductivity.

$\mu$ -EXAFS at Mn K-edge evidences that  $\text{Ca}^{2+}$  tends to segregate at the electrolyte-electrode interface and enters the perovskite A site of LSM.

$\mu$ -XANES at the Nb  $L_3$ -edge shows that the environment of niobium in LNC is tetrahedral in LNC. The clear evidence of octahedral environment in LSM demonstrates that also Nb drifts in the perovskite B site of LSM. XANES simulations confirm this interpretation. The availability of the LSM matrix to host Nb is attributed to the well known structural flexibility of perovskite materials.

Applications are reported, showing the suitability of X-Ray Microscopy for the investigation of the interface diffusion processes involved in different electrode-electrolyte couples. LSCF/SDC and LSM/SDC bilayers were probed through SXM, showing in both cases the segregation of cations in the electrolyte phase.

## 5. References

- (1) Giannici, F.; Canu, G.; Gambino, M.; Longo, A.; Salomé, M.; Viviani, M.; Martorana, A. Electrode-Electrolyte Compatibility in Solid-Oxide Fuel Cells: Investigation of the LSM--LNC Interface with X-Ray Microspectroscopy. *Chem. Mater.* **2015**, *27* (8), 2763–2766.
- (2) Susini, J.; Salomé, M.; Fayard, B.; Ortega, R.; Kaulich, B. The Scanning X-Ray Microprobe at the ESRF“ X-Ray Microscopy” beamline. *Surf. Rev. Lett.* **2002**, *9* (1), 203–211.
- (3) Salomé, M.; Bleuet, P.; Bohic, S.; Cauzid, J.; Chalmin, E.; Cloetens, P.; Cotte, M.; De Andrade, V.; Martinez-Criado, G.; Petitgirard, S.; et al. Fluorescence X-Ray Micro-Spectroscopy Activities at ESRF. In *Journal of Physics: Conference Series*; 2009; Vol. 186, p 12014.
- (4) Tack, P.; Cotte, M.; Bauters, S.; Brun, E.; Banerjee, D.; Bras, W.; Ferrero, C.; Delattre, D.; Mocella, V.; Vincze, L. Tracking Ink Composition on Herculanum Papyrus Scrolls: Quantification and Speciation of Lead by X-Ray Based Techniques and Monte Carlo Simulations. *Sci. Rep.* **2016**, *6*.
- (5) Pascolo, L.; Borelli, V.; Canzonieri, V.; Gianoncelli, A.; Birarda, G.; Bedolla, D. E.; Salomé, M.; Vaccari, L.; Calligaro, C.; Cotte, M.; et al. Differential Protein Folding



- and Chemical Changes in Lung Tissues Exposed to Asbestos or Particulates. *Sci. Rep.* **2015**, *5*.
- (6) Dijkstra, N.; Slomp, C. P.; Behrends, T.; others. Vivianite Is a Key Sink for Phosphorus in Sediments of the Landsort Deep, an Intermittently Anoxic Deep Basin in the Baltic Sea. *Chem. Geol.* **2016**, *438*, 58–72.
- (7) Magrasó, A.; Fontaine, M.-L.; Larring, Y.; Bredesen, R.; Syvertsen, G. E.; Lein, H. L.; Grande, T.; Huse, M.; Strandbakke, R.; Haugsrud, R.; et al. Development of Proton Conducting SOFCs Based on LaNbO<sub>4</sub> Electrolyte-Status in Norway. *Fuel cells* **2011**, *11* (1), 17–25.
- (8) Magrasó, A.; Fontaine, M.-L. Investigation of Compatible Anode Systems for LaNbO<sub>4</sub>-Based Electrolyte in Novel Proton Conducting Solid Oxide Fuel Cells. *J. Power Sources* **2011**, *196* (23), 10183–10190.
- (9) Magrasó, A.; Fontaine, M.-L.; Bredesen, R.; Haugsrud, R.; Norby, T. Cathode Compatibility, Operation, and Stability of LaNbO<sub>4</sub>-Based Proton Conducting Fuel Cells. *Solid State Ionics* **2014**, *262*, 382–387.
- (10) Solé, V. A.; Papillon, E.; Cotte, M.; Walter, P.; Susini, J. A Multiplatform Code for the Analysis of Energy-Dispersive X-Ray Fluorescence Spectra. *Spectrochim. Acta Part B At. Spectrosc.* **2007**, *62* (1), 63–68.
- (11) Klementev, K. V. Extraction of the Fine Structure from X-Ray Absorption Spectra. *J. Phys. D. Appl. Phys.* **2001**, *34* (2), 209.
- (12) Rehr, J. J.; Kas, J. J.; Vila, F. D.; Prange, M. P.; Jorissen, K. Parameter-Free Calculations of X-Ray Spectra with FEFF9. *Phys. Chem. Chem. Phys.* **2010**, *12* (21), 5503–5513.
- (13) Lee, W.; Han, J. W.; Chen, Y.; Cai, Z.; Yildiz, B. Cation Size Mismatch and Charge Interactions Drive Dopant Segregation at the Surfaces of Manganite Perovskites. *J. Am. Chem. Soc.* **2013**, *135* (21), 7909–7925.

## CONCLUSIONS

The development of Solid Oxide Fuel Cells technology for clean power generation has been strongly encouraged and funded during these years, with the aim to find valid alternatives to fossil fuel based plants. The low impact emissions make this kind of devices very appealing, but the presence of currently unsolved problems, such as the long-term durability of components due to the high operating temperatures and the non competitive cost, still constitute an obstacle to their massive commercialization.

Material science has a fundamental role in finding solutions to overcome these issues and one of the main goals for research is to lower operating temperatures and reduce in this way the degradation rate of materials. To achieve this goal, it is necessary to investigate the structural properties of SOFC components in order to find correlations with their functional properties that could be useful to design materials with improved properties.

This research project was focused on the study of electrolyte materials for AC-SOFC applications working at Intermediate temperatures (600-800°C). In particular, fluorite-type  $\delta$ - $\text{Bi}_2\text{O}_3$  and perovskite-type  $\text{LaGaO}_3$  have been studied with the aim to understand the structural features that have an influence on the oxygen-ion diffusion. To this end, a combined XAS and DFT approach was used.

$\text{Bi}_{1-x}\text{Ta}_x\text{O}_{1.5+x}$  solid electrolyte has been investigated, in order to understand the role of high-valence dopants in the stabilization of the fluorite-like phase of bismuth oxide and on its oxygen-ion conductivity. It has been demonstrated that the high ionic conductivity of the material is caused by the disorder of the oxygen-ion sublattice around Bi, where oxygen-ions tend to be displaced from their regular site toward the faces of their  $\text{OBi}_4$  coordination tetrahedron, so lowering the activation energy of the system. This structural feature is likely determined by the electronic structure of the compound, where the stereochemically active Bi  $6s^2$  lone pair remains unbound with 2p oxygen orbitals. On the other side, the preferential pyrochlore-like  $\text{Ta}_4\text{O}_{18}$  aggregation motives, which tend to further aggregate to form larger clusters depending on the Ta concentration, are involved in the stabilization of the fluorite phase at room temperature, but are found to hinder oxygen-ion conductivity around the dopant site.

For what concerns perovskite-like  $\text{LaGaO}_3$ , a comprehensive theoretical study of  $\text{LaGa}_{0.875}\text{Mg}_{0.125}\text{O}_{2.935}$  integrated with XAS structural characterization, is presented. The

computational analysis is carried out taking into account only the B site doping of lanthanum gallate. This approach constitutes a preliminary step, that is however necessary for tuning the computational protocol, toward the modellization of dopant insertion also in the A site. On the other hand, some sound conclusion about the mechanism of conduction can already be drawn, taking into account that the perovskite B site is mainly involved in the oxygen hopping process. It turned out that a better equivalence of oxygen-ion conductive sites is obtained for diluted B-site dopant configurations. Vacancies are mainly set in axial positions, as a consequence of local disorder involving octahedra tilting and dihedral distortions around the Mg-sites. Simulations of defective sites of type Ga-Vo-Mg and Ga-Vo-Ga, evidenced umbrella-like distortions, characterized by oxygen-ions heavily bent towards the vacancy site. The calculation of activation energy for the oxygen-ion diffusion paths evidenced that the barrier is much larger for oxygen diffusion around Mg, axial-equatorial and equatorial-equatorial hopping paths have similar and lower energy barriers around Ga. The influence of co-doping with Mg and Co on the local structure features around the B-site in  $\text{La}_{1-x}\text{Sr}_x\text{Ga}_{1-y}\text{Mg}_y\text{O}_{3-\delta}$  and  $\text{La}_{1-x}\text{Sr}_x\text{Ga}_{1-y}(\text{Mg}, \text{Co})_y\text{O}_{3-\delta}$  has been investigated by XAS. In particular, it was found that the compositions that in literature are found to have a higher ionic conductivity (LSGM2020, LSGMC2005 and LSGMC2010) are those where the Ga-O-M (M=Mg or Co) angles are less strained and are set between 170 and 180°. The attenuation of the local distortion around Mg may be due to a size effect of  $\text{Sr}^{2+}$  and  $\text{Co}^{3+}$  that likely produces also a more evenly distributed diffusion paths of oxygen within the LG matrix.

Finally, it was taken into account the influence of the electrode-electrolyte interface on the mechanism of ionic conduction. To this concern, a detailed study about the novel use of synchrotron Scanning X-Ray Microscopy (SXM) applied to investigation of the electrode/electrolyte compatibility is reported in this thesis. The technique was tuned on the LNC-LSM couple, whose chemical stability during FC operation is well established. It turned out that SXM, allowing the combined use of  $\mu$ -XRF,  $\mu$ -EXAFS and  $\mu$ -XANES, is a powerful tool to probe cation interdiffusion at the interface between FC components. Indeed, this technique not only allows the microchemical analysis, like electron probe based methods (SEM, TEM), but it is also able to give details on the local structure of cations and on their chemical state in selected points of the map, where XANES and EXAFS spectra can be recorded. This allows understanding the compatibility issues between cell components, finely unveiling the fate of diffusing cations in annealed bilayers and highlighting interface rearrangements that can hamper ionic conductivity.

To sum up, this thesis is focused on some pivotal issues of ionic conductivity in SOFC technology, with the perspective of drawing useful hints for the design of improved FC materials. An integrated approach involving experimental study of local structure and computational simulation was exploited for the investigation of the dopant-matrix interaction in two of the top-performing oxygen-ion conductors, that are the fluorite-like  $\delta$ -Bi<sub>2</sub>O<sub>3</sub> and the perovskite-like LaGaO<sub>3</sub>. A further important aspect related to ionic conductivity, that is the electrode-electrolyte interface interaction, has been addressed by the first application of the scanning X-ray microscopy to the detailed study of the LNC-LSM couple. Exploitation of the technique to other electrode-electrolyte couples is underway.

## S.1 SUPPORTING INFORMATION

### XAS and DFT study of $\text{Bi}_{1-x}\text{Ta}_x\text{O}_{1.5+x}$ electrolytes

#### Experimental details

For the sample preparation, stoichiometric amounts of  $\text{Bi}_2\text{O}_3$  (Sigma-Aldrich 99.9%) and  $\text{Ta}_2\text{O}_5$  (Sigma-Aldrich 99.9%) were grounded in an agate mortar with the aid of about 1 mL of ethanol or 2-propanol (Panreac 96%). Then the mixture was dried for about 5 minutes in oven at  $80^\circ\text{C}$  to remove the solvent. All the samples were first calcined at  $750^\circ\text{C}$  in air for 12 h with a ramp of  $150^\circ\text{C}/\text{h}$ , then ball milled for 30 minutes, re-calcined at  $750^\circ\text{C}$  in air for 12 h, and eventually reground. Ball milling was carried out with zirconia jar and spheres using a Retsch MM200 vibrating mill. X-Ray Diffraction (XRD) data were acquired at room temperature, in a  $2\theta$  range of  $20$ - $120^\circ$ , with a step of  $0.02^\circ$  and accumulation time of 4 s. Calibration of the instrument was made with corundum powder before and after every measurement. Samples for X-Ray Absorption Spectroscopy were prepared by appropriately diluting the  $\text{Bi}_{1-x}\text{M}_x\text{O}_{1.5+x}$  powders with polyvinylpyrrolidone and pressing the mixture in a 13-mm die.

#### Impedance spectroscopy

AC conductivity of the samples with  $x = 0.22$  and  $0.25$  was measured in air with an Autolab FRA32M impedance analyzer (Metrohm). An AC voltage of 0.1 V was applied between 1 MHz and 0.1 Hz at  $180$ - $800^\circ\text{C}$  using a ProboStat high-temperature cell (NorECs). The conductivity values at  $300$ ,  $500$  and  $800^\circ\text{C}$  are reported together with the activation energy in **Table S.1.1**.

**Table S.1.1** – Goodness-of-fitting parameters (residual) on the Ta and Bi edge.

Composition	$\sigma(300^\circ\text{C})$ (mS/cm)	$\sigma(500^\circ\text{C})$ (mS/cm)	$\sigma(800^\circ\text{C})$ (mS/cm)	$E_a$ (eV)
$x=0.22$	$1.44 \cdot 10^{-4}$	0.0373	2.99	1.1
$x=0.25$	$2.21 \cdot 10^{-4}$	0.0244	1.46	0.9

## XANES analysis

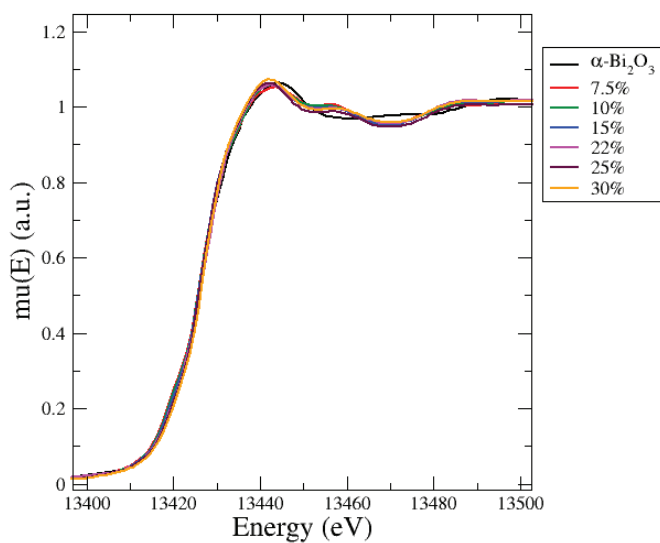


**Figure S.1.1** XANES spectra of Ta-doped samples and reference  $\alpha$ -Bi<sub>2</sub>O<sub>3</sub> (black).

## EXAFS analysis

**Table S.1.2** Goodness-of-fitting parameters (residual) on the Ta and Bi edge.

x	R-factor Ta edge (%)	R-factor Bi edge (%)
0	--	10.7
0.075	5.6	14.8
0.1	4.3	13.7
0.15	5.2	9.8
0.22	3.9	7.5
0.25	3.0	7.8
0.3	7.0	8.4

### EXAFS: Ta edge

Amplitude reduction factor was determined by fitting a reference Ta<sub>2</sub>O<sub>5</sub> powder, giving  $S_0^2 = 0.98$ . The octahedral coordination of Ta is confirmed also by important intraoctahedral colinear multiple scattering paths Ta-O-Ta-O, that are necessary for achieving a good fitting to the data.

The fitting of second shell coordination numbers around Ta, N(Ta-Bi) and N(Ta-Ta), posed peculiar problems, since any attempt to constrain these parameters led to unphysical results or very poor fitting quality. Therefore, the following approach was applied: 1) the cation-cation coordination numbers around Ta, N(Ta-Ta) and N(Ta-Bi), were at first allowed to vary freely; 2) since these two parameters are positively correlated, the fitting residual is almost unchanged as they both increase or decrease: on the other hand, the fitting residual depends strongly on the ratio of Ta-Ta vs. Ta-Bi (i.e. the EXAFS technique discriminates well between Ta and Bi in the cation sites – as can be appreciated by the differences in their amplitude and phase); 3) under the assumption that the cation sublattice is fluorite-like, and that cation vacancies are negligible, the total cation-cation coordination number is 12, so the sum of N(Ta-Ta) and N(Ta-Bi) is normalized to 12, eventually obtaining the results reported in the main text.

The confidence intervals of these coordination numbers is estimated in a similar fashion: 1) the contour plot of the function  $\exp(-\chi^2)$  as a function of N(Ta-Ta) and N(Ta-Bi) is calculated, and the horizontal and vertical spread of the ellipse corresponding to 68.5% confidence interval is selected as the confidence interval of the fitted N(Ta-Ta) and N(Ta-Bi) values; 2) the contour plot of N(Ta-Ta) and N(Ta-Bi) is normalized by superimposing another map, which represents the normalized N(Ta-Ta) value as a function of the fitted N(Ta-Ta) and N(Ta-Bi) values, i.e.:

$$N(\text{Ta-Ta})_{\text{norm}} = N(\text{Ta-Ta}) + N(\text{Ta-Bi}) / 12$$

The contour plot ellipse encloses the regions in the  $N(\text{Ta-Ta})_{\text{norm}}$  map representing the confidence interval of the normalized fitted results.

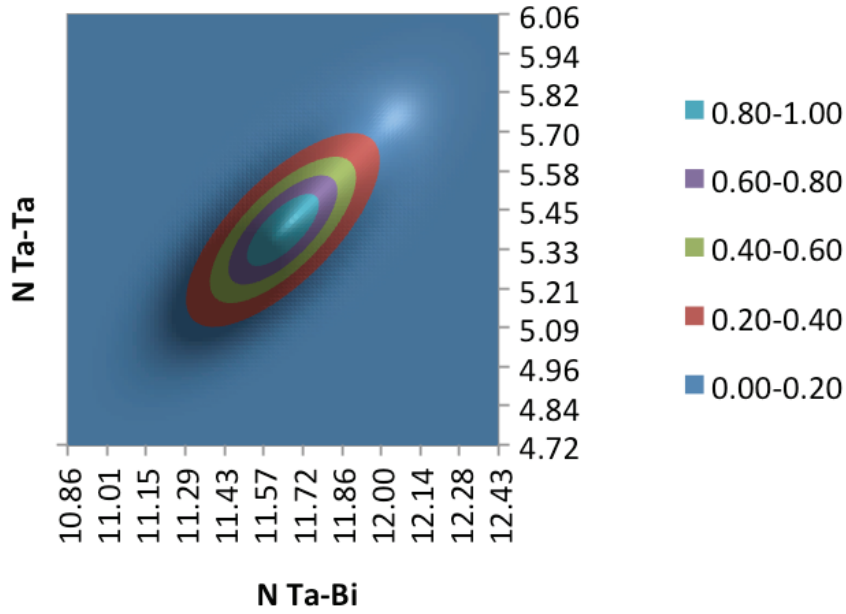


**Figure S.1.2** Contour plot of  $N(\text{Ta-Ta})$  and  $N(\text{Ta-Bi})$  for sample  $x = 0.22$ . The 68.5% confidence level falls in the yellow ellipse.

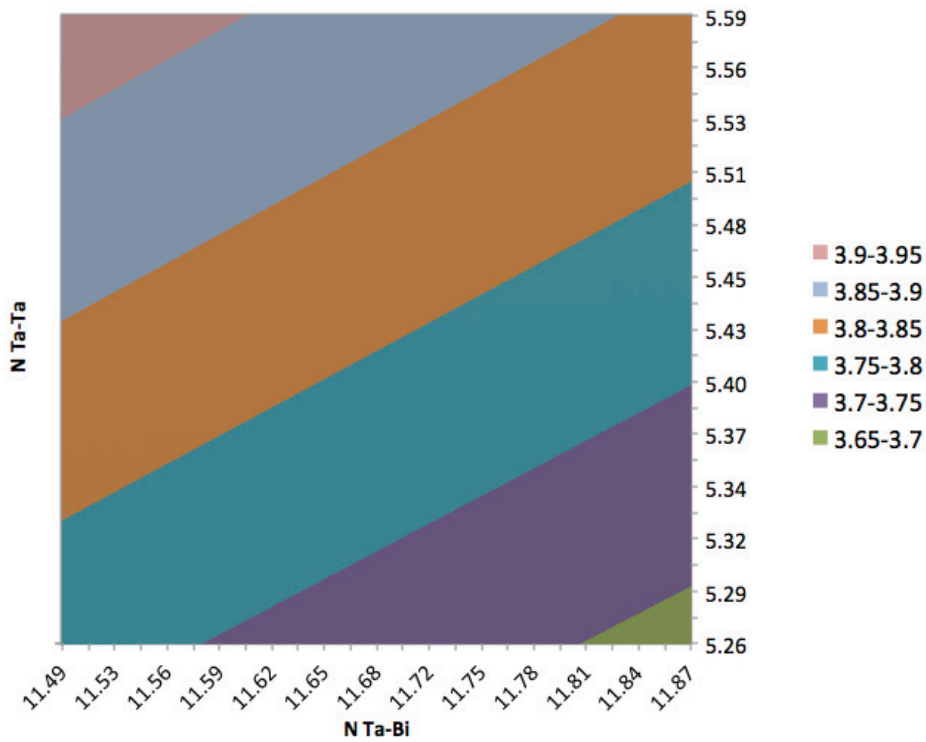


**Figure S.1.3** Normalized  $N(\text{Ta-Ta})$  value as a function of fitted  $N(\text{Ta-Bi})$  and  $N(\text{Ta-Ta})$  for sample  $x = 0.22$ .



### EXAFS: Bi edge

Amplitude reduction factor was determined by fitting a reference  $\text{Bi}_2\text{O}_3$  powder, giving  $S_0^2 = 0.65$ . Assuming that Bi and Ta cations are placed in a fluorite structure, i.e. a close-packed cubic lattice, with 8 anion sites around each cation, the average first-shell coordination number around cations is  $N_{\text{av}} = 6+4x$ , where  $x$  is the Ta content.

In order to ensure consistency in the results between Ta and Bi first shell environments, the following constraints were set up during the fitting. Since the Ta edge analysis confirms that  $\text{Ta}^{5+}$  ions are 6-coordinated, the first shell coordination numbers around  $\text{Bi}^{3+}$  have to take into account the preferential interaction of oxygen vacancies with the Ta dopant. This means that if Ta is surrounded by 6 oxygen atoms, the effective Bi-O first shell coordination number must be higher than the average  $N_{\text{av}}$  value in order to compensate for the Ta-vacancy clustering. Therefore, the total  $N(\text{Bi-O})$  coordination number was constrained during the fit to be higher than a  $N_{\text{min}}$  value that is consistent with the preferential interaction of oxygen vacancies with the Ta dopant.

This is calculated simply as  $N_{\text{min}} = (N_{\text{av}} - x \cdot N(\text{Ta-O})) / (1-x)$ .

Finally, the Bi-O third shell coordination number was fixed according to oxygen stoichiometry, since the cation-vacancy association is averaged out as the distance from the absorbing atom increases. The  $N_{\text{av}}$  and  $N_{\text{min}}$  values are reported in **Table S.1.3 together** with the average third shell coordination number  $N_{\text{III}}(\text{M-O})$ .

**Table S.1.3** Stoichiometric amount of Ta ( $x$ ) for the composition  $\text{Bi}_{1-x}\text{Ta}_x\text{O}_{1.5+x}$ , average first shell coordination number around cations  $N_{\text{av}}$  M-O, minimum coordination number around Bi assuming all Ta atoms as 6-coordinated ( $N_{\text{min}}$  Bi-O), and average coordination number of the third shell around cations ( $N_{\text{III}}$  M-O).

$x$	$N_{\text{av}}$ (M-O)	$N(\text{Ta-O})$	$N_{\text{min}}$ (Bi-O)	$N_{\text{III}}$ (M-O)
0.075	6.3	5.9	6.3	18.9
0.10	6.4	6.0	6.4	19.2
0.15	6.6	6.2	6.7	19.8
0.22	6.9	6.1	7.1	20.6
0.25	7.0	6.1	7.3	21
0.3	7.2	6.4	7.5	21.6

**Table S.1.4** Results of the EXAFS analysis of undoped Bi<sub>2</sub>O<sub>3</sub>. The first shell Bi-O is split in two contributions, the second shell is split in three contributions: the sum of their coordination numbers is constrained to 6 and 12, respectively; the different contributions for each shell share the same disorder factor. Distances (R, in Å), coordination numbers (N) and disorder factors ( $\sigma^2$ , in 10<sup>-2</sup> Å<sup>2</sup>) are reported. Uncertainties are reported in parentheses.

Bi-O			Bi-Bi			Bi-O		
R	N	$\sigma^2$	R	N	$\sigma^2$	R	N	$\sigma^2$
2.18(1)	4.4(1)	0.79(3)	3.58(1)	6	0.6(5)	3.85(1)	24	5.24(5)
2.48(1)	1.6(1)	0.79(3)	4.11(1)	1.2	0.6(5)			
			4.40(1)	4.8	0.6(5)			

### DFT calculations

Density functional and basis sets were validated on the  $\alpha$ -Bi<sub>2</sub>O<sub>3</sub> structure, by comparing the cell parameters obtained at different level of theory with the experimental values (Pereira A.L.J; Errandonea, D.; Beltrán; Gracia, L.; Gomis, O.; Sans, J.A.; García-Domene, B.; Miquel-Veyrat, A.; Manjón, F.J.; Muñoz, A.; Popescu, C. *J. Phys.: Condens. Matter* **2013**, 25, 475402). These are shown in Table S.5.

**Table S.1.5** Lattice parameters and cell volume obtained with various GGA (PBE, PBEsol, B3PW91, SOGGA) and hybrid (PBE0, B3LYP) functionals for the monoclinic  $\alpha$ -Bi<sub>2</sub>O<sub>3</sub> unit cell. Experimental data from Pereira et al. *J. Phys.: Condens. Matter* **2013** 25, 475402.

	a (Å)	b (Å)	c (Å)	$\beta$ (°)	V (Å <sup>3</sup> )
<b>Experimental</b>	5.849	8.166	7.510	113.00	330.1
FUNCTIONAL	a (Å)	b (Å)	c (Å)	$\beta$ (°)	V (Å <sup>3</sup> )
<b>PBE</b>	5.914	8.016	7.378	112.96	322.1
<b>PBEsol</b>	5.898	7.858	7.301	113.01	311.4
<b>B3PW91</b>	5.867	7.974	7.346	113.19	315.9
<b>SOGGA</b>	5.892	7.811	7.280	112.98	308.4
<b>PBE0</b>	5.857	7.922	7.322	113.17	312.3
<b>B3LYP</b>	5.889	8.176	7.439	113.39	328.7

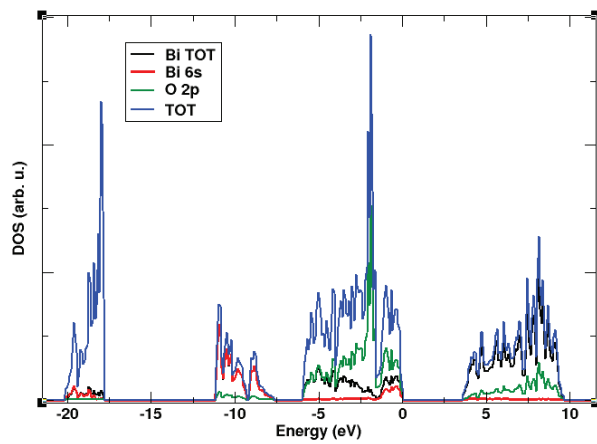


**Figure S.1.4** Calculated total and partial DOS of  $\alpha\text{-Bi}_2\text{O}_3$  (B3LYP)

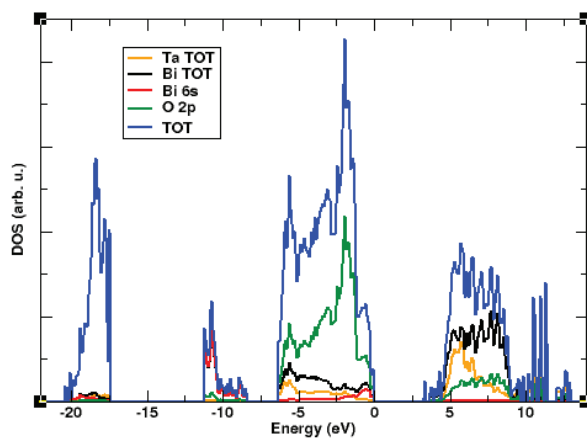


**Figure S.1.5** Calculated total and partial DOS of  $\text{Bi}_{0.75}\text{Ta}_{0.25}\text{O}_{1.75}$  configuration A (B3LYP)

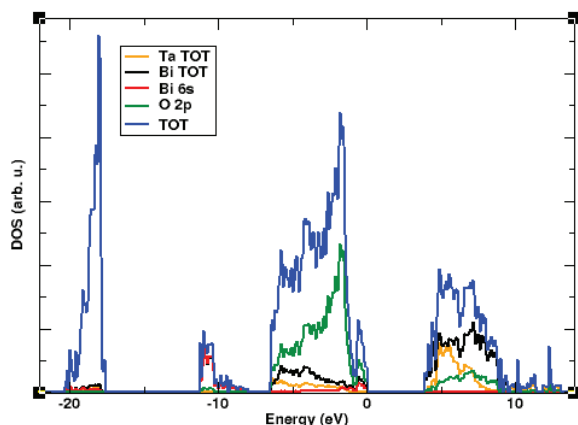


**Figure S.1.6** Calculated total and partial DOS of  $\text{Bi}_{0.75}\text{Ta}_{0.25}\text{O}_{1.75}$  configuration B (B3LYP)

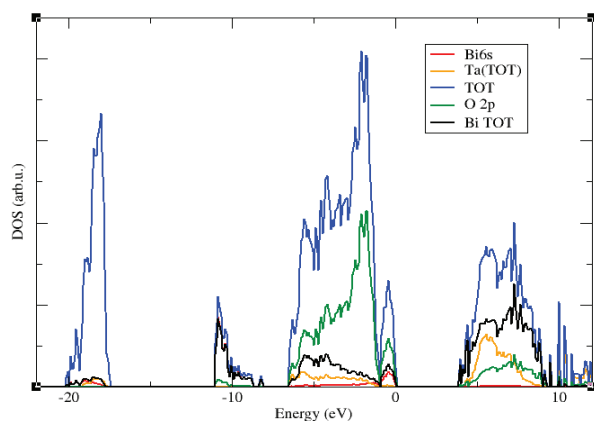


**Figure S.1.7** Calculated total and partial DOS of  $\text{Bi}_{0.75}\text{Ta}_{0.25}\text{O}_{1.75}$  configuration C (B3LYP)

$\text{Bi}_{0.75}\text{Ta}_{0.25}\text{O}_{1.75}$  with isolated  $\text{Ta}_4\text{O}_{18}$  clusters: cartesian coordinates of the optimized B3LYP structures

```

TA      1.490196295241E+00  1.375110889505E+00  1.420214962815E+00
TA     -1.243236696187E+00 -1.287453607193E+00 -4.242129017459E+00
BI      4.142975878304E+00 -3.966404134142E+00 -1.439209085046E+00
BI     -4.142675141586E+00 -1.399197261704E+00  4.176665014171E+00
BI      4.213013870731E+00 -1.377061967828E+00 -4.185329942364E+00
BI     -1.167463690195E+00 -4.230867032930E+00  4.261330542563E+00
TA     -3.963143201424E+00 -1.187852951704E+00 -1.441966023836E+00
BI      1.495960321877E+00 -3.932172055371E+00 -4.037607661813E+00
BI     -1.430460800580E+00 -1.350485480020E+00  1.463728677161E+00
TA      4.174970618054E+00  1.284474713639E+00  4.167860289945E+00
TA      4.224692830477E+00  3.916540403554E+00  1.395406162539E+00
TA     -1.471954317107E+00 -3.904878493160E+00 -1.187229219941E+00
TA     -3.957163525711E+00 -3.987421524870E+00 -3.966258980101E+00
BI      1.182491000969E+00 -1.189060188170E+00 -1.220788491158E+00
TA      1.486439092881E+00  4.023192136598E+00  4.011076363211E+00
BI     -4.061680999786E+00 -3.931160162862E+00  1.481252997266E+00
BI     -4.076992412284E+00  1.277525931544E+00 -4.109935148033E+00
BI      4.151583926917E+00 -1.383960220491E+00  1.375494209370E+00

```

BI	-1.459329716219E+00	1.364854538576E+00	4.062137555039E+00
BI	1.348499602411E+00	3.985438488141E+00	-1.659060654155E+00
BI	-1.455045715953E+00	4.066972380936E+00	1.326636578756E+00
BI	4.105798926697E+00	1.261948545879E+00	-1.415229243657E+00
BI	1.213496289020E+00	-1.320467466855E+00	4.011036364470E+00
BI	-4.074116399806E+00	1.268909185141E+00	1.346059135115E+00
BI	4.160995517855E+00	3.946453372804E+00	-4.000483802734E+00
BI	-1.404213395972E+00	1.380511747027E+00	-1.385209779736E+00
BI	-1.350092226751E+00	3.966238147874E+00	-4.037285328004E+00
BI	3.849046644309E+00	-3.933298169895E+00	4.000717638626E+00
BI	1.403730856352E+00	-4.275497682126E+00	1.112552990125E+00
BI	-3.998874951032E+00	4.040161979322E+00	4.067131464839E+00
BI	-4.042278127394E+00	3.937971985468E+00	-1.365583617832E+00
BI	1.428372132502E+00	1.150449518693E+00	-4.116764754624E+00
O	-5.400484382227E+00	-2.020386732262E-01	5.408493805501E+00
O	-5.326100166419E+00	-5.575864065034E-01	-7.948970151921E-02
O	-2.287272390201E-02	-4.067782307179E-02	5.305551793741E+00
O	-2.701055217468E-01	5.288637466407E+00	-6.020233664552E-01
O	2.464941344189E+00	-3.004853701025E+00	2.529762759022E+00
O	-2.789980735503E+00	2.664874298200E+00	-2.659207330235E+00
O	-2.859660808490E+00	2.803707047478E+00	2.614415951490E+00
O	2.808571698352E+00	2.542910157442E+00	-2.868443196444E+00
O	2.345923227859E+00	6.103252206968E-02	1.895241448553E-01
O	-2.432276232321E+00	-1.715131869438E-01	-5.356971013815E+00
O	3.699919107165E+00	5.196920337481E+00	3.538147141223E-02
O	-3.277004368394E+00	5.467489662797E+00	-5.216100794714E+00
O	2.044737737683E-01	1.928180796935E+00	1.208020246584E-01
O	-3.202428080234E-01	-3.015534523975E+00	3.852146910237E-01
O	5.277726612668E+00	2.299793796976E+00	-5.501730843739E+00
O	1.733413277038E-02	3.621225218762E+00	5.149297200642E+00
O	-5.673135158769E+00	-3.188421543464E+00	2.704023960733E-01
O	-5.422477981381E+00	2.916269136939E+00	1.264357269724E-01
O	2.152951646239E-01	-8.239721084449E-02	2.059534535337E+00
O	-5.295777270818E+00	-4.610913124738E-02	-2.568455353101E+00
O	5.309579368417E+00	7.274217786520E-02	2.975947962069E+00
O	3.599353140651E-01	5.181135545152E+00	-3.261737046815E+00
O	-4.824529555087E-02	-2.804417687091E-01	-3.099721046916E+00
O	-2.645673024110E+00	-6.795810681001E-01	-2.760491360324E+00
O	2.713563446479E+00	7.009257580126E-01	2.905019123880E+00
O	2.923882623650E+00	5.283496981775E+00	-2.688009979348E+00
O	-2.757763966086E+00	3.251736202264E-02	2.787849629172E+00
O	5.256102597304E+00	-2.596481967166E+00	2.940830834471E+00
O	8.381990892051E-01	2.734642177785E+00	2.696396463336E+00
O	5.416794891814E+00	2.759337583802E+00	-2.680558289846E+00
O	-2.531342896313E+00	-2.719744680134E+00	-4.542124031215E+00
O	2.421103895690E+00	-2.863544709731E+00	-6.741511280033E-01
O	-2.724307438864E+00	2.684662213199E+00	5.330331239530E+00
O	2.842480216645E+00	2.646020379020E+00	8.257324892037E-01
O	-8.850508820417E-01	-2.385407178585E+00	3.268458739919E+00
O	-4.593206657808E+00	-2.648928361777E+00	-2.549112699118E+00
O	2.571522660554E+00	-2.086608776601E-01	-2.611371832194E+00

O	-2.598883703170E+00	-5.239547367551E+00	2.960340588431E+00
O	-2.819389770099E+00	-2.572689032917E+00	-6.121300040972E-01
O	2.928334717071E+00	-2.454017993032E+00	5.245413077326E+00
O	6.590365175500E-02	-2.584367647626E+00	-5.130003947955E+00
O	3.089216212065E+00	1.952834017754E-01	-5.338995206989E+00
O	-2.905301791116E+00	7.712440373088E-02	-2.263932486976E-01
O	-5.251899448701E+00	-5.266332274688E+00	-3.288547021767E+00
O	2.641120375783E-01	-5.185217199956E+00	2.909288838415E+00
O	1.963399680714E+00	-5.102832073067E+00	5.134096419715E+00
O	-2.763169015376E+00	-5.110724789163E+00	1.757937594943E-01
O	-5.216634341807E+00	-3.065593984115E+00	-5.168279762106E+00
O	-5.977365879600E-01	-2.797359868695E+00	-2.414498239645E+00
O	4.768961588362E+00	2.637123523320E+00	2.803295837633E+00
O	2.747910243798E+00	2.772608226305E+00	4.680549480727E+00
O	2.891919253277E+00	4.701236677447E+00	2.665126265776E+00
O	-2.627939401121E+00	-4.674256992952E+00	-2.555334748571E+00
O	-5.197682827339E+00	5.060866993544E+00	2.041478627189E+00
O	-2.571286558957E+00	2.769585062024E+00	-7.659849591519E-02
O	-7.601529579087E-02	2.670211428312E+00	-2.776397944294E+00

**Bi<sub>0.75</sub>Ta<sub>0.25</sub>O<sub>1.75</sub> with tantalum strings: cartesian coordinates of the optimized B3LYP structures**

TA	1.280721816287E+00	1.440562197937E+00	1.503933678036E+00
BI	-1.412701327753E+00	4.109921703570E+00	-4.177675045417E+00
BI	3.953202522729E+00	-4.038135837419E+00	-1.433689732597E+00
TA	-4.020904480848E+00	-1.377847968986E+00	4.105811295342E+00
BI	3.996680284497E+00	-1.415347414903E+00	-4.147399214400E+00
TA	-1.272793449734E+00	-3.973833958153E+00	4.067941860603E+00
BI	-4.004566542796E+00	4.013366321725E+00	-1.424582338623E+00
BI	1.168806674292E+00	-4.303004438233E+00	-4.430823576065E+00
TA	-1.426583036046E+00	-1.415986096408E+00	1.354643882909E+00
TA	4.009387074298E+00	1.255516429738E+00	4.087955360970E+00
TA	4.040608863868E+00	4.023015715387E+00	1.475019716353E+00
BI	-1.190856181210E+00	1.111041529942E+00	-1.149882541153E+00
BI	-3.973501594458E+00	1.399401009229E+00	-4.146830722833E+00
BI	1.406916235300E+00	-1.314348995194E+00	-1.393339096326E+00
TA	1.447861177953E+00	3.987615662236E+00	4.226697549791E+00
TA	-4.002575472628E+00	-4.135805393115E+00	1.482586355786E+00
BI	-3.803528367283E+00	-3.929512986083E+00	-4.281263903922E+00
BI	4.189200033458E+00	-1.684847052646E+00	1.308108958944E+00
BI	-1.617211973194E+00	1.137024101626E+00	4.046322876725E+00
BI	1.024586718897E+00	4.051971565249E+00	-1.322376959661E+00
BI	-1.464967432428E+00	4.007131856003E+00	1.293443443197E+00
BI	3.784256528050E+00	1.463322289856E+00	-1.299606040064E+00
BI	1.485923025189E+00	-1.419959165677E+00	4.288184524400E+00
BI	-4.044640939247E+00	1.307171946090E+00	1.167089129792E+00
BI	4.041331657051E+00	4.104366034819E+00	-3.853155256742E+00
BI	-1.354556006028E+00	-3.981363948161E+00	-1.607957317758E+00
BI	-1.032800569256E+00	-1.353023841356E+00	-4.248730958614E+00

BI	4.052437492381E+00	-4.131951653065E+00	4.403605778552E+00
BI	1.623368384980E+00	-4.279161029615E+00	1.523504952788E+00
BI	-4.169593630834E+00	3.742943253970E+00	4.273514469564E+00
BI	-4.049006014356E+00	-1.295466197066E+00	-1.717804596000E+00
BI	1.333432595006E+00	1.430099539736E+00	-3.971600442899E+00
O	-4.892552280596E+00	4.994152918317E+00	-5.139179192826E+00
O	4.892768839152E+00	-4.477178796504E-01	-4.243794626867E-01
O	4.394137456558E-01	-1.154359733937E-01	-5.507621542283E+00
O	-4.409743157394E-01	5.292445606756E+00	-5.893045350635E-02
O	2.930852694314E+00	-3.207503063337E+00	2.857706002280E+00
O	-2.520306720485E+00	-2.535145266556E+00	-3.007594461301E+00
O	-2.918733271094E+00	2.221166035244E+00	2.717197328695E+00
O	2.507154695324E+00	2.867326678928E+00	-2.568475848304E+00
O	1.730350898328E+00	4.587813818474E-01	-1.168855760369E-01
O	-1.755591826242E+00	-4.938549613078E+00	-5.467514084707E+00
O	3.180182296152E+00	-5.397018617117E+00	3.059310536654E-01
O	-3.180555479831E+00	2.326606561420E-02	5.260685202190E+00
O	7.711364609017E-02	2.652408159408E+00	4.089984726550E-01
O	-5.289216959349E+00	-2.070706675843E+00	5.367446866257E+00
O	3.629250431900E-01	3.786615560634E+00	-5.353299410265E+00
O	-5.358812930801E+00	-3.298820886691E+00	2.792114029908E-01
O	-1.245812601545E-01	1.392949878556E-01	1.902739550531E+00
O	5.017238915595E+00	5.086000986540E+00	-2.083877632503E+00
O	-5.323402421936E+00	-3.137781368465E-03	3.363784179753E+00
O	-1.063849938568E-01	5.382449940060E+00	-2.792811204686E+00
O	-2.852844250294E+00	-5.171098378484E+00	-2.739741519237E+00
O	2.649993570996E+00	7.155070983883E-01	2.726782405063E+00
O	2.771856857672E+00	-4.907391043165E+00	-3.138802134542E+00
O	-2.576895927198E+00	-6.940227710737E-01	2.857688346076E+00
O	-2.713111289282E-01	2.680953625159E+00	-2.500220968097E+00
O	-4.648213210190E+00	-2.678300185832E+00	2.746031442408E+00
O	6.465126215381E-01	2.710617213849E+00	2.976394336335E+00
O	-5.299986517982E+00	-2.928222882100E+00	-2.861519502569E+00
O	-2.427319427856E+00	2.853300702107E+00	5.234865291165E+00
O	2.442331736130E+00	-2.563369185504E+00	3.421450869556E-01
O	-2.704648923731E+00	-2.696165965169E+00	4.667250897430E+00
O	2.718809250977E+00	2.712742627964E+00	9.077577306554E-01
O	-6.316373289693E-01	-2.702455443196E+00	2.597522856326E+00
O	5.284464532348E+00	2.461539785529E+00	-2.715831550029E+00
O	2.826382212617E+00	2.297595023774E-01	-2.843918118881E+00
O	-2.645614561164E+00	-4.686779064722E+00	2.841454695765E+00
O	-2.633792597311E+00	2.605052809902E+00	-8.740608246215E-03
O	2.620214315009E+00	-2.812733866140E+00	-5.568096646746E+00
O	-6.219894140811E-02	-2.772488931847E+00	5.164813911719E+00
O	5.306137431566E+00	3.328670576954E+00	2.109502652745E-01
O	3.369507834323E+00	-5.640496358016E-02	5.352033833424E+00
O	-3.342807708493E+00	5.384535764673E+00	2.323253417443E-01
O	-5.020909934676E+00	-3.026682806898E-01	-3.482734731738E+00
O	1.248248670079E-01	-5.281692180360E+00	3.664423663428E+00
O	2.642116953858E+00	5.275443960643E+00	5.219098188743E+00
O	-2.613693202175E+00	-1.159270677702E-01	3.663363492801E-01

O -3.707028006644E-01 -1.635441592749E+00 -2.183474652367E-01  
 O -5.345797370032E+00 2.106124205659E+00 5.215117416432E+00  
 O 2.581338361241E-01 -2.733674785834E+00 -3.077636232724E+00  
 O 4.660349438179E+00 2.714814978610E+00 2.830438918133E+00  
 O -2.666096562743E+00 -2.812416344005E+00 8.547696302887E-01  
 O 2.677292961929E+00 2.580006793926E+00 4.721313936427E+00  
 O 2.601133025255E+00 4.709189950279E+00 2.726182208268E+00  
 O -2.796146207411E+00 5.182433228307E-01 -2.445209587397E+00  
 O 5.350006317094E+00 5.389114322899E+00 2.220454817911E+00  
 O 1.017773028729E-01 -3.517471786263E-02 -2.773327788724E+00

## S.2 SUPPORTING INFORMATION

### XAS and DFT investigation on doped LaGaO<sub>3</sub>

#### DFT calculations benchmark

Five different DFT methods were considered for the description of the pure LG unit cell, with orthorhombic space group *Pbnm*. The PBE0 functional better reproduced experimental cell parameters, giving a difference of 0.25%, 0.06% and 0.53% respectively on a, b and c, and 0.22% on the volume of the cell. Results are reported in **Table S.1**.

**Table S.2.1** Cell parameters (a, b, c) in Å and volume (V) in Å<sup>3</sup> obtained with different DFT methods compared to experimental data taken from Morozov, A.N et al. *Kristallografiya* **1993**, 38, 149-159.

Functional	a	b	c	V
Exp	5.4858(9)	7.7642(1)	5.5139(5)	234.8(6)
PBE0	5.472	7.759	5.543	235.4
B3LYP	5.552	7.870	5.584	244.0
SOGGA	5.439	7.712	5.549	232.8
B3PW	5.489	7.784	5.558	237.5
PBE	5.530	7.845	5.598	242.8

The electronic structure of pure LG was initially tested using the PBE0, B3LYP and PBE functionals in order to investigate the effect of the functional on the electronic band gap energy value (**Table 8**).



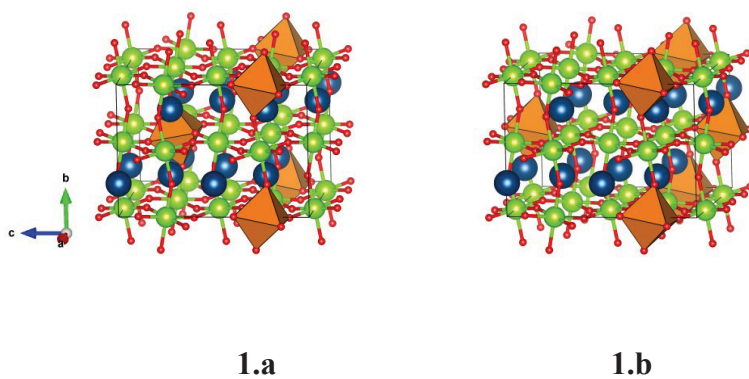
**Table S.2.2** Band gap values (eV) computed for pure LG Pbnm unit cell at different levels of theory.

Functional	Band gap (eV)
PBE0	7.11
B3LYP	6.17
PBE	4.29

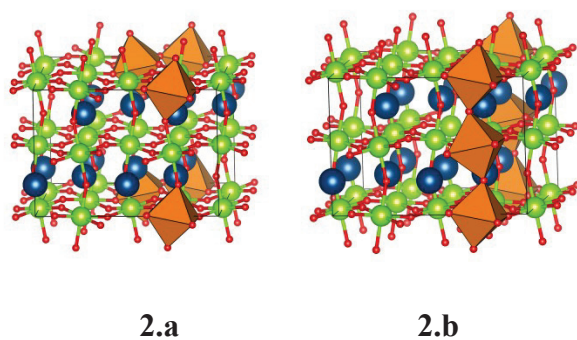
### Symmetry Independent Configurations (SICs)

**Figure S.2.1** Symmetry Independent Classes (SICs) for a (2x1x2) supercell of LGM0125, grouped in three macro-classes: **1)** Mg-layered, **2)** Mg-clustered and **3)** Mg, Ga-layered. Oxygen, lanthanum and gallium in red, blue and green, respectively. The Mg polyhedra are shown in orange.

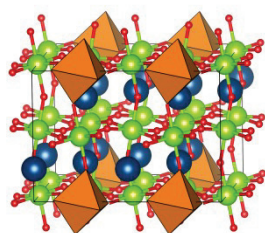
#### Mg-LAYERED



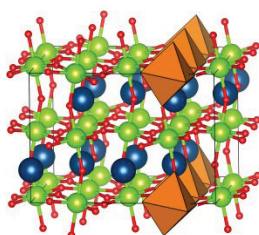
#### Mg-CLUSTERED



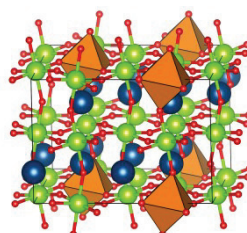
## Mg, Ga-LAYERED



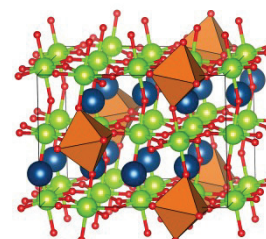
3.a



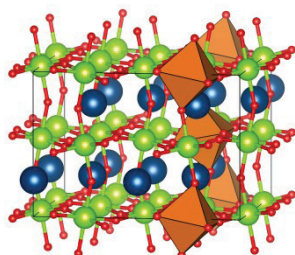
3.b



3.c



3.d



3.e

## EXAFS Ga K-edge

Theoretical EXAFS signals were calculated with GNXAS by embedding the absorber in a  $\text{LaGaO}_3$  cluster, using a cutoff radius of 8 Å. Amplitude reduction factor was determined by fitting a reference  $\text{Ga}_2\text{O}_3$  powder, giving  $S_0^2 = 0.85$ .

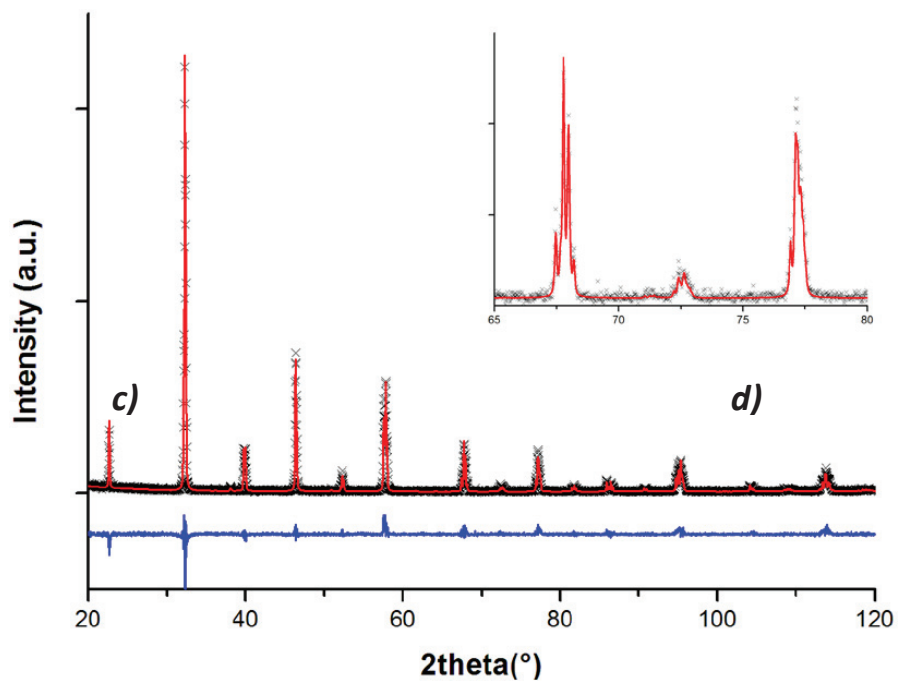
EXAFS data analysis was carried out taking into account statistical considerations in order to test out the validity of model. The maximum amount of information that can be extrapolated from EXAFS data can be evaluated by means of the Nyquist formula:

$$N \approx \frac{2\Delta K \Delta R}{\pi} + 2$$

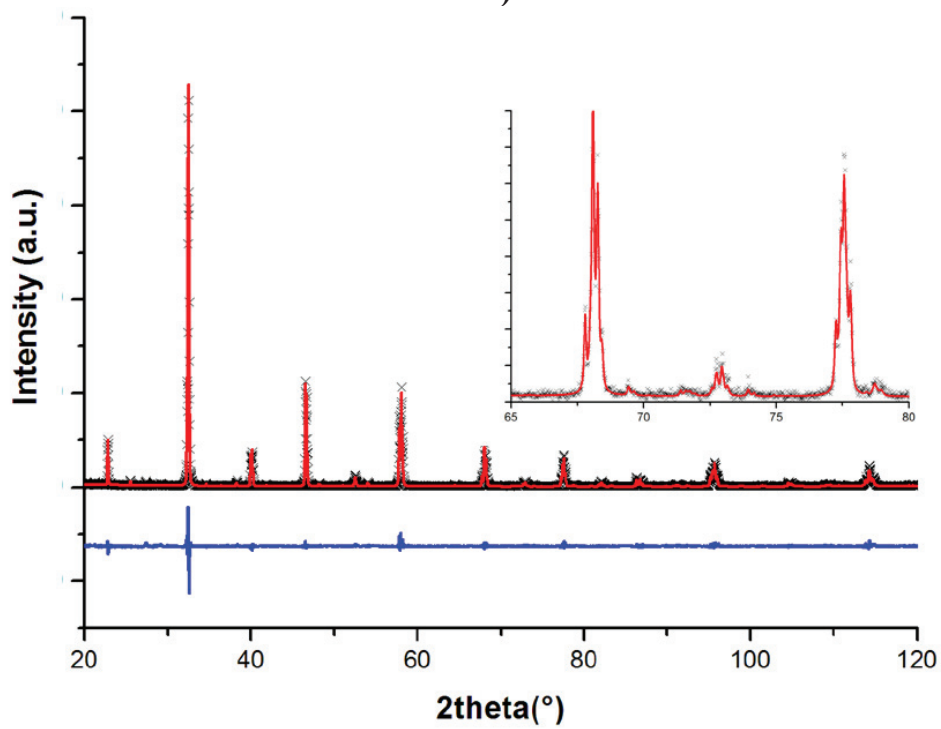
where  $\Delta K$  is the range in the  $k$  space,  $\Delta R$  is the  $R$  range of the Fourier Transform and  $N$  is the number of independent points.

All EXAFS data analysis on both pure  $\text{LaGaO}_3$  and doped  $\text{LaGa}_{0.875}\text{Mg}_{0.125}\text{O}_{2.935}$  was carried out in  $k$ -space and weighting data in  $k^2$ . The range in  $k$  space was kept between 2.00-12.50 Å<sup>-1</sup> ( $\Delta k=10.50$  Å<sup>-1</sup>), while the range in  $R$  space was fixed between 0.00 and 8.00 Å ( $\Delta R=8.00$  Å) leading to 55.60 independent points and only 15 free parameters fitted.

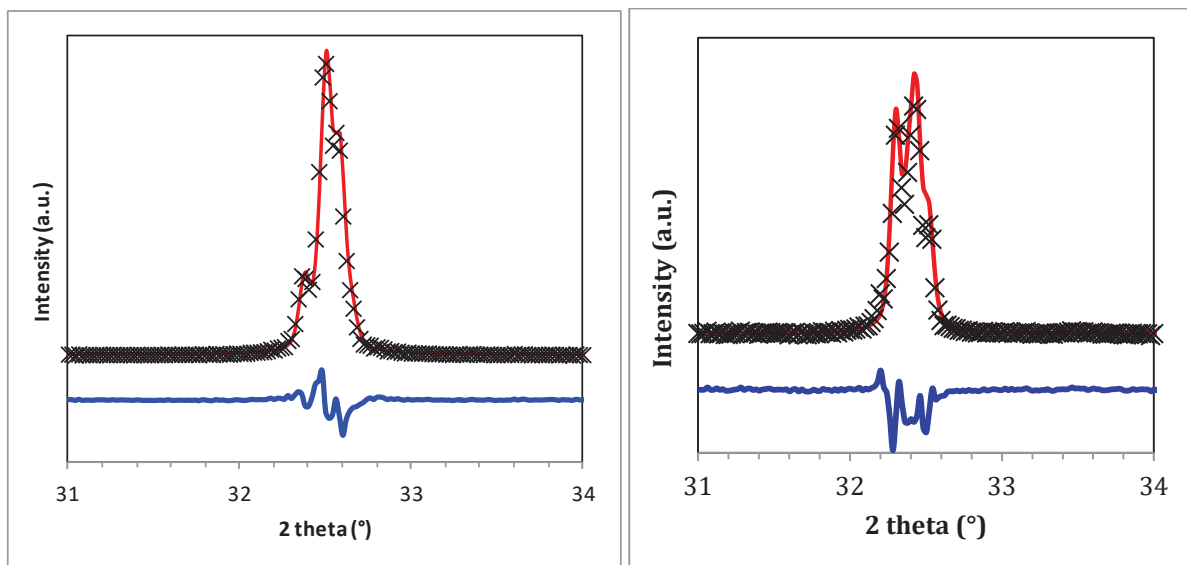
# X-Ray Diffraction



a)



b)



**c)**

**d)**

**Figure S.2.2** Rietveld refinement on **a)** pure LG and **b)** LGM0125 X-ray Diffraction pattern. Experimental data are shown as black crosses, fitting and residual as red and blue lines, respectively. Comparison between samples **c)** without Co co-doping (pure LG) and **d)** with Co co-doping (LSGMC2010). The peak at 32.5° is splitted in the case of a  $R-3c$  phase (LSGMC2010), when Sr concentration is increased at 20% [References: Trofimenko, N. et al. *Solid State Ionics* **1999** 118, 215-227. Tas, A. C. et al. *J. Am. Ceramic Soc.* **2000** 83 12 2954-2960; Kajitani, M. et al. *Chem. Mater.* **2003** 15 3468-73; Kajitani, M. et al. *Chem. Mater.* **2005** 17 4235-4243]

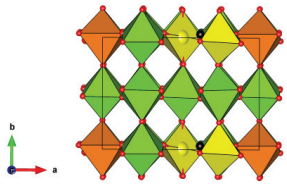
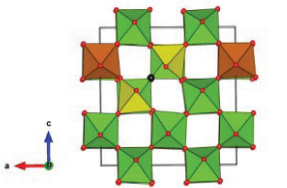
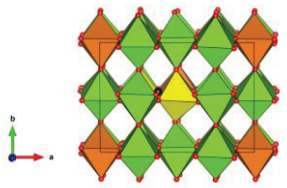
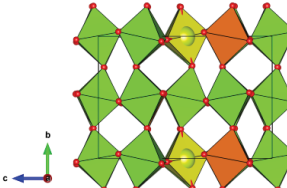
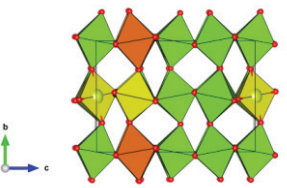
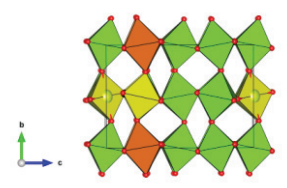
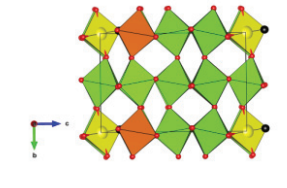
## SIC: Models and notations

28 possible oxygen vacancy configurations were all fully-optimized (unit cell and atomic positions). i) 13 for the *Mg-layered* macro-class, resulting from: two axial Mg-Vo-Ga, two equatorial Mg-Vo-Ga, two axial Ga-Vo-Ga and seven equatorial Ga-Vo-Ga configurations; ii) 9 for the *Mg-clustered* macro-class, obtained from one axial Mg-Vo-Ga, one equatorial Mg-Vo-Ga, one equatorial Mg-Vo-Mg, three axial Ga-Vo-Ga and three equatorial Ga-Vo-Ga configurations; iii) 6 for the *Mg, Ga-layered* macro-class, built from one axial Mg-Vo-Ga, one equatorial Mg-Vo-Ga, two axial Ga-Vo-Ga and two equatorial Ga-Vo-Ga configurations. All 28 oxygen vacancy configurations considered and their relative energy stability among each macro-class are shown in the following tables.

### Mg-layered

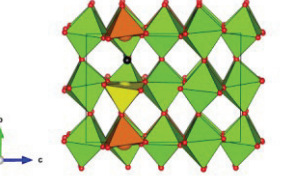
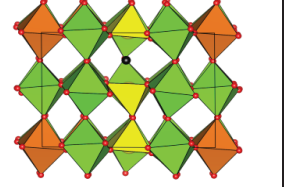
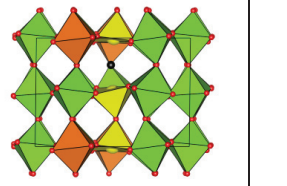
**Table S.2.3** (2x1x2) supercells (80 atoms) of the thirteen configurations of the doped LGM0125 belonging to the Mg-layered macro-class considered for structural analysis and their relative energies expressed in kcal/mol. Ga polyhedra are drawn in green, Ga polyhedra hosting the vacancy in yellow, Mg polyhedra in orange, oxygen atoms in red and vacancy site in black. La atoms are omitted for clarity.

Ga-Vo <sup>3</sup> -Ga <sub>ax</sub>	Ga-Vo <sup>5</sup> -Ga <sub>ax</sub>	Mg-Vo <sup>1</sup> -Ga <sub>ax</sub>
0.00	0.06	0.76
Ga-Vo <sup>3</sup> -Ga <sub>eq</sub>	Ga-Vo <sup>5</sup> -Ga <sub>eq</sub>	Mg-Vo <sup>1</sup> -Ga <sub>ax</sub>
2.19	2.46	2.54

		
Ga-Vo <sup>3</sup> -Ga <sub>eq</sub>	Ga-Vo <sup>3</sup> -Ga <sub>eq</sub>	Ga-Vo <sup>3</sup> -Ga <sub>eq</sub>
2.79	3.04	3.06
		
Mg-Vo <sup>1</sup> -Ga <sub>eq</sub>	Ga-Vo <sup>3</sup> -Ga <sub>eq</sub>	Ga-Vo <sup>3</sup> -Ga <sub>eq</sub>
4.77	4.90	5.20
		
Mg-Vo <sup>1</sup> -Ga <sub>eq</sub>		
5.46		

### Mg-clustered

**Table S.2.4** (2x1x2) supercells (80 atoms) of the nine configurations of the doped LGM0125 belonging to the Mg-layered macro-class considered for structural analysis and their relative energies expressed in kcal/mol. Ga polyhedra are drawn in green, Ga polyhedra hosting the vacancy in yellow, Mg polyhedra in orange, oxygen atoms in red and vacancy site in black. La atoms are omitted for clarity.

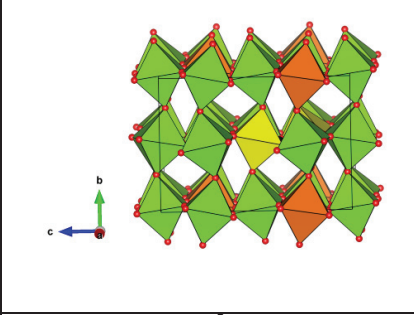
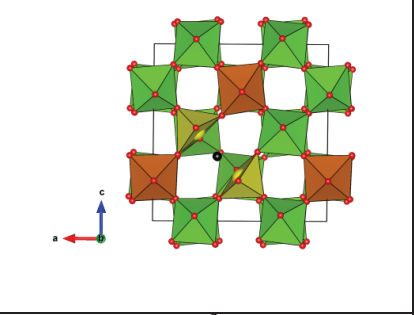
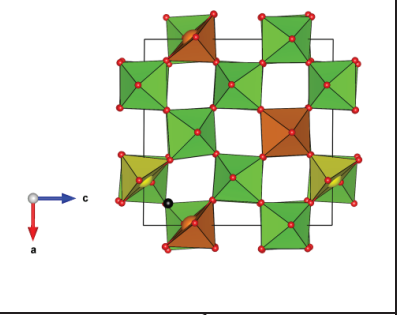
		
Mg-Vo <sup>1</sup> -Ga <sub>ax</sub>	Ga-Vo <sup>3</sup> -Ga <sub>ax</sub>	Ga-Vo <sup>3</sup> -Ga <sub>ax</sub>

0.00	1.92	2.07
Mg-Vo <sup>1</sup> -Mg <sub>eq</sub>	Ga-Vo <sup>3</sup> -Ga <sub>ax</sub>	Ga-Vo <sup>3</sup> -Ga <sub>eq</sub>
2.37	5.66	6.55
Ga-Vo <sup>1</sup> -Mg <sub>eq</sub>	Ga-Vo <sup>5</sup> -Ga <sub>eq</sub>	Ga-Vo <sup>5</sup> -Ga <sub>eq</sub>
7.07	7.78	8.91

### Mg, Ga-layered

**Table S.2.5** (2x1x2) supercells (80 atoms) of the six configurations of the doped LGM0125 belonging to the Mg-layered macro-class considered for structural analysis and their relative energies expressed in kcal/mol. Ga polyhedra are drawn in green, Ga polyhedra hosting the vacancy in yellow, Mg polyhedra in orange, oxygen atoms in red and vacancy site in black. La atoms are omitted for clarity.

Ga-Vo <sup>5</sup> -Ga <sub>ax</sub>	Ga-Vo <sup>3</sup> -Ga <sub>ax</sub>	Mg-Vo <sup>1</sup> -Ga <sub>ax</sub>

0.00	0.48	2.34
		
Ga-Vo <sup>5</sup> -Ga <sub>eq</sub>	Ga-Vo <sup>3</sup> -Ga <sub>eq</sub>	Mg-Vo <sup>1</sup> -Ga <sub>eq</sub>
3.45	4.56	6.52

### Energetic scale of the generated configurations

**Table S.2.6** Relative Energy ( $\Delta E$ ) of different vacancy positions, obtained from the SIC analysis of LGM0125, for the 28 configurations considered. All data in kcal/mol. For details about configuration notation, see text (section 3.2.1).

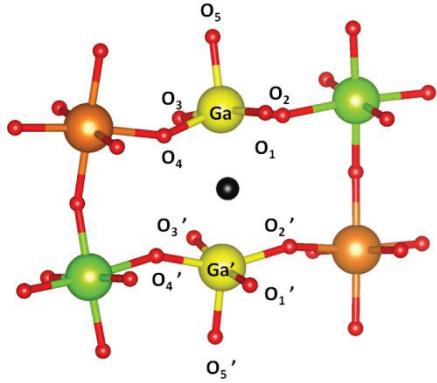
Macro-class	Configuration	$\Delta E$
Mg, Ga-layered	Ga-Vo <sup>5</sup> -Ga <sub>ax</sub>	0.00
Mg, Ga-layered	Ga-Vo <sup>3</sup> -Ga <sub>ax</sub>	0.48
Mg-clustered	Mg-Vo <sup>1</sup> -Ga <sub>ax</sub>	0.71
Mg-layered	Ga-Vo <sup>3</sup> -Ga <sub>ax</sub>	2.33
Mg, Ga-layered	Mg-Vo <sup>1</sup> -Ga <sub>ax</sub>	2.34
Mg-layered	Ga-Vo <sup>5</sup> -Ga <sub>ax</sub>	2.39
Mg-clustered	Ga-Vo <sup>3</sup> -Ga <sub>ax</sub>	2.64
Mg-clustered	Ga-Vo <sup>3</sup> -Ga <sub>ax</sub>	2.79
Mg-clustered	Mg-Vo <sup>1</sup> -Mg <sub>eq</sub>	3.08
Mg-layered	Mg-Vo <sup>1</sup> -Ga <sub>ax</sub>	3.09
Mg, Ga-layered	Ga-Vo <sup>5</sup> -Ga <sub>eq</sub>	3.45
Mg-layered	Ga-Vo <sup>3</sup> -Ga <sub>eq</sub>	4.53
Mg, Ga-layered	Ga-Vo <sup>3</sup> -Ga <sub>eq</sub>	4.56
Mg-layered	Ga-Vo <sup>5</sup> -Ga <sub>eq</sub>	4.80
Mg-layered	Mg-Vo <sup>1</sup> -Ga <sub>ax</sub>	4.97

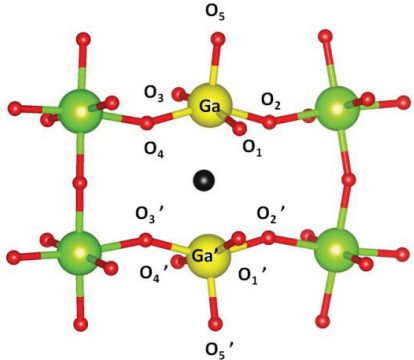
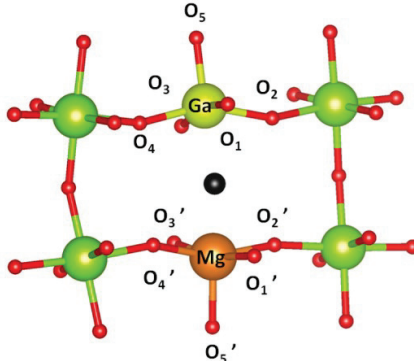


Mg-layered	Ga-Vo <sup>3</sup> -Ga <sub>eq</sub>	5.12
Mg-layered	Ga-Vo <sup>3</sup> -Ga <sub>eq</sub>	5.37
Mg-layered	Ga-Vo <sup>3</sup> -Ga <sub>eq</sub>	5.40
Mg-clustered	Ga-Vo <sup>3</sup> -Ga <sub>ax</sub>	6.37
Mg, Ga-layered	Mg-Vo <sup>1</sup> -Ga <sub>eq</sub>	6.52
Mg-layered	Mg-Vo <sup>1</sup> -Ga <sub>eq</sub>	7.11
Mg-layered	Ga-Vo <sup>3</sup> -Ga <sub>eq</sub>	7.23
Mg-clustered	Ga-Vo <sup>3</sup> -Ga <sub>eq</sub>	7.27
Mg-layered	Ga-Vo <sup>3</sup> -Ga <sub>eq</sub>	7.53
Mg-clustered	Ga-Vo <sup>3</sup> -Mg <sub>eq</sub>	7.78
Mg-layered	Mg-Vo <sup>1</sup> -Ga <sub>eq</sub>	7.80
Mg-clustered	Ga-Vo <sup>5</sup> -Ga <sub>eq</sub>	8.50
Mg-clustered	Ga-Vo <sup>5</sup> -Ga <sub>eq</sub>	9.62

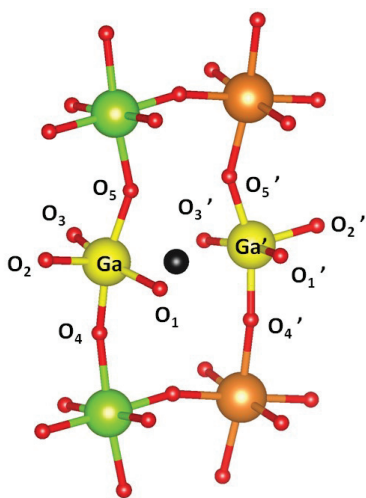
### Local structure distortions

**Table S.2.7** Selected geometric parameters around oxygen vacancies for the five considered configurations of the Mg-layered macro-class: cation-oxygen distances ( $d_{M-O}$ , Å) and  $O_{ax}$ -M- $O_{eq}$  angles ( $a_{O_{ax}-M-O_{eq}}$ , in degrees). Ga atoms in green or yellow, Mg in orange, O in red, oxygen vacancy in black. La atoms omitted for clarity.

STRUCTURE	CONFIGURATION	dM-O		aO <sub>ax</sub> -M-O <sub>eq</sub>	
	Ga-Vo <sup>3</sup> -Ga <sub>ax</sub>	Ga-O <sub>4</sub>	1.88	O <sub>5</sub> -Ga-O <sub>3</sub>	93.91
		Ga-O <sub>5</sub>		O <sub>5</sub> '-Ga'-O <sub>1</sub> '	
		Ga'-O <sub>2</sub> '		O <sub>5</sub> '-Ga'-O <sub>3</sub> '	
		Ga'-O <sub>4</sub> '	Ga'-O <sub>5</sub> '	99.23	O <sub>5</sub> -Ga-O <sub>1</sub>
		Ga'-O <sub>5</sub> '	O <sub>5</sub> -Ga-O <sub>2</sub>		
		Ga-O <sub>2</sub>	1.90	O <sub>5</sub> '-Ga'-O <sub>4</sub> '	106.27
		Ga-O <sub>1</sub>		O <sub>5</sub> -Ga-O <sub>4</sub>	
		Ga-O <sub>3</sub>	Ga'-O <sub>1</sub> '	1.96	O <sub>5</sub> '-Ga'-O <sub>2</sub> '
		Ga'-O <sub>1</sub> '	O <sub>5</sub> '-Ga'-O <sub>3</sub> '		
		Ga'-O <sub>3</sub> '			

	Ga-Vo <sup>5</sup> -Ga <sub>ax</sub>	Ga-O <sub>5</sub> Ga'-O <sub>5'</sub>  Ga-O <sub>2</sub> Ga-O <sub>4</sub> Ga'-O <sub>2'</sub> Ga'-O <sub>4'</sub>  Ga-O <sub>1</sub> Ga-O <sub>3</sub> Ga'-O <sub>1'</sub> Ga'-O <sub>3'</sub>	1.87  1.91  1.95	O <sub>5</sub> -Ga-O <sub>1</sub> O <sub>5'</sub> -Ga'-O <sub>1'</sub>  O <sub>5</sub> -Ga-O <sub>3</sub> O <sub>5'</sub> -Ga'-O <sub>3'</sub>  O <sub>5</sub> -Ga-O <sub>2</sub> O <sub>5</sub> -Ga-O <sub>4</sub> O <sub>5'</sub> -Ga'-O <sub>2'</sub> O <sub>5'</sub> -Ga'-O <sub>4'</sub>	92.97  97.48  104.74
	Ga-Vo <sup>1</sup> -Mg <sub>ax</sub>	Ga-O <sub>5</sub>  Ga-O <sub>2</sub> Ga-O <sub>4</sub> Mg-O <sub>5'</sub>  Ga-O <sub>1</sub> Ga-O <sub>3</sub> Mg-O <sub>1'</sub>	1.84 1.91  1.96	O <sub>5'</sub> -Mg-O <sub>3'</sub>  O <sub>5</sub> -Ga-O <sub>1</sub> O <sub>5</sub> -Ga-O <sub>3</sub> O <sub>5</sub> -Ga-O <sub>4</sub> O <sub>5'</sub> -Mg-O <sub>1'</sub> O <sub>5'</sub> -Mg-O <sub>2'</sub> O <sub>5</sub> -Ga-O <sub>2</sub> O <sub>5'</sub> -Mg-O <sub>4'</sub>	94.40  97.44  103.72

		Mg-O <sub>2</sub> '			
		Mg-O <sub>3</sub> '			
		Mg-O <sub>4</sub> '			
		Ga-O <sub>2</sub>	1.86	O <sub>2</sub> '-Ga'-O <sub>1</sub> '	94.23
		Ga'-O <sub>2</sub> '			
		Ga'-O <sub>4</sub> '		O <sub>2</sub> -Ga-O <sub>5</sub>	
		Ga'-O <sub>5</sub> '		O <sub>2</sub> -Ga-O <sub>3</sub>	97.94
		Ga-O <sub>1</sub>	1.93	O <sub>2</sub> '-Ga'-O <sub>5</sub> '	
		Ga-O <sub>3</sub>			
		Ga-O <sub>4</sub>		O <sub>2</sub> -Ga-O <sub>1</sub>	
		Ga-O <sub>5</sub>		O <sub>2</sub> '-Ga'-O <sub>3</sub> '	
				O <sub>2</sub> '-Ga'-O <sub>4</sub> '	101.77
		Ga'-O <sub>1</sub> '	1.98		
		Ga'-O <sub>3</sub> '			

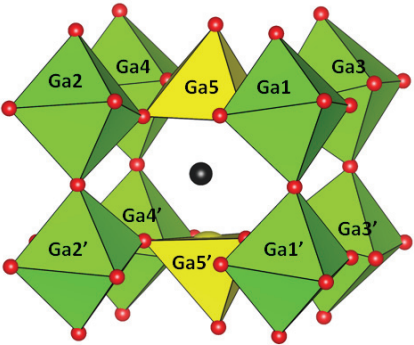
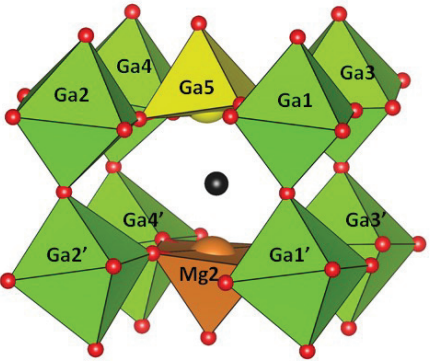


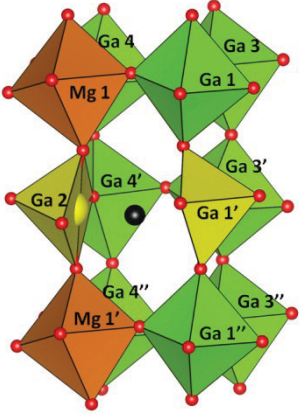
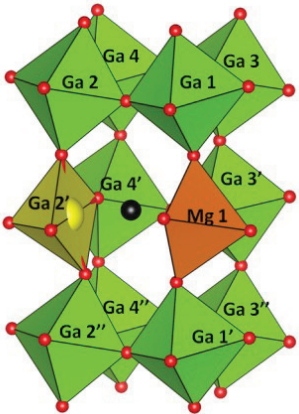
Ga-Vo<sup>3</sup>-Ga<sub>eq</sub>

	Ga-Vo <sup>1</sup> -Mg <sub>eq</sub>	Mg-O <sub>2</sub>	1.87	O <sub>2</sub> -Mg-O <sub>5</sub>	94.76
		Ga-O <sub>2</sub> '		O <sub>2</sub> -Mg-O <sub>3</sub>	
		Ga-O <sub>1</sub> '	1.94	O <sub>2</sub> -Mg-O <sub>4</sub>	98.24
		Ga-O <sub>3</sub> '		O <sub>2</sub> '-Ga-O <sub>1</sub> '	
		Ga-O <sub>4</sub> '		O <sub>2</sub> '-Ga-O <sub>5</sub> '	101.03
		Ga-O <sub>5</sub> '		O <sub>2</sub> -Mg-O <sub>1</sub>	
		Mg-O <sub>1</sub>	1.98	O <sub>2</sub> '-Ga-O <sub>3</sub> '	
		Mg-O <sub>3</sub>		O <sub>2</sub> '-Ga-O <sub>4</sub> '	
		Mg-O <sub>4</sub>			
		Mg-O <sub>5</sub>			

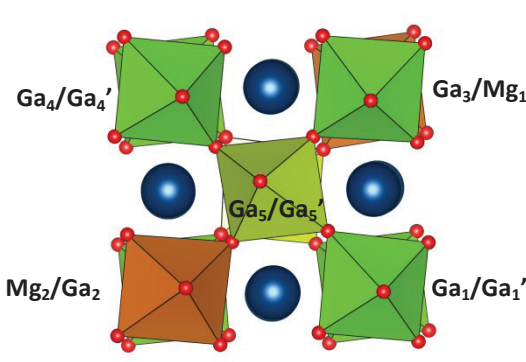
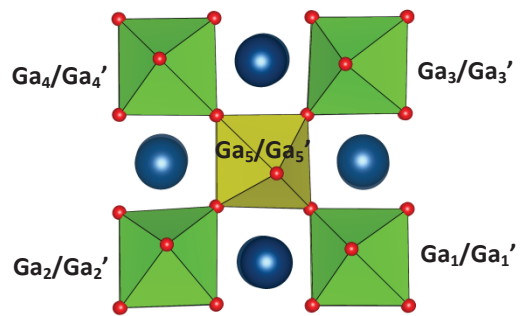
**Table S.2.8** Polyhedral representation and Ga-O-Ga' tilting angles ( $\alpha_{M-O_{ax}-Ga}$ , in degrees) for the five considered configurations of the Mg-layered macro-class. Ga polyhedra are drawn in green, Ga polyhedra hosting the vacancy in yellow, Mg polyhedra in orange, oxygen atoms in red, vacancy site in black. La atoms omitted for clarity.

STRUCTURE	CONFIGURATION	LABELS	Ga-O <sub>ax</sub> -M'
	Ga-Vo <sup>3</sup> -Ga <sub>ax</sub>	Ga1-O-Ga1' Ga4-O-Ga4'	156.92

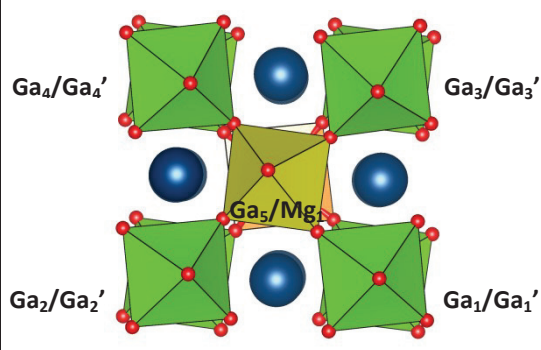
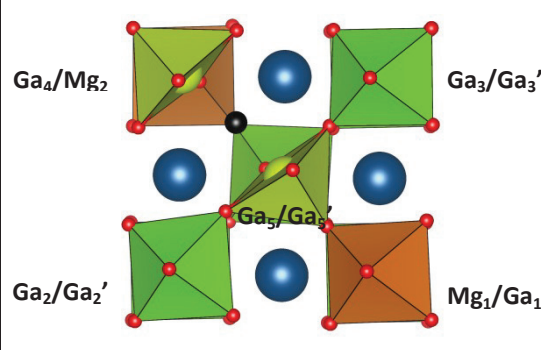
		Mg1-O-Ga2 Ga3-O-Mg2	162.28
	$\text{Ga-Vo}^5\text{-Ga}_{\text{ax}}$	Ga1-O-Ga1' Ga4-O-Ga4' Ga2-O-Ga2' Ga3-O-Ga3'	156.67
	$\text{Ga-Vo}^1\text{-Mg}_{\text{ax}}$	Ga2-O-Ga2' Ga4-O-Ga4' Ga1-O-Ga1' Ga3-O-Ga3'	157.90  162.57

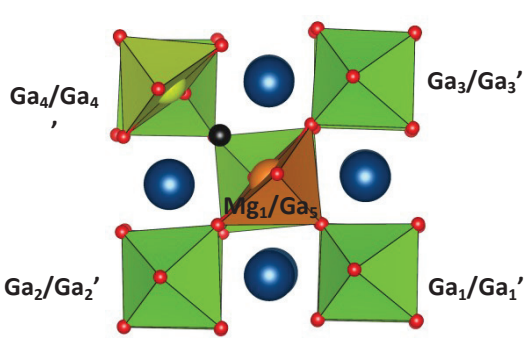
	<p>Ga-Vo<sup>3</sup>-Ga<sub>eq</sub></p>	<p>Ga1-O-Ga1'</p> <p>Mg1-O-Ga2'</p> <p>Ga3-O-Ga3'</p> <p>Ga3'-O-Ga3''</p> <p>Ga4-O-Ga4'</p> <p>Ga4'-O-Ga4''</p> <p>Ga1'-O-Ga1''</p> <p>Ga2-O-Mg1'</p>	<p>150.04</p> <p>158.51</p> <p>164.58</p>
	<p>Ga-Vo<sup>1</sup>-Mg<sub>eq</sub></p>	<p>Mg1-O-Ga1'</p> <p>Ga2'-O-Ga2''</p> <p>Ga3-O-Ga3'</p> <p>Ga3'-O-Ga3''</p> <p>Ga4-O-Ga4'</p> <p>Ga4'-O-Ga4''</p> <p>Ga1-O-Mg1</p> <p>Ga2-O-Ga2'</p>	<p>151.07</p> <p>158.96</p> <p>164.63</p>

**Table S.2.9** Dihedral angles  $d_\alpha$ ,  $d_\beta$ ,  $d_\gamma$  and  $d_\delta$  ( $O_\alpha$ - $M_x$ - $M_x'$ - $O_\alpha'$ ,  $O_\beta$ - $M_x$ - $M_x'$ - $O_\beta'$ ,  $O_\gamma$ - $M_x$ - $M_x'$ - $O_\gamma'$  and  $O_\delta$ - $M_x$ - $M_x'$ - $O_\delta'$ ) (see Figure 1.c) showing mutual rotation between equatorial oxygen ions on two underlying  $M_x/M_x'$  ( $M$ =Ga or Mg) cations. Ga polyhedra are drawn in green, Ga polyhedra hosting the vacancy in yellow, Mg polyhedra in orange, oxygen atoms in red, vacancy site in black and La atoms in blue. For definition of  $d_\alpha$ ,  $d_\beta$ ,  $d_\gamma$  and  $d_\delta$ , see **Figure 1.b**: gallium atoms are arranged in two underlying layers named  $Ga_x$  (upper plane) and  $Ga_x'$  (lower plane), while equatorial oxygen on  $Ga_x$  are referred to as  $O_\alpha$ ,  $O_\beta$ ,  $O_\gamma$  and  $O_\delta$  and those on  $Ga_x'$  as  $O_\alpha'$ ,  $O_\beta'$ ,  $O_\gamma'$  and  $O_\delta'$ . For each  $Ga_x/Ga_x'$  couple of underlying gallium atoms, four dihedral angles ( $d_\alpha$ ,  $d_\beta$ ,  $d_\gamma$  and  $d_\delta$ ) exist.

STRUCTURE	CONFIG.	LABEL	$d_\alpha$ (°)	$d_\beta$ (°)	$d_\gamma$ (°)	$d_\delta$ (°)
	Ga- $Vo^3$ - $Ga_{ax}$	Ga <sub>1</sub> /Ga <sub>1</sub> '	12.29	12.99	14.11	12.02
		Mg <sub>2</sub> /Ga <sub>2</sub>	10.37	10.07	10.56	11.67
		Ga <sub>3</sub> /Mg <sub>1</sub>	10.83	12.31	11.59	12.84
		Ga <sub>4</sub> /Ga <sub>4</sub> '	10.82	13.85	12.43	12.86
		Ga <sub>5</sub> /Ga <sub>5</sub> '	14.30	14.20	11.36	11.44
	Ga- $Vo^5$ - $Ga_{ax}$	Ga <sub>1</sub> /Ga <sub>1</sub> '	0.31	0.03	0.27	0.12
		Ga <sub>2</sub> /Ga <sub>2</sub> '	0.14	0.12	0.21	0.21
		Ga <sub>3</sub> /Ga <sub>3</sub> '	0.13	0.24	0.20	0.02
		Ga <sub>4</sub> /Ga <sub>4</sub> '	0.74	0.07	0.63	0.05



		Ga <sub>5</sub> /Ga <sub>5</sub> '	0.04	0.28	0.46	0.21
	Ga-Vo <sup>1</sup> -Mg <sub>ax</sub>	Ga <sub>1</sub> /Ga <sub>1</sub> '	12.56	15.00	15.22	13.09
		Ga <sub>2</sub> /Ga <sub>2</sub> '	13.76	12.48	11.41	13.23
		Ga <sub>3</sub> /Ga <sub>3</sub> '	12.01	13.51	14.68	14.05
		Ga <sub>4</sub> /Ga <sub>4</sub> '	11.32	13.26	12.22	14.73
		Ga <sub>5</sub> /Mg <sub>1</sub>	15.18	15.03	11.73	12.94
	Ga-Vo <sup>3</sup> -Ga <sub>eq</sub>	Mg <sub>1</sub> /Ga <sub>1</sub>	1.25	1.65	1.80	1.34
		Ga <sub>2</sub> /Ga <sub>2</sub> '	1.52	7.22	3.69	2.37
		Ga <sub>3</sub> /Ga <sub>3</sub> '	0.61	0.07	1.38	2.93
		Ga <sub>4</sub> /Mg <sub>2</sub>	0.97	10.21	0.73	7.96
		Ga <sub>5</sub> /Ga <sub>5</sub> '	1.59	7.93	0.96	14.70

	Ga-Vo <sup>1</sup> -Mg <sub>eq</sub>	Ga <sub>1</sub> /Ga <sub>1</sub> '	0.28	0.39	0.45	0.49
		Ga <sub>2</sub> /Ga <sub>2</sub> '	0.72	5.34	4.02	1.02
		Ga <sub>3</sub> /Ga <sub>3</sub> '	1.98	0.76	3.10	2.10
		Ga <sub>4</sub> /Ga <sub>4</sub> '	2.44	11.93	0.15	9.67
		Mg <sub>1</sub> /Ga <sub>5</sub>	0.85	6.74	2.11	11.43

### Density of States

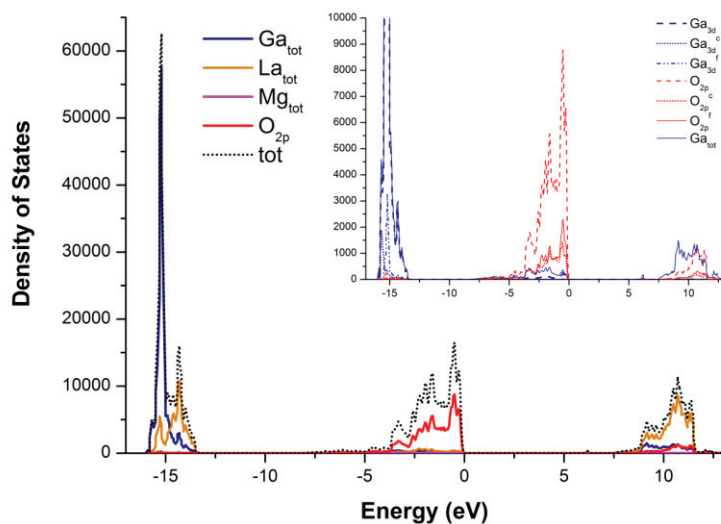


**Figure S.2.3** Total and partial PBE0 density of states of doped Ga-Vo<sup>5</sup>-Ga<sub>ax</sub>. The inset shows the atomic (Ga<sub>tot</sub>) and 3d (Ga<sub>3d</sub>) contributions of all Ga, those close (Ga<sub>3d</sub><sup>c</sup>) and far (Ga<sub>3d</sub><sup>f</sup>) from the O vacancy, as well as that of the 2p orbitals of all O atoms (O<sub>2p</sub>), and those close (O<sub>2p</sub><sup>c</sup>) and far (O<sub>2p</sub><sup>f</sup>) from the O vacancy.

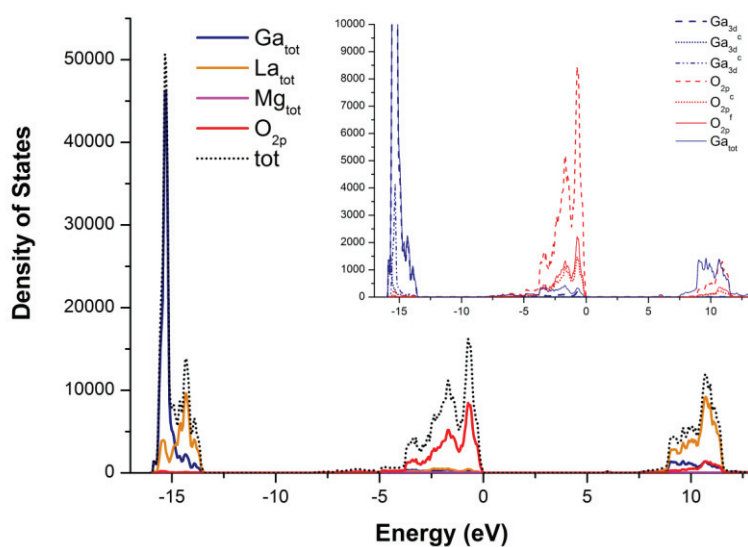


**Figure S.2.4** Total and partial PBE0 density of states of doped Ga-Vo<sup>1</sup>-Mg<sub>ax</sub>. The inset shows the atomic ( $Ga_{tot}$ ) and 3d ( $Ga_{3d}$ ) contributions of all Ga, those close ( $Ga_{3d}^c$ ) and far ( $Ga_{3d}^f$ ) from the O vacancy, as well as that of the 2p orbitals of all O atoms ( $O_{2p}$ ), and those close ( $O_{2p}^c$ ) and far ( $O_{2p}^f$ ) from the O vacancy.

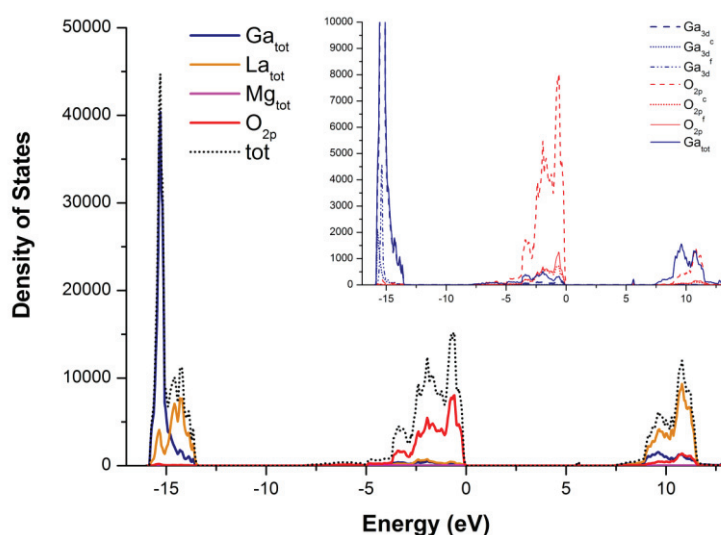


**Figure S.2.5** Total and partial PBE0 density of states of doped Ga-Vo<sup>3</sup>-Ga<sub>eq</sub>. The inset shows the atomic ( $Ga_{tot}$ ) and 3d ( $Ga_{3d}$ ) contributions of all Ga, those close ( $Ga_{3d}^c$ ) and far ( $Ga_{3d}^f$ ) from the O vacancy, as well as that of the 2p orbitals of all O atoms ( $O_{2p}$ ), and those close ( $O_{2p}^c$ ) and far ( $O_{2p}^f$ ) from the O vacancy.

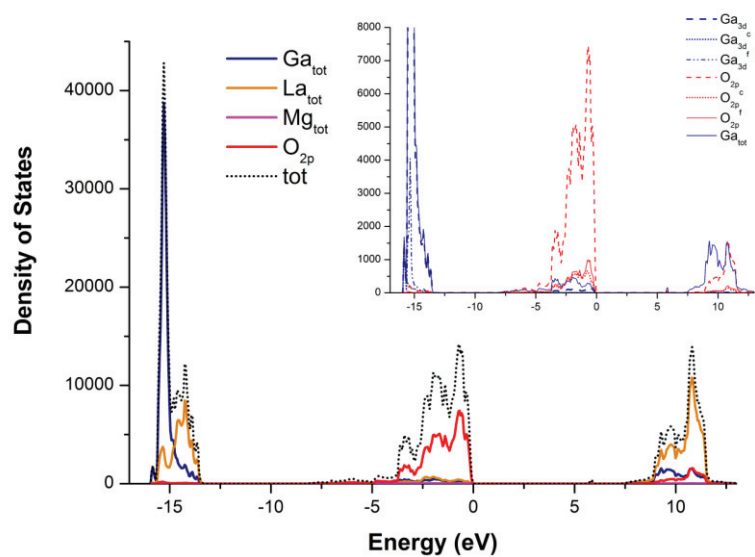


**Figure S.2.6** Total and partial PBE0 density of states of doped Ga-Vo<sup>1</sup>-Mg<sub>eq</sub>. The inset shows the atomic (Ga<sub>tot</sub>) and 3d (Ga<sub>3d</sub>) contributions of all Ga, those close (Ga<sub>3d</sub><sup>c</sup>) and far (Ga<sub>3d</sub><sup>f</sup>) from the O vacancy, as well as that of the 2p orbitals of all O atoms (O<sub>2p</sub>), and those close (O<sub>2p</sub><sup>c</sup>) and far (O<sub>2p</sub><sup>f</sup>) from the O vacancy.

## S.3 SUPPORTING INFORMATION

### Probing electrode-electrolyte interfaces by SXM

**Preparation of materials.**  $\text{La}_{0.98}\text{Ca}_{0.02}\text{NbO}_4$  (LNC) powder was synthesized by solid-state reaction. Stoichiometric quantities of precursors ( $\text{La}(\text{OH})_3$ , Treibacher Industries AG, 99.9%;  $\text{Nb}_2\text{O}_5$ , H.C. Starck, ceramic grade, 99.9%;  $\text{CaCO}_3$ , Solvay Bario e Derivati, grade CF800, 99.95%) were mixed in water for 24 hours, dried and calcined at 1100 °C for 4 hours. After sieving, the powders were isostatically pressed (1500 bar) and sintered at 1400 °C for 4 hours, obtaining a cylindrical pellet of ceramic with relative density of 97%. The phase purity of the synthesized LNC was assessed by XRD (shown in **Figure S.3.1**) and SEM/EDS.

The resulting cylindrical pellet was cut in disks of about 10 mm diameter and 1 mm thickness, and polished. The LNC disks were then surrounded with LSM powder ( $\text{La}_{0.8}\text{Sr}_{0.2}\text{MnO}_3$ , Sigma-Aldrich, >99%) and uniaxially pressed at 7 tons in a 1-inch die. After pressing, the bilayers were annealed at 1150°C for either 12 h (sample A) or 36 h (sample B). Sample C was treated at 1250 °C for 72 h. The samples were then impregnated with resin, cut to expose the interface, and the cross sections were mechanically polished down to 1  $\mu\text{m}$ . SEM/EDS was performed to confirm the mechanical integrity of the bilayers with a LEO 1450VP electron microscope (LEO Electron Microscopy, UK). A representative micrograph is shown in **Figure S.3.2**.

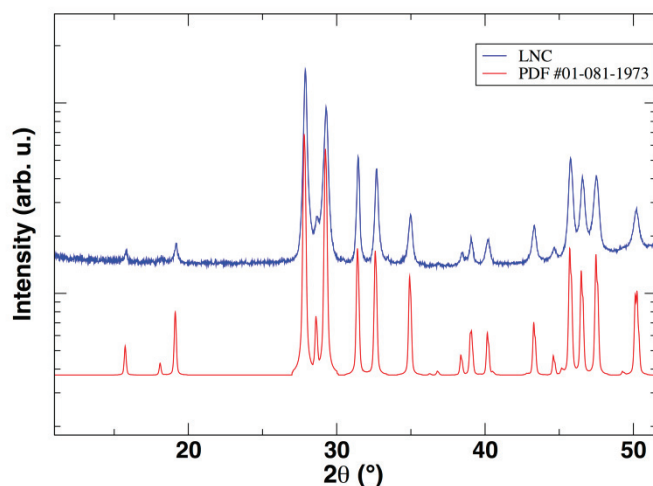


**Figure S.3.1** XRD pattern of synthesized LNC (blue) and theoretical  $\text{LaNbO}_4$  pattern from PDF file #01-081-1973 (red). Intensity is plotted in log scale to highlight the absence of low-intensity peaks due to secondary phases.

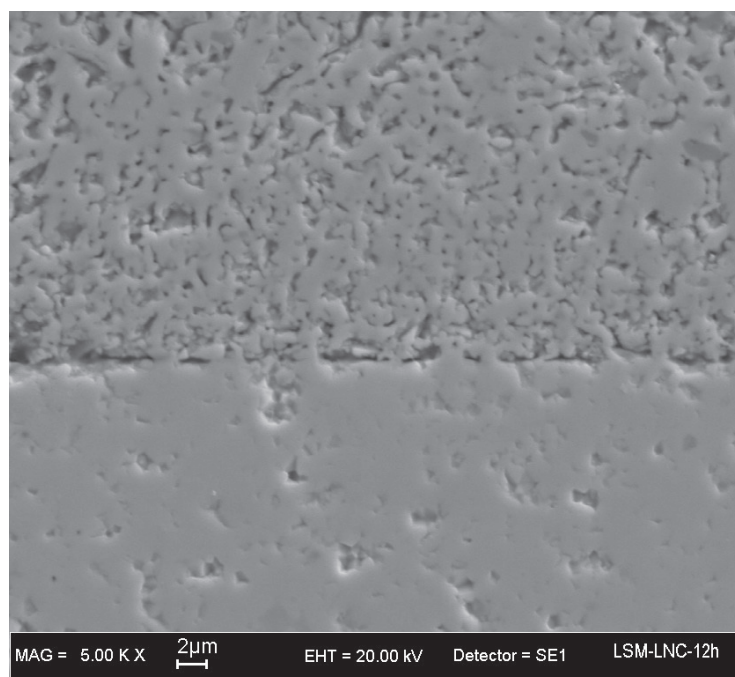


**Figure S.3.2** Sample A: SEM image in secondary electron mode showing the different microstructure of LSM (top) and LNC (bottom).

**X-ray Microspectroscopy.** The microspectroscopy SXM-II endstation at beamline ID21 of ESRF uses a focused micro-beam of monochromatic X-rays from a synchrotron undulator source.<sup>[S1]</sup> The harmonics rejection ( $10^{-3}$ ) is ensured by a set of two flat mirrors deflecting in the horizontal plane, which grazing angle and coating stripes (Si, Ni) allow tailoring the beam spectrum to the needs of the experiment. A double crystal Si(111) fixed-exit monochromator (Kohzu, Japan) is used to select and scan the energy of the monochromatic beam. The beam is focused down to a submicron probe by a fixed curvature Kirkpatrick-Baez (KB) mirrors system. Depending on the primary beam intensity at a given energy, total fluorescence from the sample and detector deadtime, in some cases an attenuator was used, obtaining a photon flux on the sample between  $5 \cdot 10^9$  and  $3 \cdot 10^{10}$  ph/s. The microscope is operated in a vacuum chamber to avoid air absorption and scattering of the beam. The change of sample is performed through a load-lock chamber. The flat sample is aligned in the focal plane of the KB mirrors with an optical videomicroscope, which allows an accurate positioning of the selected region of interest. The experimental setup is depicted in **Figure S.3.3**. The beam energy was scanned in the vicinity of Nb  $L_3$ -edge (2380 eV), La  $L_3$ -edge (5500 eV) and Mn K-edge (6550 eV) for the  $\mu$ XANES and  $\mu$ EXAFS experiments. To collect the  $\mu$ XRF maps,

the beam energy was kept fixed at 50 eV, 190 eV or 400 eV above the edge energy (for Nb, La and Mn edges, respectively).

Micro-XRF maps of the interlayer were acquired with a step size tunable between 0.25  $\mu\text{m}$  and 1  $\mu\text{m}$ . The X-ray fluorescence (XRF) photons emitted by the sample are collected using a 80  $\text{mm}^2$  Silicon Drift Diode (SDD) detector (Bruker, Germany). The sample is then raster scanned in two-dimensions in the micro-beam using piezoelectric actuators to produce a 2D XRF map. All signals were corrected for the incident flux by normalizing the signal for the X-ray beam current measured before the sample with a membrane photodiode. A complete fluorescence spectrum is acquired for each pixel, allowing off-line fitting of the spectra and deconvolution of the elemental distributions using the PyMca software.<sup>[S2]</sup> The mass fraction of each element was determined by modeling the microXRF spectra either pixel-by-pixel, or integrating the intensity over a region. **Figure S.3.4** shows the regions used to obtain the XRF results shown in Table 1 and S1. In selected spots, a microXRF spectrum was collected alongside the microEXAFS signal. In the XRF fittings, attenuation and self-absorption effects are accounted for by specifying the matrix composition, and the results were first validated using pure LNC and LSM. Examples of the signal and fitting quality are shown in Figure S5, S6 and S7. Small spurious peaks shown in dark green in the XRF plots (Al and Si) are attributed to optics and experimental chamber. Elastic and inelastic scattering peaks are indicated together as “scattering” in the plots.

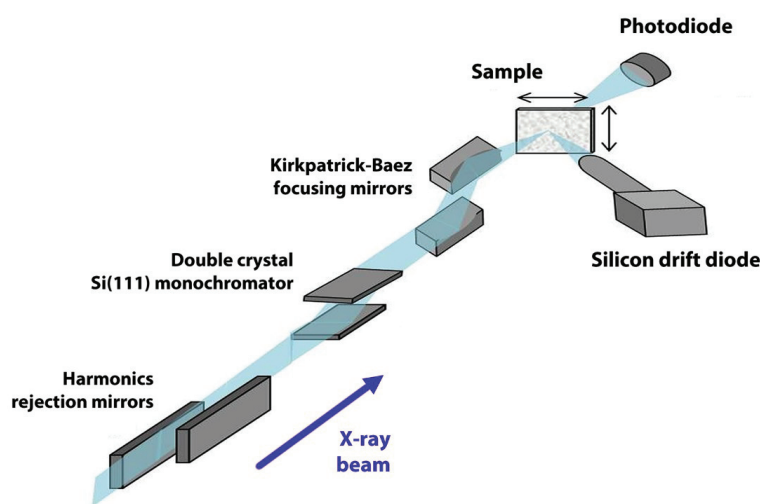


**Figure S.3.3** The X-ray microscopy setup of beamline ID21 at ESRF.

**μXRF analysis at the Mn K-edge.** Table S.3.1 reports the elemental compositions in three regions of sample A, as determined with μXRF analysis with an incident beam of 5690 eV: such energy is not high enough to excite the K fluorescence lines of Mn, so the Mn content is estimated by difference. These estimates were confirmed independently by repeating the μXRF analysis on data taken on the same regions with an incident beam energy of 6900 eV. The results are summarized in **Table S.3.1**.

**Table S.3.1.** Elemental composition (weight %) of three regions of sample A from XRF analysis at the Mn K-edge. The nominal compositions of LNC and LSM are reported for comparison. Regions 1-3 are depicted in Figure S4.

Element	Region #1 (LSM)	Region #2 (interface)	Region #3 (LNC)
La	48.61	46.27	45.73
Sr	8.723	9.157	0.002
Ca	0.0273	0.3837	0.1545
Nb	0.5452	3.8051	32.1934
Mn	22.171	21.295	0.128

**Assessment of systematic errors in μXRF analysis.** In XRF analysis, the main uncertainty in the determination of elemental concentrations is due to the matrix effect. In the case of μXRF, this may occur due to the inhomogeneity of the matrix in a given region, whereas a single matrix composition is used throughout the region. Eventually, the uncertainty in the elemental composition of the matrix propagates to the fitting results. The effect of such propagation was assessed empirically with the following method (this is described for La L<sub>3</sub>-edge): 1) in a single LSM region near the interphase, the matrix composition was imposed to vary from 70% to 130% of each cation with respect to the nominal composition, and the different fitting results (for La, Sr, Ca and Nb) were obtained; 2) the correlation curves were determined between each of the fitted results and each component of the matrix. All correlations are very strong ( $R^2 = 0.99$ ) and linear in the whole range considered; 3) the “real”



variance of the matrix in our samples was assessed by analyzing several LSM regions with a fixed matrix  $\text{La}_{0.8}\text{Sr}_{0.2}\text{MnO}_3$ . The variance in the results is about 0.02% w/w and 0.006% w/w for Sr and La, respectively. These correspond to an uncertainty on stoichiometric numbers of  $\pm 0.007$  and  $\pm 0.005$  for La and Sr, respectively. The concentration of Mn, though not determined directly from the fitting, is obtained by difference: its variance is 0.004% w/w, corresponding to  $\pm 0.015$  on the stoichiometric number; 4) using the correlation curves, the variance of the concentrations of the other cations due to the variance of the matrix is estimated: 0.0001% and 0.0004% w/w on Ca and Nb, respectively. These correspond to an uncertainty on the stoichiometric numbers of  $\pm 0.0002$  and  $\pm 0.0004$  for Ca and Nb, respectively.

**$\mu$ XANES and  $\mu$ EXAFS analysis.**  $\mu$ XANES spectra on the Nb  $L_3$ -edge were modeled up to 6  $\text{\AA}^{-1}$  after the absorption edge with Feff8.4,<sup>[S3]</sup> using the SCF and FMS control cards. In the structural models corresponding to the spectra shown in **Figure 5.2**, the Nb absorber was placed either: a) in its regular crystallographic site of monoclinic  $\text{LaNbO}_4$ ; b) in the perovskite B-site of LSM. Sr was placed in 20% of the surrounding A-sites to account for La/Sr random substitution.  $\mu$ EXAFS spectra on the Mn K-edge collected in selected points of the maps were analyzed with Viper,<sup>[S4]</sup> using theoretical amplitudes and phase shifts generated with Feff8.4. The fitting model of the Mn local environment was built by placing the Mn atom in the B-site of a mixed (La,Sr,Ca) $\text{MnO}_3$  perovskite: the second shell signals Mn-La, Mn-Sr and Mn-Ca were weighed according to actual stoichiometry derived by  $\mu$ XRF results. The fitting was performed in R-space up to the third shell, including multiple scattering contributions from colinear Mn-O-Mn paths. By use of constraints, the number of refined variables was kept at a minimum, i.e. 9 fitting parameters for 16 independent points according to the Nyquist criterion. The fitting results are reported in Table **S.3.2**. The first shell bond length (1.99  $\text{\AA}$ ) is consistent with a 6-coordinated mixed valence site  $\text{Mn}^{3+} / \text{Mn}^{4+}$ .<sup>[S5]</sup>

**Table S.3.2** Results of the microEXAFS analysis shown in Figure 3

	Distance (Å)	Disorder factor ( $10^{-3}$ Å)
Mn-O	1.99(2)	0.009(4)
Mn-(La,Sr, Ca)	3.32(3)	0.016(4)
Mn-Mn	3.92(3)	0.016(4)

\* Goodness-of-fit (R-factor) = 7.7 %.  $S_0^2 = 0.8(3)$  and  $\Delta E_0 = -7(1)$  eV (common to all paths). Coordination numbers are fixed from stoichiometry. The uncertainty on the last digit is reported in parentheses.

[S1] M. Salomé, M. Cotte, R. Baker, R. Barrett, N. Benseny-Cases, G. Berruyer, D. Bugnazet, H. Castillo-Michel, C. Cornu, B. Fayard, E. Gagliardini, R. Hino, J. Morse, E. Papillon, E. Pouyet, C. Rivard, V. A. Solé, J. Susini, G. Veronesi, *J. Phys. Conf. Series* **2013**, 425, 182004-1.

[S2] V. A. Solé, E. Papillon, M. Cotte, P. Walter, J. Susini *Spectrochim. Acta B* **2007**, 62, 63.

[S3] A. L. Ankudinov, B. Ravel, J. J. Rehr, S. D. Conradson, *Phys. Rev. B* **1998**, 58, 7565

[S4] K. D. Klementev, *J. Phys. D: Appl. Phys.* **2001**, 34, 209

[S5] I.G. Krogh Andersen, *J. Solid State Chem.* **1994**, 113, 320.

## Curriculum Vitae

**Name:** Marianna Gambino

**Date of birth:** 01/10/1987

**Place of birth:** Palermo

### Full Career

- January 2014 – December 2016. **Ph.D. Student in “Scienza dei Materiali e Nanotecnologie”** (University of Catania-University of Palermo).
- 20 September 2016 – 20 October 2016. **Visiting Ph.D. student at Dubble BM26 beamline of the European Synchrotron Radiation Facility (ESRF)** (Grenoble).
- 15 October 2015 – 30 April 2016. **Visiting Ph.D. student at the École Nationale Supérieure de Chimie de Paris (Chimie ParisTech) , group “Modélisation des Systèmes Complexes”** (Paris).
- 2014. **Qualification exam for the Italian board of chemists.**
- October 2013. **M.Sc. graduation in Chemistry**, University of Palermo (110/110 *cum laude*).
- May 2011 – July 2011. **Trainee at CNR-ISMN, Palermo. ”Synthesis and Characterization of Perovskite Nanostructured Materials for IT-SOFC Applications”.**
- March 2011. **B.Sc. in Chemistry.**

### List of publications

- Francesco Giannici\*, Giovanna Canu, Marianna Gambino, Alessandro Longo, Murielle Salomé, Massimo Viviani, and Antonino Martorana “Electrode–Electrolyte Compatibility in Solid-Oxide Fuel Cells: Investigation of the LSM–LNC Interface with X-ray Microspectroscopy” *Chem. Mater.* **2015** 27, 8, 2763-2766.

- Marianna Gambino , Francesco Giannici\*, Alessandro Longo, Stefania Di Tommaso, Labat, F. and Antonino Martorana “Dopant clusterization and oxygen coordination in Ta-doped bismuth oxide: a structural and computational insight into the mechanism of anion conduction” *J. Phys. Chem. C* **2015** 119, 47, 26367-26373
- Marianna Gambino\*, Stefania Di Tommaso, , Francesco Giannici, Alessandro Longo, Carlo Adamo, Frédéric Labat\* and Antonino Martorana “Defect interaction and local structural distortions in Mg-doped LaGaO<sub>3</sub> electrolyte for fuel cell application: a combined experimental and theoretical study” *J. Phys. Chem. C* **2016** (Submitted)

### Conferences (presenting author)

- Francesco Giannici, Giovanna Canu, Marianna Gambino, Alessandro Longo, Murielle Salomé, Massimo Viviani, and Antonino Martorana “Electrode–Electrolyte Compatibility in Solid-Oxide Fuel Cells Probed with X-ray Microspectroscopy” XXIII SILS Meeting, 8-10 Luglio 2015, Trento (oral presentation).
- Marianna Gambino , Francesco Giannici, Stefania Di Tommaso , Alessandro Longo and Antonino Martorana “Effect of Ta<sup>5+</sup> doping on the short-range structure of cubic Bi<sub>2</sub>O<sub>3</sub>: a X-Ray Absorption Spectroscopy and Density Functional Theory study” XXIII SILS Meeting, 8-10 Luglio 2015, Trento (poster).
- Francesco Giannici, Giovanna Canu, Marianna Gambino, Alessandro Longo, Murielle Salomé, Massimo Viviani, and Antonino Martorana “Electrode-Electrolyte Compatibility in Solid-Oxide Fuel Cells: Investigation of the Interface with X-Ray Microspectroscopy” FISMAT 2015, 28 Settembre-2 Ottobre 2015, Palermo (oral presentation).
- Marianna Gambino , Francesco Giannici, Stefania Di Tommaso , Alessandro Longo and Antonino Martorana “Ta-doped Bi<sub>2</sub>O<sub>3</sub> investigated with X-Ray Absorption Spectroscopy and Density Functional Theory” FISMAT 2015, 28 Settembre-2 Ottobre 2015, Palermo (poster).

## **Other contributions**

Francesco Giannici, Giuliano Gregori, Chiara Aliotta, Marianna Gambino, Alessandro Longo, Hugo Vitoux, Fabio Comin, Joachim Maier and Antonino Martorana “X-ray Absorption under Operating Conditions for Solid-Oxide Fuel Cells Electrocatalysts” XXIII SILS Meeting, 8-10 Luglio 2015, Trento.

## **Schools**

- Advances in Medium and High Temperature Solid-Oxide Fuel Cell Technology (14-18th July 2014, CISM, Udine)
- Hercules Specialized Course (HSC17): Dynamical Properties Investigated by Neutrons and Synchrotron X-Rays (14-19th September 2014, ESRF Grenoble)
- Energy Production, Storage and Conversion from Molecules to Devices at the Crossroads of Physical Chemistry (8-12th June 2015, Otranto - Italy)
- International School on Ab initio Modelling of Solids 2015 (19-24th July 2015, Regensburg - Germany)
- 13th School on Synchrotron Radiation: Fundamentals, Methods and Applications (14-25th September 2015, Grado - Italy)

## Acknowledgements

First of all, I would like to thank my supervisor, Prof. Antonino Martorana, for giving me the possibility to work as a Ph.D. student in his research group and for the many opportunities he offered me during these years. I would also like to acknowledge Dr. Francesco Giannici for his co-supervisor activity.

I would like to express my gratitude to Dr. Alessandro Longo, for giving me the opportunity to expand my knowledge in the field of X-Ray Absorption Spectroscopy, for sharing with me his scientific experience in this field, for his advices and for his great support and encouragement.

I am thankful to Prof. Carlo Adamo, who has given me the chance to work for six months in his research group at the École Nationale Supérieure Chimie Paris-Tech. I want to particularly thank Dr. Frédéric Labat for supervising the computational part of this work, for his guidance and for fruitful discussion. I would also like to acknowledge Prof. Carlo Adamo, Dr. Ilaria Ciofini and Dr. Frédéric Labat for providing the computational resources necessary to develop part of this research project.

All the X-Ray Absorption Spectroscopy measurements in this thesis were collected at the DUBBLE BM26 beamline of the European Synchrotron Radiation Facility in Grenoble. I would like to acknowledge Dr. Dipanjan Banerjee and the staff of BM26 for the beamtime (experiment CH4496) and for hosting me as visiting Ph.D. student for one month. I would also like to acknowledge ID21 staff for the beamtime supplied during these years (experiments ME1351, ME1373 and ME1396).

I am grateful to Dr. Leonarda Liotta and Dr. Francesca Deganello for providing some of the instrumentation of CNR-ISMN needed for the experimental part of this thesis and for their great availability and collaboration. I would also like to acknowledge Dr. Francesco Giordano for the X-Ray Diffraction measurements and Dr. Giovanna Canu of CNR-IENI (Genova) for the preparation of the electrode/electrolyte bilayers.

Thanks to Chiara, not only for her fundamental scientific contribution to the synthesis of lanthanum gallate electrolytes, but most of all for her friendship, wisdom and for the great support she gave me during these years. Thanks to Remedios, for all the good times and bad times we have shared together, for the sincere friendship and the unlimited patience.

Thanks to all the people that I have met during the months I have spent in France. Thanks to Stefania, for her precious scientific guidance and help, for her friendship and for making me discover unconventional beautiful corners of Paris. Thanks to Marta, Chiara, Maddalena, Liam, Valentino, Ivan and Bartolo for the unforgettable time we have shared together. Thanks to Alessandra, Beatrice and Aglaia, who made the time I have spent in Grenoble very special and never made me feel alone.

Thanks to my extraordinary parents for their relentless support and to my brother, who always reminds me to be strong and hold on. And finally, thanks to Roberto for his unconditioned love and for being by my side throughout these years.